MICROSTRUCTURAL CHARACTERIZATION OF A PLASMA SPRAYED ZrO_2-Y_2O_3-TiO_2 THERMAL BARRIER COATING

A thesis submitted for the degree of Doctor of Philosophy

by

Pedro Antonio Díaz Angulo

Department of Materials Engineering, Brunel University
Uxbridge, Middlesex, United Kingdom

December 1996

ABSTRACT

The use of plasma sprayed ceramic coats as thermal barrier coatings (TBCs) for the protection of metallic structures and equipment from severe thermal, abrasive and corrosive conditions has been documented extensively in the last two decades. The state-of-the-art TBCs consist of a double layer coat: a top ceramic layer and an intermediate bond coat (MCrAlY, M=Ni, Co, Fe) deposited on the alloy substrate. Zirconia, both stabilized and partially stabilized with different oxides has been used as the ceramic top coat due to its low thermal conductivity and low thermal expansion coefficient. Studies of the microstructure of the TBCs have shown aspects that can help the understanding of the properties of the coating. The ternary system ZrO_2-Y_2O_3-TiO_2 is believed to offer improved properties when it is compared to ZrO_2-Y_2O_3. However, the use of ZrO_2-Y_2O_3-TiO_2 as TBCs, a major part of this work, is not widely reported in the literature.

The purpose of this thesis was to study the microstructure of a plasma sprayed ZrO_2-Y_2O_3-TiO_2 TBC using X-ray Diffraction (XRD), Scanning Electron Microscopy (SEM), Energy Dispersive Spectroscopy (EDS), and Transmission Electron Microscopy (TEM). The evolution of the ZrO_2-phase distribution in the ceramic coat was followed by XRD after different heat treatments, with the finding that the cooling rate plays a decisive role in the final ZrO_2 phase composition. SEM studies allowed a description of the lamellae structure of the ZrO_2-Y_2O_3-TiO_2 coating. The evolution of the morphology, porosity and crack distribution in the coat after different thermal treatments were followed by SEM. Evidence of incipient sintering is observed in ZrO_2-Y_2O_3-TiO_2 coats heated at temperatures higher than 1200 °C. This should lead to poor coating performance. EDS analysis revealed an heterogeneous distribution of titanium through the coating. A detailed microstructural characterization of the as-sprayed coating was done using TEM. Microstructural features such as micro-twins, antiphase-boundaries and mottled morphology associated with "non-transformable" tetragonal ZrO_2 phase were identified. It is believed that these microstructural elements promote toughening and thermal stress relief mechanisms that provide the coating with the erosion and thermal shock resistance required for a TBC. The presence of TiO_2 is linked to a higher proportion of tetragonal ZrO_2 in the ZrO_2-Y_2O_3-TiO_2 coating, therefore improved properties of the coating are expected. The addition of TiO_2 promotes grain growth and decreases the final density in pressed and sintered ZrO_2-Y_2O_3-TiO_2 powders.

The results obtained are a contribution to the understanding of the microstructure of TBCs and to the sparse knowledge base of the ZrO_2-Y_2O_3-TiO_2 coatings. Further work should be done in the characterization of the ZrO_2-Y_2O_3-TiO_2 coatings and the study of its stability under different conditions in order to determine the real potential of this material offers as an alternative to the better known ZrO_2-Y_2O_3 TBC.

PUBLICATIONS

Results of the reseach conducted in this thesis have been and are being published as follows:

DIAZ, P. EDIRISINGHE, M. J. and RALPH, B. (1994) Characterization of a Zirconia Yttria-Titania Thermal Barrier Coating. *J. Mater. Sci. Letters*, **13**, 1595.

DIAZ, P. EDIRISINGHE, M. J. and RALPH, B. (1996) Microstructural Changes and Phase Transformations in a Plasma-Sprayed Zirconia-Yttria-Titania Thermal Barrier Coating. *Surf. Coat. Tech.*, **82**, 284.

DIAZ, P. RALPH, B. and EDIRISINGHE, M. J. (1996) Microstructural Characterization of a Zirconia-Titania-Yttria Thermal Barrier Coating. Proceedings of MRS Fall Meeting 1995, Vol 403, p 253.

DIAZ, P. RALPH, B. and EDIRISINGHE, M. J. TEM Characterization of a Plasma Sprayed ZrO_2-Y_2O_3-TiO_2 Coating. In preparation.

ACKNOWLEDGEMENTS

The author is deeply grateful to Professor Brian Ralph and Dr Mohan Edirisinghe for the assistance and guidance throughout all the stages of this work. Many thanks go to Dr A. Reynolds, Dr B. Bulpett and Ms J. Moses of the Experimental Technique Centre (ETC), and Dr S. Woodise, Ms R. Pratt and Mr P. Dodia of the Materials Engineering Department at Brunel University. The author acknowledges gratefully the financial support given by the British Council and the Consejo Nacional de Investigaciones Científicas y Tecnológicas (CONICIT), Venezuela. Special thanks to Miriam, Andrés José and Gladys Adriana.

CONTENT

1 INTRODUCTION

In most of the different refining, exploration and production processes involved in the oil industry there are problems that constitute challenges to Materials Science and Engineering. In particular, the materials for tools and for machine components exposed to drastic operational conditions such as high temperature, hot corrosion, abrasion, and erosion need to be established. Some typical examples are a) the drilling tips used in perforation procedures, b) the heat-sink designed for oil extraction, c) the cooling elements and holders inside heat exchangers used in the refining process. These operative parts have a limited useful life.

Coating treatments are known to be very effective in protecting metallic structures and equipment from severe thermal, abrasive and corrosive conditions. Historically the motivation for coating development has been concentrated on aircraft gas turbine components. Thermal barrier coatings (TBCs) have increasingly been used in the past few decades on aircraft gas turbine burners and afterburners (**Jamarini et al. 1992**). A successful coating should be refractory, chemically inert, possess good mechanical strength and thermal shock resistance, have a low thermal expansion coefficient and exhibit a thermal expansion similar to that of the superalloy substrate (**Brandon and Taylor 1989**).

The state-of-the-art TBCs for gas turbine engines are two-layer coating systems that consist of an insulating ceramic outer layer (top coat) and a metallic inner layer (bond coat) between the ceramic top coat and superalloy substrate (**Sun et al. 1993**). The intermediate bond coat, MCrAlY (where M indicates Ni, Co, Fe, or their combinations) protects the substrate from high temperature oxidation and corrosion and also provides a rough surface for mechanical bonding between the top coat and the bond coat itself. The function of the ceramic coat is to insulate the metallic substrate from high surface temperatures. ZrO_2 stabilized or partially-stabilized by the addition of MgO, CaO, Y_2O_3 or other rare-earth oxides has been used as the top coat material by virtue of its very low thermal conductivity and its relatively high coefficient of thermal expansion (for ceramics). ZrO_2-based coatings containing around 8 wt% Y_2O_3 have received the most extensive investigation (**Benner and Nagelberg 1981, Miller et al. 1987, Sun et al. 1993**). These tetragonal-cubic phase Y_2O_3-stabilized coatings have been utilized to avoid potentially severe cracking associated with the large volume change (about 6%) transition to the monoclinic phase inherent in pure ZrO_2. Nevertheless, failure of the ZrO_2-based coatings is attributed usually to destabilization and the associated phase transitions by either thermal cycling or reaction with fuel impurities (**Benner and Nagelberg 1981, Jones 1991**).

In partially-stabilized plasma-sprayed ZrO_2-Y_2O_3 coatings, as in quenched bulk material, the main phase observed at room temperature is a non-equilibrium, high-Y_2O_3 tetragonal phase (*t'*-ZrO_2), denoted as "non-transformable" because it is reluctant to transform to the monoclinic phase (**Miller et al. 1981**). Improved performance has been associated to the properties of this *t'*-ZrO_2 phase. However, the *t'*-ZrO_2 phase is unstable at high temperature and phase separation into cubic and tetragonal phases is expected with exposure to high temperature. Coating durability is believed to be determined by the residual content of *t'*-ZrO_2 phase (**Harmsworth and Stevens 1992a**).

There are few reports in the open literature dealing with the microstructure of plasma-sprayed ZrO_2 coatings and their microstructure-property relationships. For instance, **Harmsworth and Stevens** (1992a) reported a microstructural investigation of ZrO_2(6-12)wt% Y_2O_3 coatings. They described the coating as a lamellae-structure, a result of the plasma-spraying application process of the coating. They also observed cross-section foils from the bond coat to the top ceramic layer using Transmission Electron Microscopy (TEM). They reported the presence of an amorphous interfacial region between the bond coat and the ceramic coat which could be linked to the strong adhesion between these layers. Additionally they described a glassy phase in the grain boundary which would provide a diffusion path or lead to grain boundary failure. The presence of an amorphous phase between the bond coat and the substrate had been proposed previously by **Lelait et al.** (1989, 1992). They attributed this phase to the migration of aluminium from the bond coat towards the substrate. This phase is believed to give oxidation protection to the substrate.

A more detailed study has been reported by **Alpérine and Lelait** (1994) on a ZrO_2-8.5wt%Y_2O_3 ceramic coating. This study included the identification of some microstructural features associated with the *t'*-ZrO_2 phase: microtwins, antiphase boundaries (APBs) and a "tweed-like" morphology. These microstructural features have been proposed as responsible for the higher toughness of *t'*-ZrO_2 when it is compared to cubic ZrO_2 (**Alpérine and Lelait 1994, Chaim et al 1985, Michel et al. 1993**). As it can be seen, the study of the microstructure of the ZrO_2 coatings supplies relevant information that can be used in the interpretation of the properties of the coating.

Although the intentions of using TiO_2 as a ZrO_2 stabilizer have not proved satisfactory (**Pandolfelli 1989b**), the study of the ternary system ZrO_2-Y_2O_3-TiO_2 shows this system to be a potential source of *t*-ZrO_2 (**Pandolfelli 1989a, Pyda et al. 1992, 1993**). **Hofmann et al.** (1989) reported that the system ZrO_2-Y_2O_3-TiO_2 showed a better resistance to degradation in a humid atmosphere at 200 and 500° C than a ZrO_2-Y_2O_3 system because TiO_2 has a lower tendency to form an hydroxide than Y_2O_3. Therefore, the system ZrO_2-Y_2O_3-TiO_2 should offer higher toughness and better resistance to a humid environment when it is compared to the widely known ZrO_2-Y_2O_3. The ZrO_2-Y_2O_3-TiO_2 system is thought to have improved properties as thermal barrier coat, such as resistance to erosion, corrosion and thermal shock (**Metco 1984**).

The objective of this thesis was to study the microstructure of a plasma- sprayed ZrO_2-Y_2O_3-TiO_2 coating by using X-ray Diffraction (XRD), Scanning Electron Microscopy (SEM), Energy Dispersive Spectrometry (EDS) and Transmission Electron Microscopy (TEM).

The system under study in this thesis was a thermal barrier coating consisting of a plasma-sprayed ZrO_2-10wt%Y_2O_3-18wt%TiO_2 top coat and an intermediate

NiCoCrAlY bond coat on a high Cr-Ni stainless steel substrate. The samples were supplied by INTEVEP, S.A. and prepared by Plasmatec, Estado Miranda, Venezuela.

The ZrO_2-phase distribution and stability after heat treatment were studied and compared to a ZrO_2-8wt%Y_2O_3 coating by using XRD. The details of the ZrO_2-phase evolution in the ZrO_2-Y_2O_3-TiO_2 coating after different heat treatments were followed by XRD. The morphology, porosity and crack distribution were studied by SEM observation of the coating cross-sections and fracture surfaces. A detailed study of the microstructure of the ZrO_2-Y_2O_3-TiO_2 coating was conducted using TEM; some microstructural elements characteristics of each phase were identified. Comparisons between the as-sprayed coating and as-thermal treated at 1400 and 1600 °C were established. The microstructural features observed are discussed and related to the properties of the coating. Pressed and sintered ZrO_2-Y_2O_3-TiO_2 bodies, prepared from fine powder, were also examined by SEM and TEM. The information gained from these analyses was used in the discussion of the mechanisms of formation of the microstructure of the plasma sprayed coat. The mechanisms of phase transformation involved during the plasma spraying and thermal treatment of the ZrO_2-Y_2O_3-TiO_2 coat were also discussed.

2 LITERATURE REVIEW

In this Chapter some basic aspects related to ZrO_2 are presented. Special attention has been devoted towards the use of ZrO_2 in thermal barrier coatings; the state of the art, preparation and properties of these coatings have been included.

2.1 ZrO_2 CERAMICS

ZrO_2 is a case study in Materials Science and Engineering since its structure-property relationships have been very extensively examined. Atomic structure, microstructure, defects, phase transformations and processing on the one hand and thermal mechanical, electrical and optical properties on the other are intimately connected in ZrO_2 (**Subbarao 1981, Kountouros and Petzow 1993**).

The main sources of ZrO_2 are 1) Baddeleyite in Brazil, which contains 80-90% ZrO_2, with TiO_2, SiO_2, Fe_2O_3 as major impurities and 2) Zircon, $ZrSiO_4$, which occurs as secondary deposits in Kerala (India), New South Wales (Australia), and Florida (USA). With its presence as 0.02-0.03% in the earth's crust, ZrO_2 is more abundant than many metallic ores (**Subbarao 1981**).

2.1.1 The Crystal Structure

The polymorphic nature of ZrO_2 and the influence of this on the mechanical properties of this material have been studied for a few decades (**Garvie 1975, Bansal and Heuer 1972**). ZrO_2 has three allotropes: monoclinic, tetragonal and cubic. The cubic phase (c-ZrO_2) is stable from 2370 °C to the melting point (2680 + 15 °C), it has a fluorite-type crystal structure in which each zirconium is co-ordinated by eight equidistant oxygen atoms and each oxygen is tetrahedrally co-ordinated by four zirconium atoms (Figure 2.1). The tetragonal phase (t-ZrO_2) is stable between about 1170 and 2370 °C. In t-ZrO_2 each zirconium atom is surrounded by 8 oxygen atoms, four at a distance of 0.2455nm and the other four at a distance of 0.2065nm. The monoclinic phase (m-ZrO_2) is stable at all temperatures below 1170 °C.

2.1.2 Phase Transformations

In general, it can be said that two categories of phase transformations occur in ZrO_2 materials. By 1800 °C, the diffusion of both ionic species allows diffusion-controlled transformations to occur. This results in the usual phase equilibria being functions of temperature and composition, as predicted by conventional phase diagrams (**Anderson 1988, Heuer et al. 1988**). Below ≈ 1800 °C, cation diffusion becomes sluggish and transformations, when they occur, are of the diffusionless type. It has been widely accepted that the transformation $t \rightarrow m$-ZrO_2 has a martensitic nature (**Heuer and Rühle 1983, Anderson 1988, Heuer et al. 1988, Rühle and Heuer 1983**).

2.1.2.1 Diffusionless Transformations

2.1.2.1.1 Martensitic Transformation

Martensite is the name given to the hard metastable product phase which develops when Fe-C alloys are strengthened by quenching. The particular type of solid-state transition which leads to the formation of martensite is known as a martensitic reaction Although martensite in Fe-C alloys is a metastable phase and martensitic reactions are usually associated with rapid cooling, equilibrium phases form martensitically in both metallic and non-metallic systems; the transformation in t-ZrO_2 is to an equilibrium monoclinic structure (**Evans and Heuer 1980**). Martensitic transformations are usually diffusionless, occur athermally, and involve a shape deformation. This last characteristic is usually cited as the *characteristic* feature of a martensitic reaction.

A change of shape in the transforming region is the most convenient experimental criterion for recognising the occurrence of martensitic reactions. The transition is accomplished by the shearing of discrete volumes of material, resulting in a shape change. This change, in turn, implies that the product regions remain essentially coherent with the parent phase, i.e. for a given composition, there is a definite and constant orientation relation between the parent and the product crystals and there exists a definite habit plane. The misfits at the parent/product interface are periodically alleviated by twinned or slipped lamellae (Figure 2.2).

Martensitic reactions are usually athermal, i.e. they occur only when the temperature is changed. This behaviour occurs because the shape and volume changes associated with the diffusionless nature of the reaction, are not relieved by atomic migration. The resultant increase in strain energy opposes the progress of the transition, causing it to stop while still incomplete: hence only a few nuclei are active at a particular temperature. A greater driving force, which comes from larger undercooling, is required to induce further reaction. The additional strain energy of the transformation explains the occurrence of the transition over a temperature range (instead of a single characteristic temperature) and the existence of a hysteresis in the forward (cooling) and reverse (heating) reactions.

On cooling, the transformation invariably begins at a characteristic "martensitic start" temperature M_s, and is complete when the temperature falls to M_f. The transformation is diffusionless in that no thermally activated diffusion is required. Many martensitic reactions occur at quite low temperatures, even near absolute zero. Furthermore, M_s is a function of pressure and such transformations can be induced by a change in pressure. Although some transitions in non-metallic solids occur at high temperatures, they are also believed to be diffusionless. In the absence of diffusion, the atomic movement must be co-ordinated and orderly, in agreement with the observation that atoms have the same neighbours in the product and parent phases and thus any atom movement is by less than an interatomic distance. Thus, the reactions must also be composition invariant, i.e. the product and parent phase must have the same composition **(Evans and Heuer 1980).**

2.1.2.1.2 *Martensitic Transformation in ZrO_2.*

ZrO_2 is one of the few oxide ceramics that undergoes a martensitic phase change. This occurs between a high temperature *t*-ZrO_2 and a low temperature *m*-ZrO_2. In pure ZrO_2 the estimated temperature M_s at which *t*-ZrO_2 spontaneously begins to transform to *m*-ZrO_2 is 1047 °C. Thermal cycling through the transformation range (800-1200 °C) causes cracking and sometimes complete disintegration of sintered specimens because a volume change of 3% accompanies this transformation **(Rühle and Heuer 1983, Evans and Heuer 1980).**

In ZrO_2-alloys, the M_s temperature decreases with *t*-ZrO_2 particle size, and is a complex function of alloying content and the local internal stress environment around a *t*-ZrO_2 particle. Further transformation is induced by a reduction in temperature below M_s, or by the application of stress if the *t*-ZrO_2 is sufficiently metastable, and it is this latter ability which leads to be toughening in ZrO_2 and ZrO_2-containing materials.

2.1.2.1.3 *Displacive Transformation c→ t-*ZrO_2.

This transformation has been described in ZrO_2-rich alloys in the ZrO_2-Y_2O_3 system (for example **Scott 1975, Heuer and Rühle 1983, Heuer et al. 1987, 1988**). If these alloys are rapidly cooled from the single *c*-ZrO_2 phase field, the *c*-ZrO_2 phase undergoes a displacive and diffusionless phase transformation to *t*-ZrO_2. The quenching process is necessary only to prevent the occurrence of diffusional phase transformations. The thermodynamic conditions defining the occurrence of this phase transformation are explained in Section 2.1.5.

2.1.3 ZrO_2 Stabilization

Both the structural and electrical properties of ZrO_2 depend on the phase content and the phase stability in the first instance, and control of these parameters is achieved by alloying with other oxides in conjunction with specific sintering and heat treatment sequences (**Bansal and Heuer 1972, Butler 1985a**).

The addition of some oxides such as CaO, MgO, Y_2O_3, and rare-earth oxides lower the two transition temperatures (*m*→ *t*-ZrO_2, *t*→ *c*-ZrO_2). The incorporation of alloying elements not only decreases the transition temperatures, but decreases the linear thermal expansion coefficient of the two-phase material, and also the volume change associated with the *m*→ *t*-ZrO_2 change (**Subbarao 1981, Butler 1985a**).

2.1.3.1 ZrO_2 Alloys

The three main types of alloyed ZrO_2 ceramics are shown schematically in Figure 2.3. The types shown can be classified as:

a) Fully-stabilized ZrO_2 (FSZ), having the *c* fluorite microstructure, with a suitable solute content.

b) Partially-stabilized ZrO_2 (PSZ), having a *c* + *t* (+ *m*) microstructure in which the *t*-ZrO_2 phase is in the form of a fine (≈ 0.1-0.2 μm) metastable precipitate normally produced by ageing. The doping agent is present at a concentration less than that for complete stabilization.

c) Tetragonal ZrO_2 polycrystal (TZP), having a fully *t*-ZrO_2 microstructure of fine (< ≈ 1μm) grain size produced by controlled processing of extremely fine starting powder. The schematic features presented in Figure 2.3 are common to ZrO_2-MgO, ZrO_2-CaO and ZrO_2-Y_2O_3 binary systems, but only for ZrO_2-Y_2O_3 is the *t*-ZrO_2 phase field extensive. Hence, only Y_2O_3-stabilized TZP (Y-TZP) has been successfully fabricated.

2.1.3.2 The Partially-Stabilized ZrO_2 (PSZ)

Originally, the designation PSZ was generally used for partially-stabilized ZrO_2. It is still sometimes used for all materials that have not been fully-stabilized. The standard-type or classical materials in question contain metastable, convertible particles in the form of fine-grained crystalline precipitation products measuring up to 0.1 μm within cubic crystals of about 50 μm in size. This type of material had already been empirically produced with various degrees of stabilization before the particular action mechanisms were clarified. The production techniques are now well known in both theory and practice: sintering in a temperature range in which only the cubic phase exists (requiring very high temperatures that occasion the formation of a coarse crystalline microstructure) followed by defined cooling or quenching, and subsequent tempering at appropriate temperatures, whereby the metastable particles precipitate within the cubic crystals. The technical expertise centres on knowing the conditions under which the most particles will form to an optimal size. Depending on the nature of the heat treatment employed, the materials can be made to display maximum strength or a combination of less than maximum strength and exceptionally high thermal shock resistance (for example **Bansal and Heuer 1972, Butler 1985a, Scott 1975, Reckziegel 1993, Michel et al. 1993**).

The PSZ consists of single grains containing *m*- and *c*-ZrO_2 domains. As the original *t*-ZrO_2 domain converts to the stable *m*- ZrO_2 form on cooling, the stresses resulting from the accompanying volume increase, instead of rupturing the ceramic, are believed to be relieved by plastic deformation (slip) of the cubic grain around pores and inclusions in the monoclinic-cubic hybrid phase. The fact that PSZ has a lower linear thermal expansion coefficient than pure *m*-ZrO_2 as well as fully-stabilized *c*-ZrO_2 contributes to the better thermal shock resistance of the PSZ (**Butler 1985a, Reckziegel 1993, Michel et al. 1993**).

2.1.3.3 The Tetragonal ZrO_2 Polycrystal (TZP)

This type of material was intentionally crafted on the basis of knowledge gained on transformation-toughening mechanisms. The basic idea evolved out of the notion that it should be possible to construct a dense microstructure consisting exclusively of minute *t*-ZrO_2 crystallites that remain metastable -at least those below the material surface- down to room temperature, staying available for transformation toughening, thus the name TZP. Indeed, the idea was proven feasible using extremely fine crystalline ZrO_2 starting materials in which a stabilizer (usually Y_2O_3) is homogeneously distributed. The sintered product exhibits a high-density microstructure in which all of the individual crystallites remain below the critical size, above which *t*-ZrO_2 particles do not remain metastable at room temperature. Now that TZP materials can be produced from nearly 0.1 % metastable *t*-ZrO_2 crystallinity, it is not at all surprising to find that the strength of such materials significantly surpasses that of PSZ-type material, in which only a portion of the microstructure consists of metastable *t*-ZrO_2 precipitates (**Nettleship and Stevens 1987**).

2.1.3.4 Stabilization Mechanisms

Although there are different theories and hypotheses to explain metastability of the high-temperature phases (*c*- and *t*-ZrO_2) at low temperatures, the controlling mechanisms responsible are still unknown. It has been established that the particle size has a considerable influence on the *t*→ *m*-ZrO_2 transformation temperature. **Garvie** (1965) estimated the critical crystallite size for the stabilization of the *t*-ZrO_2 was about 30nm; crystallites larger than this critical value, transform to the stable *m*-ZrO_2.

Stabilization by addition of CaO, Y_2O_3, MgO, CeO_2 has been known for many years but the mechanism is still uncertain. In searching for stabilizing oxides, the general criteria have been: 1) the radius of the oxide cation should be close to that of Zr^{4+} (0.080nm) so that it may fit in the crystal lattice without serious distortion; 2) the oxide cation should have a stable +2 or +3 oxidation state; and 3) the crystal structure of the stabilizing oxide itself should be cubic or tetragonal (**Kountouros and Petzow 1993**).

Stabilizing oxides with cation oxidation states below 4+ i.e. Mg^{2+}, Ca^{2+}, Y^{2+} generate oxygen vacancies in the oxide lattice and these are thought to be important in producing stabilization of the *t*- and *c*-ZrO_2 phases. However, CeO_2 where the cation is Ce^{4+} and no oxygen vacancies are produced, is still an effective ZrO_2 stabilizer (**Jones 1991**) . Therefore it appears that the stability of the *t*- and *c*- ZrO_2 phases by tetravalent Ce^{4+} dopant cation are not affected by oxygen vacancies. It has been found that in CeO_2-stabilized TZP after sintering at 1400 °C in air, Ce^{4+} ions partially reduce to Ce^{3+}. The auto-reduction is associated with the creation of oxygen vacancies for charge neutrality (**Kountouros and Petzow 1993**).

2.1.4 Toughening Mechanisms

2.1.4.1 Toughness

Toughness implies that, on fracture, crack propagation is accompanied by some plasticity, but ceramic materials do not generally deform plastically at room temperature. The brittle behaviour can be expressed by the Griffith equation:

$$\sigma_f = (2E\gamma/\pi c)^{1/2} \qquad 2.1$$

where E is the modulus of elasticity, γ is the surface energy and c the size of a pre-existing flaw or crack which will propagate in a brittle manner when the local stress reaches σ_f. Since E and γ are constant, the only route normally available for increasing the fracture strength σ_f, is by reducing the flaw size. This is the method which has been adopted, in developments of hydraulic cements. However, with

ZrO_2 ceramics, an opportunity exists for an alternative approach. The stress-induced phase change can be considered as a form of plasticity, i.e. a shape change in response to an applied load, in just the same way that slip or twinning are forms of plastic deformation in normal ductile crystalline materials. If a material exhibits one (or more) of these mechanisms of plasticity during crack propagation, then there is an effective increase in fracture strength as the effective γ in the Griffith equation is increased. Hence manipulation of the martensitic transformation (together with reducing the flaw size) forms the basis for the development of tough structural ZrO_2 ceramics (**Butler 1985b**).

2.1.4.2 Stress-Induced Transformation Toughening

The basis of this type of toughening is that ZrO_2 particles, precipitates, or small grains below a certain critical size (much below 1 μm), retained in the metastable *t*-ZrO_2 form, can be induced to transform by the stress field of an extending crack (**Rühle and Heuer 1983, Evans and Heuer 1980, Butler 1985b**). At the crack tip, the stress field acts to relax the matrix-constraining force which keeps local regions of *t*-ZrO_2 symmetry, and to provide the necessary shear-strain component to assist the martensitic transformation. Thus crack propagation is retarded by the transformed and transforming particles in the zone ahead of the crack tip. After the crack has passed by, the transformed particles, by virtue of their volumetric expansion, subject the crack walls to a compressive back stress, reducing the magnitude of the tensile forces around the crack (Figure 2.4). This leads to increased toughness. The maximum achievable strength toughness level depends on the transformation potential of the metastable particles, i.e. on their internal structure with the respective stabilizer atoms, their size and the surrounding structure.

Various mechanisms have been suggested to account for the strengthening and toughening of PSZ ceramics. **Garvie and Nicholson (1972)** refer to the sub-grain structure of PSZ ceramics in which 100nm domains of pure ZrO_2 are distributed in a stabilized *c*-ZrO_2. These domains undergo the *t*→ *m*-ZrO_2 transformation on cooling. The volume increase associated with this phase change produces extensive microcracking. Because of the large number of cracks they propagate only in a quasi-static way and the sample retains most of its strength.

Green (1973) studied the fracture toughness of Ca-PSZ in conjunction with its microstructure, and drew attention to the formation of a microcrack zone at the tip of the propagating crack. The stresses developed during the transformation of the pure ZrO_2 grain present at the grain boundaries lead to separation and weakening of the grain boundaries and consequent strength degradation. The initial stable crack propagation is attributed to the increase in the microcrack-zone size. This zone absorbs energy by processes such as secondary crack formation, surface roughening and crack branching.

There has been an intense interest in the mechanical behaviour and thermal processing of PSZ to achieve maximum strength and toughness. **Porter and Heuer** (1979) subjected commercial Mg-PZS to a solution anneal at 1850 °C for 4h. TEM studies revealed inter and intragranular monoclinic particles both of which were formed from t-ZrO_2 and transformed to the m-ZrO_2 during cooling below the M_s temperature. The intergranular particles are believed to have been present during sintering while the intragranular particles are probably formed by precipitation during the post-sintering cooling. Solution-annealed samples essentially consisted of c-ZrO_2 solid solution though a small amount (3%) of a second phase occurs as small plate precipitates (5nm).

Enhanced mechanical properties (strength and fracture toughness) were obtained by ageing at 1400 °C for 4h. Under these conditions, t-ZrO_2 solid solution precipitated in a matrix of c-ZrO_2 solid solution, is retained metastable during cooling. If the t-ZrO_2 particles were converted to the stable m-ZrO_2 phase during cooling, the mechanical properties of the material were found to be poorer (**Porter and Heuer 1979**).

2.1.4.3 Microcrack Toughening

The microcrack toughening also relies on the $t \rightarrow m$-ZrO_2 martensitic transformation, but instead of the M_s temperature of the ZrO_2 regions being just below room temperature, so that transformation can be effected by stress, as for stress-induced transformation toughening, the stability of the ZrO_2 is controlled such that the M_s is just above the room temperature, and so the transformation takes place on cooling the ceramic from the firing or ageing temperature. The volume expansion of the transformation creates tangential stresses, which cause microcracking of the matrix around the particles. The strain energy of a fracture crack is lowered, since the microcracks can extend in response to the stress field of the crack and interact with the main crack to cause crack branching, blunting, and deflection (Figure 2.5). The ceramic is toughened, but optimum conditions are not attained if the ZrO_2 is either too large, or too closely spaced, when the microcracks can readily link up (**Butler 1985b**).

2.1.5 Microstructural Features in ZrO_2-12%wtY_2O_3 Ceramics

Chaim et al. (1985) found different microstructural features in ZrO_2-12wt%Y_2O_3 ceramics after annealing at 1550, 1400 and 1200 °C. After annealing at 1550 °C followed by rapid cooling they observed 90° twins and antiphase boundaries (APBs). As the sample was rapidly cooled, they attributed these features to a composition-invariant *c*→ *t*-ZrO_2 displacive transformation (**Heuer and Rühle 1983, Heuer et al. 1987, 1988**). The *t*-ZrO_2 product of this transformation has been denoted as *t'*-ZrO_2 and called non-transformable because of its reluctance to undergo the conventional *t*→ *m*-ZrO_2 martensitic transformation, however, it is unstable to high temperature annealing. This *t'*-ZrO_2 appears to be an ubiquitous component in plasma-sprayed ZrO_2-8wt%Y_2O_3 thermal barrier coatings (**Miller et al. 1981**).

The formation of twins and APBs, can be understood by considering the free energy vs. composition diagram (Figure 2.6), which is for a temperature so low that diffusive jumps of atoms cannot occur (**Heuer and Rühle 1983, Heuer et al. 1987, 1988, Butler 1985a**).

Compositions between C_o and C_2, after quenching to this temperature will remain single-phase *c*-ZrO_2 indefinitely, although they are in principle unstable to diffusional decomposition to a two-phase mixture of C_1 and C_2. On the other hand, compositions to the left of C_o can undergo a composition-invariant *c*→ *t*-ZrO_2 transformation, leading to an energy reduction of ΔF'. In this transformation, any of the cubic *a* axes can become the *c* axis of the *t*-ZrO_2 phase, leading to 90° twins (**Chaim et al. 1985, Miller et al. 1981, Isihizawa et al. 1986, Takeheshi et al. 1986**).

The APBs also originate during this transformation (**Chaim et al. 1985, Alpérine and Lelait 1994**). The lattice geometry of *c*-ZrO_2 is face centred cubic (fcc, space group *Fm3m*), as shown in Figure 2.7a; each lattice point has associated with it one zirconium atom and two oxygen atoms (one "molecule" of ZrO_2). The lattice geometry of *t*-ZrO_2 is primitive (space group *P42/nmc*) but it is conventional to use a larger cell whose volume is more nearly equivalent to the fcc cell of *c*-ZrO_2; it shows C-centred symmetry (Figure 2.7b). Each lattice point in this cell has two "molecules" of ZrO_2 associated.

Any lattice point in *c*-ZrO_2, say 000, can serve as the nucleus for the formation of *t*-ZrO_2 by this diffusionless transformation. If an adjacent region of crystal nucleated *t*-ZrO_2 at any equivalent but different lattice point, say ½0½ or one of its symmetry-related equivalents, impingement of these two domains during growth would cause an antiphase domain boundary to form. In addition to the tetragonal distortion of the unit cell in *t*-ZrO_2, it further differs from *c*-ZrO_2 in that the oxygen atoms move off their ¼¼¼ (and symmetry-related) fluorite positions; this is shown in exaggerated form in Figure 2.8. Across an APB, oxygen atoms are in disregistry; adjacent pairs of atoms are not in their correct "up-down" displacements off the ¼¼¼ and related positions (**Chaim, et al. 1985, Alpérine and Lelait 1994**).

Comparison of the as-sintered, slowly cooled and the 1550 °C heat-treated and rapidly cooled ZrO_2-Y_2O_3 specimens suggests that formation of fine *t*-ZrO_2 precipitates and the occurrence of the displacive *c*→ *t*-ZrO_2 transformation may be competitive phase transformations (**Chaim et al. 1985**). In this interpretation, it is assumed that the matrix phase of the "tweed" (Figure 2.9) microstructure materials has cubic symmetry and that if precipitation occurs on cooling through the two-phase field (Figure 2.6), the conditions for the displacive reaction must be lost. This could occur if the matrix supersaturation is adequately relieved or if the coherency strain energy raises the free energy of the remaining *c*-ZrO_2 matrix. In this latter case, the crossover composition would move to lower Y_2O_3 contents so the actual composition (12 wt% Y_2O_3) would not be below C_0, except possibly by cooling below room temperature. On the other hand it is possible that the matrix has tetragonal symmetry; i.e. the *c*→ *t*-ZrO_2 transformation has occurred subsequent to the precipitation of the low-solute *t*-ZrO_2 particles. Unfortunately, it is difficult to distinguish between small *t*-ZrO_2 precipitates in a strained *c*-ZrO_2 matrix and small *t*-ZrO_2 precipitates in a *t'*-ZrO_2 matrix using conventional TEM.

2.2 THERMAL BARRIER COATINGS

The use of thermal barrier coatings (TBCs) as a process increases the substrate material capability via overlaying a thermal insulation and strain-tolerant ceramic layer on critical air-cooled metal components. In this way, increased engine efficiency and power or increased durability of components can be achieved (**Wu et al. 1990, DeMasi-Marscin and Gupta 1994, Meier and Gupta 1994**).

Since the late 1970s, research on TBCs has been intensive. Early studies engaged in the improvements of overlaying techniques and selection of materials to be used for TBCs, e.g. optimal plasma-spraying parameters, chemical compositions of bond coats, ZrO_2 top coat stabilized with various types and quantities of stabilizer (MgO, CaO and Y_2O_3). In recent years, progress on TBCs has been achieved, with both improvements in material properties and understanding of the degradation mechanisms under various operating conditions. Despite previous efforts, the relationships between spraying parameters, coating characteristics and properties of TBCs under thermal cycling conditions have not been fully evaluated. Also, the degradation mechanisms of TBCs operated at elevated temperatures (higher than 1000 °C) are still under dispute and further study is needed (**Wu et al. 1990**).

2.2.1 State of the Art

The state-of-the-art TBCs employ a two layer coating system that consists of an insulating ceramic outer layer (top coat) and a metallic inner layer (bond coat) (**Taylor et al. 1992**). The bonding coat is an essential part of the system because of its stress-relieving properties and its high temperature oxidation resistance and because it provides a key for the firm adhesion of the ceramic coating. MCrAlY (M = Fe, Co, Ni or mixture) obtained by air plasma spraying was originally used as the bond coat material for most TBCs. MCrAlY bond coat obtained by vacuum plasma spraying is regarded as more durable than air plasma-sprayed bond coat and is also used today. It is recognised that the ultimate failure of the TBC is strongly influenced by bond coat oxidation which is a crucial factor in coating lifetime prediction (**Taylor et al. 1992, Sun et al. 1993a, b**).

A candidate material for the ceramic coat must posses certain characteristics. It should be refractory, chemically inert, posses good mechanical strength and thermal shock resistance, have good wear and erosion resistance, be phase stable but most importantly of all posses a low thermal conductivity and low thermal expansion coefficient which should be similar to that of the substrate. There are relatively few ceramics which posses high thermal expansion coefficients and this has focused attention on ZrO_2 ($11\text{-}13 \times 10^{-6}$ °C). Although ZrO_2 has a low thermal conductivity and a suitable expansion match with the substrate, the already described polymorphism of ZrO_2 necessitates that it be alloyed with other oxides. Hence more candidate materials become available depending on the alloy system chosen (**McPherson 1989**).

ZrO_2 stabilized or partially-stabilized (PSZ) by the addition of oxides of magnesium, calcium, yttrium or other rare-earth oxides have been chosen as the top coat material by virtue of its very low thermal conductivities and relatively high coefficients of thermal expansion (for ceramics) to minimize the coating substrate mismatch. Numerous authors have shown that TBCs producing the highest thermal mechanical resistance are those where the Y_2O_3 level is in the range 6-9 wt%. Typical state-of-the art TBCs utilise ZrO_2 partially-stabilized with 8 wt% Y_2O_3 (**Wu et al. 1990, Lelait et al. 1989**).

Miller et al. (1987) found ZrO_2-8wt%Y_2O_3 to be superior as a coating than the other ceramics they tested. Graded coatings which consist of a graded bond/ceramic coat mixture, are unsuitable for use at high temperature (**Jamarini et al. 1992**).

Compared with other ceramic materials, it has been found that the thermal fatigue life time of ZrO_2 coatings is longer than that of Al_2O_3 under the same conditions (Wu et al. 1990, Chen et al. 1992).

2.2.2 Coating Application Processes

2.2.2.1 Plasma Spray Application Process

The preferred method for producing TBCs is currently the plasma-spray process, because with care, it is capable of economically producing durable and reproducible coatings. The production properties and service behaviour of TBCs are inter-linked in a complex way and depend on many factors. Among these, it can be mentioned: plasma spray parameters, powder quality, bond coat and substrate chemistry, ceramic coating composition, microstructure, layer thickness and the operating thermal regime and environment (Heintze and McPherson 1988a).

A brief description of the plasma application process follows: the ceramic or metallic powder is fed into a high temperature, high velocity plasma arc where the powder particles melt as they are propelled towards the substrate. The molten material splats onto the substrate to build up the desired coating. A schematic of a plasma torch is shown in Figure 2.10.

Spray parameters must be optimised before a quality coating can be produced. Furthermore, the process must be carefully monitored to ensure reproducibility. There are many parameters that must be adjusted and controlled which make the task of optimisation and process control difficult. Parameters which must be considered include those affecting torch design such as nozzle diameter, powder injection location and injection angle. Parameters which control the torch operation include arc power, stand off distance, primary gas, secondary gas, arc gas flow rate, carrier gas flow rate and powder feed rate. Parameters which affect the powdered material include size distribution, shape and crystallographic phase distribution (Heintze and McPherson 1988a).

2.2.2.2 Alternative Coating Application Processes

The electron-beam physical-vapour deposition (EB-PVD) process is a potential alternative method for preparing ceramic TBCs. In this process a high energy electron beam is used to heat and vaporize a ceramic feed stock. The vapour travels along the line of sight to the substrate on which it condenses atom by atom. When the ceramic is ZrO_2-Y_2O_3, the process is carried out under a low partial pressure of oxygen in order to preserve the stoichiometry of the ZrO_2. The interface between the bond coat and the ceramic is smooth and differs from the rough interface required for plasma-sprayed coatings. The ceramic exhibits columnar growth after deposition of an initial thin region of dense ceramic. This columnar growth is believed to reduce the elastic modulus in the plane of the coating to near zero. As a result outstanding lifetimes have been reported for TBCs deposited using EB-PVD. However, reproducibility and the feasibility of coating complex geometries remain issues (**Heintze and McPherson 1988a**).

Sputter deposition is another coating application process that has been investigated extensively (**Fancey et al. 1993, Prater and Moss 1983**). The process occurs when a negatively charged target is bombarded with ions thereby, causing the target material to be ejected. The ejected material then deposits on a positively charged substrate. The advantage of sputtering is that it is a low temperature process which is capable of producing a range of microstructures. This includes a columnar structure similar to the structure formed by EB-PVD process. However, as yet it has not been possible to prepare a sputtered TBC with properties approaching those of a plasma-sprayed coating by this process (**McPherson 1989**).

Other processes are capable of spraying ceramics and metallic materials. These include the older flame spray gun and newer techniques such as detonation guns, water stabilized plasma spraying and hypersonic spraying. The flame spray gun has not produced satisfactory ZrO_2-based TBCs.

2.2.3 Structure formation

2.2.3.1 Plasma Spraying

A plasma-sprayed coating is built up layer-by-layer from individual splat particles which have melted or become semi-molten during passage through the plasma arc. The microstructure, thermal conductivity, cohesive and adhesive strength of a coating will be dependant on the bonding between these splats or particles and their packing arrangement and density (**McPherson 1989, Taylor et al. 1992**).

Each lamellae that forms the coating solidifies as a separate entity so that the internal structure of each may be considered individually. The two principal parameters which govern this are the velocity of the particles on impact and the viscosity of the particles as they flow. These are not controlled directly in the plasma spray process but are influenced by the temperature of the particles and the velocity of the arc. These are in turn influenced by the parameters of the process that can be controlled: the plasma gas flow and current density, the torch geometry, powder morphology, density, spraying variables such as deposition temperature of the substrate, surface transverse rate, thickness per pass, etc.

From plasma modelling studies, different particles have been identified, arising from the fact that different powder particles follow different trajectories through the plasma torch before being quenched on impact with the substrate. Ideally, all the incident particles which strike the substrate should be molten. Unmelted particles bounce off reducing the deposition efficiency and partially melted particles are incorporated within the deposit modifying its microstructure and properties.

2.2.3.2 Nucleation - Lamellae Formation

The cooling rate is extremely rapid considering the good thermal contact between the impinging drop and the substrate and the small thickness of the drop. Crystallisation of a liquid occurs by nucleation and crystal growth but if the nucleation rate within the time interval between the melting point and the glass transition temperature is such that no nuclei are formed, the liquid hardens to form an amorphous structure or glass. Metastable crystalline phases can also form directly from the liquid if it is rapidly cooled. The crystal size and morphology within lamellae depend upon the relative nucleation and growth rates of crystals from the melt (McPherson 1989). In general, high cooling rates give rise to a high nucleation rate, the lamellae are polycrystalline with a crystal size much smaller than conventionally processed material. In most cases it seems that rapid nucleation occurs at the cooler surface of the flattened droplet with large undercooling and crystals grow rapidly in the opposite direction to the heat flow forming a columnar grain structure. Rapid crystal growth leads to rapid evolution of the heat of fusion, an increase in temperature and suppression of further nucleation. However, if the crystal growth rate is relatively low further nucleation occurs as the liquid undercools and a very fine equiaxed grain structure is formed.

Segmentation, microcracking and internal stresses are also generated during quench cooling of individual splat particles. This give rise to a microstructure which contains a high density of cracks parallel to the substrate, normal to the substrate and some porosity. Coating density is approximately 85-90% the theoretical density.

2.2.4 Microstructure and Coating Properties

The structure of the ceramic is believed to have a profound influence on the coating durability, this is because structural properties such as porosity and microcrack distribution are believed to impart a tolerance to thermal stresses in the material. Coating density, which is a measure of the porosity, has been found to affect the coating lifetime and thermal physical properties (**Heintze and McPherson 1988a, Pawlowski et al. 1985**).

2.2.4.1 Porosity Distribution

McPherson (1989) studied some Al_2O_3 coatings and found that increasing the power input to the torch for a given powder particle size, increases the total porosity and ultimately produces a mono-dispersed pore size distribution. Some bimodal distributions of pores were also described for these Al_2O_3 coatings. The results suggest that there are two types of porosity present in a coating, coarse porosity associated with defects in the structure (due to incomplete filling of the interstices between previously deposited particles, which is more likely if the impacting particles are not completely molten) and fine pores which are an inherent feature of coatings, which has been interpreted as incomplete contact between lamellae during the process of coating formation.

2.2.4.2 Microcracks Distribution

SEM examination of the surfaces of individual lamellae of plasma-sprayed ceramic coatings also shows a network of fine cracks perpendicular to the lamella plane which are formed by stresses produced from the constraint of the thermal contraction of the lamella by the underlying material during cooling from the solidification temperature. These cracks will not form in metallic coatings because the thermal strain may be accommodated by plastic flow (**Pawlowski et al. 1985, Heintze and McPherson 1988a**).

2.2.5 Mechanical Properties

The mechanical behaviour of the coating is strongly influenced by the porosity which generally degrades the mechanical properties of materials. Differences in pore microstructure between various coating types may be used to explain differences in coating tensile strength. Properties such as electrical and thermal conductivity, and elastic modulus are reduced by the presence of pores which reduce the effective cross sectional area of the material. Brittle fracture is sensitive to defect size and the strength is determined by the largest crack present.

The elastic modulus of a ceramic coating is much lower than of the bulk material, of the order of 1/5. This reduction can be explained just in terms of a random distribution of spherical pores but is consistent with the model of narrow planar pores between lamellae with a relatively small fraction of "true contact areas". The elastic Young's modulus of plasma-sprayed ZrO_2 coating has been quoted as 48 GPa compared with around 200 GPa for the sintered ceramic (approx. 1/4). The presence of pores, microcracks and interlamellar cracks has been shown to reduce the elastic modulus of plasma-sprayed Al_2O_3 to around 20% of the value of a monolithic ceramic. This microstructure gives the coating a degree of flexibility, enabling it to withstand the strain due to thermal expansion mismatch and thermal cycling (**Kountouros and Petzow 1993, Taylor 1992, Heuer and Rühle 1983, Jasim 1992**).

2.2.6 Thermal Properties

Two effects can influence the thermal diffusivity or conductivity of a TBC. The first is the phase structure and the second is the crack morphology. The thermal conductivity of plasma-sprayed coatings is also much lower than that of the bulk material. Heating at elevated temperatures causes an increase in conductivity. This can be explained in terms of the model for fine interlamellar porosity (**Prater and Moss 1983**).

A survey of thermal properties of dense polycrystalline ceramics demonstrates that for any given alloy system, *m*-ZrO_2 has a higher thermal conductivity than either *c*- or *t*-ZrO_2. Thermal conductivity and diffusivity are structure-sensitive properties and changes in the porosity or crack morphology could mask any changes due to a composition difference. The effect of microcracks on thermal conductivity has been analysed by a number of authors and some expressions have been developed for calculation of the effective thermal conductivity (**McPherson 1989**). In general thermal conductivities of plasma-sprayed coatings are one third to one fifth of sintered ceramics (**Fancey et al. 1993, Taylor 1992**).

2.2.7 Phase Transformations in ZrO_2 TBCs

ZrO_2 TBCs containing 6-8% wt Y_2O_3 consist almost entirely of *t*-ZrO_2 which does aid transformation to the monoclinic phase under stress. These coatings are superior to fully-stabilized (*c*-ZrO_2) coatings in certain applications, apparently because *t*-ZrO_2, having a higher thermal expansion coefficient and thermal conductivity than *c*-ZrO_2, is more resistant to thermal shock on superalloy substrate (**Prater and Moss 1983**).

The most durable coatings are those formed from compositions taken from the two-phase or partially-stabilized region of the ZrO_2-Y_2O_3 equilibrium phase diagram (Figure 2.11). This diagram predicts a phase separation during cooling into a high-Y_2O_3 *c*-ZrO_2 phase (fluorite, C), and a low-Y_2O_3 *t*-ZrO_2 phase (T), between 2300 and 600 °C. With further cooling to room temperature this equilibrium low-Y_2O_3 *t*-ZrO_2

phase is expected to transform martensitically to the *m*-ZrO_2 (M), which has a lower free energy at lower temperatures. Under certain conditions, explained in Section 2.1.2, the *t*-ZrO_2 phase may be retained metastable at room temperature.

In partially-stabilized plasma-sprayed ZrO_2-Y_2O_3 coatings, as in quenched bulk material, the main phase observed at room temperature is a non-equilibrium, high-Y_2O_3 *t*-ZrO_2 phase (*t'*-ZrO_2). This phase, denoted as "non-transformable", differs from the metastable low-Y_2O_3 *t*-ZrO_2 phase because it is stable with respect to the monoclinic transformation. This phase forms because the quenching process prevents compositional adjustments required for development of equilibrium amounts of the low-Y_2O_3 *t*-ZrO_2 and high-Y_2O_3 *c*-ZrO_2 phases. Thus only minor amounts of those phases are observed (**Miller et al. 1981, Miller et al. 1983**).

The *t'*-ZrO_2 is unstable with respect to diffusion at high temperatures. Therefore, additional phase separation into the equilibrium high-Y_2O_3 *c*-ZrO_2 and low-Y_2O_3 *t*-ZrO_2 phases can be expected with high temperature exposure. On cooling, a large volume expansion is associated with the transformation of the high temperature low-Y_2O_3 *t*-ZrO_2 to the low temperature *m*-ZrO_2. Because of stresses associated with the volume change, the formation of increasing amounts of the "transformable", low-Y_2O_3 *t*-ZrO_2 phase should be detrimental to the integrity of the plasma-sprayed coating. The coating lifetime is in direct relation to the amount of *t'*-ZrO_2 phase present in the ceramic (**Alpèrine and Lelait 1994, Miller et al. 1983**).

When samples of *t'*-ZrO_2 phase are annealed at 1200-1600 °C, the original *t'*-ZrO_2 phase should in theory, decompose to form two equilibrium *t*- and *c*-ZrO_2 phases. On cooling to room temperature, the high-Y_2O_3 phase may be retained as *c*-ZrO_2 or it may transform to a high-Y_2O_3 *t'*-ZrO_2; the low-Y_2O_3 phase may transform to the *m*-ZrO_2 phase.

Heuer et al. (1988) characterized the thermal stability of a plasma-sprayed coating, ZrO_2-8.6mole%$YO_{1.5}$, whose composition is in the partially-stabilized, two-phase field (Figure 2.11), and determined quantitatively by X-ray diffraction the phases present after spraying and after ageing at temperatures typical of the surface temperature.

Anderson (1988) studied ZrO_2-(6-9)wt%Y_2O_3 coatings, a metastable phase appears during plasma spraying and is retained thereafter (Figure 2.11). This phase with high-Y_2O_3 content is *t*-ZrO_2, and is called *t'*-ZrO_2, as it has been said above, to distinguish it from the low-Y_2O_3 content *t*-ZrO_2 phase which is the equilibrium phase. He explained this phase as the results from the high quenching rate during plasma spraying (about 10^6 °Ks^{-1}) preventing the diffusion-controlled decomposition of the high temperature *c*-ZrO_2.

Taylor et al. (1992) followed the decomposition of different compositions ZrO_2-Y_2O_3 coatings during annealing at 1400 °C by X-ray diffraction. The results support the hypothesis that low-Y_2O_3 *t*-ZrO_2 and high-Y_2O_3 *t'*-ZrO_2 phases are formed. Only for 4 and 6 wt% Y_2O_3 coatings was any *m*-ZrO_2 phase observed, the content of this phase was dependent on the cooling rate. They also found that the non-transformable *t'*-ZrO_2 was susceptible to high temperature annealing treatments.

2.2.7.1 Implications of the Phase Transformations on ZrO_2 TBCs

The phase transformations described play an important role in the long term durability of ZrO_2-Y_2O_3 TBCs. A particularly important concern is the possibly adverse effect of a large increase in the amount of the transformable *t*-ZrO_2 phase. That is, while a 0.1 mole fraction of this phase may be beneficial, or at least tolerable, an increased amount may cause detrimental cracking of the coating due to the martensitic transformation. There are some factors to lessen the severity of thermal degradation of the coating. First, the non-transformable *t*-ZrO_2 phase decomposes rather slowly, especially at lower temperatures. Second, only the outer surface of the coating is exposed to the highest temperatures and temperature drops through the coating thickness. Thus most of the coating may be able to avoid the increased stresses brought about by the transformation.

The reason for the superior durability of partially-stabilized ZrO_2-Y_2O_3 coatings has not yet been established. Possibly, expansion of the small fraction of transformable *t*-ZrO_2 precipitates, as they convert to the monoclinic phase on cooling, acts to create a highly favourable microcrack network. Microcracked structures are, in general, common to all plasma-sprayed ceramics. However, the structure arising from the partially-stabilized compositions may be especially favourable. Other toughening models such as precipitation "hardening" cannot yet be excluded.

A stress-induced transformation toughening model has been used to explain the high fracture toughness of a very low-Y_2O_3 100% tetragonal ZrO_2-Y_2O_3 material. This model cannot apply to compositions richer in Y_2O_3 where the *t*-ZrO_2 phase does not transform under stress (**Pawlowski et al. 1985**).

The stress-induced transformation (*t*→ *m*-ZrO_2) toughening mechanism was described in Section 2.1.4. A high proportion of transformable *t*-ZrO_2 is achieved if the martensite start temperature, M_s is around room temperature. The M_s temperature is a function of grain size, stabilizer type and concentration. It has been observed that a ZrO_2-(10-15)wt%CeO_2 plasma-sprayed coating contains a large proportion of *t*-ZrO_2 which transforms to *m*-ZrO_2 on quenching (**Taylor 1992, et al. 1992**).

2.2.8 Thermomechanical Resistance of ZrO_2-Y_2O_3 TBC

It is well known that the thermomechanical resistance of TBCs in the ZrO_2-Y_2O_3 system is strongly dependent upon the amount of Y_2O_3 added to the ZrO_2 (**Isihizawa et al. 1986, Miller et al. 1983, Bennett 1986**). It is generally observed that the coating lifetime in high-temperature cyclic conditions shows a sharp maximum at intermediate Y_2O_3 contents, which correspond to ZrO_2 partial stabilization (7-8 wt% Y_2O_3) associated with the presence of a non-equilibrium *t'*-ZrO_2 phase. At higher Y_2O_3 contents, corresponding to the fully-stabilized *c*-ZrO_2 phase, the thermomechanical resistance of the coatings drops significantly. There are two explanations for this phenomenon: first, the *t'*-ZrO_2 phase obtained during plasma spraying for partially-stabilized ZrO_2 TBCs is a metastable phase, which does not easily decompose into the equilibrium *t*- + *c*-ZrO_2 phases (Figure 2.11) and consequently does not undergo the martensitic transformation into the *m*-ZrO_2

phase. Second, the intrinsic toughness of the *t'*-ZrO_2 phase is believed to be higher than that of the fully-stabilized *c*-ZrO_2 (FSZ) phase (**Michel et al. 1993**).

2.2.9 Microstructure of ZrO_2-Y_2O_3 Coatings

Alpérine and Lelait (1994) investigated the microstructure of both *c*- and *t'*-ZrO_2 phases to explain the higher toughness of *t'*-ZrO_2. However, although many fundamental studies have been devoted to the mechanical resistance and microstructure of monolithic ZrO_2-based ceramics, only a few studies report microstructural investigations of plasma-sprayed ZrO_2 TBCs.

2.2.9.1 As-Sprayed Specimens

Alpérine and Lelait (1994) found that the ZrO_2-8.5wt%Y_2O_3 ceramic coating was composed of a single *t'*-ZrO_2 phase. This phase was, indeed, crystallographically very close to the equilibrium cubic phase, since its c/a ratio only differed from unity by around 1.3 percent. They described the coating, through Transmission Electron Microscopy (TEM) observations, as composed of small, well-defined elongated *t'*-ZrO_2 grains (typically 1 x 0.25 μm^2). The tetragonality of the *t'*-ZrO_2 phase was evidenced in the diffraction mode by the presence of weak reflections of the type {odd, odd, even} (with the relevant index permutations). Imaging of the *t'*-ZrO_2 phase was hence achieved with the dark field technique using these reflections. Inside the *t'*-ZrO_2 grain, they observed two particular microstructural features: twinning of the grain and a domain structure inside each diffracting twin.

Alpérine and Lelait (1994) attributed this twin microstructure to the theoretically equal probability that the small distortion of the cubic lattice leading to the tetragonal symmetry could be along any of the three original <100> cubic axes, as explained in Section 2.1.5. The domain microstructure inside the twins, arises because of the lowering of the crystal symmetry during the *c*→ *t'*-ZrO_2 transformation. If two *t'*-ZrO_2 domains, one nucleated at (000) in the parent cubic cell and the other at (½,0,½) or (0,½,½), grow and come into contact, they will be separated by an antiphase boundary (APB). This APB contrast is clearly observed inside the different twins.

2.2.9.2 Annealed Samples

In the same work **Alpérine and Lelait (1994)** found that the two main microstructural features observed in as-sprayed specimens were also present after annealing at 1100 °C for 100 hours. The APB structure varied: the boundaries straightened. This was described as a classical ripening phenomenon leading to a minimum energy configuration. A second phase, seen as very fine and defined precipitates was observed in the *t'*-ZrO_2, forming a "tweed-like" microstructure. The typical size of the precipitates was of the order of 10 x 6 nm^2. The peculiar arrangement of the precipitates forming the tweed-like structure could be one solution that minimizes the total elastic strain energy by the creation of a bcc pseudo-network (pseudo-cell parameter ≈ 20nm) where the local strains generated by many individuals cancel out. It is likely that these precipitates, which contain more yttrium than the matrix, are composed of the equilibrium cubic phase, which appears as soon as solid-state diffusion has allowed the migration of yttrium ions. The appearance of these precipitates can thus be looked at as the first stage of the return to equilibrium of the *t'*-ZrO_2 phase.

The fact that special microstructural elements are being observed in the *t'*-ZrO_2 region of the ZrO_2-Y_2O_3 phase diagram, which cannot be observed in the high yttrium content cubic region, may help to understand the high intrinsic toughness of the *t'*-ZrO_2 phase associated with its microstructure; it could, in fact, be thought of in terms of structural toughening, i.e., the ability of a *t'*-ZrO_2 grain to dissipate crack propagation energy (**Michel et al. 1993**). A crack propagating in a ZrO_2 grain will follow one of the easiest cleavage planes. In the fcc cubic cell these planes are the eight <111> planes. In a tetragonal phase such as *t'*-ZrO_2, this situation differs somewhat. A projection of the crystallographic cell along the <100> axis is shown in Figure 2.12. Atomic bonds are there of two different kinds: shorter bonds (more energetic) and longer bonds (easier to break). It is possible to see in Figure 2.12 that some planes normal to the fourfold axis of the tetragonal cell only intercept low energy bonds. These planes could be the ones along which a crack would propagate with a minimum consumption of crack energy. These planes are less numerous in a tetragonal cell than <111> planes in a cubic cell (which is due to the fact that the medium has a lower symmetry). A first consequence of this is that a crack meeting a twin boundary must deviate at right angles, since the tetragonal *c* axes are orthogonal to each other in two neighbouring twins. Also, the propagation of a crack through an APB is likely to consume some energy, for similar reasons.

This analysis finds some support in the work reported by **Michel et al. (1993)** dealing with toughness measurements and fracture of *c*- and *t'*-ZrO_2 single crystals, the latter showing a twin structure similar to the one described above. These authors indicate that the intrinsic toughness of the *t'*-ZrO_2 phase is about three times that of the cubic phase.

The crack tip propagating through a *t'*-ZrO_2 grain having developed the "tweed" microstructure, is likely to deviate each time it meets a precipitate, for two reasons. First, the easy cleavage plane differs in the *t'*-ZrO_2 matrix and in the cubic precipitate, so that the crack should deviate from $(100)_t$, or $(010)_t$, to $<111>_c$. Second, before meeting the precipitate, the crack tip will meet the stress field developed near the interface between the matrix and the precipitate. No exact calculation of this stress field is currently available, but it is high enough to prevent the cubic precipitates from growing beyond a critical size of about 10 nm at 1200 °C. This stress field could well also cause the crack to bypass the precipitate. It can be seen that the chances are that the tweed microstructure is able to dissipate a lot of crack propagation energy, by a "micro-composites" mechanism.

It should be noted that the fact that the precipitates are of cubic symmetry does not account for the toughening mechanism described here above. It has been suggested (**Alpérine and Lelait 1994**) that this is due to the stress field generated by mismatch between matrix and precipitates, whatever their respective crystallographical natures and intrinsic toughness, which could make the crack "zig zag" through the "pseudo-ordered" network of the precipitates and consume large amounts of energy in propagating. This mechanism is made possible by the fact that the tweed precipitates are themselves stabilized by the stress field at temperatures up to 1200 °C. At higher temperatures (1300 °C and above), the stress field no longer constitutes a high enough potential barrier to prevent solid-state yttrium diffusion; the cubic precipitates grow, leading to a progressive disruption of the tweed microstructure and transformation of the matrix *t'*-ZrO_2 into the stable, low- Y_2O_3 , *t*-ZrO_2 phase.

2.2.10 Failure Mechanisms in TBC

2.2.10.1 Strain Accommodation

It is generally agreed that the life limiting factor in predicting TBC life is oxidation of the bond coat. Thus, it is important that the strain-accommodation capability of the ceramic is not impaired either during thermal cycling or by high temperature exposure. There are likely to be two possible causes for this: sintering and microcrack healing, or a significant increase in microcracking which would weaken the coating, causing it to disintegrate. In fact the available evidence suggests that for ZrO_2-MgO alloys, the converse may be true, i.e. the precipitation of MgO produces a controlled degree of random microcracking that enhances the properties. Accordingly, it is important to evaluate the effect on coating properties of long-term high temperature exposure for which in the first instance it is necessary to consider the phase stability of these alloys (**Taylor et al. 1992, Fancey et al. 1993**)..

The bond coat (MCrAlY) is probably the least creep-resistant portion of the coating system, giving deformation rates above 0.1% strain per second above 850 °C. Such plasticity is well known for these materials: it can occur at very low stress levels and in extreme cases can lead to failure of the MCrAlY. However, it can be expected, that stresses arising from expansion mismatch between the bond coat and the substrate, and between the bond coat and the ceramic may be rapidly relieved, possibly within a few seconds, by bond coat creep at temperatures above 800°C. This capability will depend on the plasticity of the particular bond coat and on possible ageing mechanisms which may also apply, and decrease the plasticity of the bond coat. If the bond coat does not plastically deform during a thermal cycle, the ceramic would be put under increasing tension as the temperature rises because the expansion coefficients of the bond coat and substrate are far higher than the ceramic. Cooling would merely relieve these tensile stresses. However, if bond coat deformation does occur, compressive stresses will be generated on cooling, whose size may depend critically on the cooling rate (**Bennett 1986**).

The mechanism which appears best to describe the observed phenomena is as follows. Bond coat deformation at high temperature causes strain isolation of the ceramic layer. On cooling, the bond coat cannot completely isolate the ceramic, and biaxial compressive stresses are produced in the ceramic in the plane of the coating. With progressive oxidation, the ability of the bond coat to deform rapidly during cooling is reduced, and the level of compressive stress increases progressively, cycle by cycle. Factors such as the maximum bond coat temperature, dwell at high temperature, and rate of cooling will thus affect thermal cycle life, whereas the heating rate should play a minor role (**Bennett 1986**).

The biaxial compressive stress produces a tensile stress normal to the plane of the coating which acts on any pre-existing flaws and defects to promote delamination of the coating (Figure 2.13). It can clearly be seen that the highest compressive stress in the coating will be close to the bond coat/ceramic interface, and in practice this is the area where coating failure most frequently occurs. The delamination interrupts heat transfer so that on heating, this area of the coating rapidly attains flame or gas stream temperature. Massive compressive stresses result and the coating can fail with explosive force.

The roughness of the bond coat/ceramic interface is another factor which must be considered in any description of bond coat behaviour, as the thermal cycle durability of any given bond coat-ceramic coating system increases with increasing interfacial roughness. This has often been attributed to an improvement in interfacial adhesion based on a mechanical keying mechanism of bonding (**Bennett 1986**). This proposal might be valid if failure as a result of thermal cycling occurred at the bond coat-ceramic interface, but as the failures are predominantly cohesive within the ceramic coating adjacent to the bond interface, this cannot be the correct explanation. It is far more likely that the geometrical effects on the transmission of the stresses across the interface are more important in affecting durability than any alteration to the bond strength.

Prolonged exposure to a high temperature oxidising environment may lead to coating failure. The stresses leading to failure are believed to result from thermal expansion mismatch between the ceramic and metallic layers and failure appears to be strongly influenced by bond coat oxidation. Other factors such as possible ceramic sintering and bond coat rigidity, may also play an important role in the failure of TBCs. The actual failure is generally within the ceramic layer near the bond coat layer. Failure is believed to be the result of slow crack growth and microcrack link-up within the ceramic (**Heintze and McPherson 1988b**). Stresses may also arise from rapid heating owing to exposure to a high heat flux. However, optimum TBCs have demonstrated a remarkable resistance to high heat flux.

Although MCrAlY alloys are still regarded as excellent candidates for bond coat application, after a long period of operation, Al from the bond coat is depleted to the extent that it can no longer form a continuous Al_2O_3 scale on the bond coat surface to hinder the oxidation. Therefore pre-treatments e.g. aluminizing or preoxidation have been performed on the bond coat surface before deposition of the ceramic top coat to improve the oxidation resistance of the bond coat and to suppress the formation of undesirable bond coat oxides (**Lih 1991, et al. 1992, Chang et al. 1991, Sun et al. 1993a, b**). These improvements have been found to increase the life TBCs owing to the reduction of bond coat oxidation. However, bond coat oxides growth inwards underneath the Al_2O_3 pre-coat might induce additional stress to damage the TBCs.

Miller and Lowell (1982) found that ceramic coatings of thickness 0.38 mm exposed to a plasma flame at 3000 °C for cycles of 0.5 s produced a gradient of about 1100 °C across the ceramic in that time. After 3000 such cycles a ZrO_2-8wt%Y_2O_3 coating showed no sign of distress. However, a ZrO_2-12wt%Y_2O_3 coating displayed severe craze cracking after 250 cycles and a ZrO_2-20wt%Y_2O_3 sample spalled off after only one cycle. Severe bond coat pre-oxidation caused failure of ZrO_2-12wt%Y_2O_3 coatings in these tests but specimens heat treated in argon did not fail.

2.2.10.2 Oxidation

The ZrO_2-based ceramics used for TBCs are fully-oxided materials, so oxidation is restricted to degradation of the bond coat. However, the ZrO_2 helps to transport oxygen from the gas stream to the bond coat by two mechanism: ionic transportation through the lattice by reverse movement of oxygen ion vacancies, and gaseous diffusion along the tortuous networks of interconnected microcracks and pores. It is probable that, depending on the chemistry and stress level of the ceramic and the nature of the gas stream, these two mechanisms will provide different contributions towards the overall oxidation rate. Furthermore, the oxygen partial pressure at the ceramic/bond coat interface should be substantially less than in the free gas stream, and the ceramic will thus depress oxidation rates relative to uncoated material, and since the role of the ceramic is to reduce metal temperatures, this too will reduce the oxidation rate **(Bennett 1986)**.

Since the ceramic suppresses oxidation, in some applications it is even possible to use materials with relatively poor oxidation resistance as bond coats, and providing bond coat temperatures remain below 950 °C, simple Ni-Cr alloys can be used successfully. Admixing free aluminium to these alloys produces an exothermic reaction on plasma spraying through air, which is known to promote higher deposition efficiency and higher bond strength. The resultant coating is rapidly oxided above this temperature, and isothermal soaking under a typical thermal barrier ceramic for as little as 150h at 1050 °C can cause complete conversion of the bond coat from metal to oxide. As this occurs in a stress-free condition, the ceramic remains adherent until the system is allowed to cool. High expansion mismatch stresses, and poor mechanical integrity in the oxided bond coat then combine to cause dramatic ceramic exfoliation.

The simplest bond coat systems contain little aluminium in solution, so the aluminium in the substrate alloy diffuses readily into the bond coat and is consumed by the oxidation reaction. Under thermal cycle conditions, the bond coat is oxided progressively, leading to a gradual decline in plasticity and mechanical strength which contributes to the spallation of the ceramic layer. Compared with simpler bond coat alloys, the more oxidation resistant MCrAlY materials (M = Ni, Co, Fe or mixtures) degrade far less readily, positively protecting the substrate alloy, and dramatically increasing the thermal cycle life of any given ceramic. For both coating systems, the eventual failure occurs in the ceramic coating, not in the bond coat (**Sun et al. 1993a, b**).

2.2.10.3 Corrosion

There have been limited applications of TBCs to ground or sea based turbines because stabilizers such as Y_2O_3, MgO and CaO react with sulphur and vanadium from fuels of industrial quality. Cracking and porosity are major problems associated with plasma-sprayed coatings. Significant cracking and porosity can lead to degradation at low temperature, together with destabilization, spalling and loss of thermal insulation and corrosion protection at higher temperatures. Fine microcracks and porosity allow penetration of the environment, including the constituents of the fuel, through the coating and attack of the substrate (**Jones 1989**). The corrosion of ceramic oxides by molten vanadate/sulphate engine deposits (i.e. hot corrosion) is still a relatively little studied topic (**Reckziegel 1993**). The molten vanadate corrosion of ZrO_2-Y_2O_3 is a well known problem which tends to prohibit the burning of vanadium-contaminated fuel in engines which use ZrO_2-Y_2O_3 coating or components. The reaction between Y_2O_3 and molten vanadate deposits on the ZrO_2-Y_2O_3 surface produce YVO_4 with a resultant "leaching out" of Y_2O_3 and destabilization and/or degradation of the ZrO_2-Y_2O_3. An understanding of the corrosion reaction is beginning to be developed, but little has yet been reported on the specific laboratory methods for evaluating the relative vanadate corrosion resistance of ZrO_2-Y_2O_3 (**Reckziegel 1993, Jones 1989**).

Jones (1989) found that $NaVO_3$ induced a tetragonal to monoclinic destabilization of the ZrO_2 structure in a ZrO_2-Y_2O_3 system. He followed this destabilization by X-ray diffraction on the basis of the ratio of intensities of the monoclinic $11\bar{1}$ peak to the tetragonal 111 peak. Crystals of YVO_4 were also identified on a ZrO_2-Y_2O_3 surface, confirming the reaction between Y_2O_3 and V_2O_5. Addition of SO_3 increased the destabilization rate because of higher V_2O_5 activity via the reaction:

$$2NaVO_3 + SO_3 \longrightarrow Na_2SO_4 + V_2O_5$$

It is usually adequate in corrosion studies to simply estimate the extent of destabilization from the X-ray diffraction spectra by the relationship:

$$\%\ destabilization = 100\,M/(M+T)$$

where M corresponds to the monoclinic $11\bar{1}$ peak height, and T the tetragonal 111 peak height

2.2.11 TBC Microstructure Investigations

2.2.11.1 X-ray Diffraction Analysis

Identification of the *c*- and *t*-ZrO_2 phases by X-ray diffraction (XRD) is difficult because the differences in crystal structure are small. Deconvolution of diffraction peaks is required to distinguish between the cubic and tetragonal phases. The amounts of monoclinic (C_m), tetragonal (C_t) and cubic (C_c) phases existing in plasma-sprayed ZrO_2 coatings have been determined using integrated and corrected intensity ratios in the {400} and {111} regions of the XRD patterns using different mathematical expressions. Equations 2.2-2.4 have been used by several authors to correct overlapping effect in the XRD quantification of ZrO_2 phases; where $I_m(11\bar{1})$ is the integrated intensity under monoclinic $(11\bar{1})$ peak (**Iwamoto 1985, Reckziegel 1993, Evans 1984, Toraya 1984a, b**).

$$C_m = \frac{0.82[I_m(11\bar{1}) + I_m(111)]}{0.82[I_m(11\bar{1}) + I_m(111) + I_{tc}(111)]} \qquad 2.2$$

$$C_t = (1 - C_m)\frac{1.14[I_t(400) + I_{tc}(004)]}{1.14[I_t(400) + I_{tc}(004)] + I_c(400)} \qquad 2.3$$

$$C_c = 1 - [C_m - C_t] \qquad 2.4$$

Although the differentiation of tetragonal and cubic peaks is difficult, the results obtained are quite helpful in the investigation of phase transformations on ZrO_2 TBCs under some treatments. For instance, **Iwamoto (1985)** examined the ***t*→ *m*-**ZrO_2 transformation in the coating under indentation, fracture and/or heat treatment using this method (Figure 2.14).

Heintze and McPherson (1988) used this method in the evaluation of phase transformations of a ZrO_2 TBC after heating and grinding. They proved a phase transformation occurred in his test coating after grinding.

Miller et al. (1983) studied the phase stability in a plasma-sprayed ZrO_2-Y_2O_3 during ageing, using X-ray diffraction patterns. They observed that a non-equilibrium tetragonal phase forms by a diffusionless process during the rapid quench associated with the plasma-spray process. This phase decomposed slowly at high temperatures via cation diffusion into a high Y_2O_3 cubic phase and a low Y_2O_3 tetragonal phase. The cubic phase is either retained on cooling or it transforms to a new tetragonal phase, depending on the ageing temperature. The decomposition of the non-equilibrium tetragonal phase into the equilibrium phase can be expected to play an important role in long term coating durability.

2.2.11.2 Electron Microscopy

Considerable work have been done using electron microscopes on the characterization of the microstructure of ZrO_2 bulk ceramics including the different alloyed ZrO_2 types which describe the crystal structures and phase transformations under thermal treatments (for example **Lee 1993, Ingel et al. 1988, Bielicki et al. 1988, Rühle 1988, Unal et al. 1990, Majumdar 1991, Ishiguro 1985, Hirota 1986, Liu et al. 1993**). A few studies regarding the microstructure of ZrO_2 TBCs have been reported (**Alpérine and Lelait 1994, Lelait et al. 1989, 1992, Harmsworth and Stevens 1989, 1992a, b**). For instance, it has been reported the formation of a Al_2O_3 scale in the ZrO_2-Y_2O_3- NiCrAlY coating interface, and based on the microstructural observations (**Lelait et al. 1989**).

Brindley and Leonhardt (1993) proposed a metallographic technique for evaluation of TBCs to provide an adequate polished surface for a repeatable interpretation of coating structures by Light Microscopy and Scanning Electron Microscopy (SEM) observations. The technique combines epoxy impregnation, sectioning, polishing and interference layering. They used a final reactive Pt coating to enhance the contrast in during SEM observations. The interference layer increases the contrast and makes the interpretation or the structures less ambiguous.

Harmsworth and Stevens (1992b) characterized the microstructure of a ZrO_2 plasma-sprayed TBC using Transmission Electron Microscopy (TEM). They report their observations on cross-sectional foils from the bond coat to the outer surface. They found an amorphous interfacial region between the bond coat and the ceramic layer, providing a strong fusion between the two layers. On the other hand, they describe the presence of a grain boundary glassy phase which provides a path for grain boundary coating failure. They observed in the coating, containing 6-8 wt% Y_2O_3, large twinned grains with monoclinic symmetry. These monoclinic grains were often observed in clusters, suggesting that the transformation of one grain initiates further transformation or partial transformation of adjacent grains, due to the volume expansion associated with $t \rightarrow m$-ZrO_2 transformations. The volume expansion is also thought to initiate grain boundary cracking along the weaker grain boundary described above. The presence of these monoclinic grain clusters in coating compositions greater than 8% Y_2O_3 is thought to arise from the spraying of heterogeneous starting powders which gives rise to areas in the coating with low stabilizer contents. The presence of transformed monoclinic grain within the coating structure is believed to increase coating toughness and durability and so increases the resistance to thermal shock.

Shiojiri et al. (1988) state that the amount of monoclinic phase present and the transformability of the coating must be closely controlled. Too much transformation (< 6% Y_2O_3) will cause rapid deterioration of properties due to increased cracking and segmentation. However if no monoclinic phase is present (> 12% Y_2O_3), then little or no toughening capability exists in the coating, leading to poor thermal shock behaviour on thermal cycling.

Wu et al. (1989b), studied the microstructure and failure of ZrO_2-8wt%Y_2O_3 by SEM and Electron Microprobe analyses. They identified in spalled off TBCs, irregular aggregates of bond coat out-grown (Ni, Co)(Cr, Al)$_2$O$_4$ spinels attached to the bottom of the spalled off top coat. These spinel phases, which were observed to grow rapidly on the surface of the bond coat out-grown Al_2O_3 scale, might initiate cracks and accelerate spalling of the top coat during operation.

2.2.11.3 X-ray Photoelectron, Auger and Raman Spectroscopy

Other powerful analytical techniques have been used in the TBCs characterization. **Arfelli et al.** (1990) used X-ray photoelectron spectroscopy (XPS) and X-ray induced Auger spectroscopy to investigate impurity segregation of Si, Na, Al in a 20nm thin layer in a ZrO_2 25.5wt%CeO_2-2.5Y_2O_3 plasma-sprayed TBC, as a function of high temperature thermal treatment in air.

Majumdar (1991) studied the surface and grain boundaries of Y_2O_3-stabilized ZrO_2 using XPS, observing yttrium segregation at the surface as well as at the grain boundaries. He found chemical shifts for Zr and Y. Characteristic differences were observed for the monoclinic and the tetragonal phases owing to their different oxygen co-ordinations.

The quite well defined bands for *t*-, *m*- and *c*-ZrO_2 phases in Raman spectroscopy have been used to identify and follow phase transformations on ZrO_2-Y_2O_3 ceramics under different treatments (**Benner and Nagelberg 1981**).

2.3 ZrO_2-TiO_2 ALLOYS

The study of ZrO_2-TiO_2 alloys started some time ago and **Brown and Duwez** (1954) proposed a phase diagram for the ZrO_2-TiO_2 system based on the existence of the compound $ZrTiO_4$ (Figure 2.15). They also found that the addition of TiO_2 to ZrO_2 lowered the temperature for the transformation *t*→ *m*-ZrO_2. **Ingel et al.** (1988) studied the addition of TiO_2 to ZrO_2 as an alternative stabilizer for *t*-ZrO_2. ZrO_2 alloyed with 8% TiO_2 was rapidly solidified in order to determine if the *t*-ZrO_2 could be obtained by kinetic means alone. The alloy was quenched on to a room temperature substrate, and it solidified in a different manner to the CeO_2 and Y_2O_3 alloys. An uniformly fine-grained structure observed by SEM suggested that TiO_2 acted as a heterogeneous-nucleation agent during the solidification process. XRD, Selected Area Electron Diffraction (SAED) and Analytical Electron Microscopy (AEM) confirmed that TiO_2 formed a monoclinic solid solution with ZrO_2 and no *t*-ZrO_2 was found in the system studied. The overall microstructure consisted of colonies of *m*-ZrO_2 intersecting each other and small grains of $ZrTiO_4$ phase. Where differently oriented colonies met, strain contrast and microcracks were visible.

Pandolfelli et al. (1989a) found that in the ZrO_2-TiO_2 system *t*-ZrO_2 was not retained at room temperature. The addition of TiO_2 decreased the martensitic transformation temperature of ZrO_2, but this was insufficient to retain the *t*-ZrO_2 to room temperature. TiO_2 promoted grain growth and inhibited densification of ZrO_2 for compositions sintered in air. The presence of $ZrTiO_4$ was verified only in compositions with 18 and 21 mole % of TiO_2. **Pandolfelli et al.** (1989b) also studied ternary systems and prepared TZP by sintering ZrO_2-16.5TiO_2-5.6CeO_2. They found a highly stable tetragonal phase in this system, consisting of large grains.

Bateman et al. (1988) studied some ZrO_2-TiO_2 and ZrO_2-MgO-TiO_2 systems and found that TiO_2 acts as a sintering aid and grain growth inhibitor for ZrO_2. The ZrO_2-TiO_2 binary system exhibited a large tetragonal phase field and therefore it would offer the possibility of yielding a *t*-ZrO_2 polycrystal (TZP) material, however, they found that the *t*-ZrO_2 was not retained at room temperature in the binary ZrO_2-TiO_2 system.

Hofmann et al. (1989) report that the system ZrO_2-Y_2O_3-TiO_2 showed a better resistance to degradation in a humid atmosphere at 200 and 500° C than a Y-TZP, because TiO_2 has a lower tendency to form a hydroxide than Y_2O_3.

Pyda et al. (1992, 1993) studied the system ZrO_2-Y_2O_3-TiO_2 as a potential source of TZP and found that the *t*-ZrO_2 was dominant in a particular composition range. They also established that the grain growth of the *t*-ZrO_2 was promoted by the addition of TiO_2, but at high TiO_2 concentrations (23-28 mole %) it was inhibited. They suggest that elongated grains of $ZrTiO_4$ crystallising at the *t*-ZrO_2 grain boundaries were responsible for this phenomenon. The same research group studied different compositions of the same system and obtained two different kinds of material: one of high fracture toughness and high hardness composed of a *t*-ZrO_2

solid solution and the other one mainly of monoclinic phase of slightly lower fracture toughness and much lower hardness **(Haberko et al. 1991)**.

The use of any of these ZrO_2-TiO_2 alloys as a TBC has not been extensively documented. A ZrO_2-Y_2O_3-TiO_2 composite is commercially available for coating purposes and remarkable properties such as excellent thermal shock, erosion and corrosion resistant are associated with it **(Metco Inc 1984)**.

2.4 FIGURES

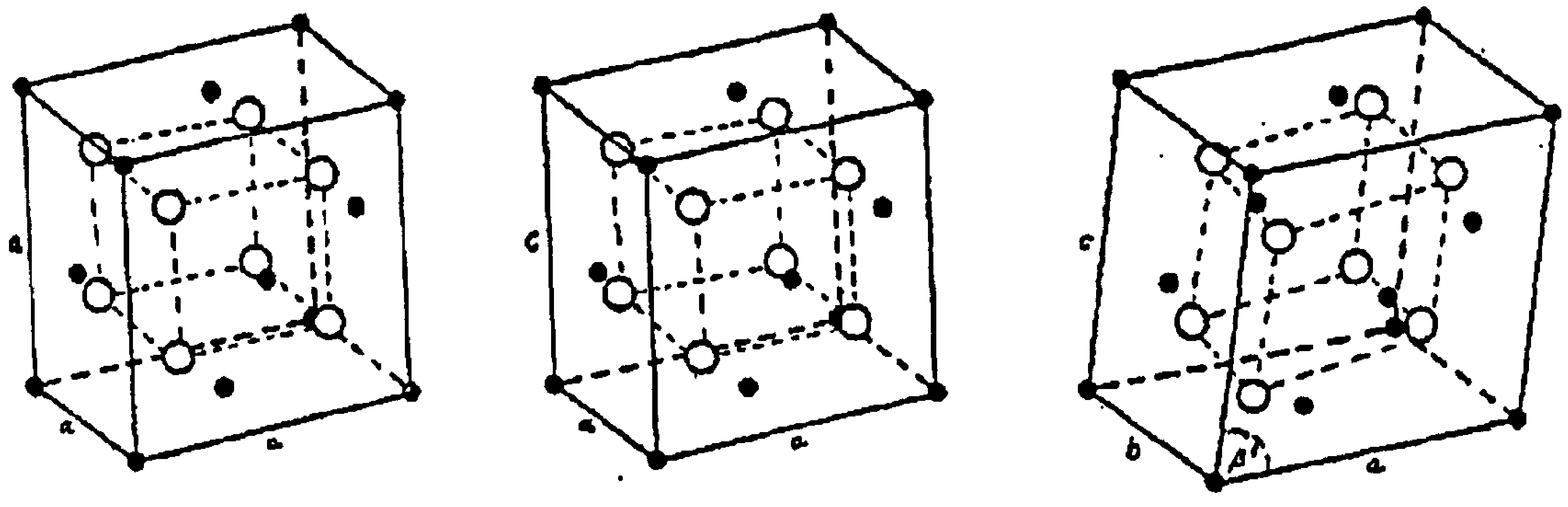

cubic tetragonal monoclinic

Figure 2.1 Crystalline structure diagram of ZrO_2 (after Heuer and Rühle 1983).

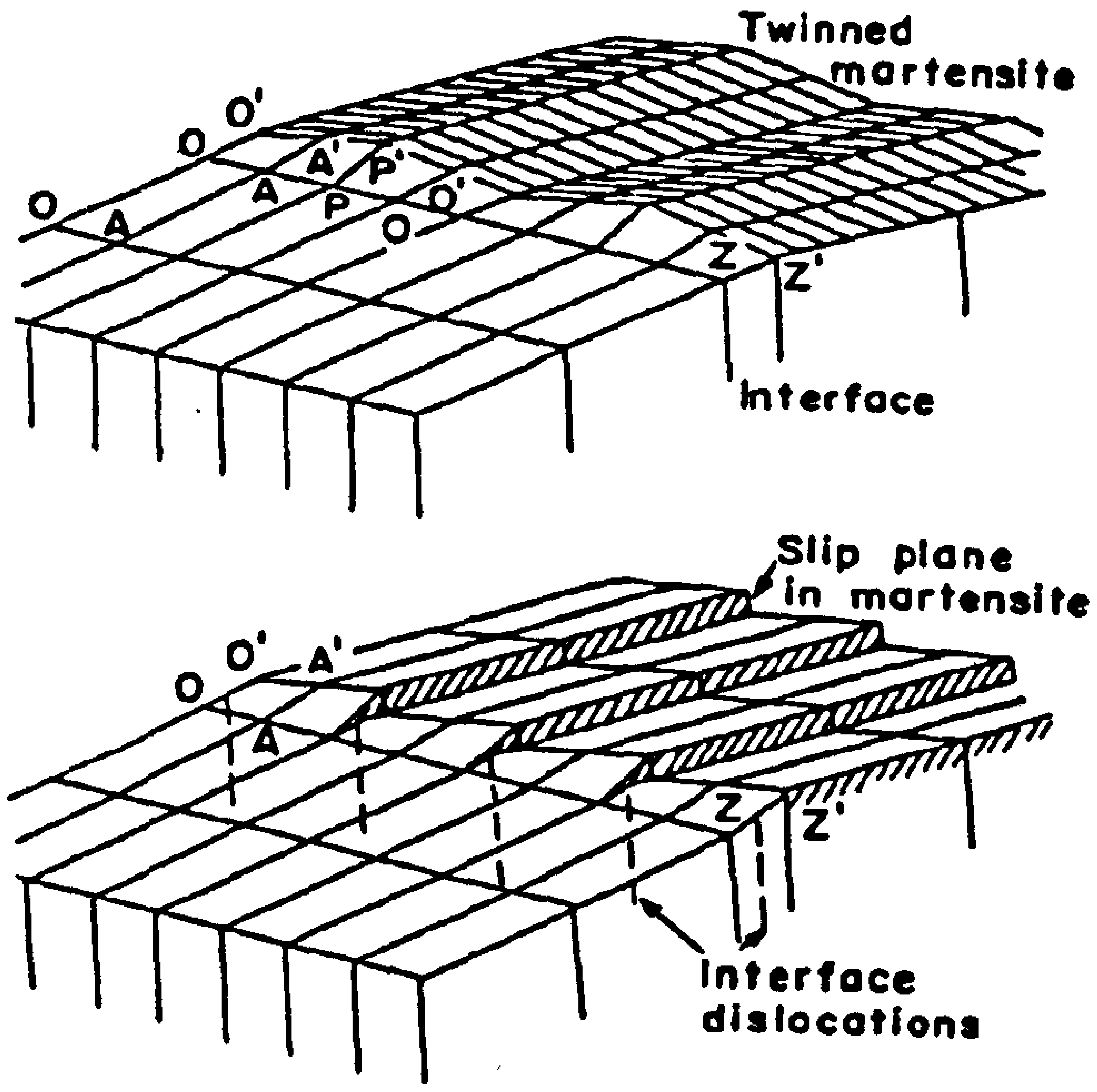

Figure 2.2 Drawing showing internally twinned and dislocated martensite (after Evans and Heuer 1980).

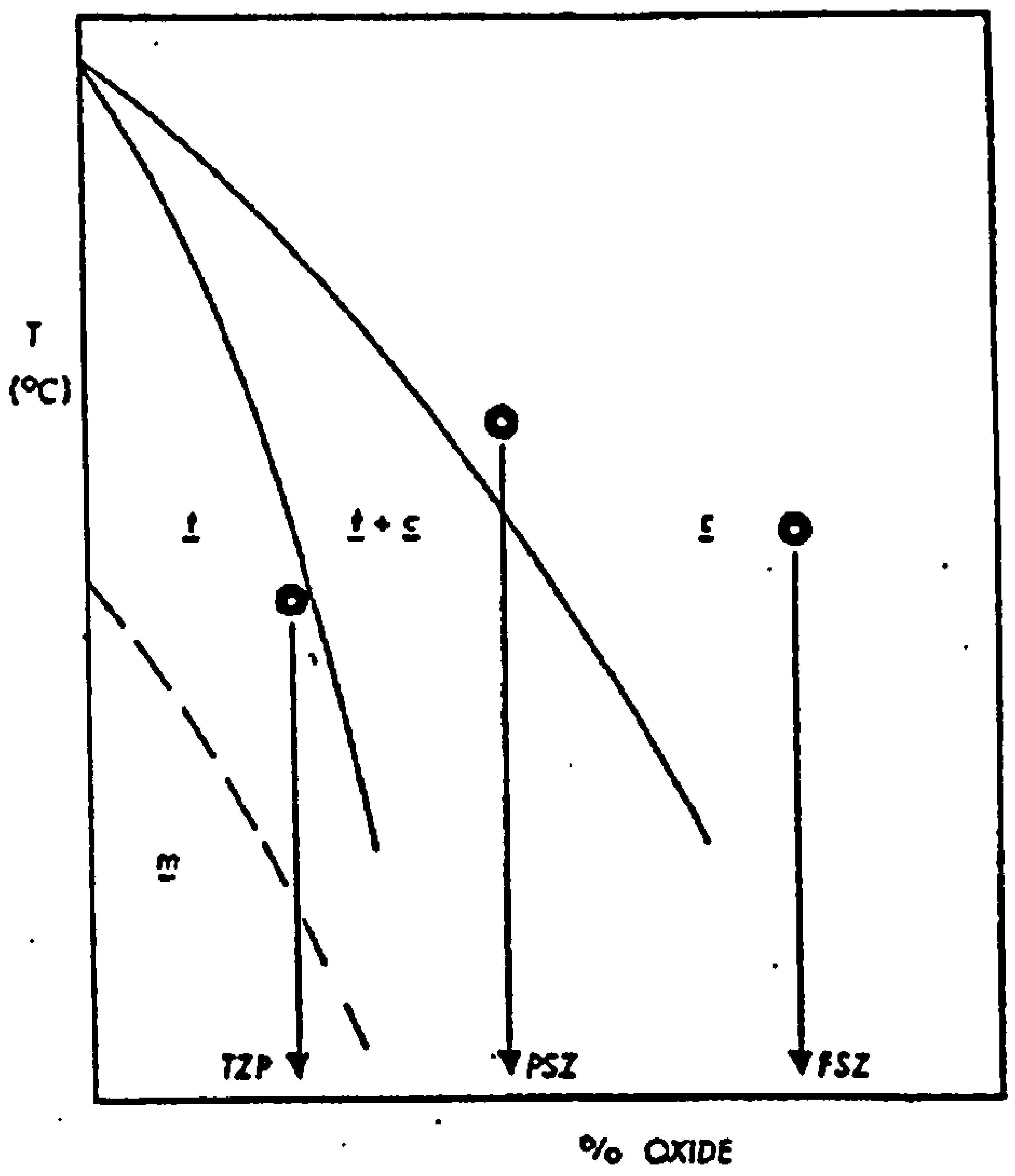

Figure 2.3 The essential features of binary phase diagrams between ZrO_2 and the oxides MgO, CaO and Y_2O_3 (after Butler 1985a).

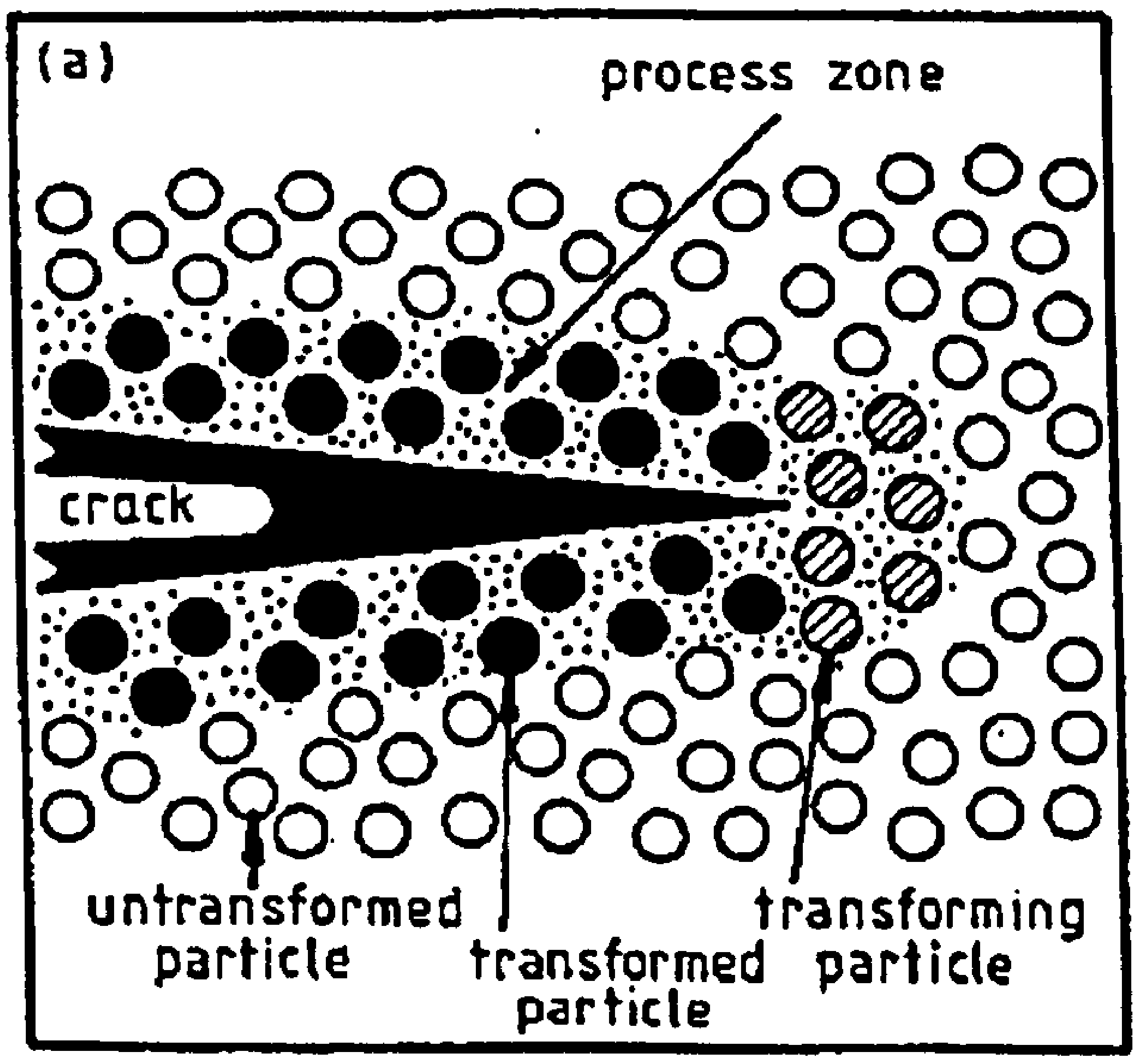

Figure 2.4 Schematic of the stress-induced transformation toughening (after Butler 1985b).

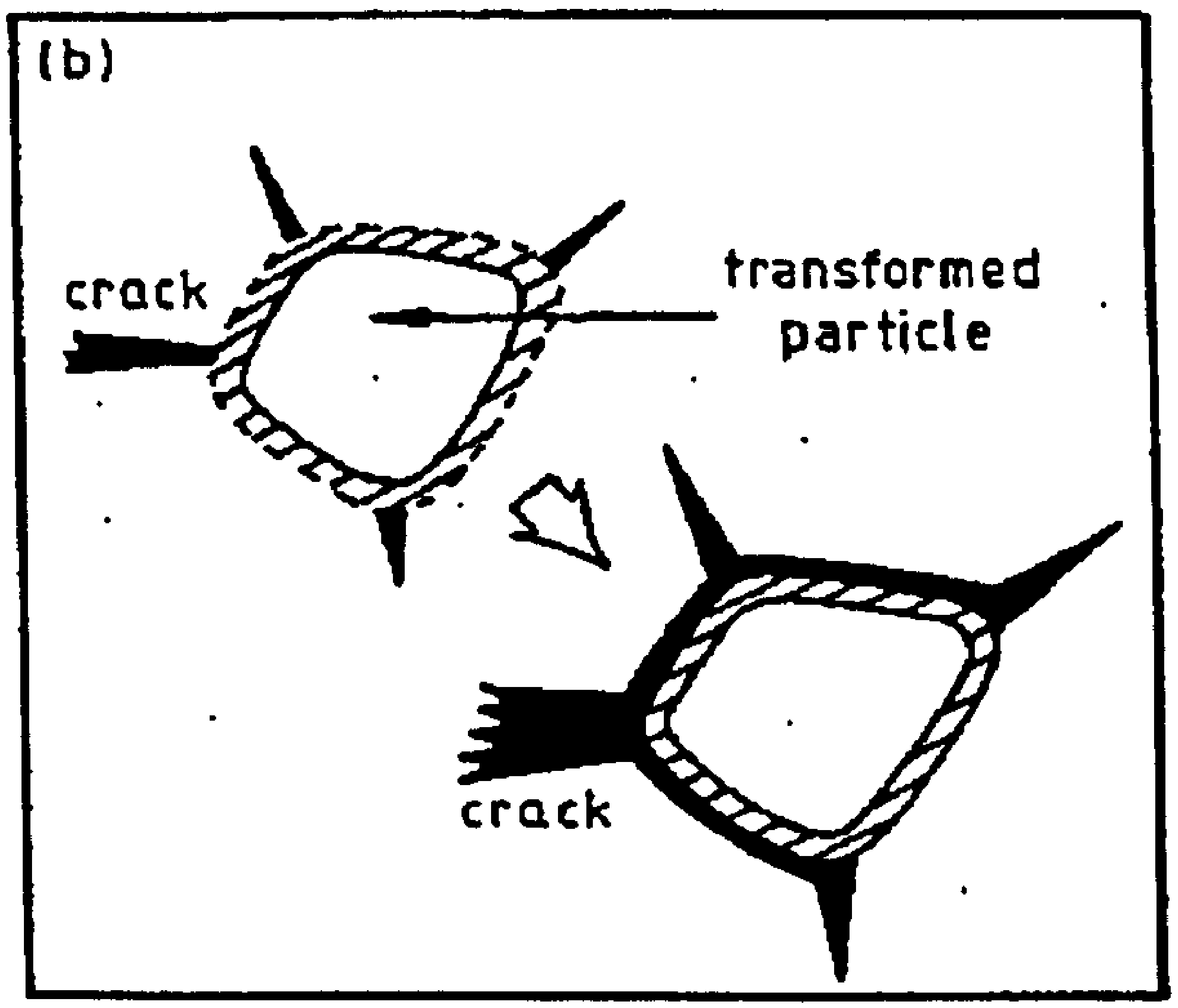

Figure 2.5 Schematic of microcrack toughening (after Butler 1985b).

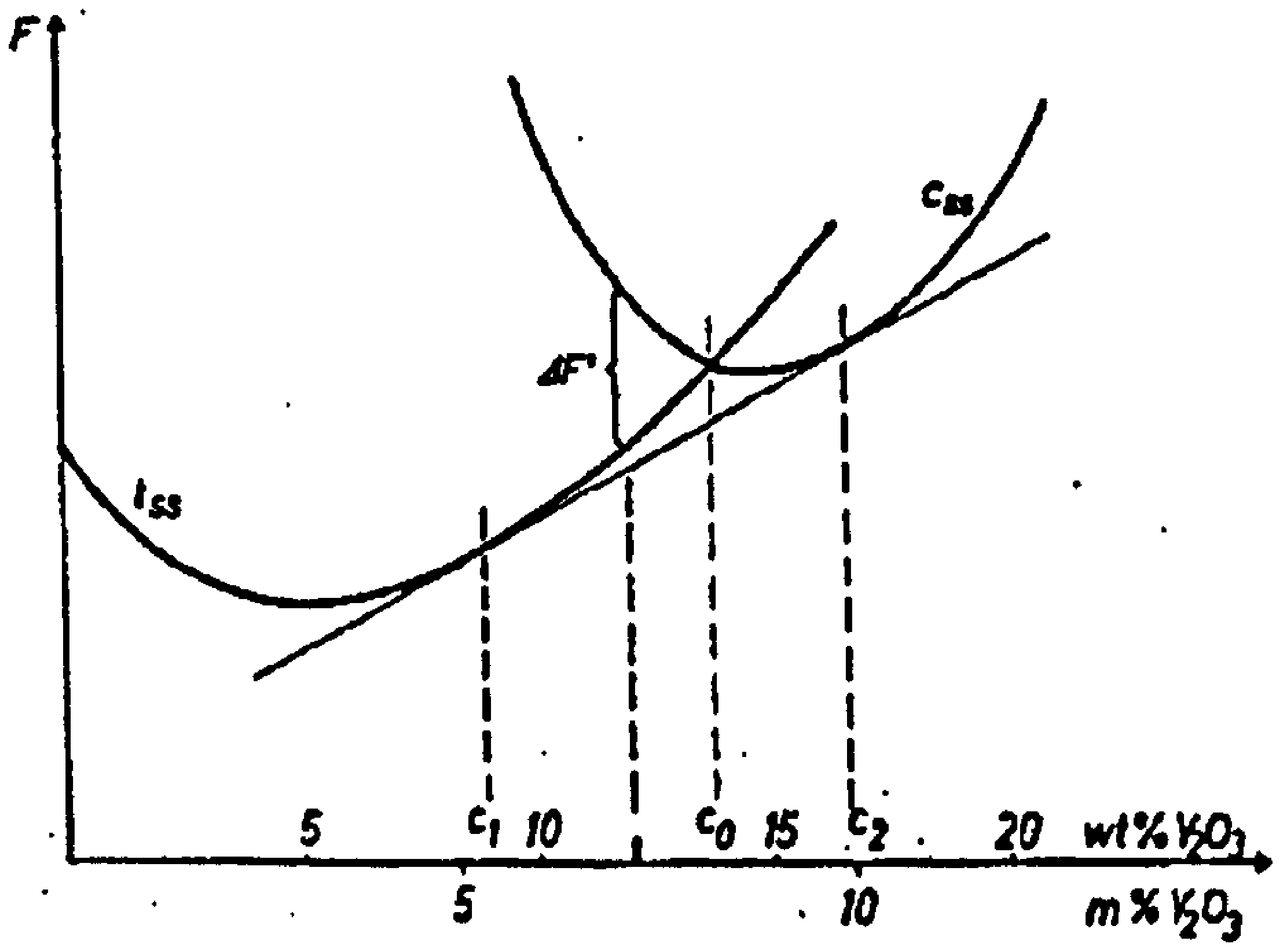

Figure 2.6 Schematic free energy vs. composition curves for *c*- and *t*-ZrO_2 at temperature *T*. A displacive *c* → *t*-ZrO_2 transformation can occur for compositions between C_1 and C_0 if quenched to *T* or below (after Chaim et al. 1985).

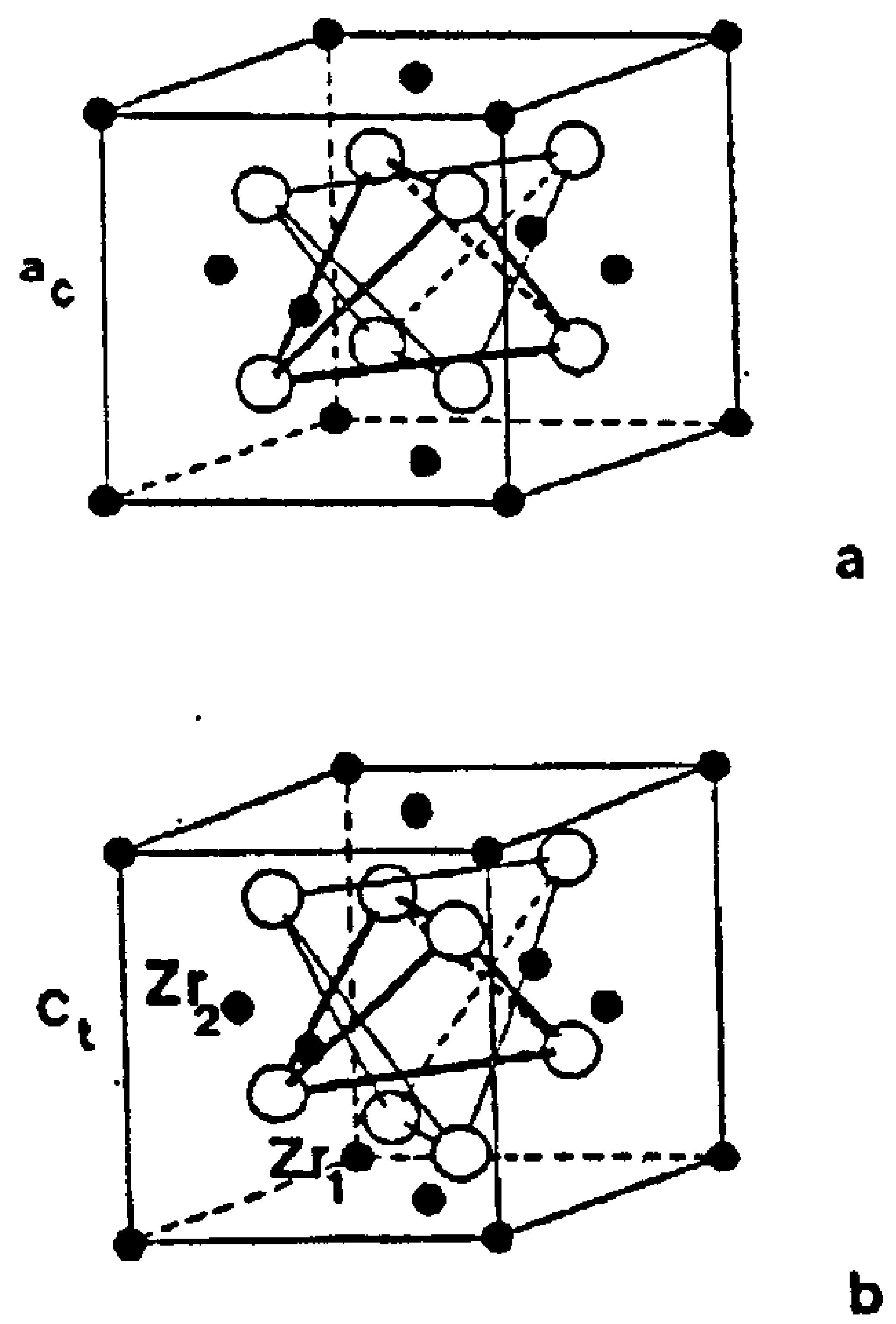

Figure 2.7 Crystal structures of *c*- and *t*-ZrO_2: a) cubic unit cell; two oxygen tetrahedrons within the *c* lattice are shown , (b) *t*- unit cell lattice; one flattened and one elongated oxygen tetrahedral present (after Heuer et al. 1987).

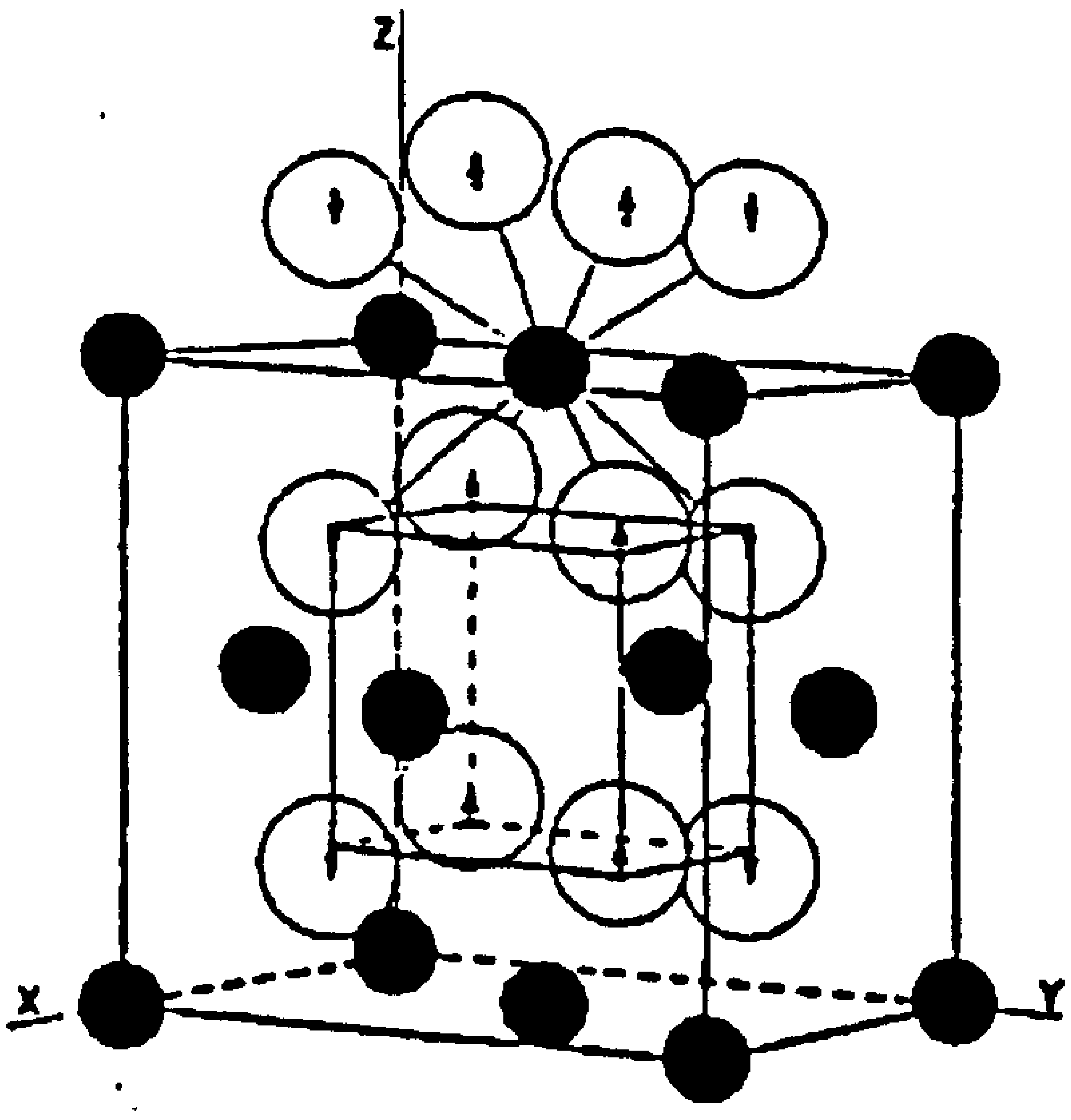

Figure 2.8 Structure of *t*-ZrO_2 showing displacements of oxygen atoms after their ¼¼¼ and symmetry related positions in an exaggerated manner (after Chaim et al. 1985).

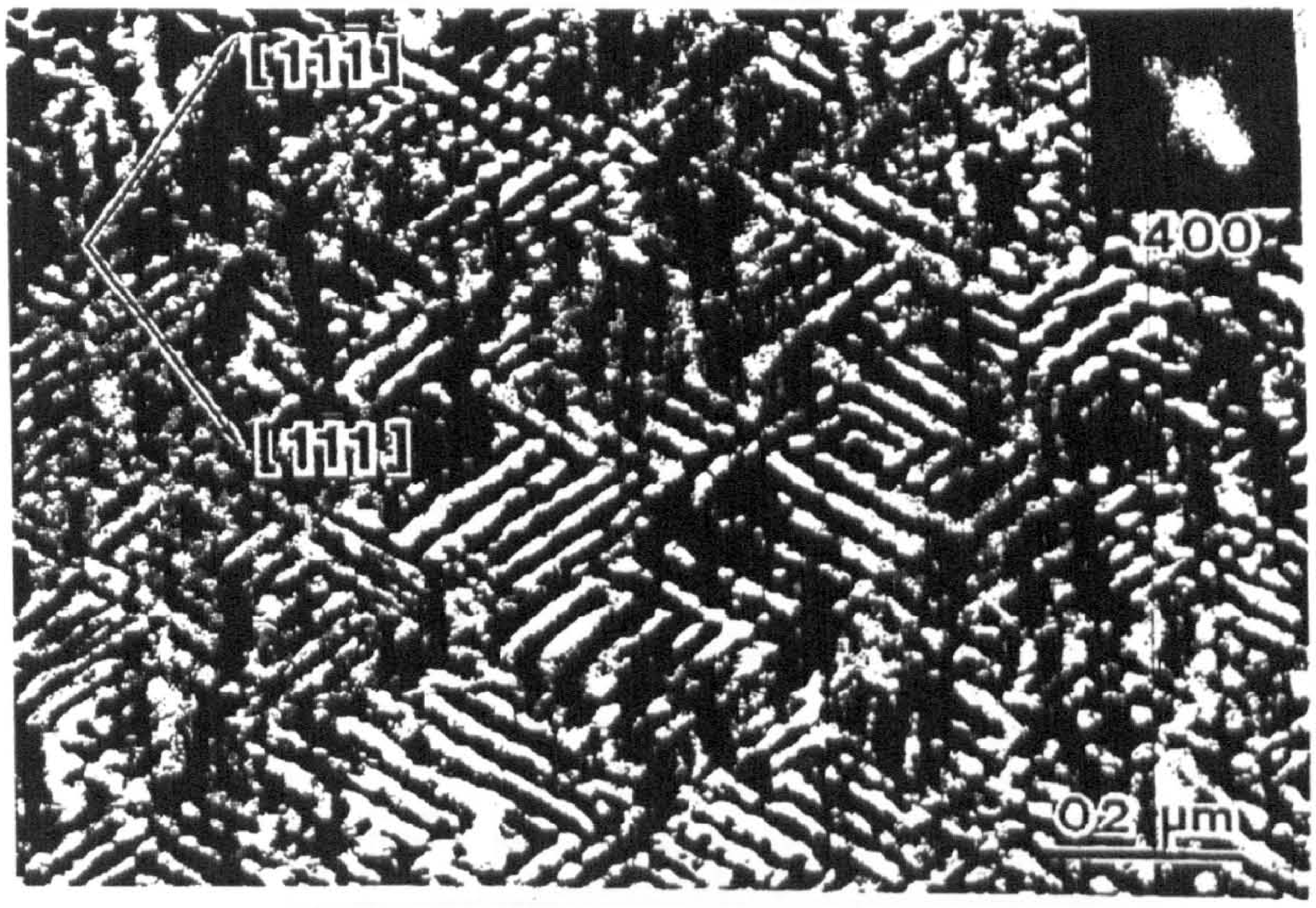

Figure 2.9 Bright Field TEM micrograph of a 4 mole% Y-PSZ, showing a "tweed-like" modulated structure formed after ageing at 1700 °C (after Sakuma et al. 1986)

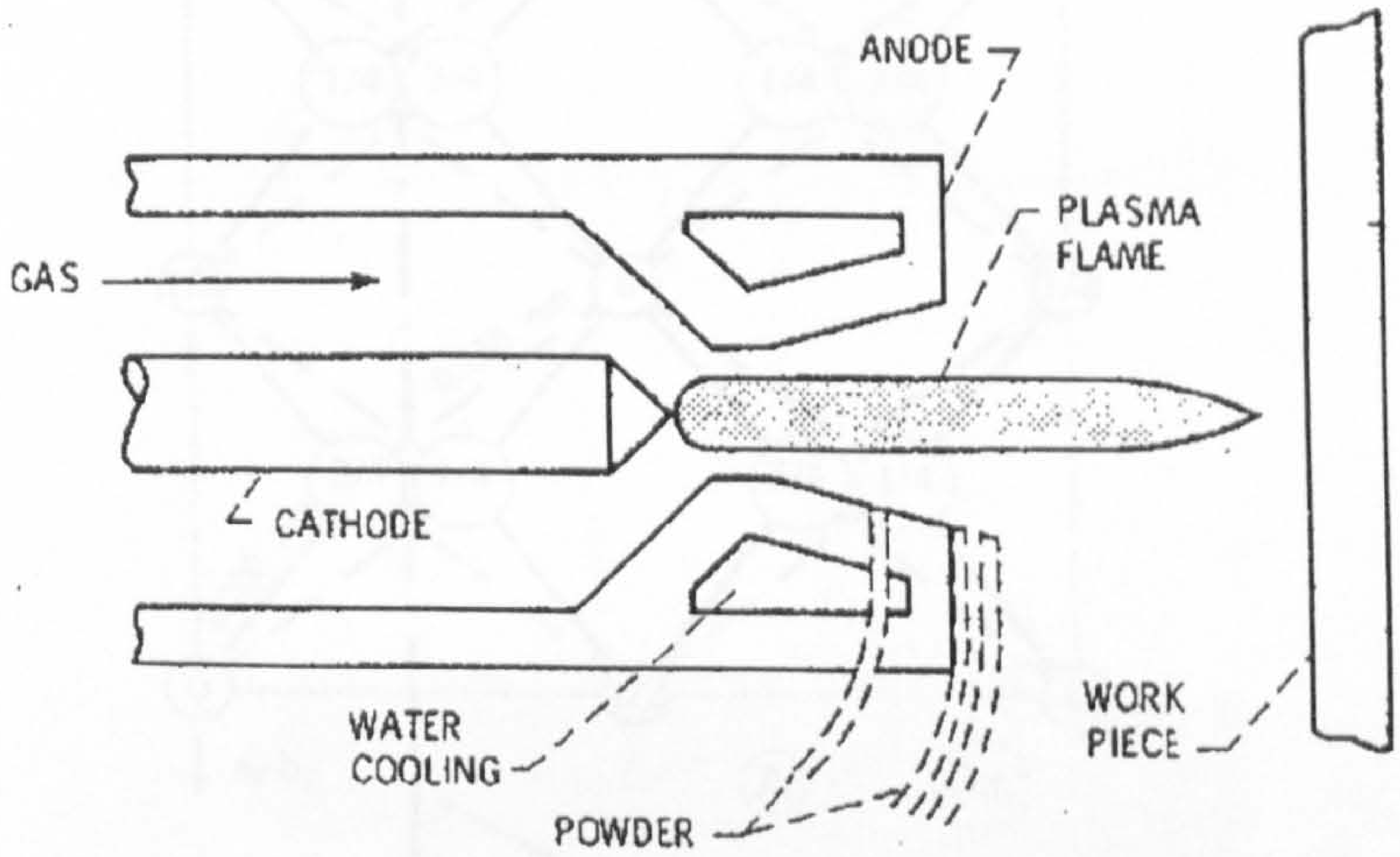

Figure 2.10 A plasma torch diagram for TBC application (after Heintze and McPherson 1988b).

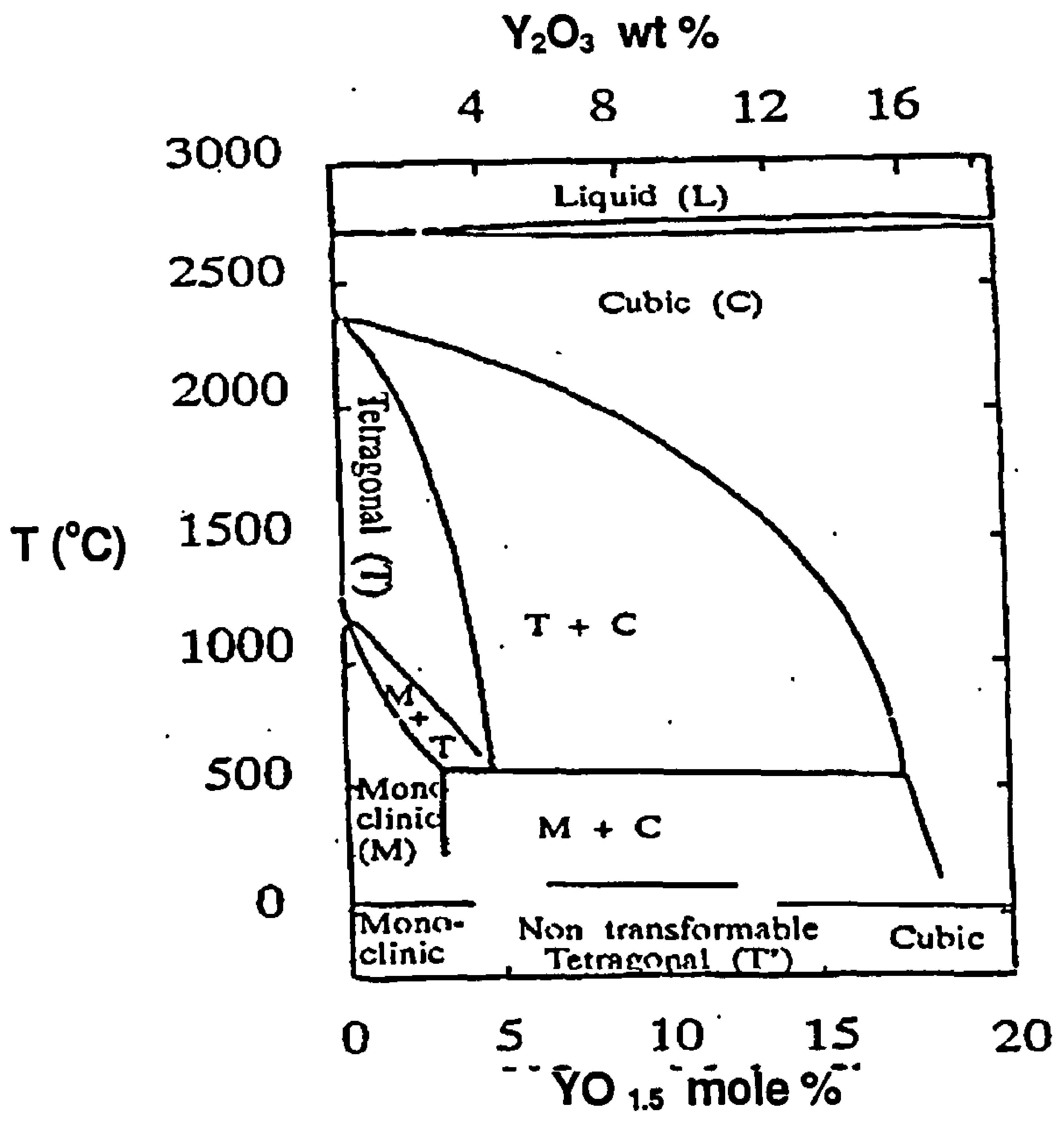

Figure 2.11 Phase Diagram for ZrO_2-Y_2O_3 (After Scott 1975).

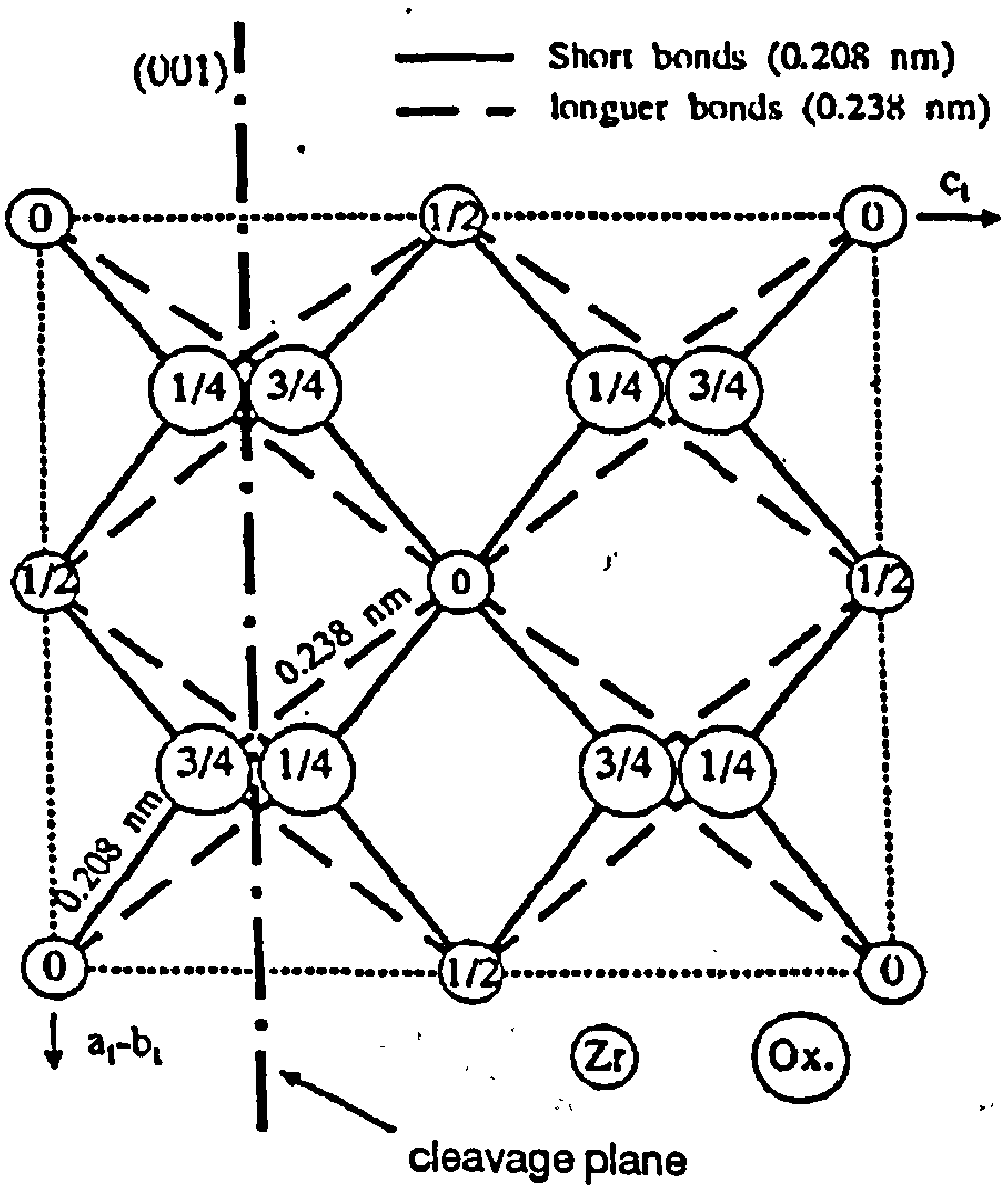

Figure 2.12 Schematic representation of a t' crystallographic cell; projection along [100] axis; existence of an easy cleavage plane perpendicular to (001) (after Alpérine and Lelait 1994).

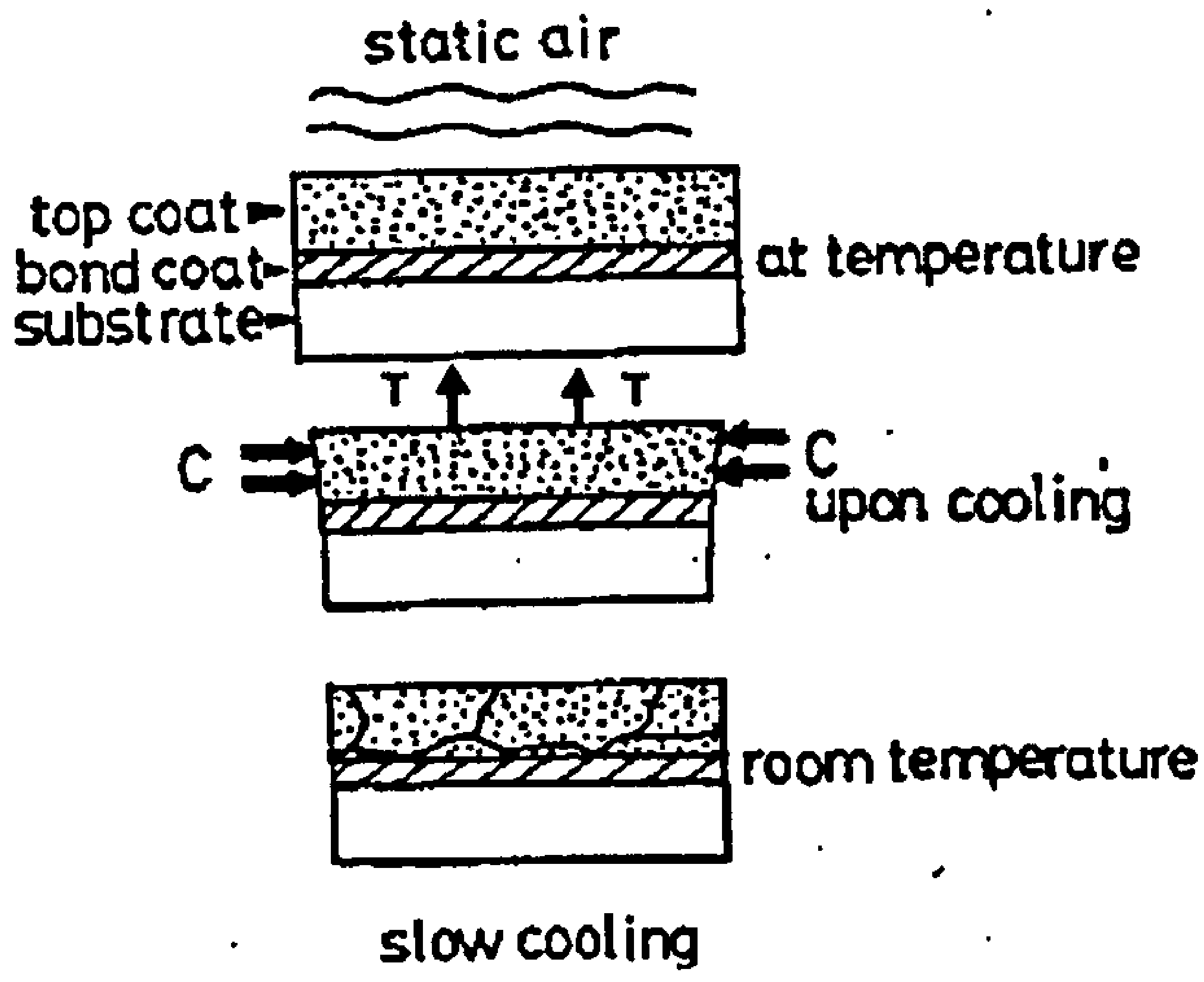

Figure 2.13 Schematic representation of the effects of thermal shock on the cracking modes of top coating upon coating. C, T are compressive and tensile stress respectively (after Wu et al. 1989a).

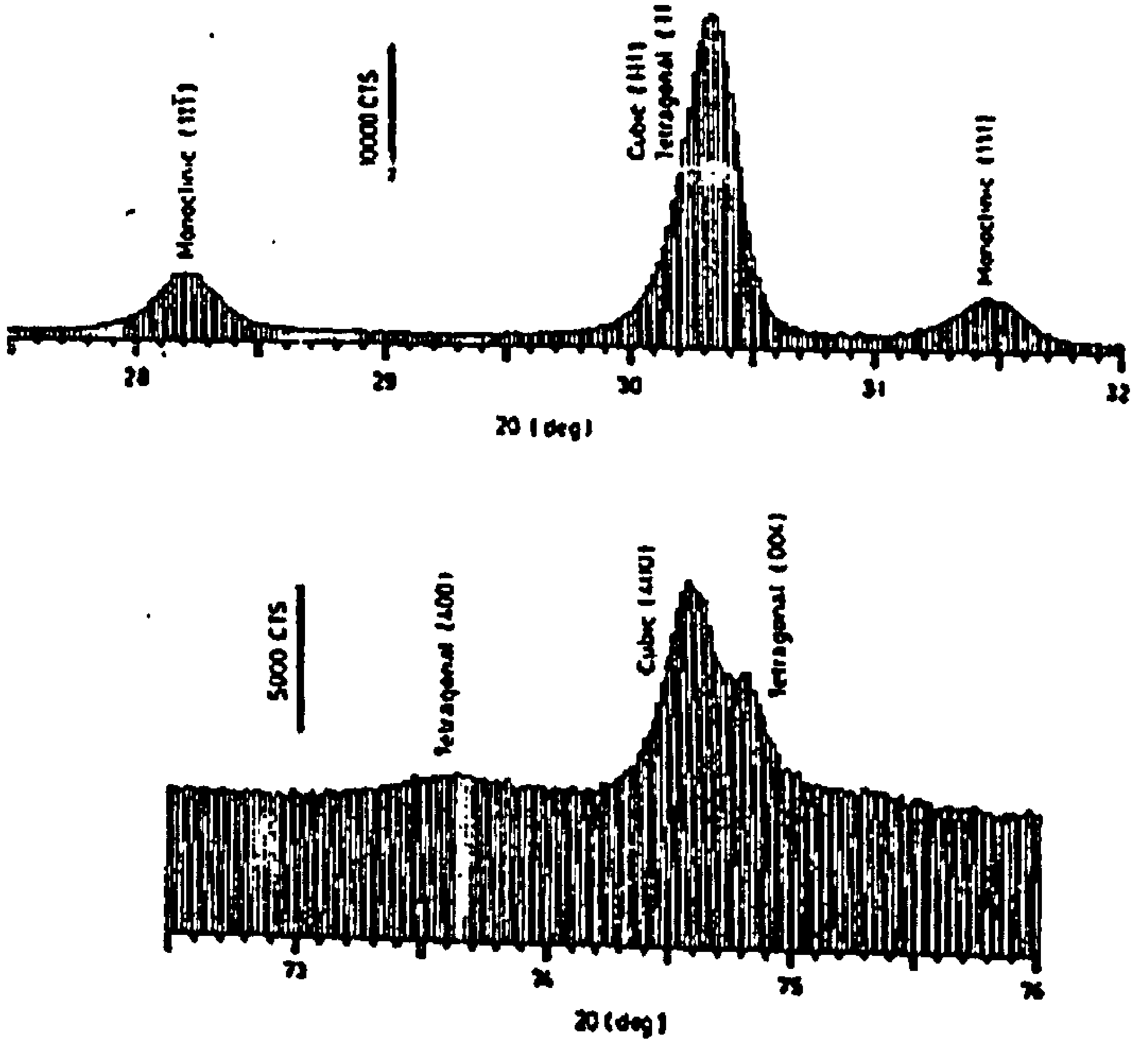

Figure 2.14 Typical XRD pattern of a ZrO_2-Y_2O_3 TBC (after Iwamoto 1985).

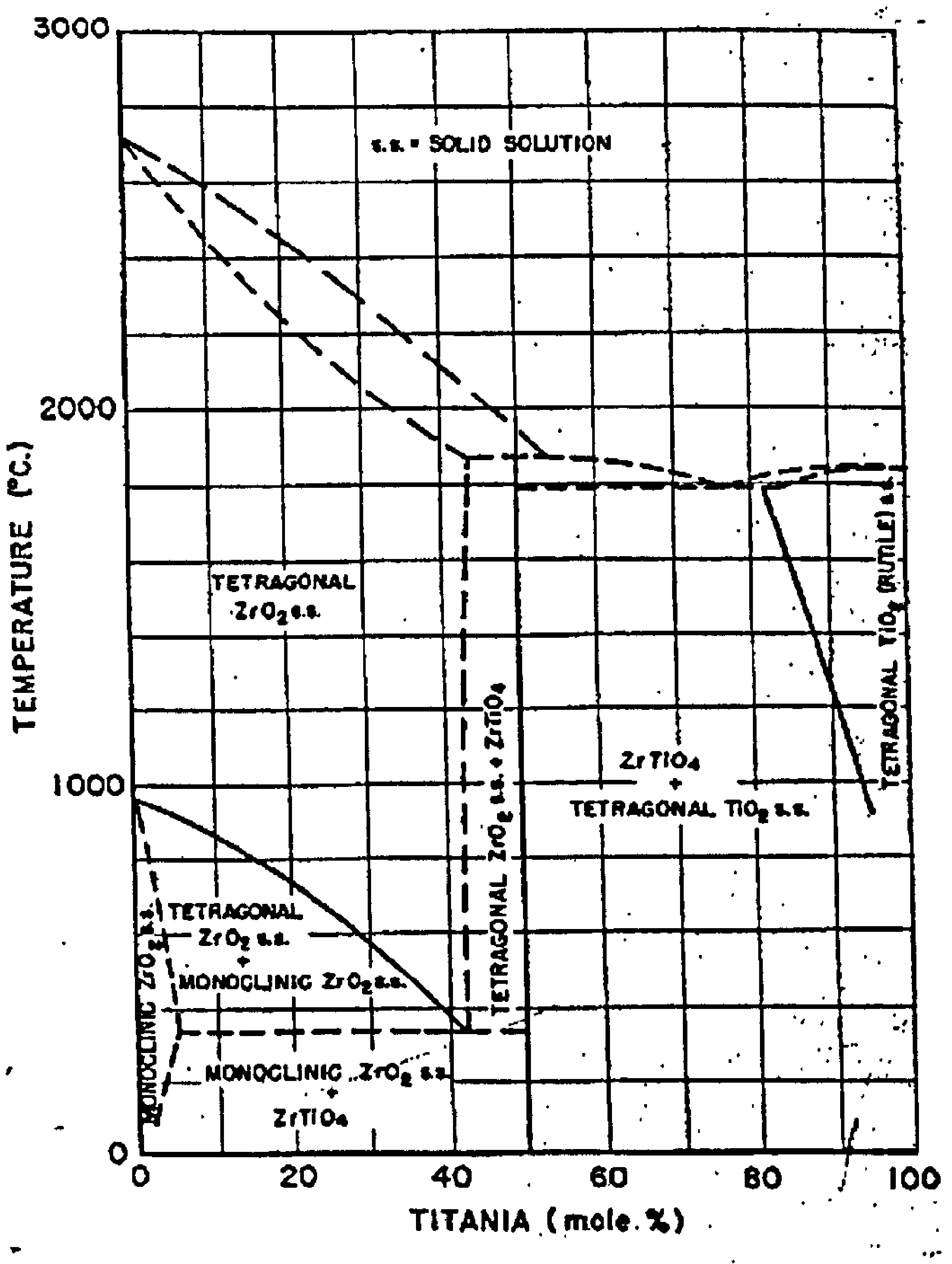

Figure 2.15 ZrO_2-TiO_2 phase diagram (after Brown and Duwez, 1954).

3 EXPERIMENTAL DETAILS

3 .1 SPECIMENS

The specimens consisted of pieces of stainless steel covered by a ceramic coat (ZrO_2-Y_2O_3-TiO_2 or ZrO_2-Y_2O_3) with an intermediate metallic bonding coat (NiCrAlCoY). Table 3.1 shows the chemical composition of each specimen component.

The stainless steel pieces were cleaned by blasting with Al_2O_3 and the bond coat was deposited by thermal spraying using an oxyacetylene flame. Subsequently the ceramic coating was sprayed using a 60V, 600 A H_2-Ar plasma.

Both types of samples were prepared by Plasmatec (Edo. Miranda, Venezuela) and supplied by Intevep, S.A. (Edo. Miranda, Venezuela).

3 .2 X-RAY DIFFRACTION

X-ray Diffraction (XRD) patterns of ceramic powders used for the plasma spraying and the as-sprayed ceramic coats were obtained using a Philips PW 1710 X-ray diffractometer with Ni filtered Cu Kα radiation of wavelength 0.15418 nm. Scans in the range 10-90° were recorded using a step size of 0.02°, and scan speed of 0.02° s^{-1}. The XRD patterns of the ceramic coats were obtained from the surfaces in the as-sprayed and as-polished conditions. Powdered samples of the coating were also analysed by XRD in order to evaluate possible transformations due to mechanical stress.

The mole fraction of monoclinic (C_m), tetragonal (C_t) and cubic (C_c) ZrO_2 were calculated using Equations 2.2- 2.4.

3 .3 SCANNING ELECTRON MICROSCOPY

The morphology and size of the ZrO_2-Y_2O_3-TiO_2 and ZrO_2-Y_2O_3 powders used in the preparation of the coatings were analysed using Scanning Electron Microscopy (SEM). A JEOL JXA-840A microscope was used. The surface, fracture surface, and cross section of the coatings were also studied by SEM. Images were obtained with the secondary electron (SE) and backscattered electron (BE) detectors activated in order to use the topographical and composition contrasts, respectively. Chemical composition information of the coatings and powders were obtained by Energy Dispersive Spectrometry (EDS), using a Link X-ray detector-analyser, model AN10,000, attached to the microscope.

3 .3 .1 Powders

The ceramic and bond coat powders used in the coating preparation were analysed by SEM and EDS. Drops of a diluted suspension (0.1 %) of the powder in methanol were deposited on a flat stub. Once the methanol had evaporated, the dispersed powder was covered with carbon to ensure electron conductivity.

3 .3 .2 Cross-Sections

Transverse sections of the specimen were cut to display the arrangement between substrate, bond and ceramic coat. The cut specimen was embedded in an acrylic thermosetting resin in such a way as to expose the cross section face to the surface (Figure 3.1). This surface was ground manually using a sequence of SiC papers and afterward polished successively using cloth discs impregnated with 1 and 0.25 µm diamond pastes. Finally, the samples were coated with carbon in an evaporator before the SEM and EDS analysis.

3 .3 .3 Fracture Surfaces

The surfaces obtained from the fracture of the ZrO_2-Y_2O_3-TiO_2 coat as-sprayed and as-thermal treated (as described in Section 3.5.2) were examined using SEM. The fracture surfaces were coated with gold by sputtering to ensure electron conductivity during the SEM observations.

3 .4 TRANSMISSION ELECTRON MICROSCOPY

The Transmission Electron Microscopy (TEM) characterization consisted of bright field (BF) and dark field (DF) imaging of the specimens selected for analysis. Information about the crystallography of the specimens was obtained from Selected Area Diffraction Patterns (SADP) or by Electron Microdiffraction. An analytical transmission electron microscope JEOL 2000-FX operating at 200 kV with a Link AN10,000 X-ray detector-analyser system was employed.

Samples of the ceramic coat were separated from the substrate and prepared for analysis under the transmission electron microscope. Two methods were used: a) suspension of the powdered specimen in methanol , and b) thin sections prepared by using ion beam thinning.

3 .4 .1 Suspension of the Ceramic Coat

In this method, a sample of the ceramic coat was pulverised using an agate mortar to get a very fine powder. An initially diluted (0.1 wt%) suspension in methanol was prepared from this powder. The suspension was set in an ultrasound bath for 180 seconds. After most of the suspension had sedimented, a sample from the liquid was taken and further diluted (1:20) with methanol. About three drops of this final suspension was deposited with a micro-pipette onto a 100 mesh holey carbon coated copper grid.

3 .4 .2 Ion Beam Thinning Principle

In this process, known as sputtering, a beam of inert gas ions at an energy of several keV is used to remove material from the surface of the specimen. Sputtering occurs when any ion carrying more than 100eV of energy hits the surface of the target. The sputtering yield *Y* (the number of atoms ejected by each incident ion or atom) increases with the ion energy and as the mass of the bombarding ion increases, but *Y* decreases as the atomic mass of the specimen increases, as shown in Figure 3.2. In practice, argon is used; lighter inert gases (helium, neon) thin too slowly and heavier ones (krypton, xenon) are too expensive.

Although Y increases with beam energy, at the same time the depth of ion penetration and the risk of damage increase. The optimum energy is thus in the range of 1-10 keV, and a value between 3-6 keV is generally used (Goodhew 1973, 1984). The sputtering yield also depends on the angle at which the ions hit the surface (Figure 3.3). There is a maximum at between 10 and 30°. In the later stages of the thinning it is not the thinning rate but depth of damage or differential thinning rates between two phases which are important and hence many specimen are finished at a glancing angle (5-10°) (Goodhew 1973, 1984). This differential thinning can also be minimised by specimen rotation.

The arrangement of the ion beam thinning is shown in Figure 3.4. The specimen chamber is evacuated to approximately 1.33×10^{-3} Pa but the argon flow in the two guns brings the operating pressure up to between 1.33 and 0.133 Pa. The gun anodes are held at the chosen potential and the ion beam is emitted from a hole in the cathode (at earth potential). The specimen is mounted in such a way that the two ion beams can strike it at a glancing incidence from above and below. The specimen is held between two tantalum diaphragms with a 3 mm hole that maintains the specimen centrally in the holder.

3 .4 .3 Preparation of the Ceramic Coat by Ion Beam Thinning

3 .4 .3.1 Pre-Thinned Sections

Samples of the ceramic coat were separated from the bond coat, then planar and cross-sections of the ceramic coat were obtained. Afterwards these were ground manually using SiC paper, and finally polished with 1 and 0.25 µm diamond pastes. These polished sections, about 100 µm thick, were then mounted between two tantalum diaphragms and located in the specimen chamber of the ion beam thinner for final thinning.

3 .4 .3.2 Specimen Thinning

An Ion Tech B403 sputter machine was used for the preparation of thin sections of the ceramic coat. It was operated initially at 6 kV and in the final stage at 4 kV. The initial angle of incidence ϕ, was approximately between 30 and 45°, the final ϕ was limited by the equipment to about 20°. The specimen was rotated during the sputtering to diminish differential etching and production of artifacts.

3 .4 .4 Preparation of the Coating Cross Section

Pieces (20x20x5mm) of the whole coating including the substrate were thinned on both sides (top coat and steel substrate) manually using SiC grinding paper, in order to have available the interfaces substrate/bond coat/ceramic coat for the analysis. The ceramic face was polished with 1 and 0.25 μm diamond pastes. The polished ceramic faces of two pieces were bonded against each other using a cyano-acrylate resin as shown in Figure 3.5.

Transverse slices (1 mm thick) from this specimen arrangement (Figure 3.5) were obtained using a diamond saw. A preliminary 3x3x1 mm section was ground with SiC paper and then polished with 1 and 0.25 μm diamond pastes. In order to preserve the integrity of the specimen section, this was mounted in a 800 μm hole-copper grid, using a cyano-acrylate resin while grinding and polishing were done on the opposite face. The final pre-thinned section, about 100 μm thick, was fixed between two 800 μm hole-copper grids, and then located in the ion beam for further thinning as described in Section 3.4.3.2.

3 .5 THERMAL TREATMENT

3 .5 .1 Heat Treatment of ZrO_2-Y_2O_3-TiO_2 and ZrO_2-Y_2O_3 Coatings

Disks of stainless steel covered by the ZrO_2-Y_2O_3-TiO_2 and ZrO_2-Y_2O_3 coatings (Table 3.1) were heated in a programmable furnace, in air to 900 °C using a heating ramp of 3 °C/minute and a dwell time of 24 hours. Afterwards they were left to cool to room temperature inside the furnace (about 8 hours). The resulting samples were examined by SEM and XRD.

3.5.2 Heat Treatment of ZrO_2-Y_2O_3-TiO_2 Coating

3.5.2.1 Air atmosphere

Type 2 specimens of ZrO_2-Y_2O_3-TiO_2/NiCrCoAlY coating (Table 3.1) were heated in a programmable furnace (3 °C/minute) at either 900, 1200, 1400, or 1600 °C for 24 hours, in a static air atmosphere. After the heat dwell time was completed, the samples were quenched to room temperature.

3.5.2.2 Argon Atmosphere

In order to evaluate the influence of the bond coat oxidation and the coating integrity during the thermal treatment of the coating, some experiments were also done under an argon atmosphere. A tube furnace with a heating programmer was used for this purpose. A heating ramp of 3 °C/minute and a dwell time of 24 hours were used for treatments either at 900, 1000, 1100 or 1200°C. During all the heat treatment, a current of argon was passed through the tube furnace. Subsequently, the samples were left to cool down slowly, inside the furnace under the current of argon for about eight hours.

3.6 POWDER COMPACTS

In order to compare the microstructure of ZrO_2-Y_2O_3-TiO_2 and ZrO_2-Y_2O_3, some powder compacts were prepared using commercially available plasma spraying powders as detailed below. Similar experiments were also conducted using fine powder mixtures prepared in the laboratory, as shown in Table 3.2.

3.6.1 Pressing

Disks of each powder (0.6 g) were prepared in an 11 mm diameter die, using a pressure of 625 MPa. About 3 wt% stearic acid was added to aid the powder compaction and to reduce powder-mould friction. Larger disks of 30 mm of diameter were prepared from 5.0 g of the ZrO_2-Y_2O_3-TiO_2(A) and ZrO_2-Y_2O_3 fine powders using a pressure of 277 MPa. No pressing additive was used in this case.

3 .6 .2 Sintering

The pressed disks of ZrO_2-Y_2O_3-TiO_2 and Y_2O_3-ZrO_2 plasma spray powders and fine powders were fired under an air atmosphere in a programmable furnace at different temperatures; 1350, 1400, 1450 or 1550 °C for 1 hour, using a heating ramp of 3 °C/minute, and left to cool down inside the furnace (about 8 hours).

The larger pressed disks (30 mm diameter) from the fine powders were heated (3 °C/minute) at 1350 °C for 1 hour, and then left to cool down inside the furnace. The sintered products were annealed at 1600 °C for 4 hours. The surface of the sintered and annealed products were analysed by SEM and XRD.

3 .6 .3 Characterization of the Sintered Bodies

3 .6 .3.1 Density

The bulk density of the sintered bodies was determined using the immersion in mercury method, based on the Archemides` Principle. In this method, the weight necessary to immerse a sample in mercury is measured and related to the weight of the sample in air and the density of mercury to determine the bulk density of the sample (Ashworth 1969).

$$\rho_s = (W_1/W_2)\rho_{Hg} \qquad 3.1$$

where, ρ_s is the density of sample to be determined, W_1 is the weight of the sample in air, W_2 is the weight necessary to immerse the sample in mercury, and ρ_{Hg} is the density of mercury.

3 .7 TABLES AND FIGURES

Table 3.1 Details of the specimens used

Component	*Chemical Composition (wt%)*	*Other details*
Substrate	Stainless steel (18Cr, 9Ni)	**Type 1:** Disc, 32 mm diameter and 15 mm thick. **Type 2:** Coupons 5x30x100 mm.
Bond coat	Ni (17Cr, 5.5Al, 2.5Co, 0.5 Y_2O_3)	Powder particle size 45-150 µm
ZrO_2-Y_2O_3-TiO_2 Metco 143	ZrO_2 (10 Y_2O_3, 18 TiO_2)	Powder particle size 5-75 µm
ZrO_2-Y_2O_3 Metco 204B-NS	ZrO_2 (8Y_2O_3)	Powder particle size 45-75 µm

Table 3.2 Materials used to prepare sintered bodies

Powder	*Commercial Description*	*Main Composition (wt%)*	*Particle size (µm)*
ZrO_2-Y_2O_3	HSY-3⑴	ZrO_2-5.4 Y_2O_3	0.7
TiO_2	R-SM3⑵	TiO_2	0.18
ZrO_2-Y_2O_3-TiO_2(A)	HSY-3 + R-SM3 mixture (84:16)	ZrO_2-4.5Y_2O_3-16TiO_2	0.18-0.7
ZrO_2-Y_2O_3-TiO_2(B)	Metco 143⑶	ZrO_2-10Y_2O_3-18TiO_2	5-75

⑴ Mandoval Ltd, UK.
⑵ Tioxide Chemicals Ltd, UK.
⑶ Sulzer Metco, UK.

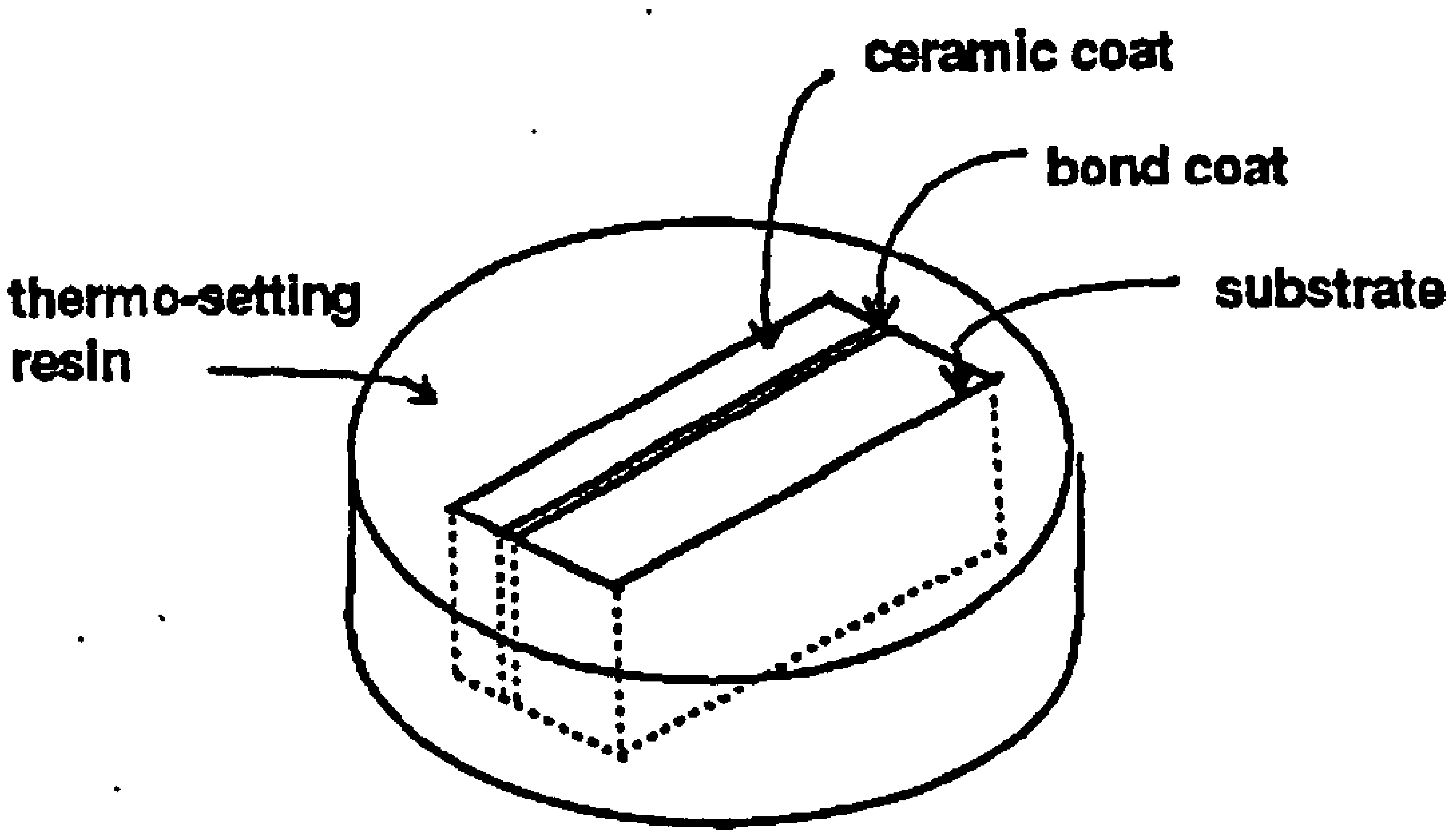

Figure 3.1 Preparation of coating cross-section to be analysed by SEM.

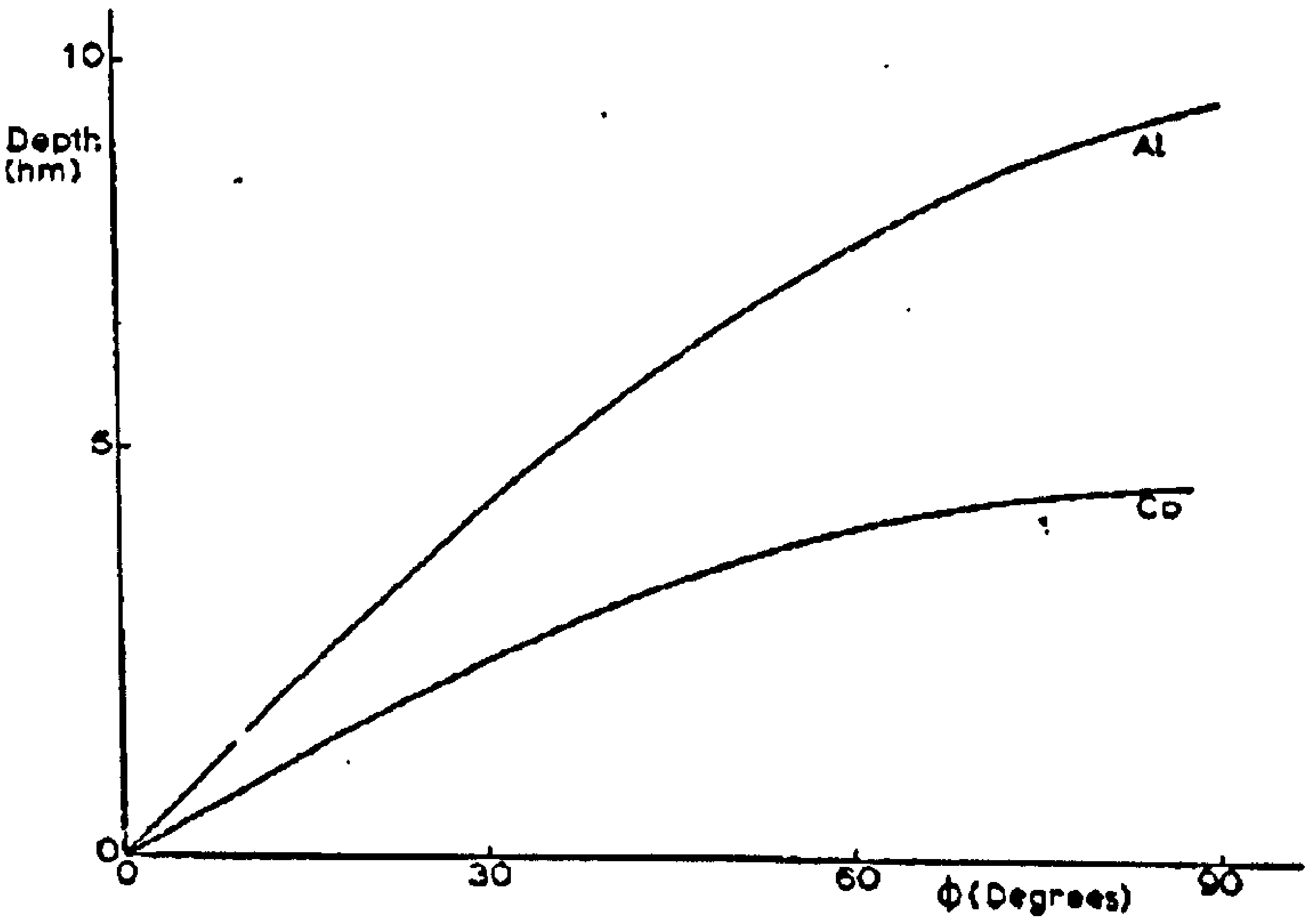

Figure 3.2 The depth of penetration of argon ions in Al and Co as a function of the angle between the beam and the specimen (at 6 keV) (after Goodhew 1973).

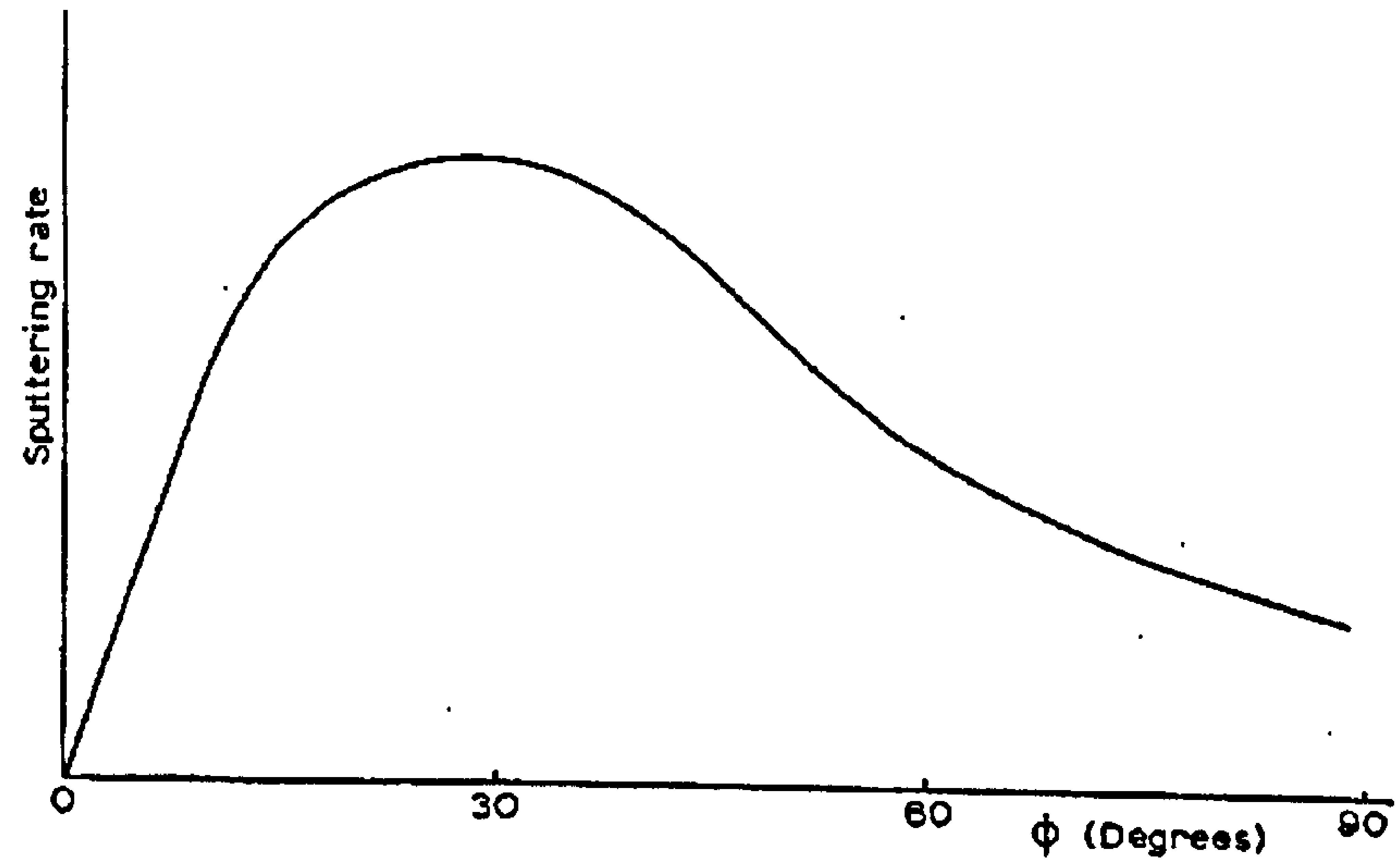

Figure 3.3 The variation of sputtering yield Y (arbitrary units) with the angle of incidence ϕ (after Goodhew 1973).

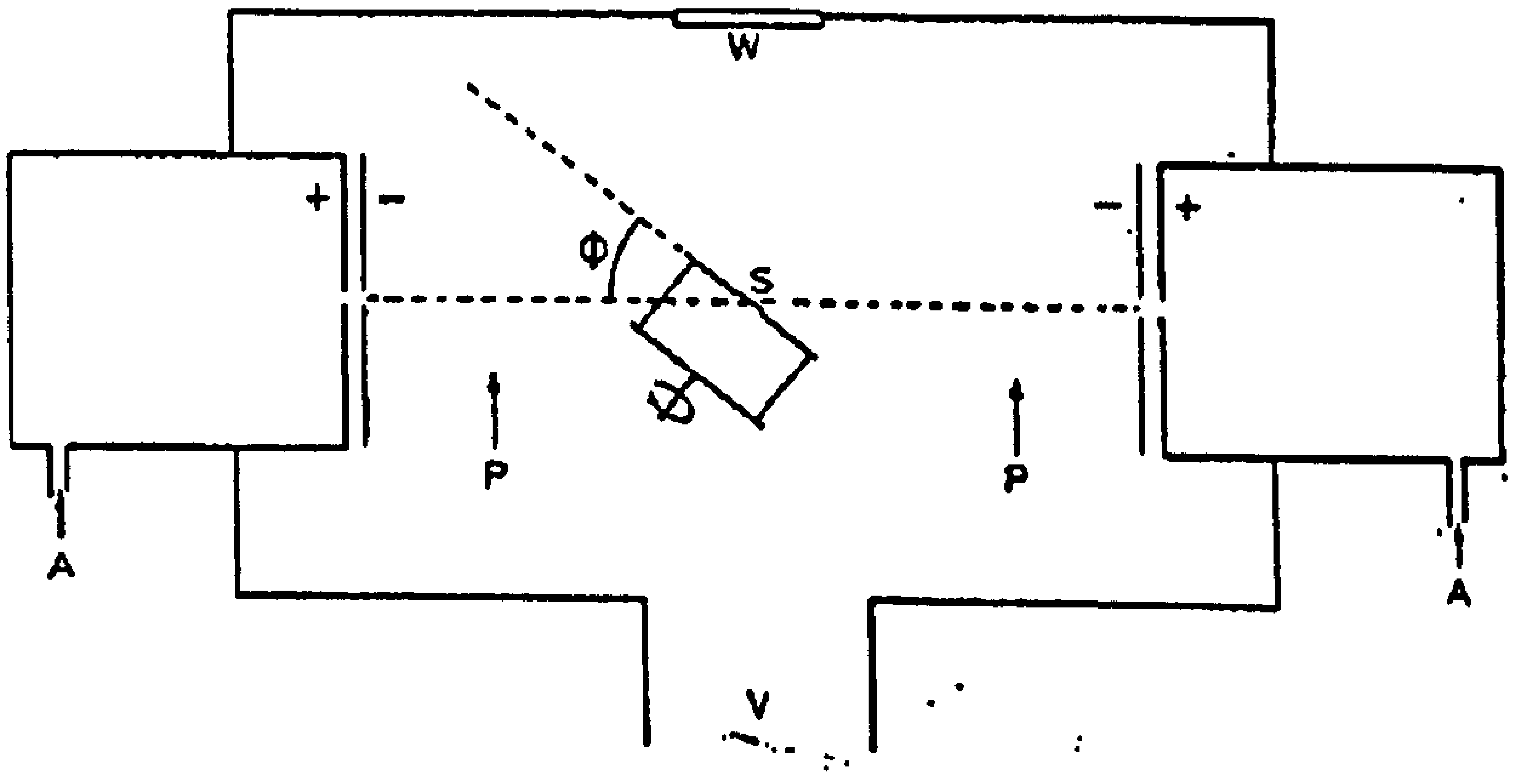

Figure 3.4 Schematic diagram of an ion beam machining apparatus, A: argon inlets, S: specimen, W: window for observation, V: vacuum pumps, P: retractable probes for ion beam current measurement, ϕ : angle of incidence (after Goodhew 1973).

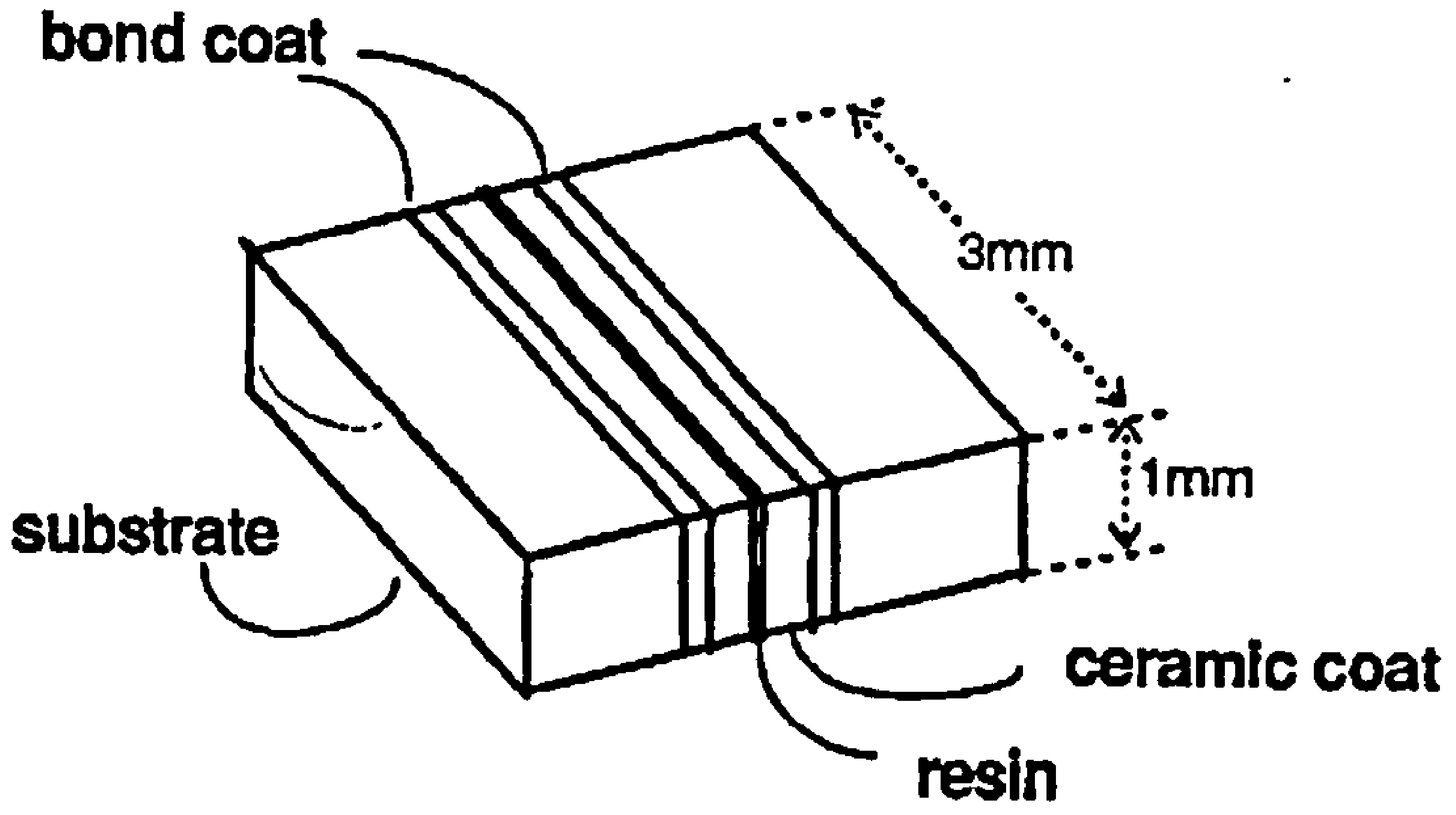

Figure 3.5 Assembly used in the preparation of a thin section of the coating sample for observation of the interfaces.

4 X-RAY DIFFRACTION

4.1 RESULTS

4.1.1 Powders

Figure 4.1 presents the XRD pattern for the ZrO_2-Y_2O_3-TiO_2 powder prior to plasma-spraying. This pattern indicates that ZrO_2 is present mainly in the monoclinic form, identified using the $(11\bar{1})_m$ and $(111)_m$ reflections. This is corroborated by inspection of the ZrO_2 phase distribution calculated from the XRD pattern (Table 4.1). Y_2O_3 (cubic) is identified from the $(211)_c$, $(222)_c$ and $(400)_c$ peaks. TiO_2 is present in the powder under the anatase form, identified by the $(101)_t$ and $(200)_t$ reflections. The XRD pattern of the ZrO_2-Y_2O_3 powder is shown in Figure 4.2. In contrast with the case of ZrO_2-Y_2O_3-TiO_2 powder, ZrO_2 is present in its three forms, and Y_2O_3 was not detected.

4.1.2 As-Sprayed Ceramic Coats

The XRD patterns of the ZrO_2-Y_2O_3-TiO_2 (5.2 mole% Y_2O_3, 26.4 mole% TiO_2) and ZrO_2-Y_2O_3 (4.5 mole% Y_2O_3) ceramic coats show that ZrO_2 is present in its three polymorphs (Figure 4.3). XRD calculated values for of *m*-, *t*- and *c*-ZrO_2 present in each coat are given in Table 4.2 and show that most of ZrO_2 in the ZrO_2-Y_2O_3 coat is in the form of *c*-ZrO_2, while the concentration of *m*-ZrO_2 is very low. On the other hand, the content of *t*-ZrO_2 in the ZrO_2-Y_2O_3-TiO_2 coat is almost twice the value of that in the ZrO_2-Y_2O_3 coat.

The XRD patterns of the powdered ceramic coats (not included here) showed no significant differences in comparison with the as-sprayed ceramic coat XRD patterns. The proportions of *m*-, *t*- and *c*-ZrO_2 in each coat were very similar in the as-sprayed and as-polished conditions (Tables 4.2 and 4.3, respectively). However, a higher *t*-ZrO_2 concentration was observed in the polished specimen, in a greater extent in the ZrO_2-Y_2O_3-TiO_2 coat.

4.1.3 Ceramic Coats Treated at 900 °C

The phase distribution of ZrO_2 in the thermally treated ceramic coats were calculated from the corresponding XRD patterns (Table 4.4). Comparing with the values calculated for the as-sprayed coats, some differences can be observed. After thermal treatment, an increment of the *t*-ZrO_2 content can be detected at the expense of the *c*-ZrO_2 content. This is evident to a greater extent in the ZrO_2-Y_2O_3-TiO_2 coat. The concentration of *m*-ZrO_2 remained practically constant.

4.1.4 Phase Distribution after Thermal Treatment

The XRD pattern of the type 2 ZrO_2-Y_2O_3-TiO_2 coat (Table 3.~~1~~2) is presented in Figure 4.4. Cubic, tetragonal and monoclinic forms of ZrO_2 can be observed. The presence of $ZrTiO_4$ in the coat was also identified. This was not observed in the XRD pattern of the type 1 ZrO_2-Y_2O_3-TiO_2 coats (disk specimens), shown in Figure 4.3. The ZrO_2 phase distribution was also different as shown in Table 4.5; the *m*-ZrO_2 concentration was lower. X

Figure 4.5 shows the variation of the ZrO_2-phase distribution in the ZrO_2-Y_2O_3-TiO_2 coat after thermal treatment in air and argon. The mole fraction of *m*-ZrO_2 remained almost constant after both thermal treatments. There is a clear tendency of *t*-ZrO_2 to increase at the expense of *c*-ZrO_2 after heating in an air and quenching, this is more evident at high temperatures (> 1200 °C). By contrast, in the thermal treatment carried out in argon with a slow cooling rate, a slight decrease of the *t*-ZrO_2 content can be observed.

4.1.5 Sintered Bodies

Figure 4.6 shows the XRD patterns of three types of pressed bodies sintered at 1350 °C. These were prepared from: a) mixture of powders ZrO_2-Y_2O_3-TiO_2(A) , b) the ZrO_2-Y_2O_3-TiO_2(B) powder used for plasma-spraying, and c) ZrO_2-Y_2O_3 powder (Table 3.2). Figure 4.7 shows the variation of the ZrO_2-phase distribution as a function of the sintering temperature.

In the case of the ZrO_2-Y_2O_3 and the ZrO_2-Y_2O_3-TiO_2(A) sintered specimens, most of the ZrO_2 was present as *t*-ZrO_2. However, the mole fraction of *t*-ZrO_2 decreases as the sintering temperature is increased. The sintered ZrO_2-Y_2O_3-TiO_2(B) plasma-spray powder consisted of *t*-ZrO_2 , *c*-ZrO_2, and *m*-ZrO_2. At a high temperature (> 1450 °C) a low proportion of *m*-ZrO_2 was present in the fired body, while the concentration of *t*-ZrO_2 became slightly higher.

After annealing the ZrO_2-Y_2O_3 and ZrO_2-Y_2O_3-TiO_2(A) 1350 °C sintered bodies at 1600 °C for 4 hours some decomposition of the *t*-ZrO_2 was observed. The XRD patterns of the sintered bodies indicate they consisted of *t*-ZrO_2 while the XRD pattern of the annealed specimens show the presence of *t*- and *c*-ZrO_2 (Figure 4.8).

Another important feature observed, which is clearer in the XRD patterns of the sintered bodies, is the displacement of the $(004)_t$, $(400)_t$ and $(004)_c$ peaks with the addition of TiO_2. Figure 4.8 shows a detail of the XRD patterns from the ZrO_2-Y_2O_3 and ZrO_2-Y_2O_3-TiO_2(A) pressed powders sintered at 1350 °C and from these bodies annealed at 1600 °C for 4 hours. The peaks appear as doublets due to the Cu X-ray source which contains the CuKα(1.5406 nm) and CuKβ (1.5444 nm) radiations. For practical purposes, the more intense peak from the doublet has been considered.

After comparing the XRD patterns of the ZrO_2-Y_2O_3 and ZrO_2-Y_2O_3-TiO_2(A) sintered bodies, it can be observed that the $(004)_t$ peak has been shifted from 73 to 72.6°, while the $(400)_t$ peak (74.3°) has shifted to a higher 2θ value (75°). A similar displacement is also detected in the $(400)_c$ peak (73.9 to 74.1°) on comparing the XRD patterns of the sintered bodies annealed at 1600 °C. Therefore, considering the *t*-ZrO_2 phase, the *a*-axis has contracted and the *c*-axis has expanded due to the addition of TiO_2. The *a*-axis of the *c*-ZrO_2 is also expanded due to the addition of TiO_2.

4 .2 DISCUSSION

The expressions used for the calculation of the *m*-, *t*- and *c*-ZrO_2 mole fractions give good approximate values; with a 5% deviation as an estimated error (**Miller et al.** 1981). These expressions take into account the overlapping of the $(111)_c$ and $(111)_t$ peaks and introduce a correction based on the intensities of the $(004)_c$, $(400)_t$ and $(004)_t$ reflections. Unfortunately the intensity of the diffracted X-rays is rather low in this region (71-75°) and this affects the precision of the calculations. In general, the plasma-sprayed coatings analysed by XRD gave a low-intensity pattern (maximum peak intensity about $1x10^3$ counts) compared with the sintered bodies XRD (maximum peak intensity about $5x10^3$ counts). Consequently, the determination of ZrO_2-phase distribution in the sintered bodies had a higher precision associated with it. In spite of this, it was found that the calculation of *m*-, *t*- and *c*-ZrO_2 mole fractions using Equations 2.2-2.4, offered a useful tool to evaluate tendencies of change after different treatments of the ZrO_2 coats under study.

4 .2 .1 Powders

In the ZrO_2-Y_2O_3-TiO_2 powder used for the coating preparation, ZrO_2 had not been stabilized by the content of Y_2O_3 (5.2 mole%) or TiO_2 (26.4 mole%). Therefore, it existed mainly as *m*-ZrO_2. The TiO_2 was determined to be in the mixture as anatase, whereas it is expected to be present as rutile according to the ZrO_2-TiO_2 phase diagram (Figure 2.15). This suggests that the powder investigated consisted of a mechanical mixture of the constituents rather than a solid solution of them.

Although some stabilization was observed in the ZrO_2-Y_2O_3 powder used for plasma-spraying, as identified by the presence of *t*- and *c*-ZrO_2, there was a considerable amount of *m*-ZrO_2 remaining. The differences observed in these two powders are caused possibly by the differences in preparation method of each powder rather than the proportion of Y_2O_3 or TiO_2 present.

4 .2 .2 As-Sprayed ZrO_2-Y_2O_3 Coat

In this coat, the phase composition found was different to that predicted by the ZrO_2-Y_2O_3 phase-diagram (Figure 2.11). Using this diagram, the ZrO_2-Y_2O_3 coat (8 wt% Y_2O_3) would consist mainly of *t*-ZrO_2 after being rapidly cooled from an initially high temperature state, that occurs during the plasma-spraying process. However, *m*- and *c*-ZrO_2 were present in significant proportions. This might be an indication that there have been changes in the cooling rate of the plasma-sprayed material. Thus a combination of mechanisms would operate during cooling, leading to the *m*- and *c*-ZrO_2 observed in the coat.

Most of the *t*-ZrO_2 found in the coat corresponds to the "non-transformable" tetragonal ZrO_2 (*t'*-ZrO_2) reported as a characteristic feature of ZrO_2 plasma-sprayed coats. After grinding the surface of the coat, no evidence of stress-induced *t*→*m*-ZrO_2 transformation was detected since the concentration of *m*-ZrO_2 was the same.

4 .2 .3 As-Sprayed ZrO_2-Y_2O_3-TiO_2 Coat

Stabilization of ZrO_2 is evidenced in this coating by the presence of the *t*- and *c*-ZrO_2 with the accompanying decrease of *m*-ZrO_2 content, when compared with the powder used in the coat preparation.

The ZrO_2-phase distribution in this coat was different to that predicted by the ZrO_2-Y_2O_3-TiO_2 phase composition-diagram (Figure 4.9). This diagram indicates that a ZrO_2 system with a composition similar to the coat (5 mole% Y_2O_3, 26 mole% TiO_2) would consist of *t*-ZrO_2 and $ZrTiO_4$. However, an appreciable amount of *m*-ZrO_2 was found in the coat and $ZrTiO_4$ was not detected.

The *m*-ZrO_2 content was much higher than in the ZrO_2-Y_2O_3 coat. However, it must be noted that the ZrO_2 in the ZrO_2-Y_2O_3-TiO_2 powder used for the coat preparation, was present as *m*-ZrO_2 almost in all its totality, therefore if some unmelted material is present in the plasma-sprayed coat some *m*-ZrO_2 may be associated with it. On the other hand, *t*→*m*-ZrO_2 transformation may have taken place during the plasma spraying process; differences on the cooling rate along the coat thickness may be the origin of this transformation (Section 7.4).

The concentration of *t*-ZrO_2 is almost twice that found in the ZrO_2-Y_2O_3 coat. As both coats have almost the same concentration of Y_2O_3, it can be deduced that the TiO_2 is the responsible for the increase in *t*-ZrO_2 in the plasma-sprayed coats. An increment of the Y_2O_3 concentration would not be expected to cause the same effect due to the fact that at higher Y_2O_3 levels, the ZrO_2 is present as the *c*-ZrO_2 phase, as predicted by the ZrO_2-Y_2O_3 phase diagram (Figure 2.11), and reported for ZrO_2-Y_2O_3 plasma-sprayed coatings with high concentrations of Y_2O_3 (Miller et al. 1983).

4.2.4 Phase Distribution after Thermal Treatment

Type 2 ZrO_2-Y_2O_3-TiO_2 specimens used in these experiments had a lower content of *m*-ZrO_2 (Table 4.5). Since the same powder was used in the preparation both types of specimens, there must be some differences in the plasma-spraying parameters used in each case. For instance, the temperature of the substrate is very important because it determines the cooling rate of the coating; slow cooling rates would allow diffusion processes take place which affect the final ZrO_2-phase distribution in the coat specimen. Unfortunately no further details about the plasma-spraying parameters used in each case are available to determine exactly the cause of the difference in ZrO_2 phase distribution in these two ZrO_2-Y_2O_3-TiO_2 coats.

In the XRD pattern of this ZrO_2-Y_2O_3-TiO_2 coat $ZrTiO_4$ was also identified. According to the ZrO_2-TiO_2 phase diagram (Figure 2.15), there is a $ZrTiO_4$ + tetragonal TiO_2 solid solution region corresponding to TiO_2 concentrations higher than 50 mole%. Considering that the coat had only 26 mole% of TiO_2, this TiO_2 must be distributed irregularly through the coating enabling $ZrTiO_4$ to be present in those zones richer in TiO_2.

After heat treatments in air the specimens were quenched to room temperature. The coats quenched from high temperatures (> 1200 °C) showed a clear increase in the *t*-ZrO_2 concentration. This must be due to diffusionless *c*→ *t*-ZrO_2 transformation, as any diffusion has been restricted by the fast cooling (Sections 7.4, 7.6). On the other hand, after the heat treatment in argon, the specimens were left to cool down inside the furnace and this took over 8 hours. A slight decrease of the *t*-ZrO_2 concentration was seen as the temperature of the treatment was increased. As the cooling rate in this case was very low, diffusional processes may have taken place. Thus at a high temperature, *t*-ZrO_2 decomposition to *c*- and *m*-ZrO_2 could be initiated (Section 7.4-7.6).

4 .2 .5 Sintered bodies

In the sintered bodies prepared from the ZrO_2-Y_2O_3-TiO_2(A) and ZrO_2-Y_2O_3 powders, ZrO_2 was present only as *t*-ZrO_2. *m*-ZrO_2 was not detected. As the sintering temperature was raised, a decrease of the *t*-ZrO_2 was noted, accompanied by an increase in the *c*-ZrO_2 concentration which suggests decomposition of *t*-ZrO_2 could take place at high temperatures. The ZrO_2-Y_2O_3-TiO_2(B) sintered bodies prepared from the powder used for plasma-spraying had a different ZrO_2 phase distribution; ZrO_2 was present as *m*-, *t*- and *c*-ZrO_2. As the temperature was raised, the *c*- and *m*-ZrO_2 concentrations decreased, increasing the *c*-ZrO_2 content.

The evolution of the ZrO_2 phase distribution in for ZrO_2-Y_2O_3-TiO_2(A) and ZrO_2-Y_2O_3 sintered bodies were almost identical. The main differences in ZrO_2 phase distribution observed in comparison with the ZrO_2-Y_2O_3-TiO_2(B) sintered bodies, should be due to the TiO_2 concentration and particle size of the powders. In the plasma-spray powder, almost all the ZrO_2 was present as *m*-ZrO_2 and the particle size was much larger than that in any of the fine powder used (Table 3.2). Further discussion is presented in Section 7.7.

The expansion of the *c*-axis and the contraction of the *a*-axis observed in ZrO_2-Y_2O_3-TiO_2, has been explained by **Kountouros and Petzow** (1993) in terms of the preferred repulsion between Ti^{4+} cations and the effective double positive charged oxygen vacancies in the [001] direction (Figure 4.10). The length changes in the directions [100] and [001] suggest that the Ti^{4+} cations are incorporated in preferential sites which cause a repulsion between the dopant cations and the vacancies. Thus the *c*-axis expands and the *a*-axis contracts.

4 .3 TABLES AND FIGURES

Table 4.1 Approximate molar fraction of monoclinic, tetragonal and cubic ZrO_2 phase present in ceramic powders used in the preparation of the coatings.

Phase	ZrO_2-Y_2O_3-TiO_2	ZrO_2-Y_2O_3
Monoclinic	0.97	0.34
Tetragonal	0.01	0.19
Cubic	0.02	0.47

Table 4.2 Approximate molar fraction of monoclinic, tetragonal and cubic ZrO_2 phase present in the two as-sprayed ceramic coats.

Phase	ZrO_2-Y_2O_3-TiO_2	ZrO_2-Y_2O_3
Monoclinic	0.15	0.03
Tetragonal	0.46	0.25
Cubic	0.39	0.72

Table 4.3 Approximate molar fraction of monoclinic, tetragonal and cubic ZrO_2 phase present in the two as-polished ceramic coats.

Phase	ZrO_2-Y_2O_3-TiO_2	ZrO_2-Y_2O_3
Monoclinic	0.13	0.03
Tetragonal	0.53	0.28
Cubic	0.34	0.69

Table 4.4 Approximate molar fraction of monoclinic, tetragonal and cubic ZrO_2 phase present in the ceramic coats thermally treated at 900 °C for 24 hours.

Phase	ZrO_2-Y_2O_3-TiO_2	ZrO_2-Y_2O_3
Monoclinic	0.16	0.04
Tetragonal	0.68	0.31
Cubic	0.16	0.65

Table 4.5 Approximate molar fraction of monoclinic, tetragonal and cubic ZrO_2 phase present in type 2 ZrO_2-Y_2O_3-TiO_2 coat specimens.

Phase	ZrO_2-Y_2O_3-TiO_2
Monoclinic	0.07
Tetragonal	0.54
Cubic	0.39

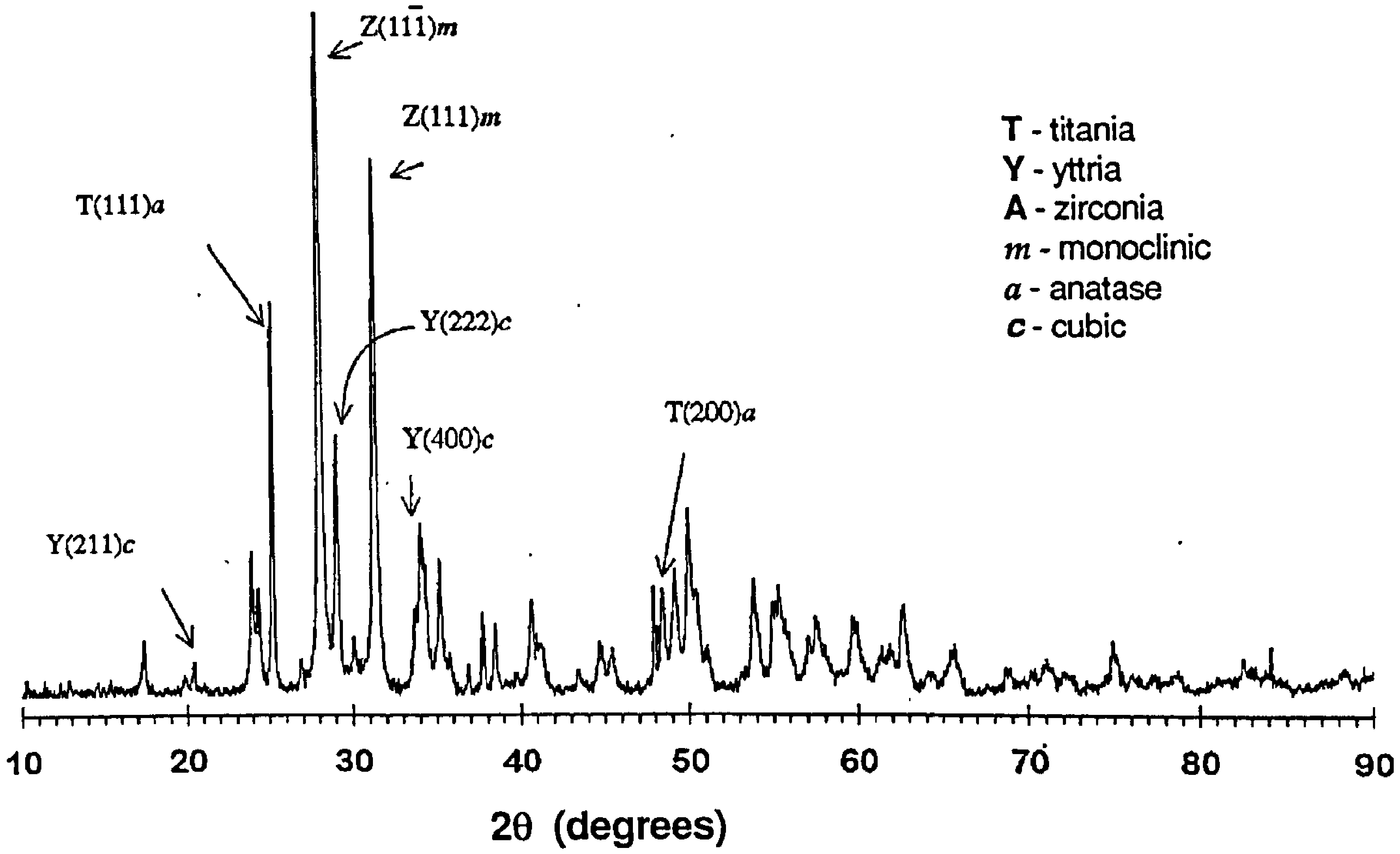

Figure 4.1 XRD pattern of the ZrO_2-Y_2O_3-TiO_2 powder used in the preparation of the coat. For clarity, not all the peaks have been labelled.

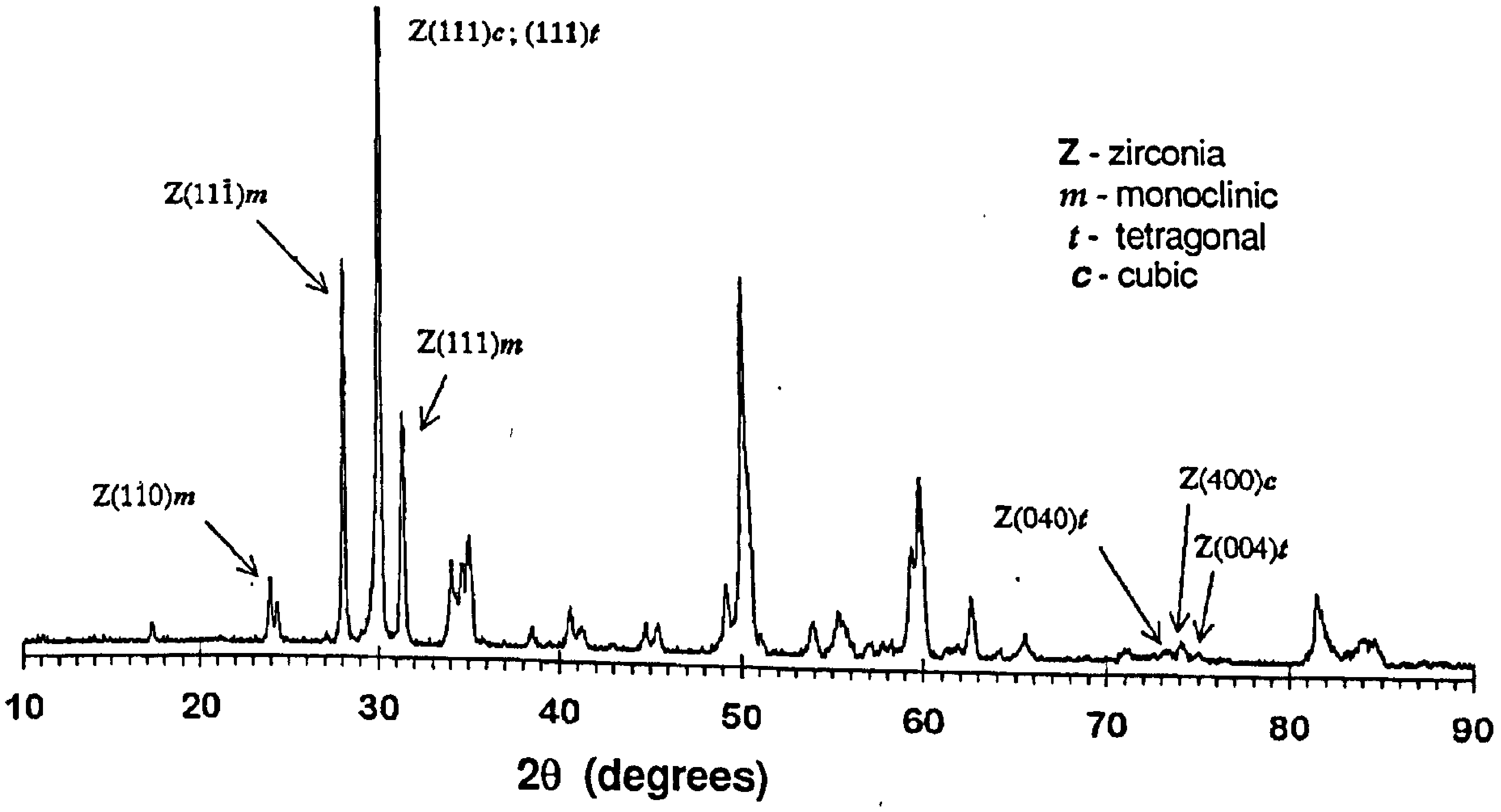

Figure 4.2 XRD pattern of the ZrO_2-Y_2O_3 powder used to prepare the coat. For clarity, not all the peaks have been labelled.

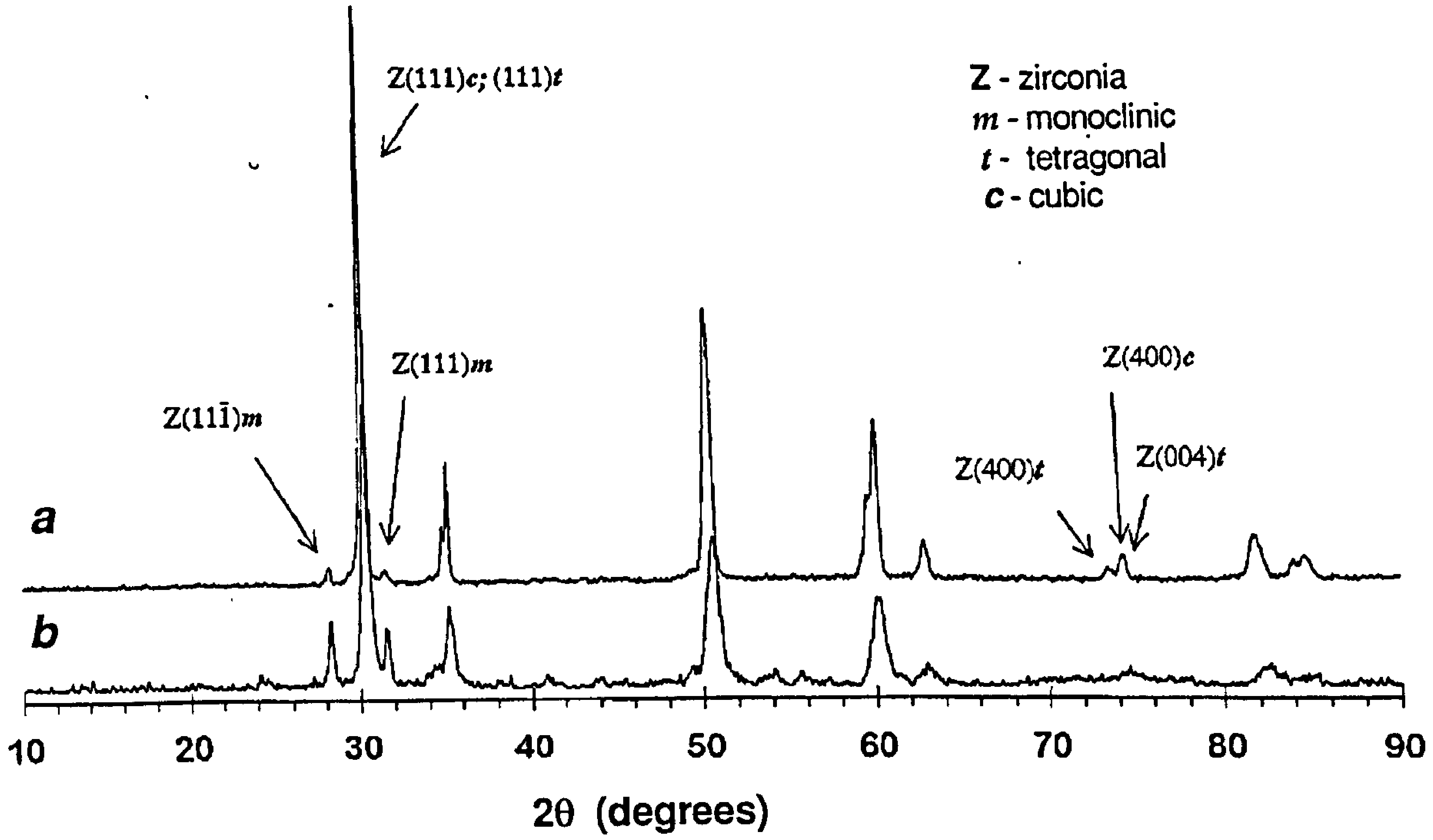

Figure 4.3 XRD patterns of the (*a*) ZrO_2-Y_2O_3, and (*b*) ZrO_2-Y_2O_3-TiO_2 as-sprayed coats. For clarity, not all the peaks have been labelled.

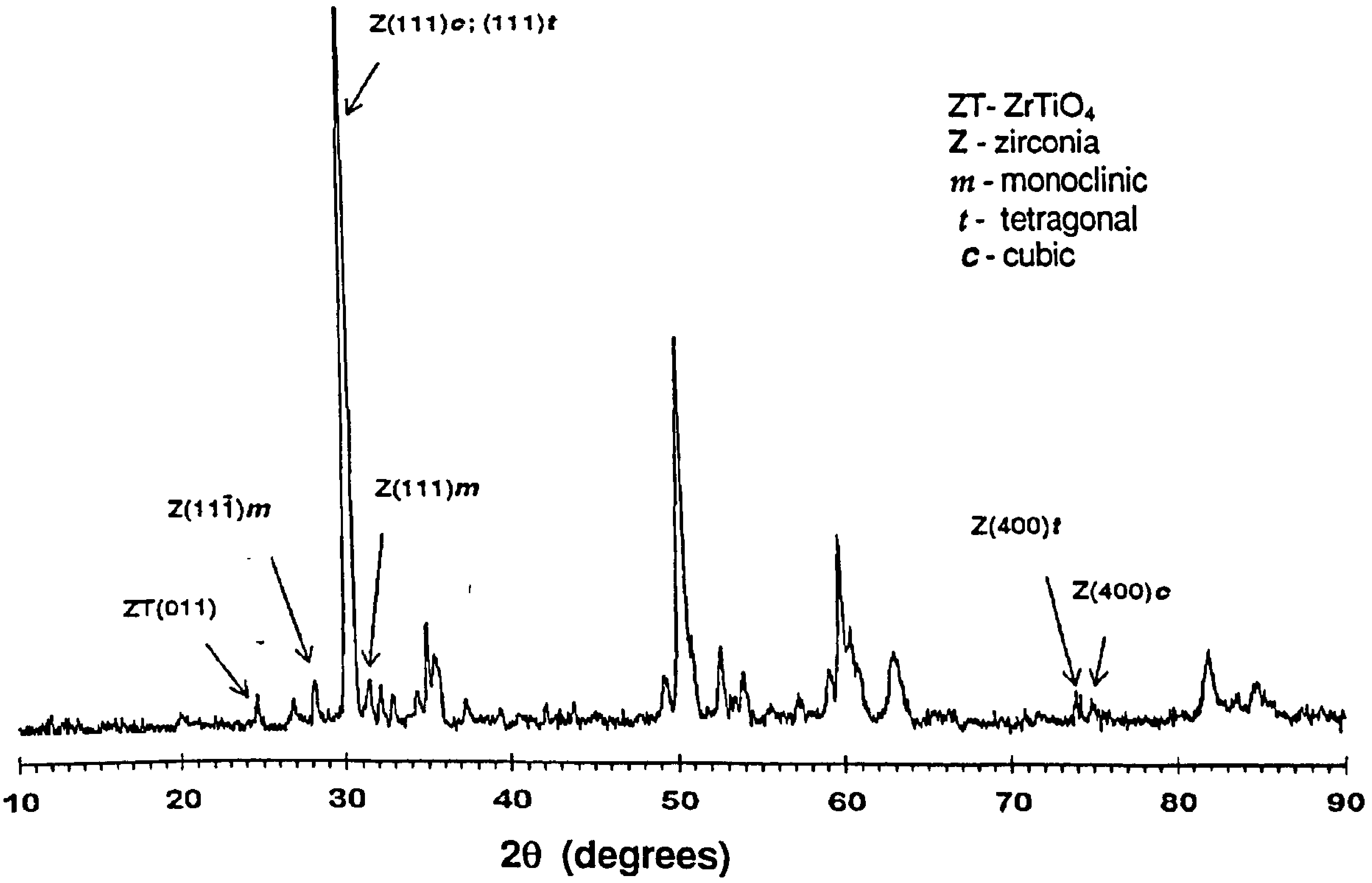

Figure 4.4 XRD pattern of type 2 specimens of the ZrO_2-Y_2O_3-TiO_2 plasma-sprayed coat. For clarity, not all the peaks have been labelled.

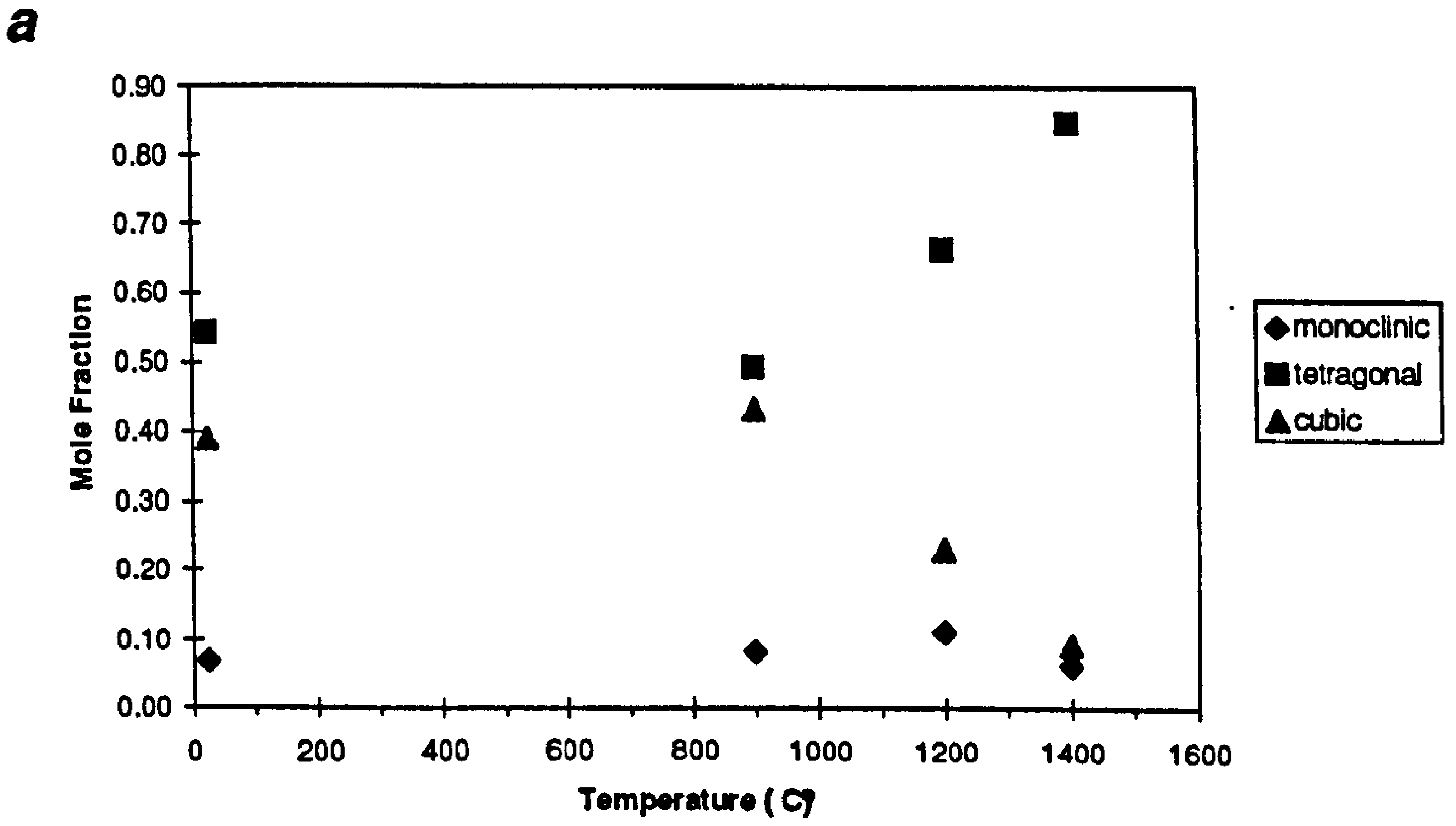

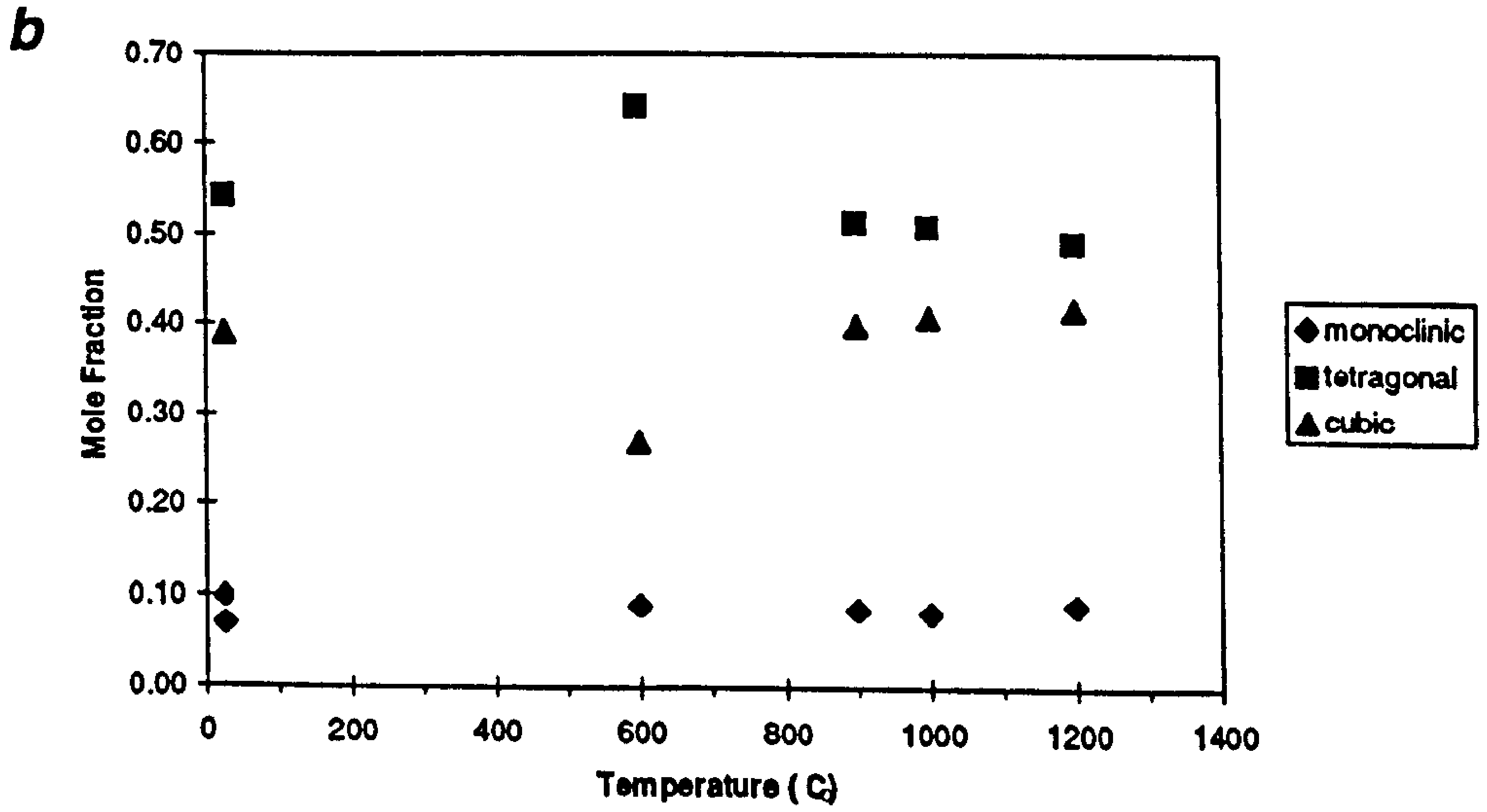

Figure 4.5 ZrO_2-phase distribution in the ZrO_2-Y_2O_3-TiO_2 coat after thermal treatments in (*a*) air and (*b*) argon, calculated from the respective XRD patterns.

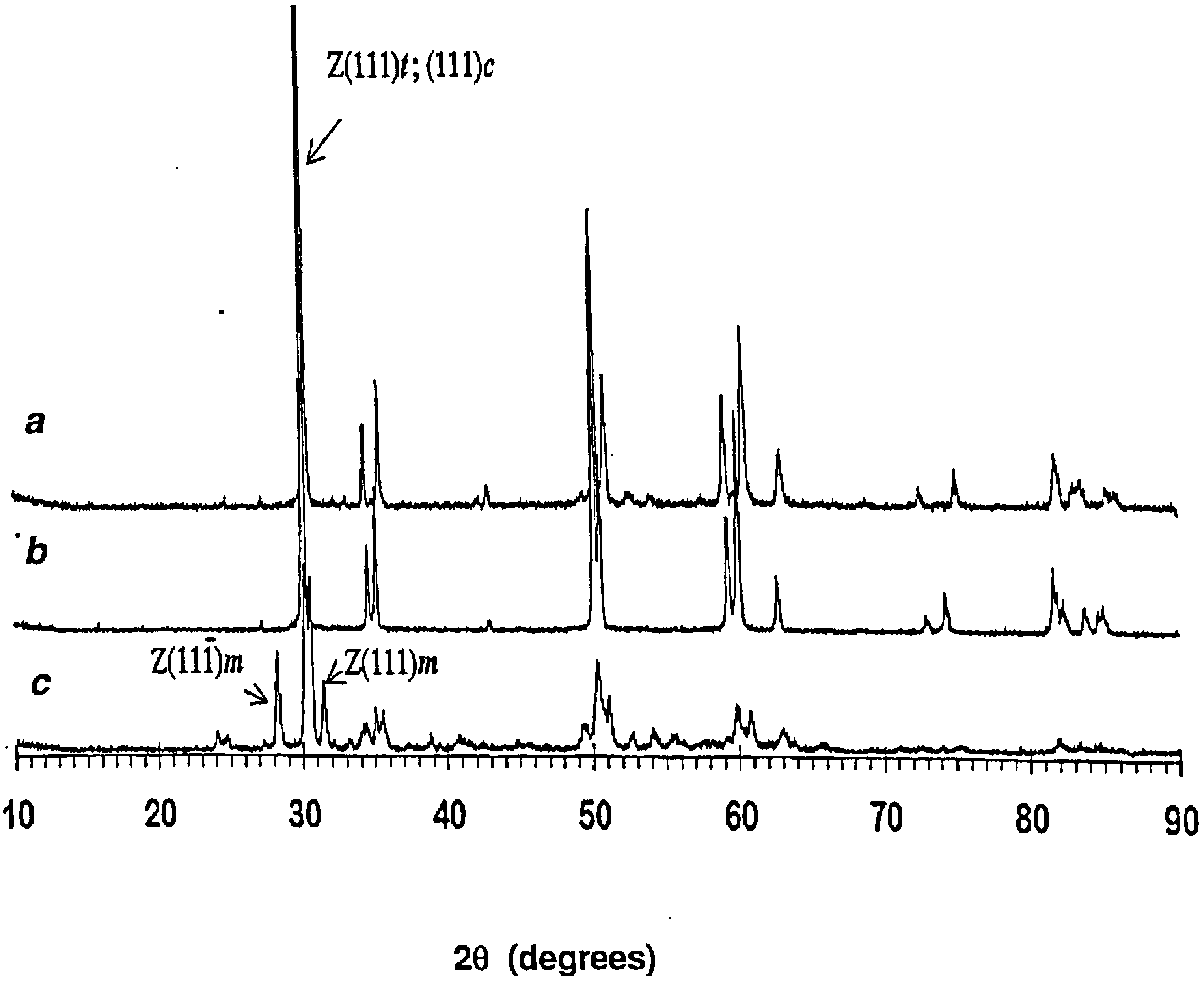

Figure 4.6 XRD pattern of the pressed-powder disks sintered at 1350 °C, prepared from: (*a*) ZrO_2-Y_2O_3 and (*b*) ZrO_2-Y_2O_3-TiO_2(A) powders, and (*c*) ZrO_2-Y_2O_3-TiO_2(B) powder used for plasma-spraying, as described in Table 3.2. Z, *m*, *c* and *t* refer to ZrO_2, monoclinic, cubic and tetragonal, respectively.

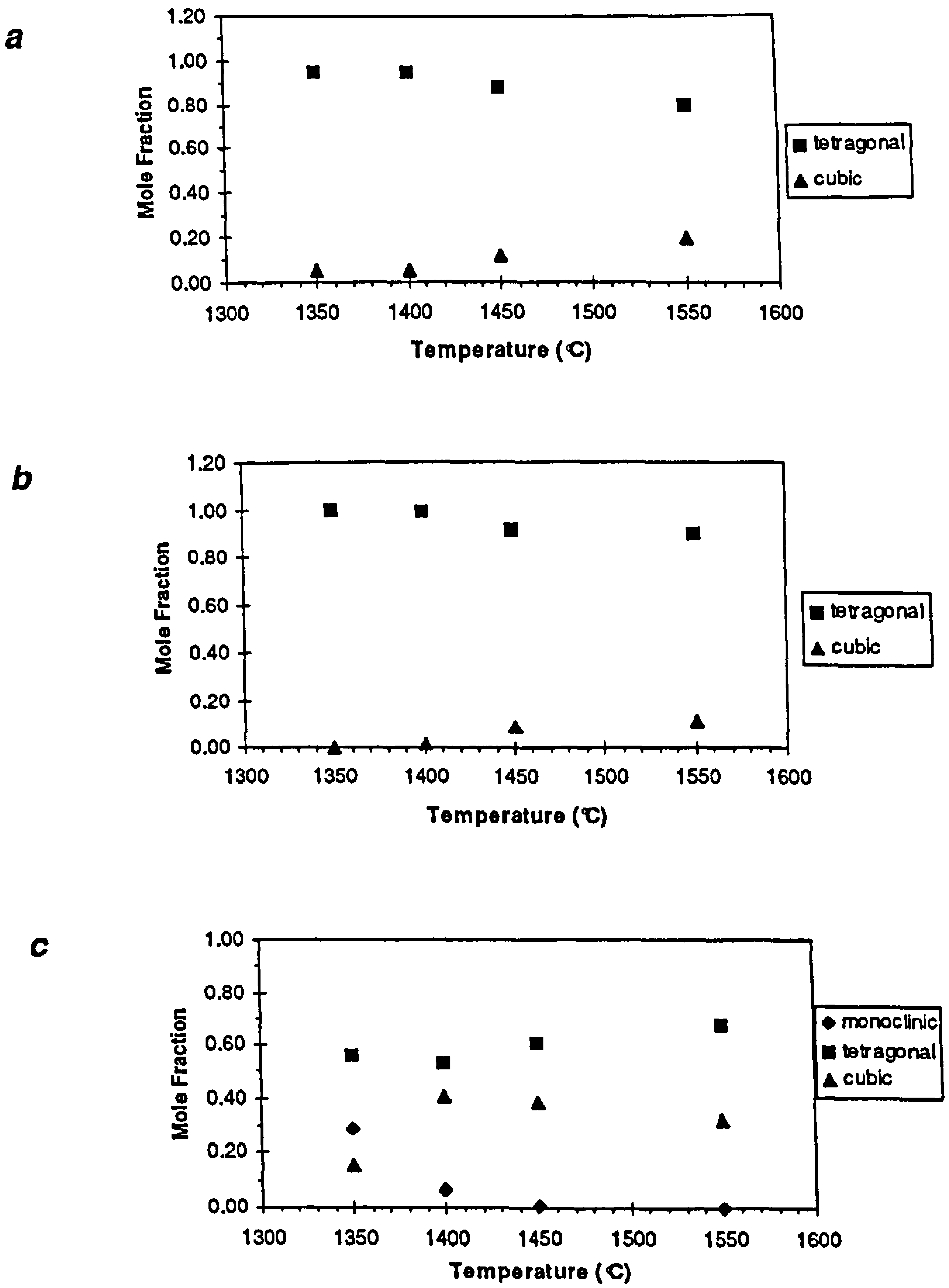

Figure 4.7 ZrO_2-phase distribution calculated from the XRD patterns for the sintered bodies prepared from (*a*) ZrO_2-Y_2O_3 powder, (*b*) ZrO_2-Y_2O_3-TiO_2(A), and (*c*) the ZrO_2-Y_2O_3-TiO_2(B) powder used for plasma-spraying.

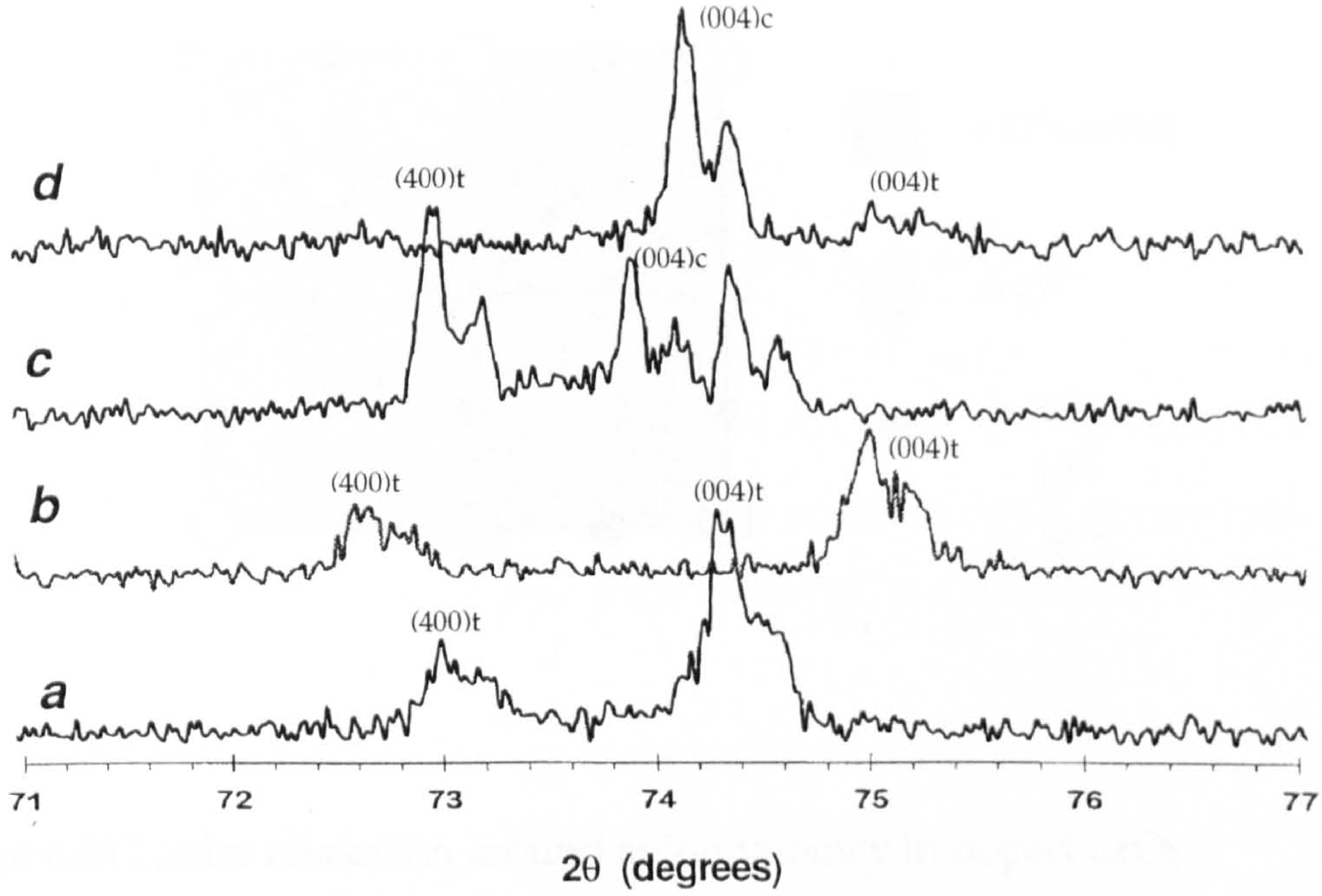

Figure 4.8 Detail of XRD patterns from (***a***) ZrO_2-Y_2O_3 and (***b***) ZrO_2-Y_2O_3-TiO_2(A) powders sintered at 1350 °C, and from these bodies annealed at 1600 °C for 4 hours: (***c***) ZrO_2-Y_2O_3 and (***d***) ZrO_2-Y_2O_3-TiO_2(A).

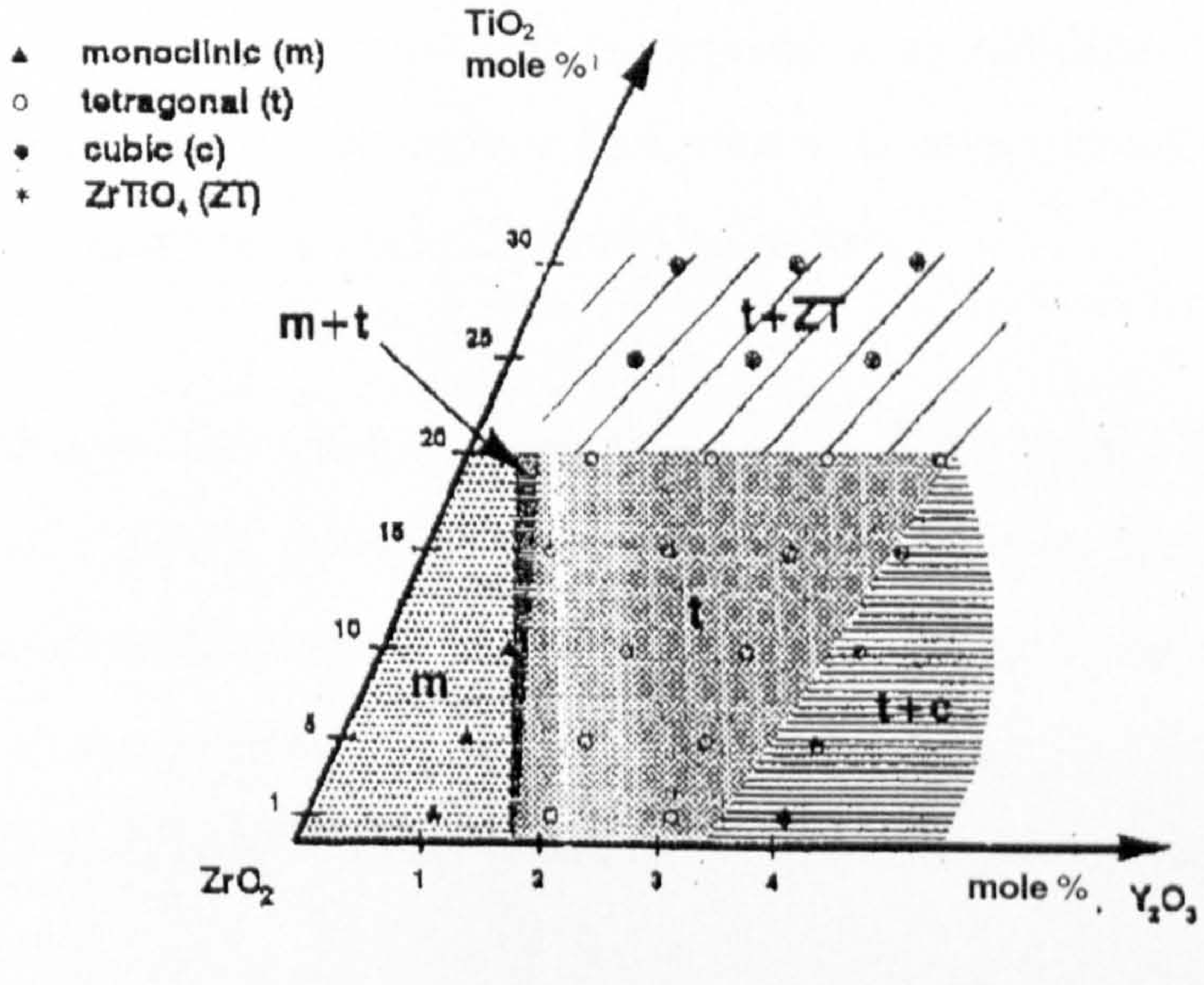

Figure 4.9 Phase regions of the ZrO_2-Y_2O_3-TiO_2 compositions for compact samples sintered between 1300 and 1450 °C up to 3 hours (after Kountouros and Petzow, 1993).

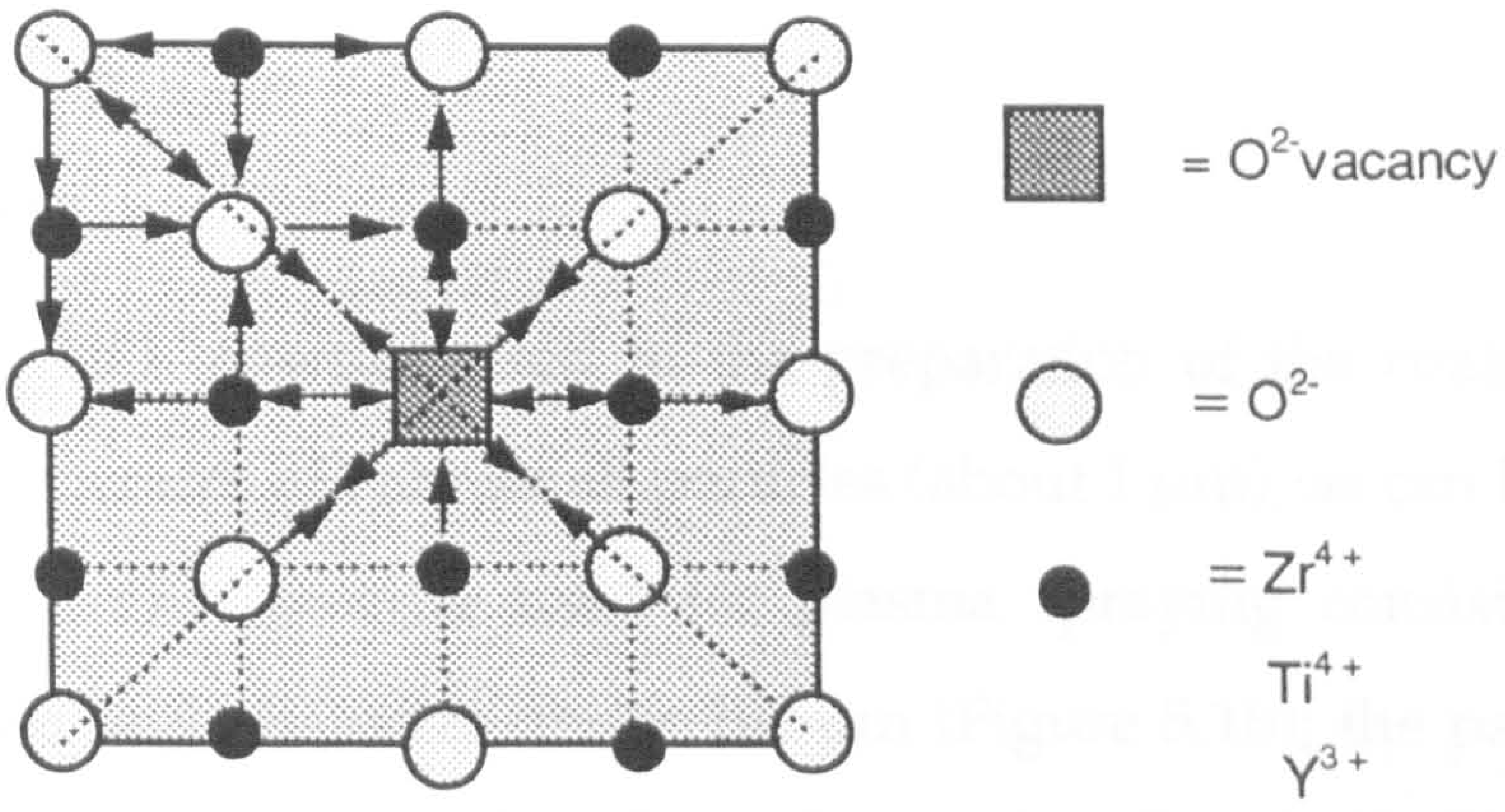

Figure 4.10 Lattice relaxation around anion vacancy in doped ZrO_2
(after Kountouros and Petzow 1993).

5 SCANNING ELECTRON MICROSCOPY

5.1 RESULTS

5.1.1 Powders

The ZrO_2-Y_2O_3-TiO_2 powder, used in the preparation of the coating, consisted of spherical agglomerates of very small particles (about 1 μm), as can be seen in Figure 5.1a. The ZrO_2-Y_2O_3 powder used for plasma spraying consisted of spherical-shaped particles with diameter under 100 μm (Figure 5.1b); the particles are larger and have a denser appearance than those observed in ZrO_2-Y_2O_3-TiO_2 powder.

The bond coat powder has the appearance of a sintered and crushed powder as can be seen in Figures 5.2.a and 5.2.b; it is a mixture of larger particles about 100 μm in diameter and smaller ones (< 10 μm in diameter). Its microanalysis reveals that the larger particles contain Ni and Cr and the smaller particles consist of Al, Co, and Y.

5.1.2 As-Sprayed Coatings

Figures 5.3a and 5.3b show typical SEM images obtained from the surfaces of ZrO_2-Y_2O_3-TiO_2 and ZrO_2-Y_2O_3 top coats respectively. Both coating surfaces show a similar appearance: ceramic material is deposited as solidified splats or lamellae, some with microcracks on the surface and others contain unmelted ceramic material in the form of agglomerates and dispersed particles.

Typical SEM images from the cross-section of the ZrO_2-Y_2O_3-TiO_2/NiCrCoAlY and ZrO_2-Y_2O_3/ NiCrCoAlY coatings are presented in Figures 5.4a and 5.4b. In both images it is possible to distinguish the two components of the coating: the ceramic and the bond coats, overlaying on the substrate surface. The substrate surface was not completely flat; it had some roughness detected as an uneven substrate-bond coat line border.

The ceramic coats had a more porous appearance than the bond coat; fine pores (< 5 μm) were distributed along the ceramic coat together with a few voids of varied dimensions (5-30 μm). However, it is possible to distinguish a higher proportion of fine pores in the ZrO_2-Y_2O_3-TiO_2 ceramic coat. Another feature common in both ceramic coats was the presence of cracks; they extended through the coat and some of them were branched.

The NiCrCoAlY bond coat (Figure 5.5a) used in both coatings presented some dark layers. The EDS analysis (Figure 5.5b) revealed that there was an increased concentration of aluminium in these dark zones.

A closer view of the ZrO_2-Y_2O_3-TiO_2 coat (Figure 5.6a) shows that there were zones of unmelted material entrapped in the melted matrix. It is also possible to observe at least three zones of different contrast (intensities of grey). The EDS analysis (Figure 5.6b) revealed a higher concentration of titanium in the dark zones, when compared to the lighter zones (Figure 5.6.c). The darker the appearance of the zone, the higher the concentration of titanium associated with it.

5.1.3 Thermally Treated Coatings

The SEM study of the ZrO_2-Y_2O_3/NiCrCoAlY and ZrO_2-Y_2O_3-TiO_2/NiCrCoAlY coating surfaces after thermal treatment at 900 °C for 24 hours showed no signs of appreciable changes on the top ceramic coat (Figures 5.7a and 5.7b); the appearance of these surfaces was similar to that described in Section 5.1.2. However, the cross-sections images of these coatings (Figures 5.8a and 5.8b) show some evolution of the microstructure, mostly in the ceramic coat; the ends of the voids were smoothed and appeared interconnected with other voids, pores or cracks; small pores joined together to form bigger pores.

5.1.4 Thermal Treatment of ZrO_2-Y_2O_3-TiO_2/NiCrCoAlY Coating

5.1.4.1 As-Sprayed Coating

For this experiment, new specimens (type 2) were used as described in Table 3.1. Figure 5.9a corresponds to the cross-section image of this new ZrO_2-Y_2O_3-TiO_2/NiCrCoAlY coating. Compared with specimen type 1 (Figure 5.4a), the concentration and size of the ceramic coat voids were smaller. The aluminium-rich zones from the bond coat described in Section 5.1.2, were also present in this coating although they were more localised (spots).

Figure 5.9b shows a SEM image of the ZrO_2-Y_2O_3-TiO_2 coat cross-section at a higher magnification. As in the case of specimen type 1, it is possible to observe at least three zones of different intensities of grey corresponding to different concentrations of titanium. Unmelted or incompletely melted ceramic material can be also identified. Round pores, voids and cracks are distributed through the coat thickness.

5.1.4.2 Failure of Coatings

During the thermal treatment, some specimens over the thickness specification (300-500 μm), failed after heating over 700 °C; the ceramic coat spalled off, leaving the bond coat and substrate exposed. Figure 5.10a shows remains of the ZrO_2-Y_2O_3-TiO_2 coat on the substrate. Figure 5.10b shows nickel-rich crystals from the bond coat after the ceramic coat spalled off. This is confirmed by their respective EDS (Figures 5.11a and b).

Figure 5.12 shows the image of a very thick coating which failed after heating at 900 °C for 24 hours. Detailed observation of the bond coat reveals that it was very irregular in thickness, and in some points the ceramic coat was in direct contact with the substrate (Figure 5.13a). This was confirmed by EDS mapping of nickel (Figure 5.13b) which showed discontinuities in the bond coat.

5.1.4.3 Porosity Distribution

Figure 5.14a gives the distribution of relative porosity for the as-sprayed ceramic coat and after heating at 900 °C for 24 hours, calculated by image analysis of the respective cross sections SEM micrographs. The relative porosity is given by the expression:

$$P = \frac{A_p}{A_T} x100 \qquad 5.1$$

where A_p is the area of the individual pore and A_T the total area analysed. At least three populations of pores can be distinguished in these distributions. There are some differences between both distributions; it is shown that there is a reduction of the pore population that represent 2-4% in the thermally treated specimen and an increase in the porosity that represents 4-7% of the same specimen.

Figure 5.14b shows the frequency distribution of pores having an area < 2 μm² which corresponds to the higher density of pores (47% of the total). Small changes can be observed, for instance, it is possible to distinguish a reduction of the pores having an area ≤ 0.1 μm² in the thermally treated ceramic coat and an increment in the pores having an area between 0.1-0.3 μm².

5.1.4.4 Ceramic Coat Fracture

The fracture of the as-sprayed ZrO_2-Y_2O_3-TiO_2 coat showed an interlamellar appearance as observed by SEM (Figure 5.15a); cracks propagated mainly through the interlamellar areas without appreciable rupture of the lamellae.

After cooling the ceramic coating with liquid nitrogen, the fracture obtained had an intralamellar appearance, as can be seen in Figure 5.15b. A fine columnar microstructure of the deposited lamellae can also be identified; the lamellae (about 5 μm thick) are formed by columns with diameter < 1 μm. This type of fracture is also observed in the ceramic coat after heat treatments at temperatures < 1200 °C, as seen in Figures 5.16a to 5.17b.

At 1200 and 1400 °C, the nature of the fracture surfaces was different; they were inter-granular, as it is shown in Figures 5.18a to 5.19. There were some additional morphological changes. The columnar structure collapsed giving rise to smaller grains of about 1 μm in diameter. This was more evident after heating at 1400°C (Figure 5.19).

5.1.5 Sintered Bodies

Table 5.1 presents the densities of the pressed disks from the ZrO_2-Y_2O_3 and ZrO_2-Y_2O_3-TiO_2(A) powders, and the ZrO_2-Y_2O_3-TiO_2(B) powder used for plasma-spraying, sintered at 1350, 1400, 1450 and 1550 °C. The highest density was found in the bodies sintered at 1350 °C in all the cases. At this temperature, the sintered ZrO_2-Y_2O_3 had almost reached its theoretical density (Table 5.2) while the relative density of the ZrO_2-Y_2O_3-TiO_2 (A) sintered body was 82%, and 78% for the sintered body prepared from the ZrO_2-Y_2O_3-TiO_2 (B). At a higher sintering temperature, the densities of the sintered bodies decreased (Figure 5.20).

The surface of the ZrO_2-Y_2O_3 disks sintered at 1400 °C had a dense appearance and it was difficult to identify individual grain size or shape due to the extent of the sintering (Figure 5.21a). However, at 1550 °C (Figure 5.21b) it is possible to identify small grains (about 1 μm) and some larger grains (about 5 μm).

Figures 5.22a and 5.22b correspond to the SEM images of the surface of ZrO_2-Y_2O_3-TiO_2 (A) disks sintered at 1400 and 1550 °C, respectively. At 1400 °C the sintered surface was more homogeneous in grain shape and size, the grain size was about 2 μm. Figure 5.22b shows that there has been some grain growth in the specimen sintered at 1550 °C, the grain size was about 6 μm. Elongated grains (20-30 μm in length) appear regularly dispersed in this sintered specimen. The EDS analysis of these grains revealed that they had a higher concentration of titanium (Figure 5.23a) compared with the matrix (Figure 5.23b).

Figures 5.24a and 5.24b show the SEM images of the surface of ZrO_2-Y_2O_3-TiO_2(B) pressed-powder disks sintered at 1400 and 1550 °C respectively. The specimen sintered at 1400 °C showed an irregular distribution of grains of different sizes (< 5 μm) and shapes. At 1550 °C some grains grew (> 10 μm) at the expense of others. Elongated grains are also observed and these are richer in titanium as detected by EDS (Figure 5.25).

5.2 DISCUSSION OF RESULTS

5.2.1 Powders

The ZrO_2-Y_2O_3-TiO_2 powder had a more porous appearance compared to the ZrO_2-Y_2O_3 powder. Its agglomerated nature is typical of that described for powders prepared by spray drying (**Schwier 1986**). There is no evidence of solid solution formation. This is confirmed by the fact that ZrO_2, present as *m*-ZrO_2, has not been stabilized by the presence of TiO_2 or Y_2O_3 in this powder (Section 4.2.1). By contrast, the more compact appearance of the ZrO_2-Y_2O_3 powder suggests solution of the components as can be inferred from the degree of stabilization of ZrO_2 observed in this case (Section 4.2.1). The heterogeneous morphology of the NiCrCoAlY powder is typical for sintered and crushed powders as described by **Schwier** (1986).

5.2.2 As-Sprayed Coatings

There was no appreciable difference between the ZrO_2-Y_2O_3-TiO_2 and ZrO_2-Y_2O_3 as-sprayed coat surfaces. The solidified splats or lamellae observed in these surfaces indicated the high temperature reached by the deposited material during the plasma spraying process. The degree of splat spreading and variation in lamellar thickness is controlled by a number of factors such as droplet temperature, viscosity, velocity of impact, and wetting behaviour between the splat and the previously deposited material (**Harmsworth and Stevens 1992b**). The cracks present in the surface of some lamellae indicated the thermal stress which originates during the cooling stage of the material.

The NiCrCoAlY bond coat, common in both coatings, showed preferential accumulation of aluminium in some zones. It has been found that migration of aluminium to the interface bond coat/ceramic coat occurs during thermal treatment at temperatures higher than 1100 °C (**Alpérine and Lelait 1994; Harmsworth and Stevens 1992b**). The Al_2O_3 scale that is formed has a significant plasticity which would help in relieving the thermal stresses due to the mismatch of expansion coefficient in the coating. The zones observed with a higher concentration of aluminium are a possible indication of the incipient migration of aluminium.

The rough substrate/bond coat interface was a result of the substrate surface preparation prior to plasma spraying of the coating; it provides a suitable surface to promote physical bonding. However, a very irregular surface, with a high proportion of protuberances is undesirable because it may generate additional stresses localized at some points; once the substrate protuberances have expanded due to thermal treatment extra stresses are created in the interface substrate/bond coat.

In both ceramic coats some common microstructural features were observed. It was possible to identify the layered and discontinuous nature of the ceramic coat as a result of the plasma spray process. The elongated and flat voids observed in the ceramic coat corresponded to mismatch between the deposited lamellae and the material being sprayed. This was not observed in the NiCrCoAlY bond coat due to its plasticity which ensured a good match between layers. Rounded and small pores may be associated with entrapped gas, created during plasma spraying. Other voids, pores and cracks might originate in the ceramic coat during the cooling stage. Remains of unmelted material were also identified; zones of material that had not melted entirely during plasma spraying were surrounded by the melted matrix. This unmelted material preserved some porosity from the original powder, and must also be responsible for the *m*-ZrO_2 detected in the coat (Section 4.1.4).

The discontinuous microstructure observed in the ZrO_2-Y_2O_3-TiO_2 and ZrO_2-Y_2O_3 coats is known to reduce the stresses caused by the large thermal expansion mismatch between the coating and the substrate. This mismatch causes crack propagation leading to the spalling of the ceramic coat. (Pettit and Goward 1983, Harmsworth and Stevens 1992b).

The main difference between both ceramic coats is associated with the additional TiO_2 component. Titanium was heterogeneously distributed in the ZrO_2-Y_2O_3-TiO_2 coat leading to the formation of different phases rather than an uniform solid solution. It should be noted that the presence of these phases gives the coat a composite nature. A toughening mechanism can be associated with the presence of different phases; some of the crack propagation energy is consumed when the crack reaches the interface.

5.2.3 Thermally Treated Coatings

Some changes were observed in the ceramic coat after thermal treatment of the ZrO_2-Y_2O_3-TiO_2/NiCrCoAlY and ZrO_2-Y_2O_3/NiCrCoAlY coatings at 900 °C for 24 hours. This treatment caused some diffusion to take place as shown by the presence of connected pores and cracks. Branching of some of the cracks may be associated with the relief of thermal stress generated during the thermal treatment.

5.2.4 Thermal Treatment of ZrO_2-Y_2O_3-TiO_2/NiCrCoAlY Coating

5.2.4.1 As Sprayed Coating

It was possible to identify some differences between the two specimen types of ZrO_2-Y_2O_3-TiO_2/NiCrCoAlY coatings, using SEM. The denser appearance of the ceramic coat from the type 2 specimens is caused by the differences in the parameters used during plasma spraying; for instance, a higher application rate or a higher substrate temperature would improve the match between the spraying material and that already deposited as it would be hot enough to allow better bonding between layers. Since the aluminium-rich zones in the bond coat were more localised in type 2 specimens, it is possible the temperature during the preparation of the bond coat was higher in this case, promoting the migration of aluminium-rich phases. The distribution of titanium in the bond coat had the same characteristics in both types of specimens; there were phases with a higher concentration of titanium than others.

In the ceramic coat of the type 2 specimens, the proportion of material incompletely melted and containing *m*-ZrO_2, was lower than in the type 1 specimens. This is also confirmed by the lower concentration of *m*-ZrO_2 calculated for this case (Table 4.5).

5.2.4.2 Failure of Coatings

The purpose of using argon and air during thermal treatment of the ZrO_2-Y_2O_3-TiO_2/NiCrCoYAl coating was to evaluate the effect of the bond coat oxidation on the failure of the coating. However, it was found that some coatings failed after being heated either in air or argon. Thus other variables could also influence the failure of the coatings under study, as discussed below.

The main reason for failure of some ZrO_2-Y_2O_3-TiO_2/NiCrCoAlY coatings was the discontinuity found in the bond coat. The ceramic coat was in direct contact with the substrate in some areas while in others it appeared to be bonded to the NiCrCoAlY coat. The thermal mismatch is higher for areas in direct contact with the substrate than for those bonded to the substrate by the NiCrCoAlY coat. The resultant non-equilibrium stresses therefore caused the ceramic coat to spall off. The inspection of the substrate surface after some of the ceramic coat had spalled off indicated that remains of the ceramic coat were still adhered to the bond coat.

5.2.4.3 Porosity Distribution

After heating the ZrO_2-Y_2O_3-TiO_2 coat at 900 °C for 24 hours, there was a decrease in the group of pores representing $\leq 4\%$ of porosity of the specimen analysed. It is suggested that the thermal treatment above described had promoted some material diffusion, thus small pores would have joined together to form larger pores. This would correspond with the increase of the group of pores representing between 4 and 7% of the porosity of the specimen analysed.

The pore area distribution (Figure 5.14) also suggests that some material diffusion has occurred during the thermal treatment. For example pores < 0.1 μm in size decreased while the group of pores between 0.2-0.3 μm in size increased. In spite of these variations, the whole profile of the pore area distribution was maintained after the thermal treatment, therefore no difference in the coating performance should be expected due to variation in the porosity distribution after the thermal treatment described.

5.2.4.4 Ceramic Coat Fracture

Examination of the fracture surfaces of the as-sprayed and thermally treated ZrO_2-Y_2O_3-TiO_2 coats allowed confirmation of the lamellar structure of the ceramic coat inherent to the plasma spray process used in the preparation. The columnar microstructure of the lamellae was shown clearly in Figures 5.15-5.17. In principle, the column growth is expected to be normal to the substrate surface following the heat flow. However, the lamellae where not aligned parallel to the substrate but distorted and this depends on the shape of the lamellae deposited previously. The columnar microstructure of the lamellae is another element of discontinuity that gives the coating structure the ability to reduce the thermal stresses.

The interlamellar fracture observed in the as-sprayed ZrO_2-Y_2O_3-TiO_2 coat (Figure 5.15a) is an indication of a weak adhesion between lamellae. This gave the fracture of the coat some plastic character as there was no rupture of the lamellae. After cooling with liquid nitrogen the ceramic coat became more rigid and in these instances the coat fracture was brittle as indicated by the rupture of the lamellar structure (intralamellar fracture, see Figure 5.15b).

The collapse of the columnar structure of the lamellae and the appearance of grains after thermal treatment at 1200 and 1400 °C are an indication that sintering of the material has been initiated; some grains have grown at the expense of others. This was noticed after examining the fracture surface of the ceramic coat thermally treated at 1200 and 1400 °C. The inter-granular character of these fractures revealed a weak bonding between grains. Sintering has deleterious effects in the coat performance; the densification of the coat by sintering increases the thermal conductivity of the coat and reduces its thermal shock resistance.

5.2.5 Sintered Bodies

It is well known that the properties of the ceramic coat, such as thermal and electrical conductivity, density, toughness and fracture strength, could be very different from the corresponding bulk sintered body. However, the comparison between the ZrO_2-Y_2O_3-TiO_2 and ZrO_2-Y_2O_3 sintered bodies can help in understanding how the TiO_2 could affect the microstructure of the coating, and in turn, its properties.

Sintering ZrO_2-Y_2O_3 plasma spray powder was unsuccessful basically due to the large particle size of the powder. Even though it was possible to obtain some sintered bodies from the ZrO_2-Y_2O_3-TiO_2(B) plasma spray powder, their densities were lower than the equivalent specimens prepared from the ZrO_2-Y_2O_3-TiO_2(A) powder (Figure 5.20).

The ZrO_2-Y_2O_3 body sintered at 1350 °C registered the highest density, 99.4% of the theoretical density while the equivalent ZrO_2-Y_2O_3-TiO_2 (A) and (B) specimens reached 82 and 72 % of the theoretical density, respectively. This suggests that the addition of TiO_2 to the system ZrO_2-Y_2O_3 reduces the final density of sintered bodies. This feature can be interpreted taking into consideration the grain size in each case that is affected by the TiO_2 concentration and by the sintering temperature as discussed below.

The grains observed on the surface of sintered bodies were larger in the case of ZrO_2-Y_2O_3-TiO_2 than in ZrO_2-Y_2O_3 at a given sintering temperature (Figures 5.21-5.24). The grains were coarser in the sintered ZrO_2-Y_2O_3-TiO_2(B) specimens prepared from the plasma spray powder (26.4 mole% TiO_2) than that prepared from the fine powder (23.1 mole% TiO_2). Thus the addition of TiO_2 to the system ZrO_2-Y_2O_3, in the proportions studied, promotes grain growth.

The increase of the grain size by the sintering temperature was more evident in the ZrO_2-Y_2O_3-TiO_2 systems. At 1550 °C elongated grains with a relative high concentration of titanium were present together with the original equiaxed grains in these systems. These grains were longer, and regularly distributed in the ZrO_2-Y_2O_3-TiO_2 (A) sintered body. This must be due to differences in the nucleation process that took place in each case, caused mainly by differences in the particle size and degree of agglomeration of the starting powders.

The final density of the sintered body is reduced with increased sintering temperature due to the grain size increase and the consequent reduction of the material consolidation. It was shown that a higher concentration of TiO_2 (in the range studied) increased the grain size in the system ZrO_2-Y_2O_3-TiO_2 and consequently reduces the final density.

As discussed in Section 5.2.2, the addition of TiO_2 to the system ZrO_2-Y_2O_3, in the proportion studied, also promotes the appearance of a second phase which would provide a coat with improved fracture toughness.

5.3 TABLES AND FIGURES

Table 5.1 Bulk density of the sintered bodies pressed using ZrO_2-Y_2O_3 powder, ZrO_2-Y_2O_3-TiO_2(A) powder and ZrO_2-Y_2O_3-TiO_2(B) powder used for plasma spraying.

	Density (kgm^{-3})		
Temperature (°C)	ZrO_2-Y_2O_3	ZrO_2-Y_2O_3-TiO_2 (A)	ZrO_2-Y_2O_3-TiO_2 (B)
1350	5630	4460	4190
1400	5170	4330	4130
1450	4910	4270	4030
1550	5020	4250	3310

Table 5.2 Theoretical densities of the different powders used in the preparation of sintered bodies.

Density (kgm^{-3})		
ZrO_2-Y_2O_3	ZrO_2-Y_2O_3-TiO_2 (A)	ZrO_2-Y_2O_3-TiO_2 (B)
5660	5440	5370

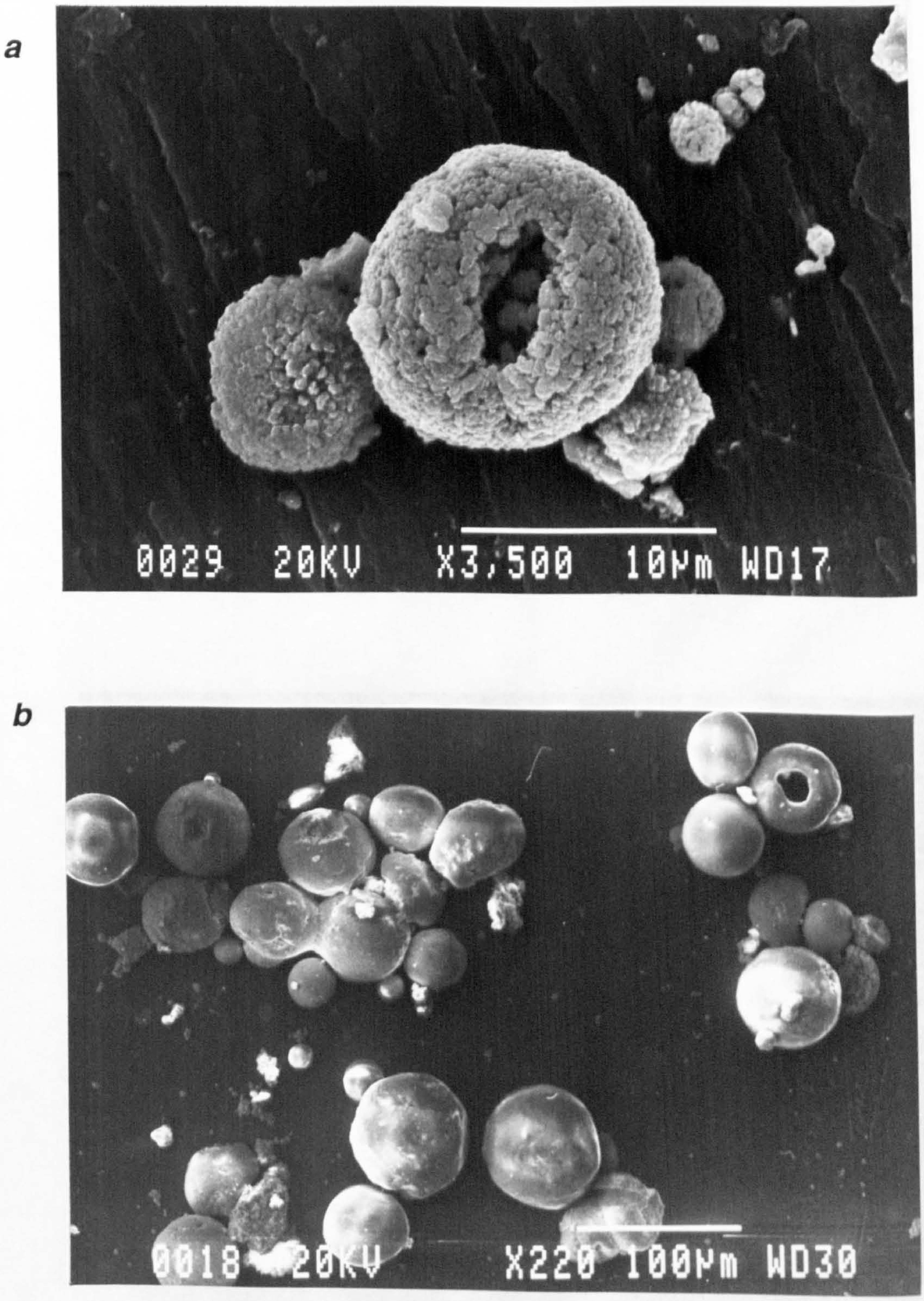

Figure 5.1 SEM micrograph of the (***a***) ZrO_2-Y_2O_3-TiO_2 and (***b***) ZrO_2-Y_2O_3 powders used in the preparation of the coatings. Secondary electron (SE) detector was used.

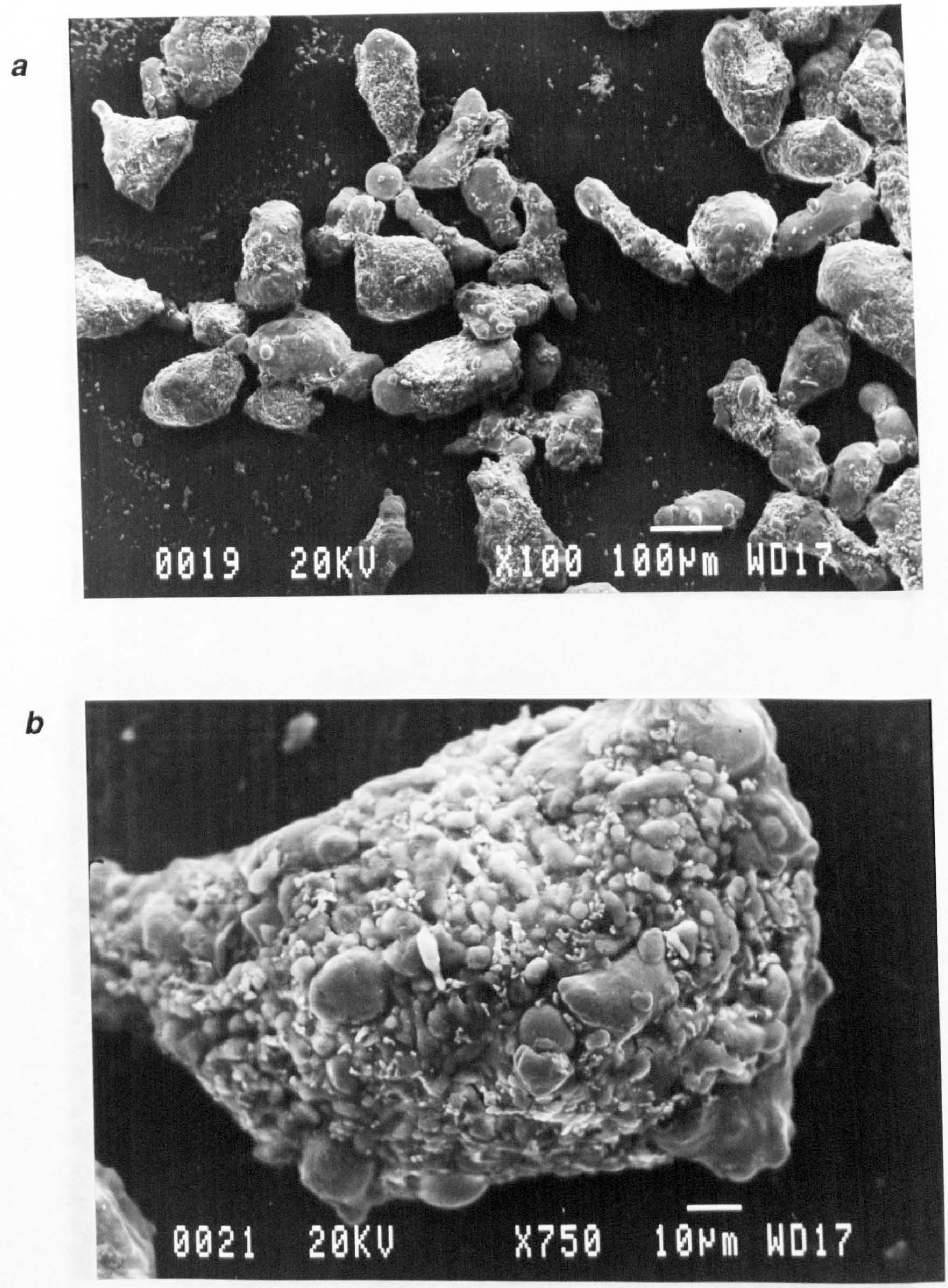

Figure 5.2 SEM micrographs of the NiCrCoAlY powder used as bond coat in the preparation of the coatings. SE detector was used

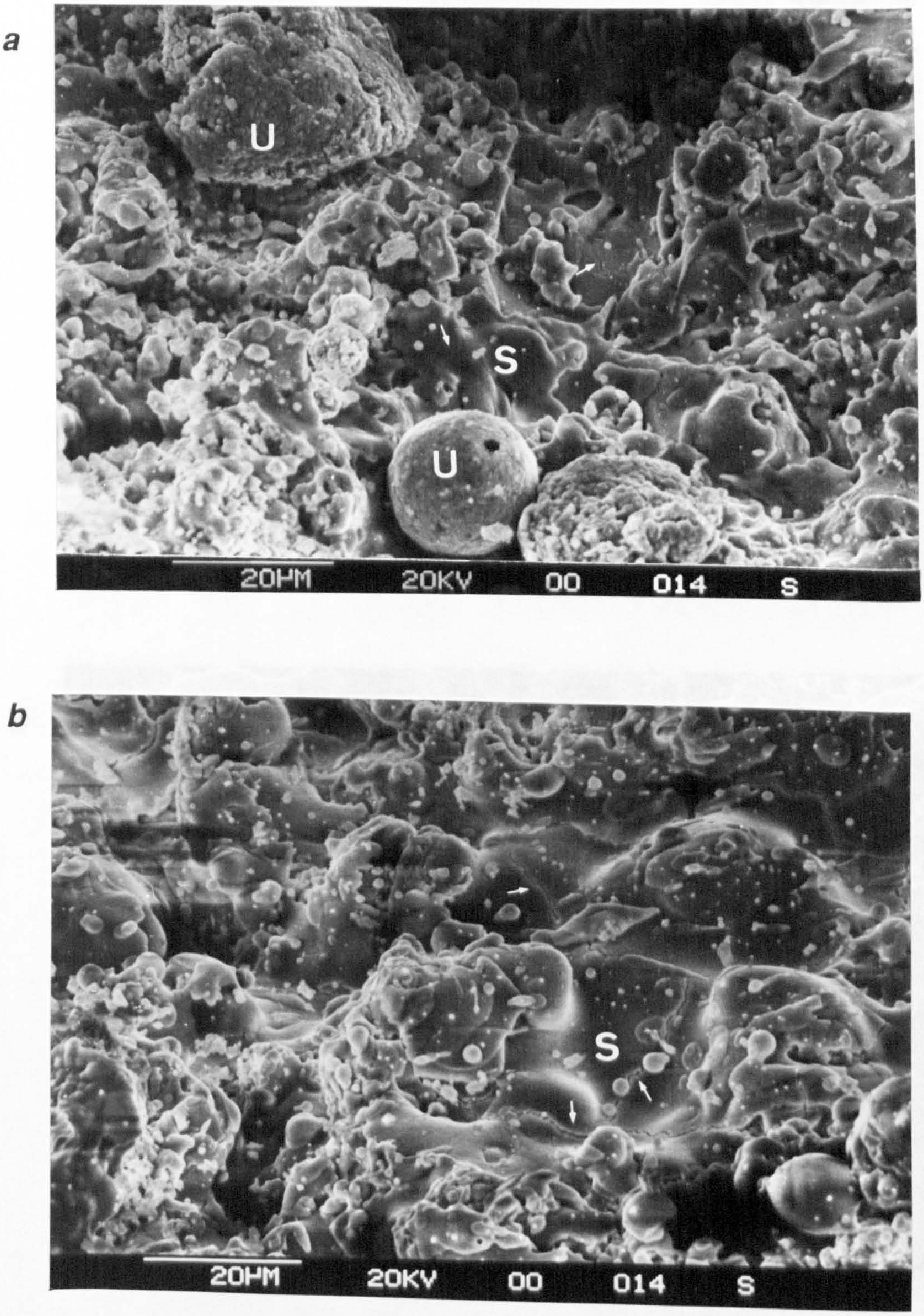

Figure 5.3 SEM images of (***a***) ZrO_2-Y_2O_3-TiO_2 and (***b***) ZrO_2-Y_2O_3 coats surfaces. Some ceramic splats (S), microcracks (arrows) and unmelted material (U) can be observed. SE detector was used.

a

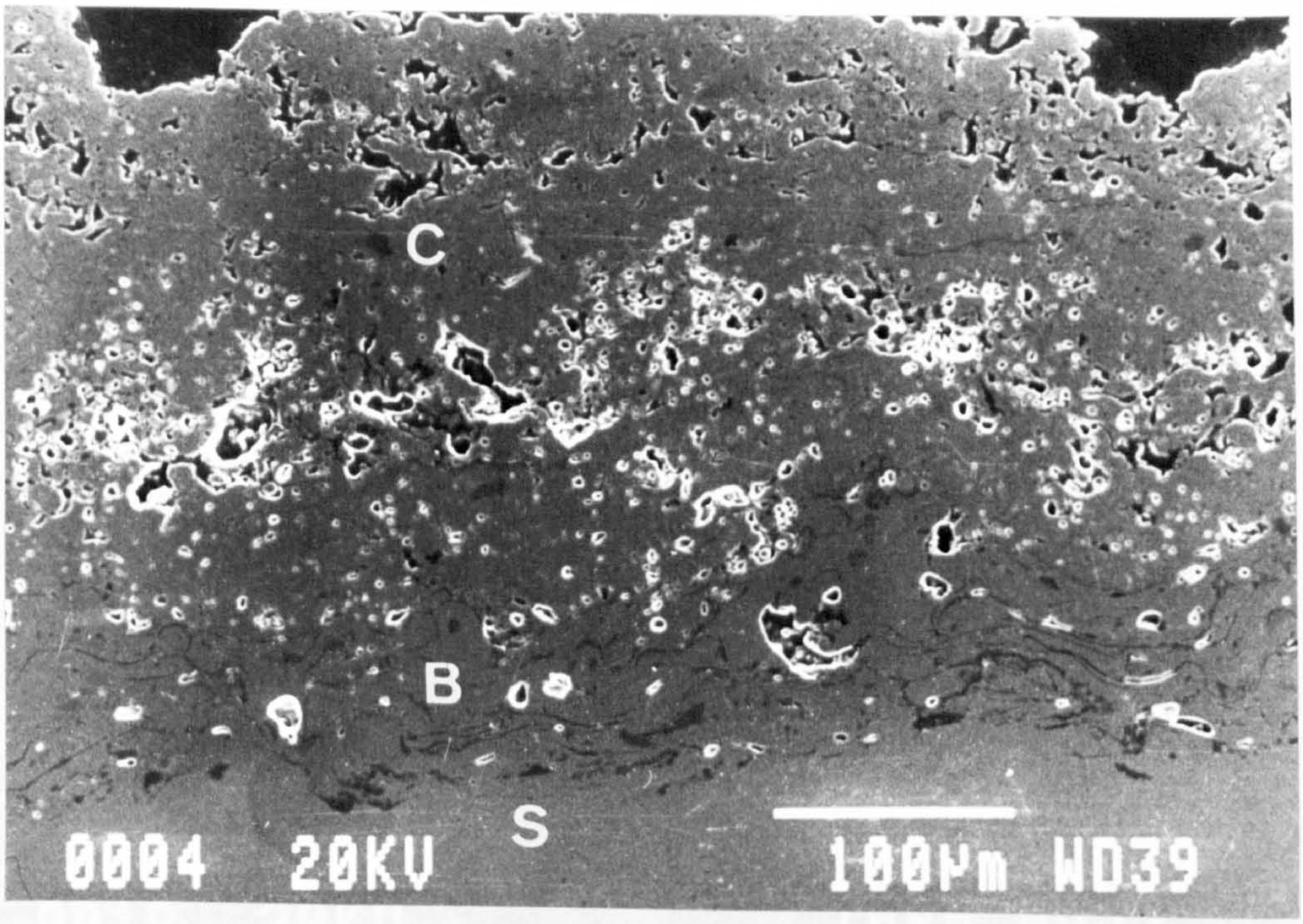

b

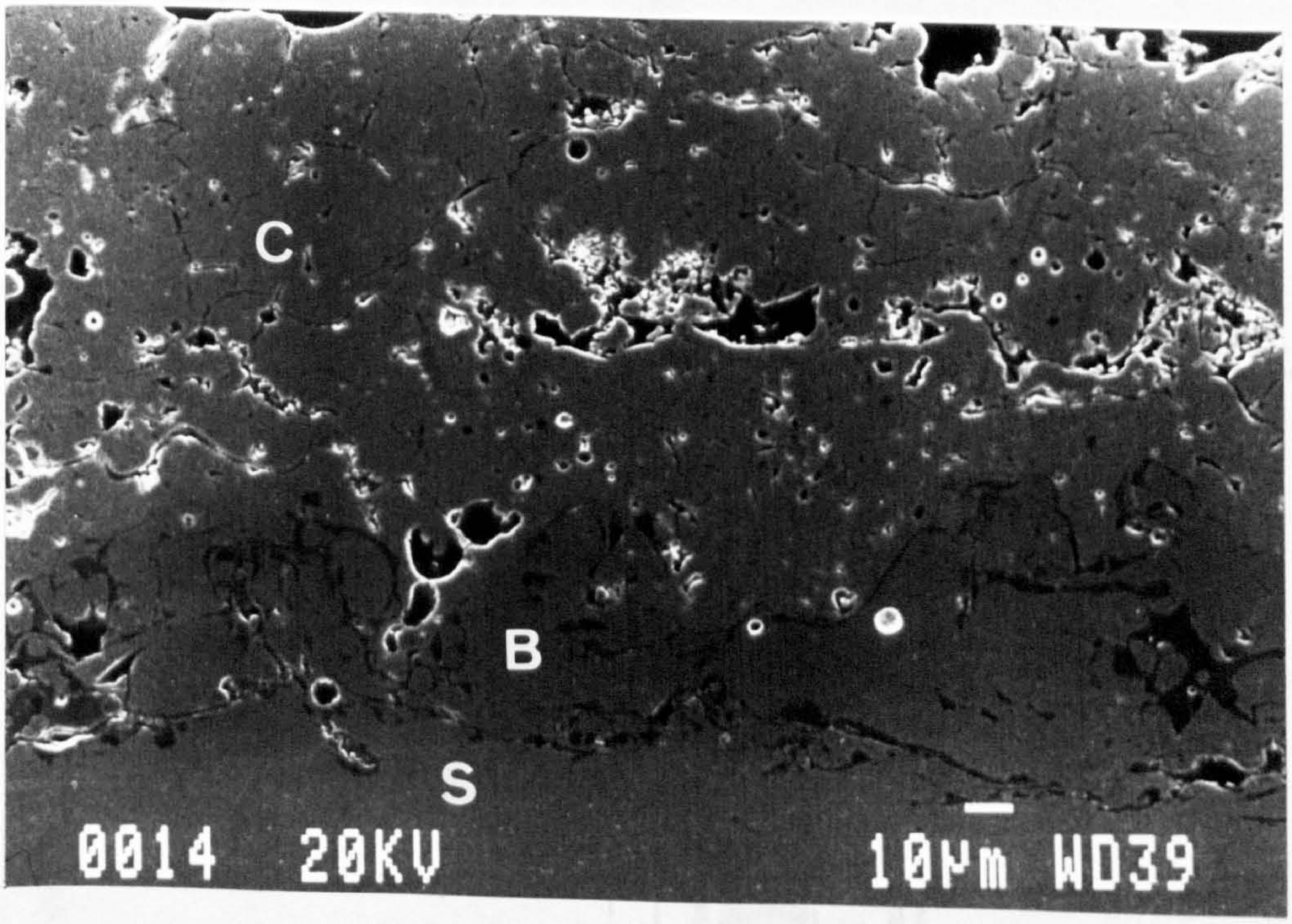

Figure 5.4 Cross-section images of the as sprayed (***a***) ZrO_2-Y_2O_3-TiO_2/ NiCrCoAlY and (***b***) ZrO_2-Y_2O_3/NiCrCoAlY coatings. B, C and S refer to bond coat, ceramic coat and substrate, respectively. SE and backscattered electron (BSE) detectors were used.

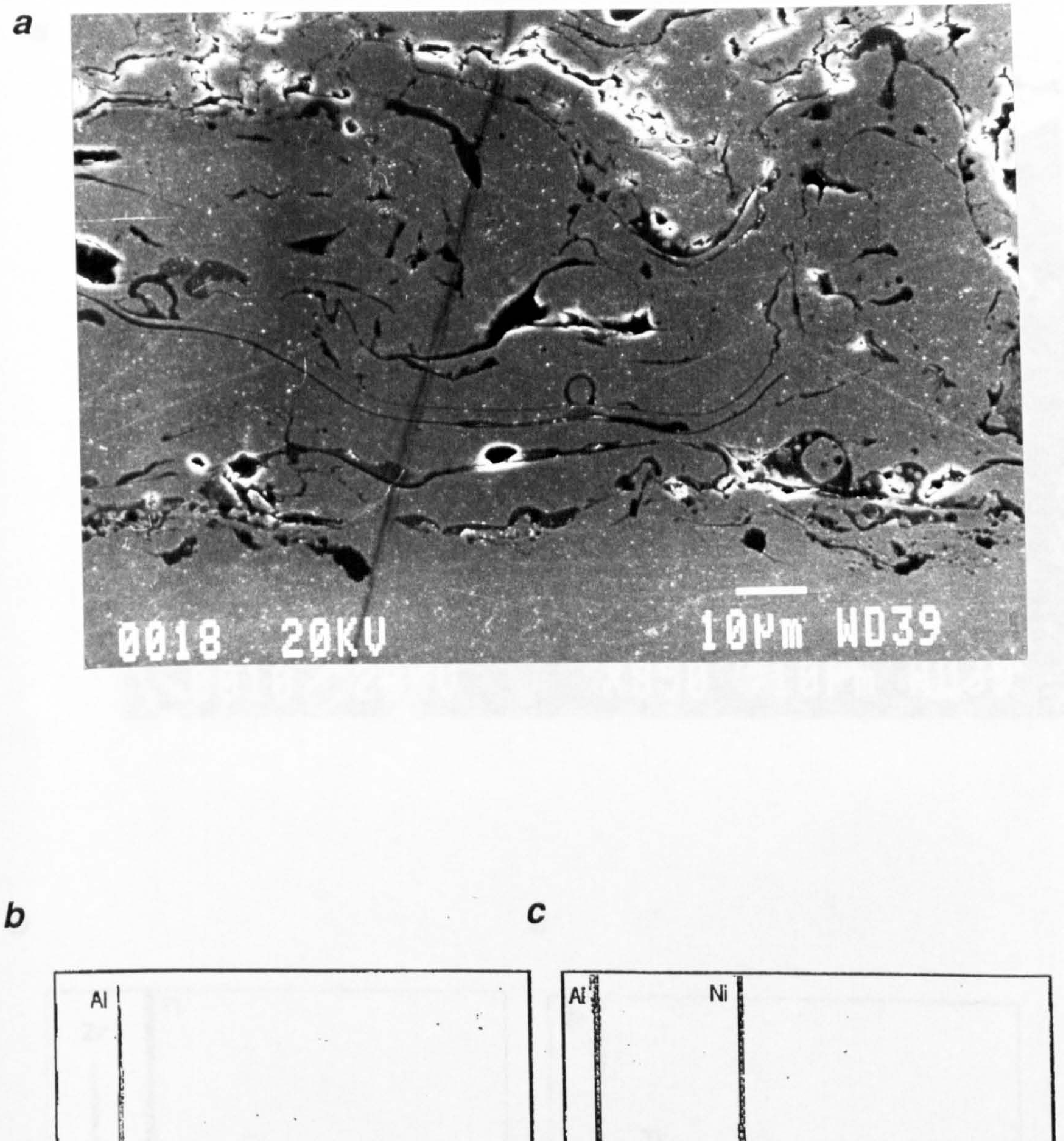

Figure 5.5 (***a***) SEM micrograph showing the NiCrCoAlY bond coat. EDS analyses of (***b***) dark and (***c***) light zones shown in (***a***). SE and BSE detectors were used.

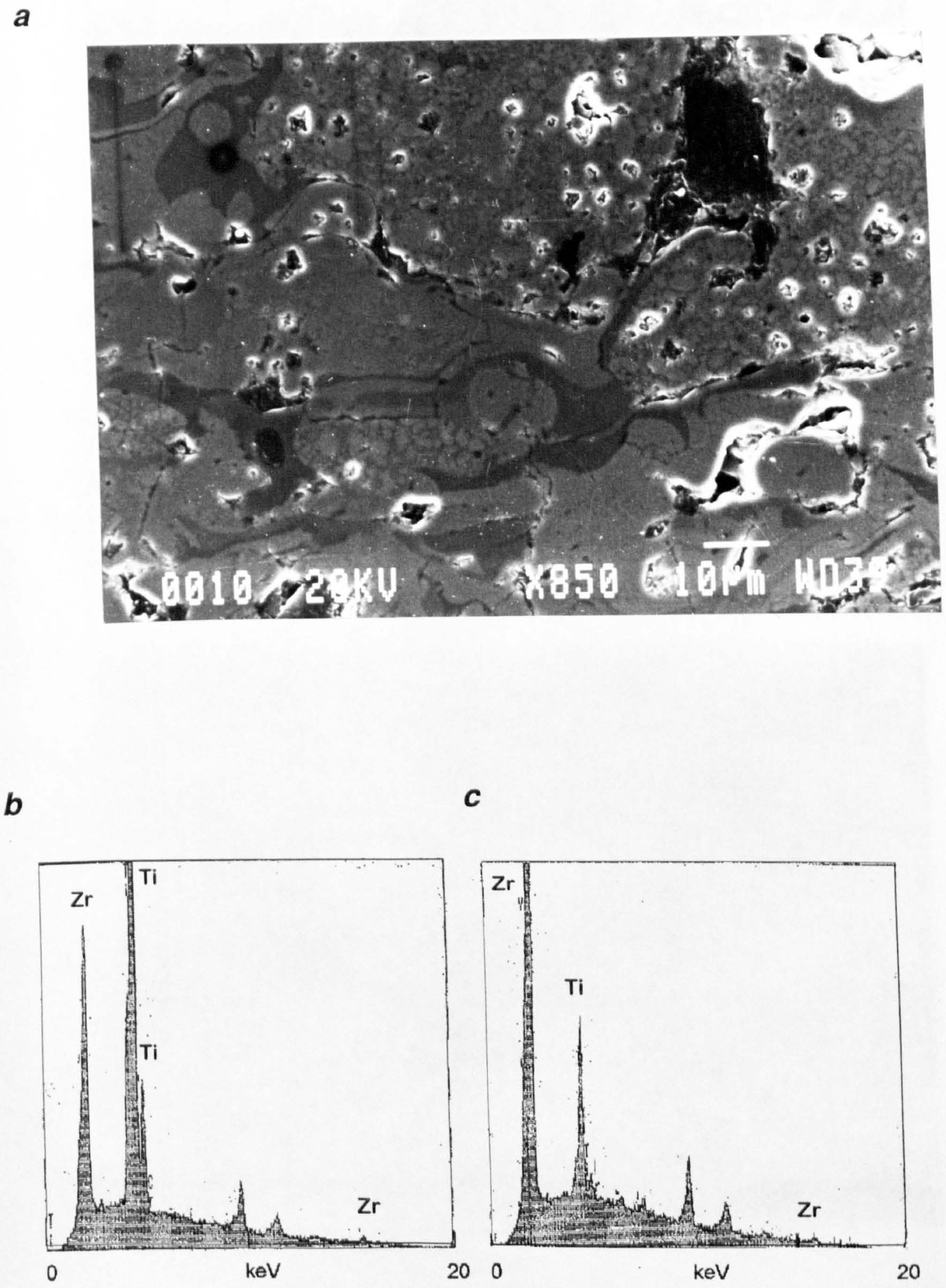

Figure 5.6 (***a***) SEM micrograph showing details of the ZrO_2-Y_2O_3-TiO_2 coat. EDS analysis of the (***b***) dark and (***c***) light zones shown in (***a***). SE and BSE detectors were used.

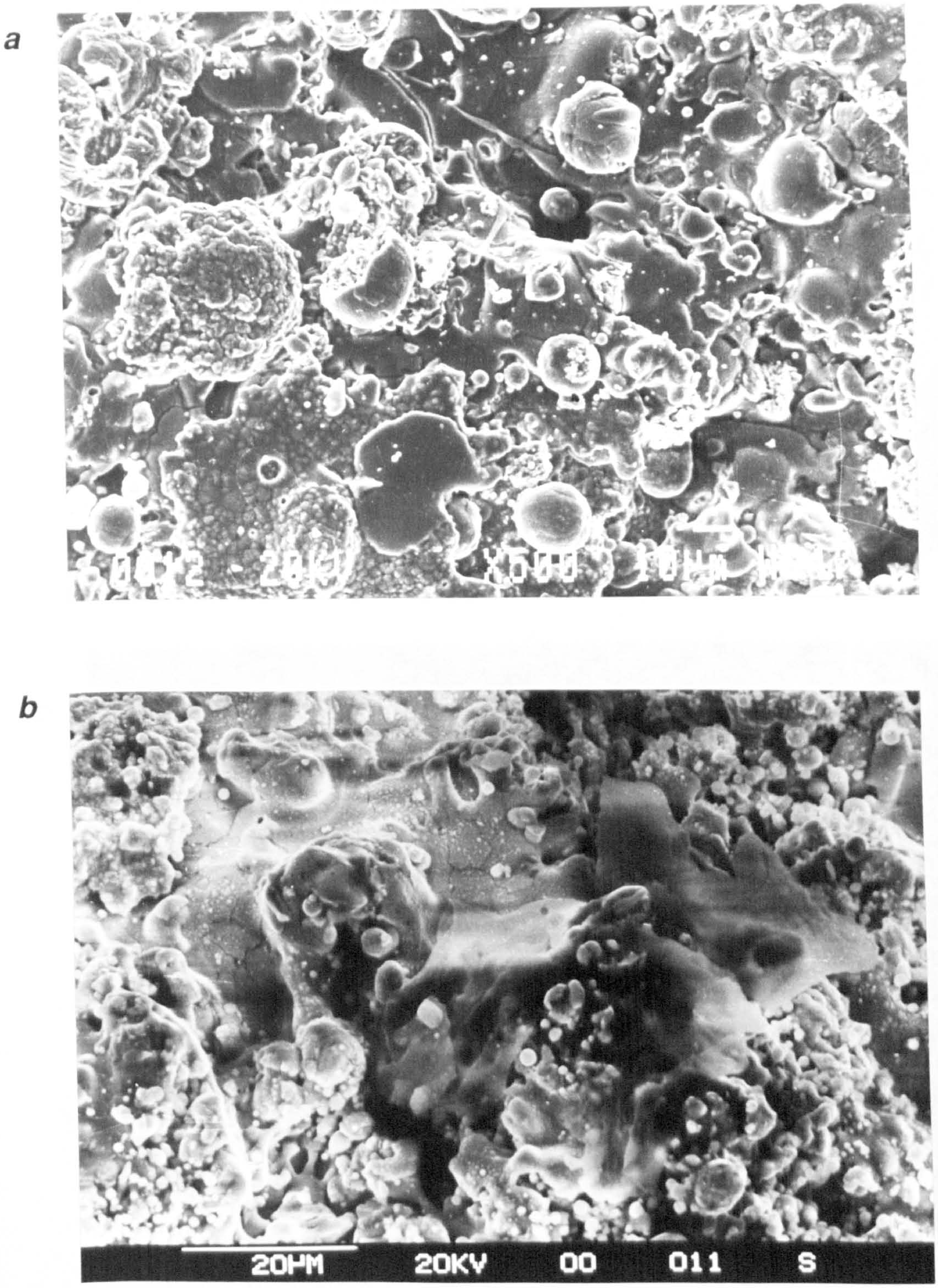

Figure 5.7 SEM images of the (***a***) ZrO_2-Y_2O_3-TiO_2 and (***b***) ZrO_2-Y_2O_3 coat surfaces after thermal treatment at 900 °C for 24 hours. SE detector was used.

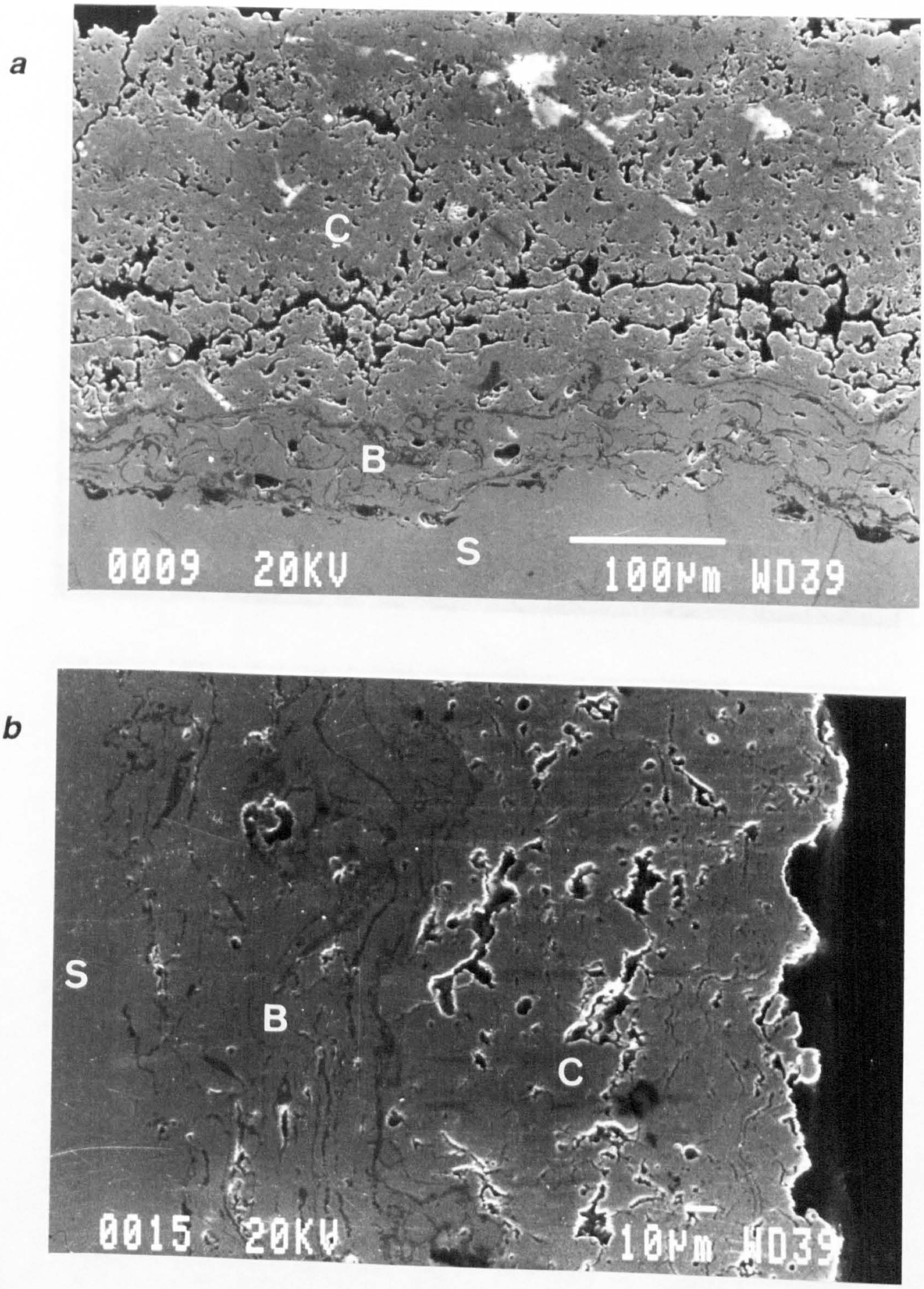

Figure 5.8 Cross-section SEM images of (***a***) ZrO_2-Y_2O_3-TiO_2/NiCrCoAlY and (***b***) ZrO_2-Y_2O_3/NiCrCoAlY coatings after thermal treatment at 900 °C for 24 hours. B, C and S refer to bond coat, ceramic coat and substrate, respectively. SE and BSE detectors were used.

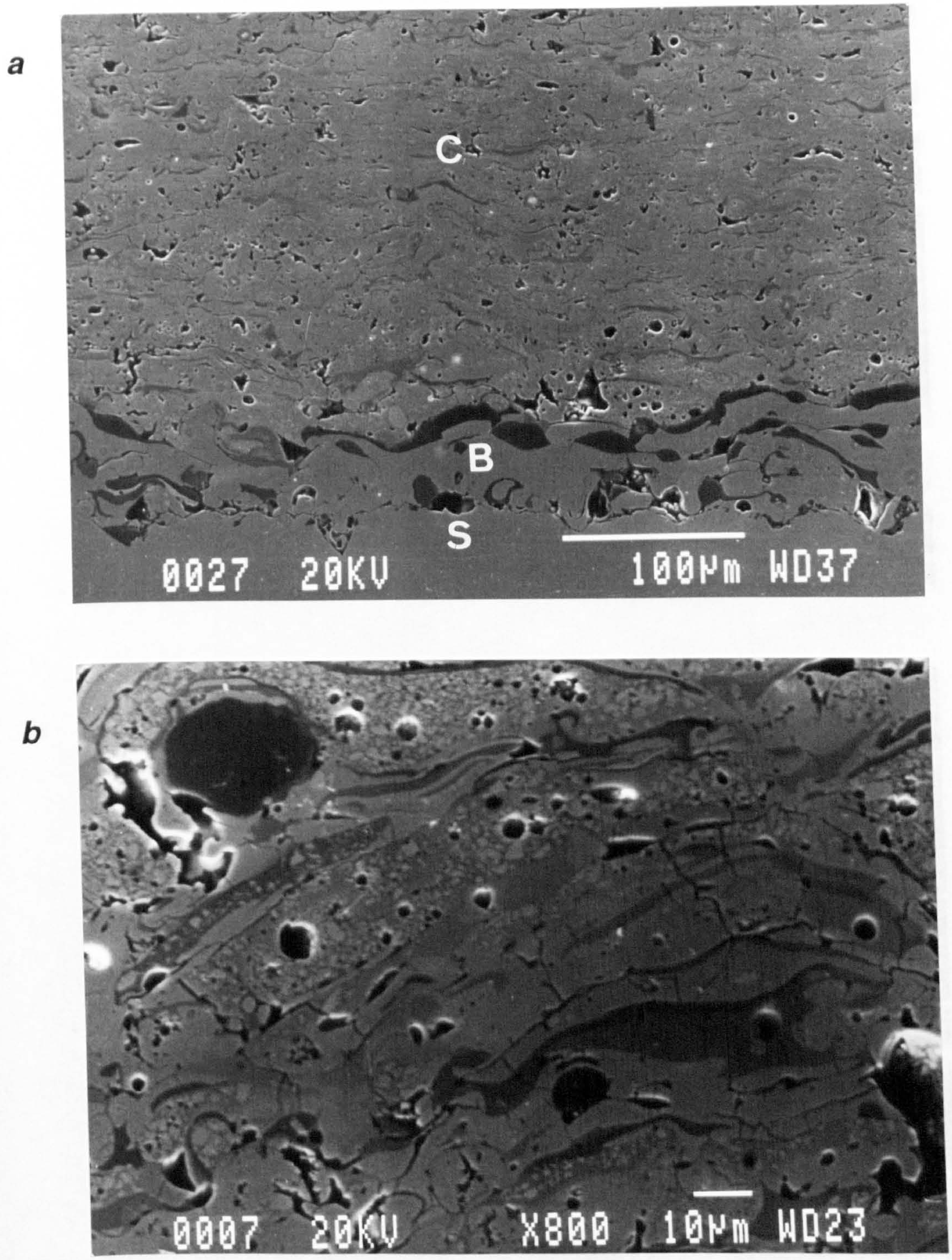

Figure 5.9 Cross-section SEM images of (***a***) plasma sprayed ZrO_2-Y_2O_3-TiO_2/NiCrCoAlY coating (type 2 specimen), and (***b***) ZrO_2-Y_2O_3-TiO_2 coat from a type 2 specimen. B, C, S and U refer to bond coat, ceramic coat, substrate and unmelted material, respectively. SE and BSE detectors were used.

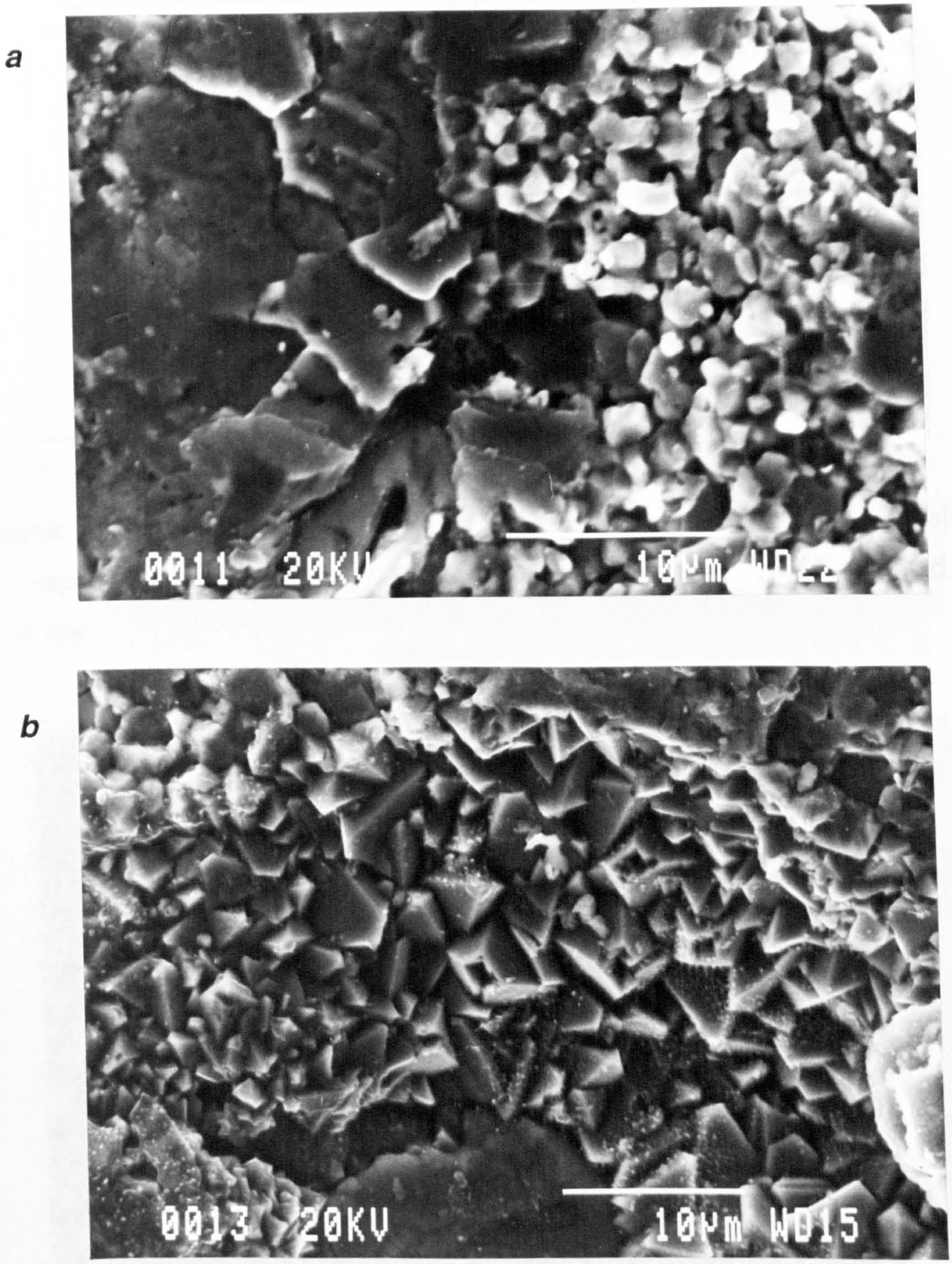

Figure 5.10 (***a***) Remains of ZrO_2-Y_2O_3-TiO_2 lamellae and grains, and (***b***) nickel-rich crystals from the bond coat, found on the surface of the substrate after the ceramic coat has spalled off by heating at 900 °C for 24 hours.

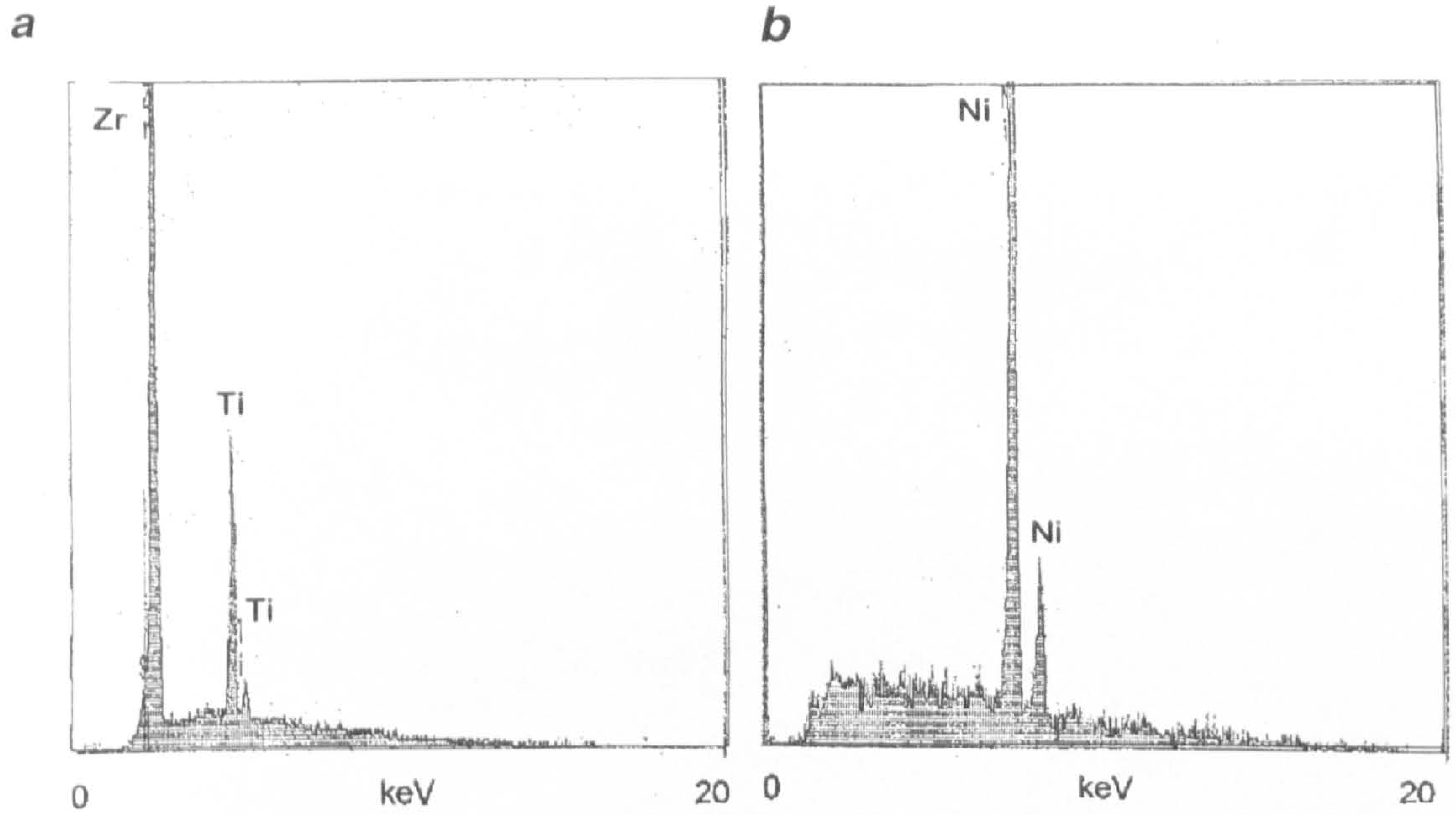

Figure 5.11 EDS analyses of the substrate surface after the ceramic coat spalling, corresponding to (***a***) ceramic lamellae and (***b***) nickel-rich particles of the bond coat remains.

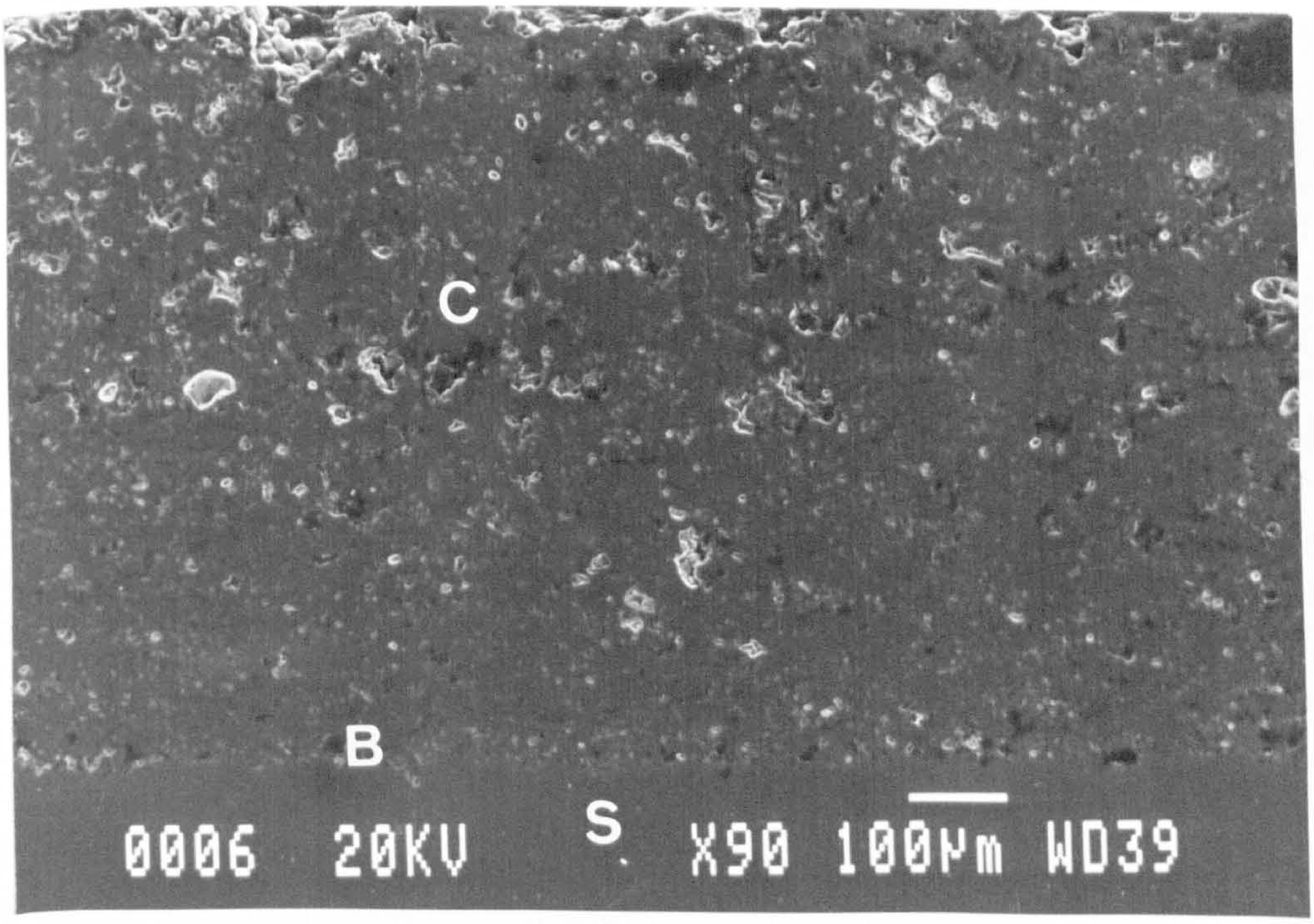

Figure 5.12 Cross-section of a failing ZrO_2-Y_2O_3-TiO_2/NiCrCoAlY plasma sprayed coating. S, B and C refer to the substrate, bond and ceramic coats, respectively. SE and BSE detectors were used.

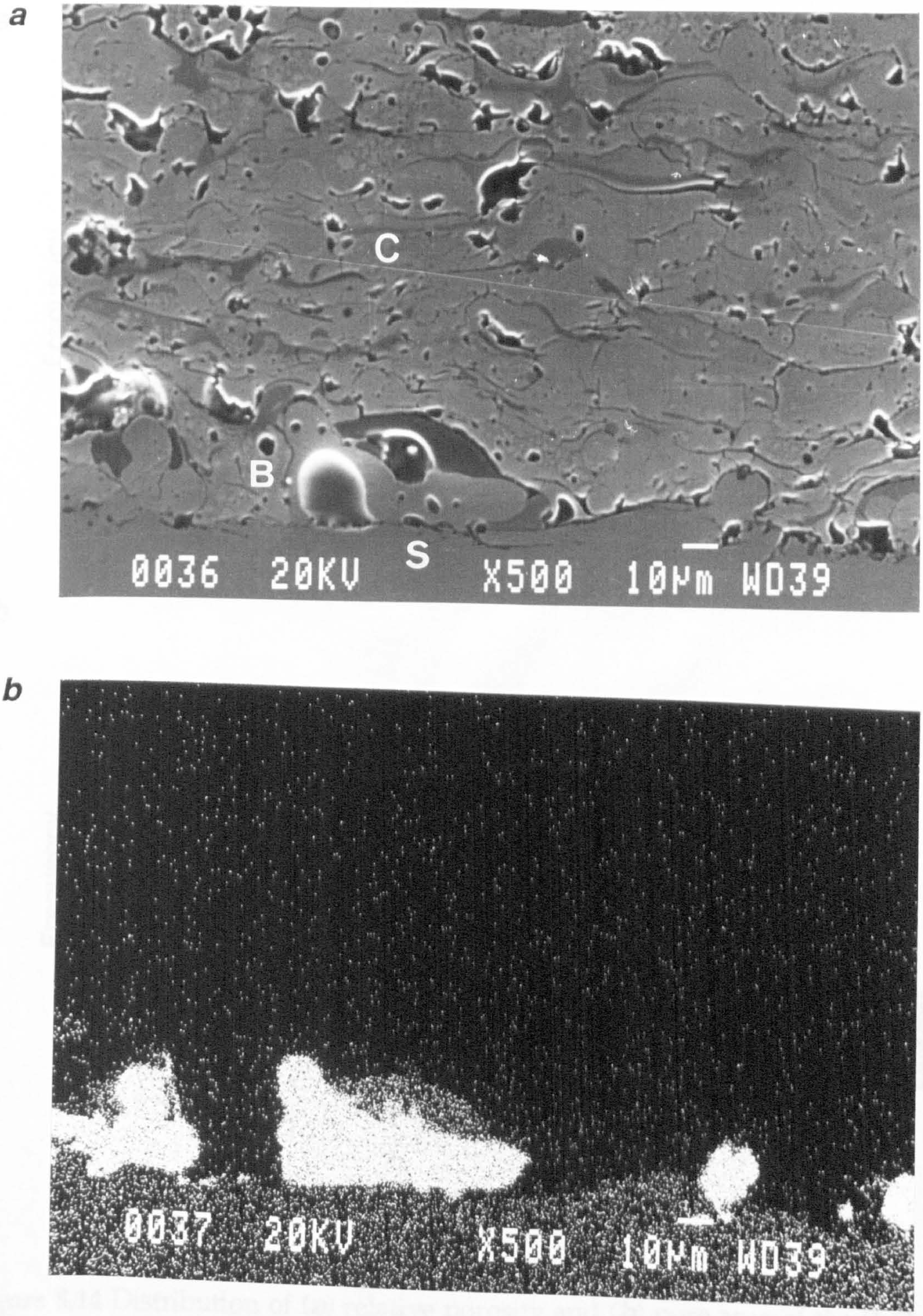

Figure 5.13 (*a*) Detail of the cross-section of a thick ZrO_2-Y_2O_3-TiO_2/NiCrCoAlY coating showing a discontinuous bond coat, SE and BSE detectors were used, (*b*) EDS mapping for nickel from the area shown in (*a*).

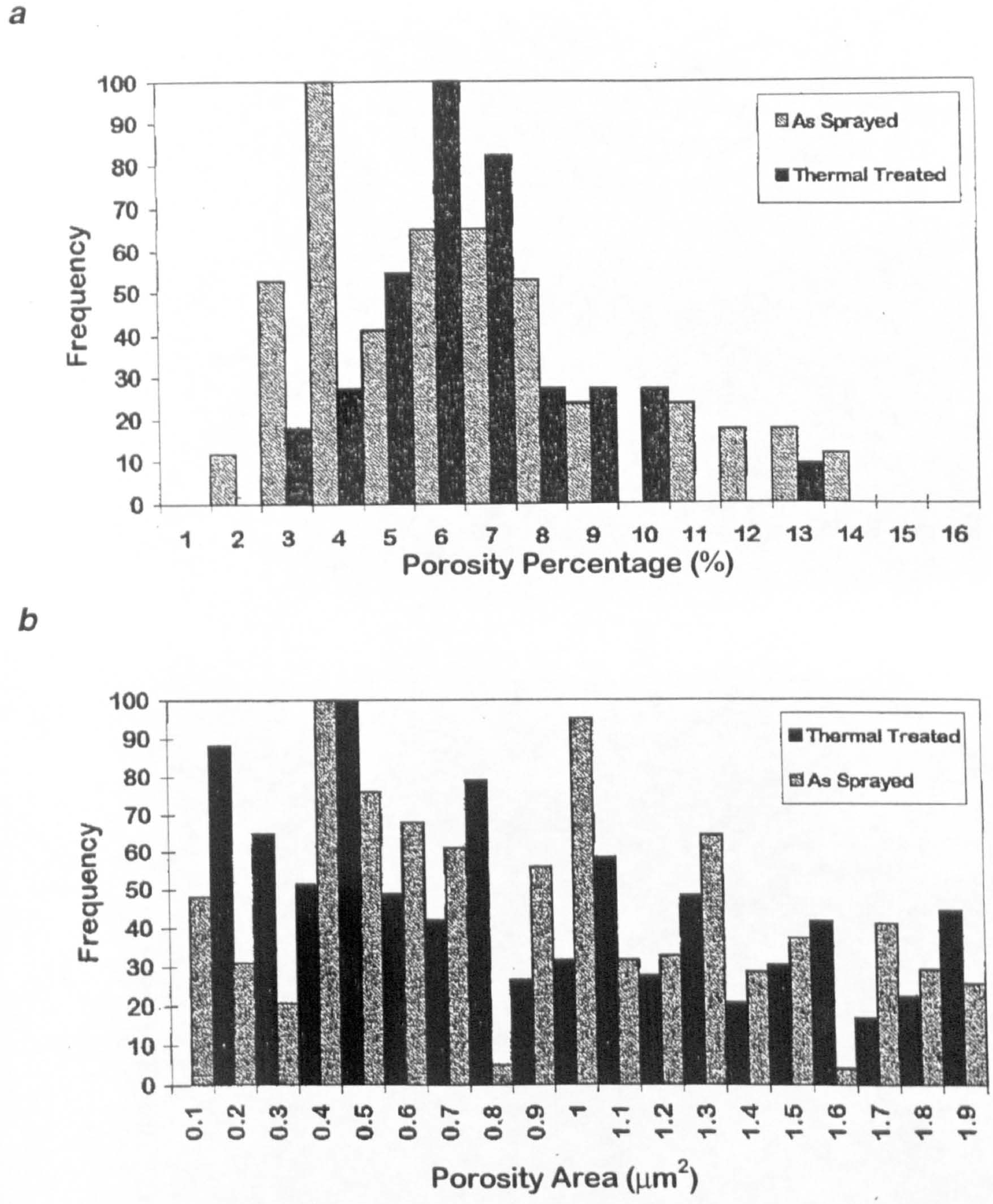

Figure 5.14 Distribution of (***a***) relative porosity and (***b***) pore area of the ZrO_2-Y_2O_3-TiO_2 coat as-sprayed and after heating at 900 °C for 24 hours, as calculated by image analysis of SEM micrographs. The pore area distribution shows the frequency of pores $\leq 2\ \mu m^2$ which corresponds to 47% of the total porosity.

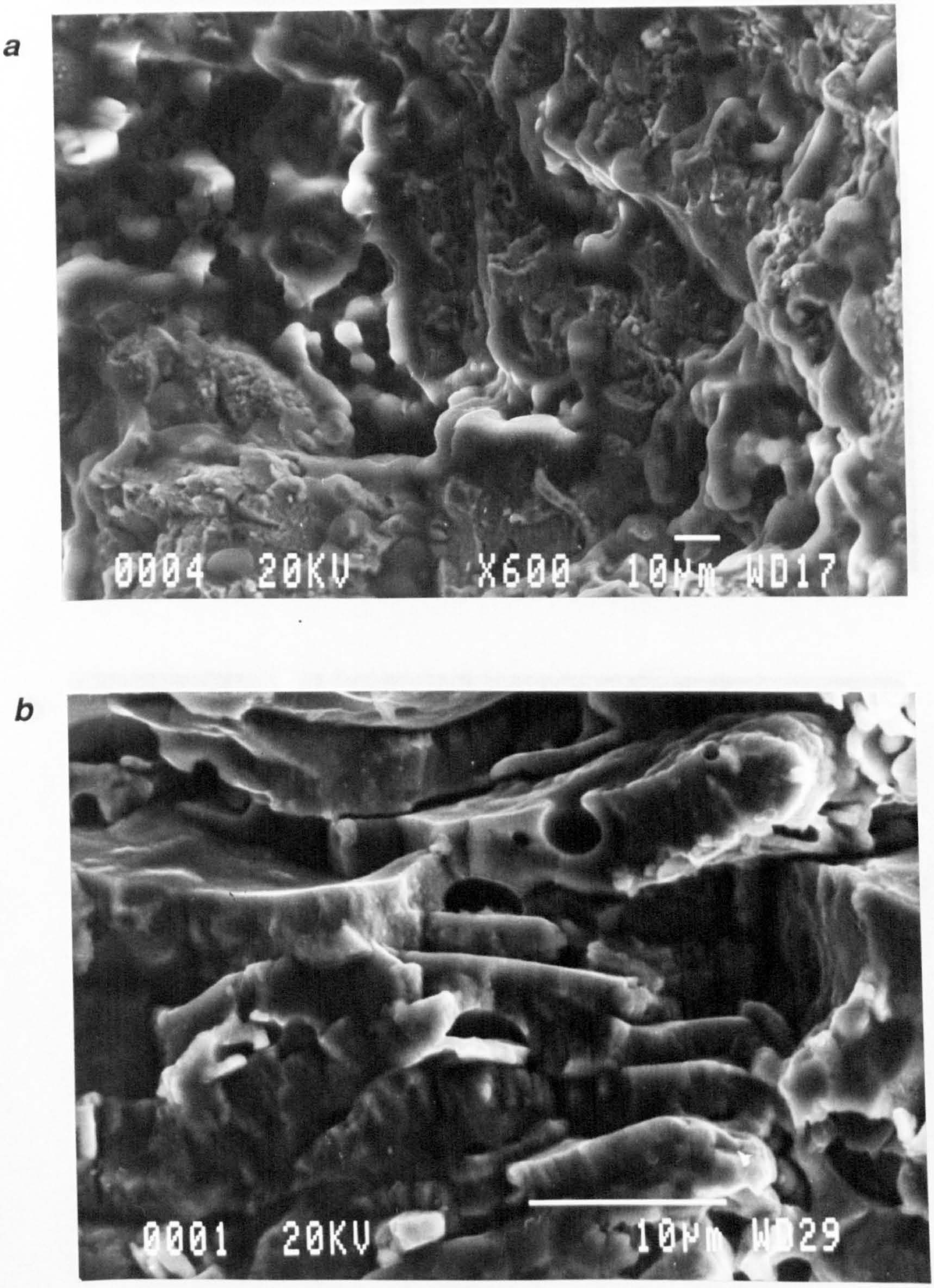

Figure 5.15 Fracture surface of the ZrO_2-Y_2O_3-TiO_2 coat (***a***) as-sprayed and (***b***) as-cooled with liquid nitrogen. SE detector was used.

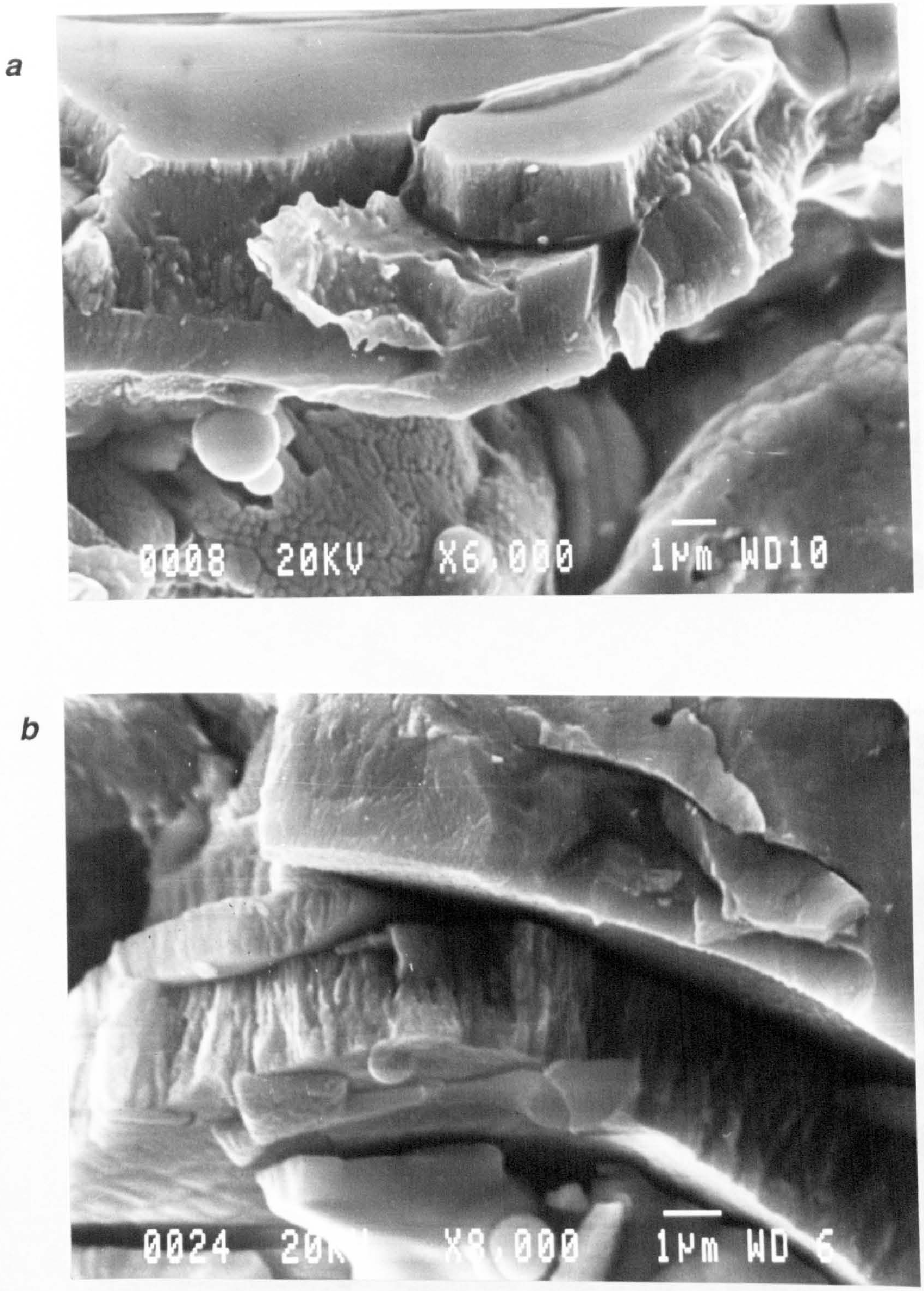

Figure 5.16 Fracture surface of a ZrO_2-Y_2O_3-TiO_2 coat heated at 900 °C for 24 hours in (***a***) air and (***b***) in argon. SE detector was used.

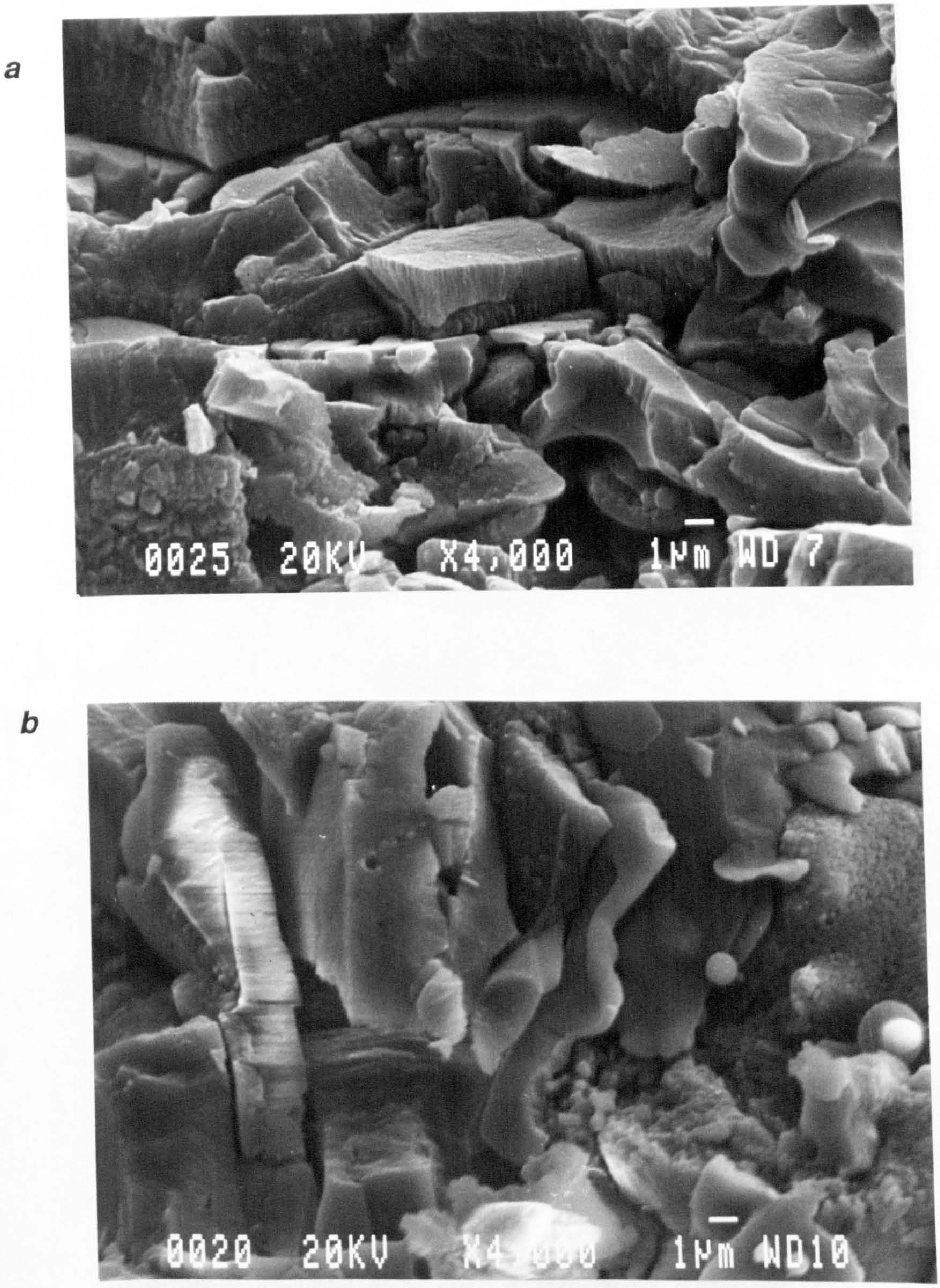

Figure 5.17 Fracture surface of ZrO_2-Y_2O_3-TiO_2 coats heated at (***a***) 1000 °C and (***b***) 1100 °C for 24 hours in argon. SE detector was used.

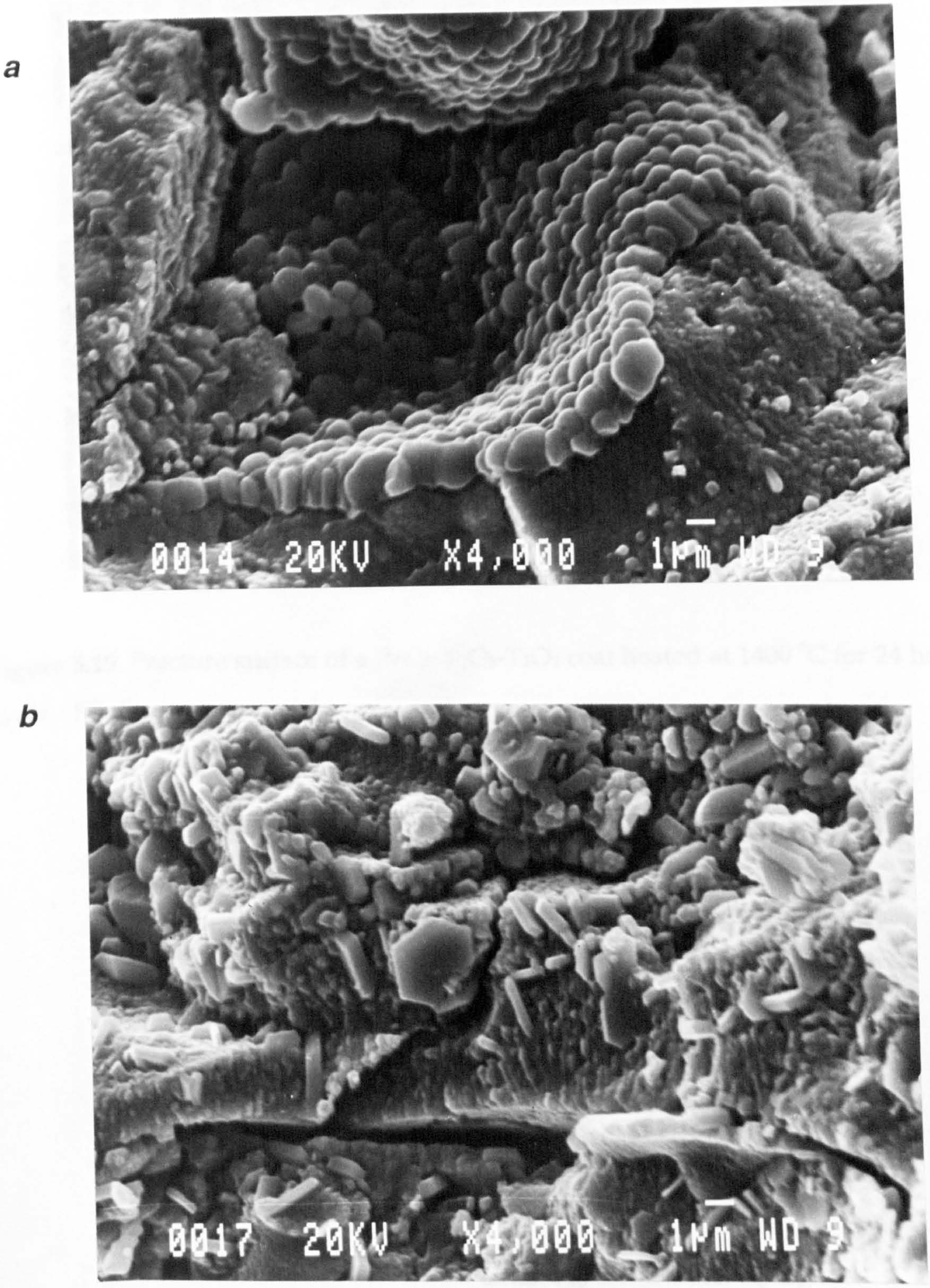

Figure 5.18 Fracture surface of ZrO_2-Y_2O_3-TiO_2 coats heated at 1200 °C for 24 hours in (***a***) air and (***b***) argon. SE detector was used.

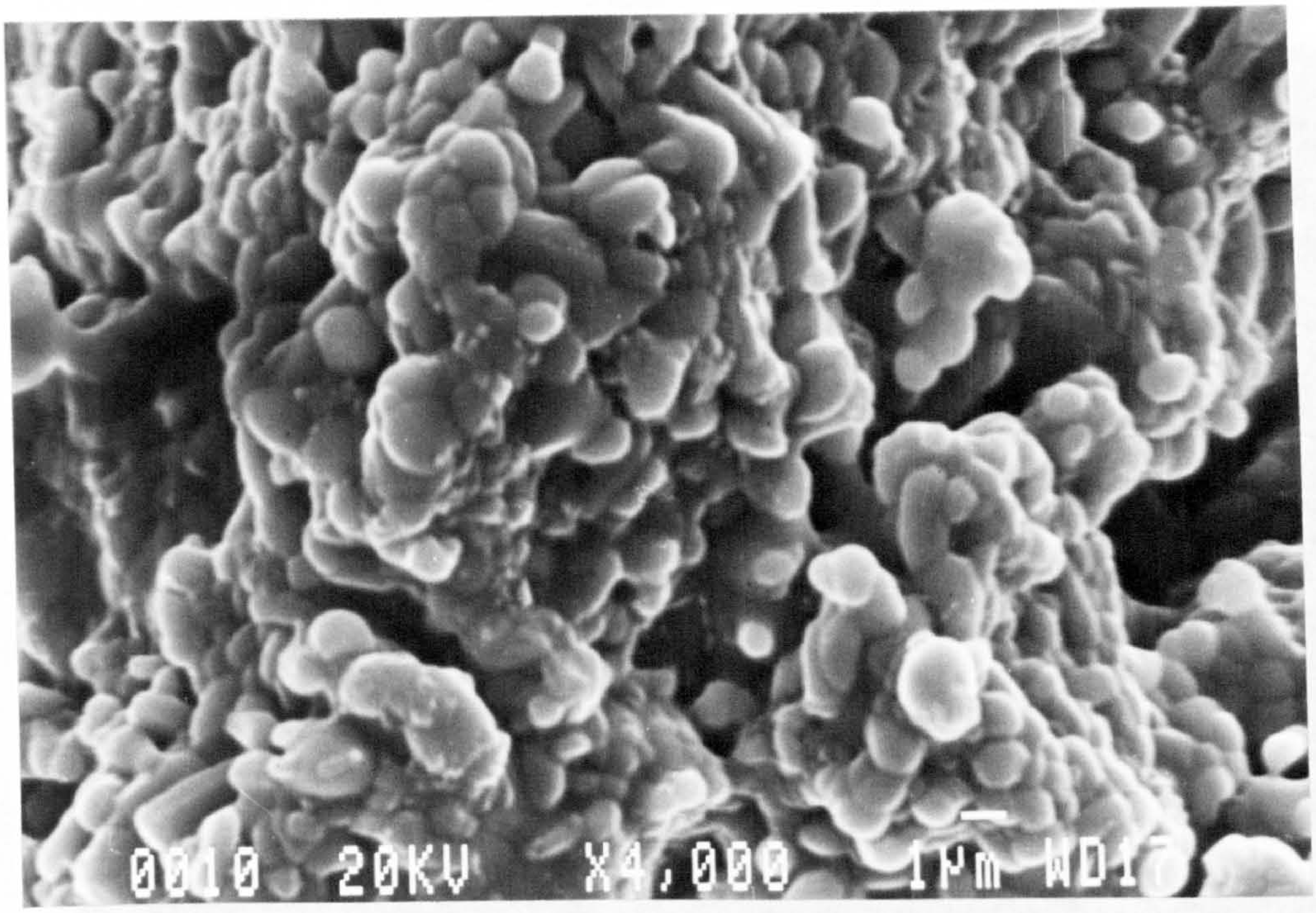

Figure 5.19 Fracture surface of a ZrO_2-Y_2O_3-TiO_2 coat heated at 1400 °C for 24 hours in air. SE detector was used.

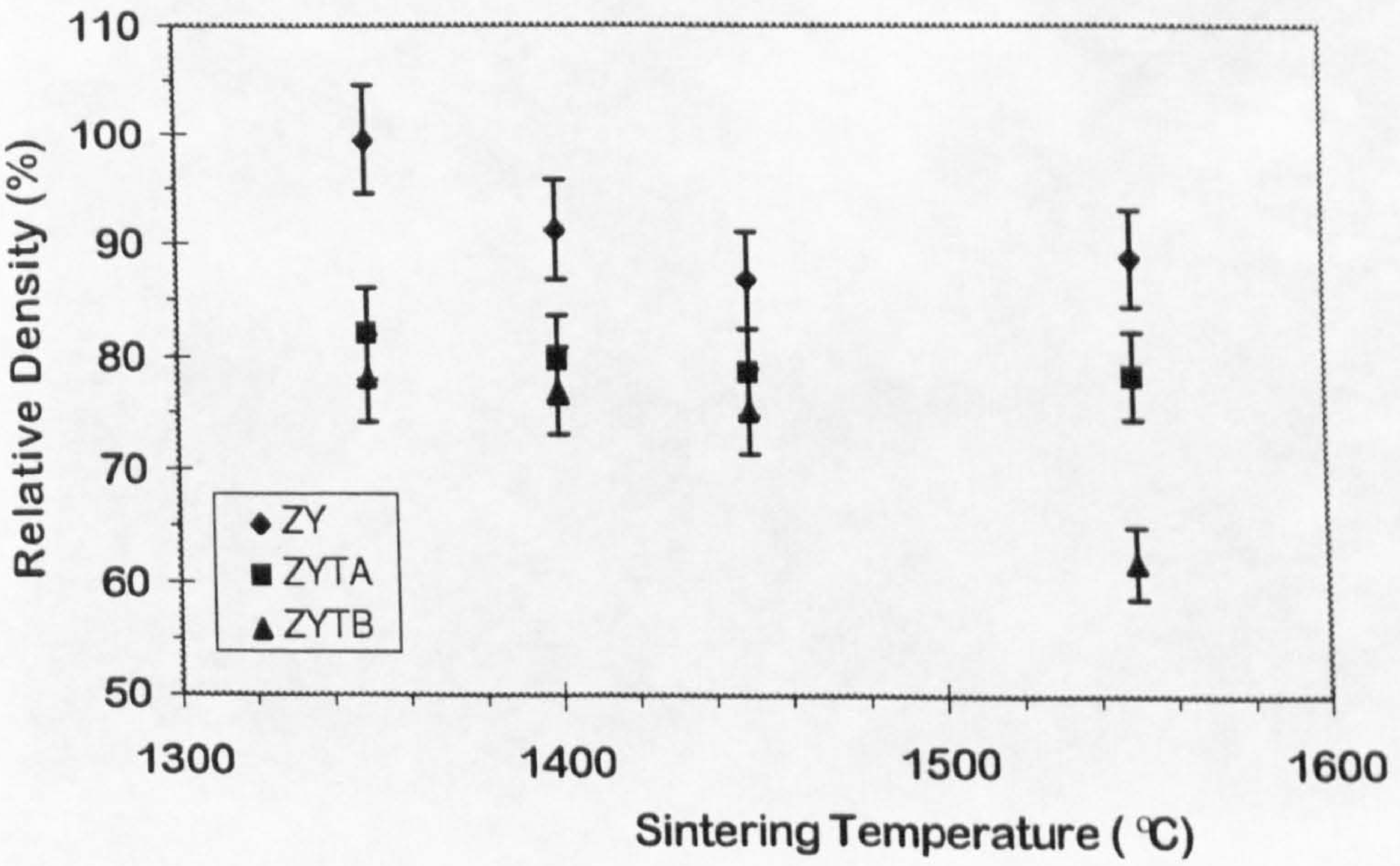

Figure 5.20 Relative density of (ZY) ZrO_2-Y_2O_3 powder, (ZYTA) ZrO_2-Y_2O_3-TiO_2(A) powder and (ZYTB) ZrO_2-Y_2O_3-TiO_2(B) powder used for plasma-spraying, pressed and sintered at different temperatures.

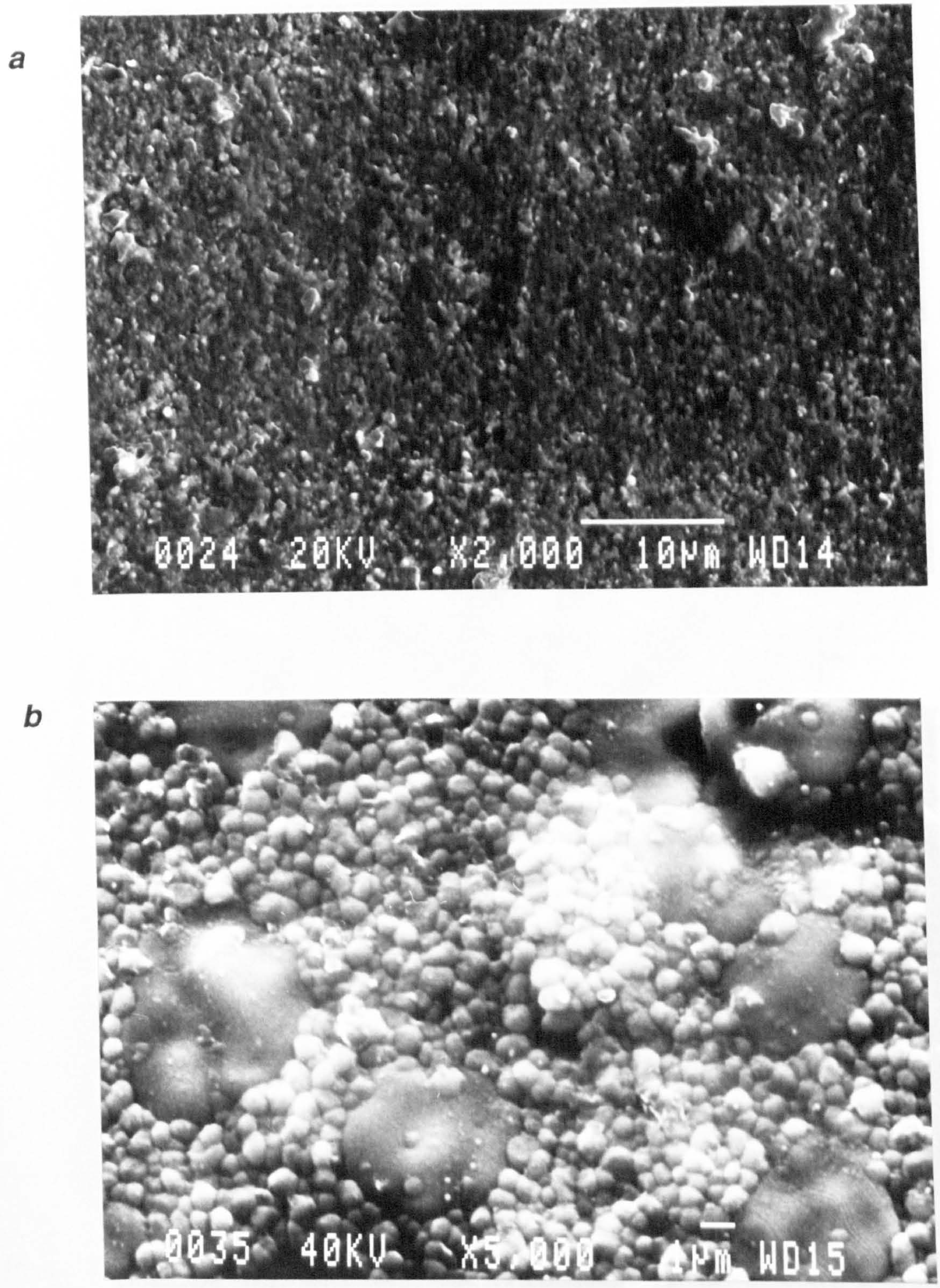

Figure 5.21 Surface of the ZrO_2-Y_2O_3 pressed-powder disks sintered at (***a***) 1400 and (***b***) 1550 °C, for 1 hour. SE detectors was used.

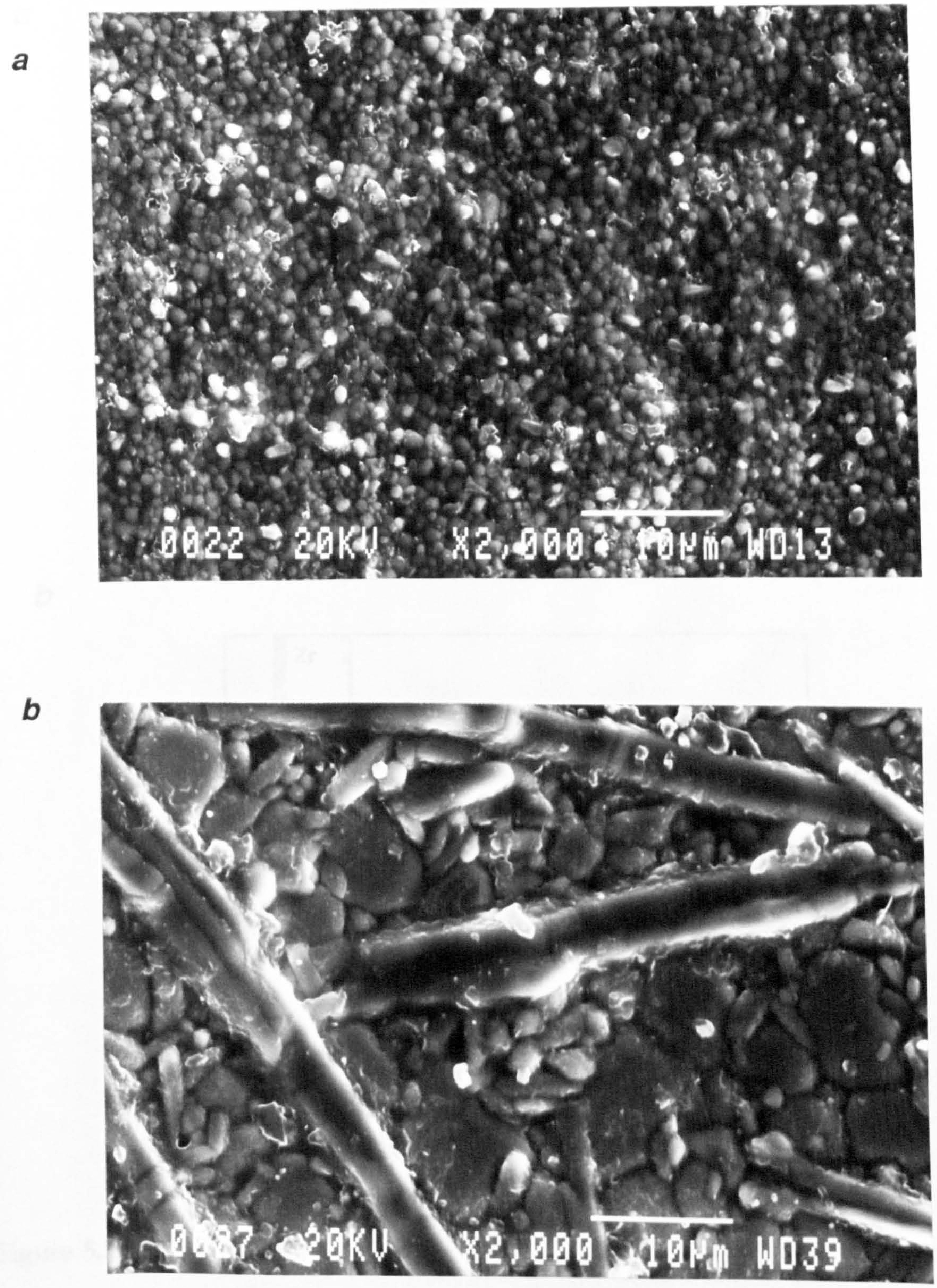

Figure 5.22 Surface of the ZrO_2-Y_2O_3-TiO_2(A) pressed-powder disks sintered at (***a***) 1400 and (***b***) 1550 °C, for 1 hour. SE detector was used.

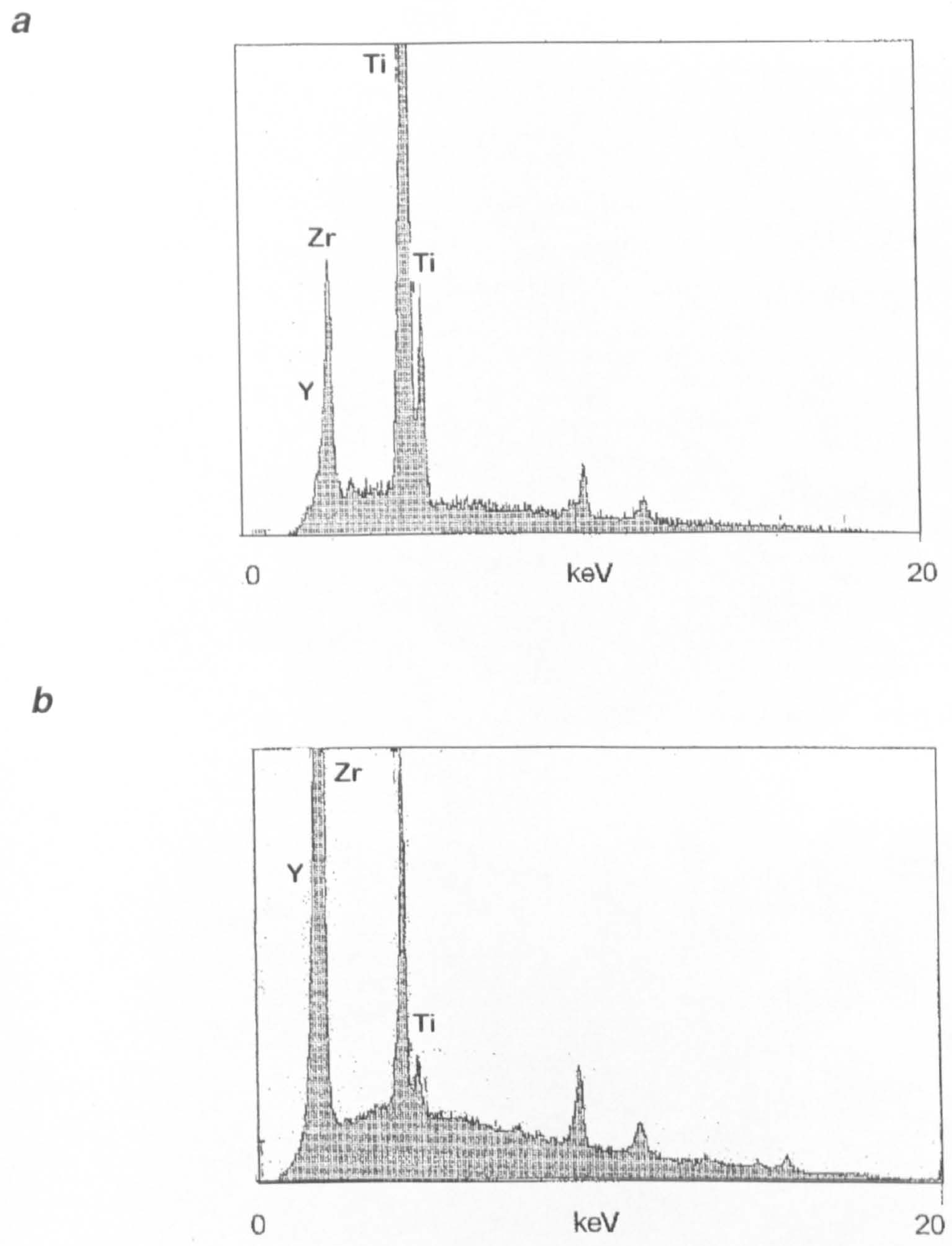

Figure 5.23 EDS analyses of (***a***) elongated and (***b***) equiaxed grains found on the surface of a ZrO_2-Y_2O_3-TiO_2 (A) pressed-powder disk sintered at 1550 °C, for 1 hour as shown in Figure 5.22b.

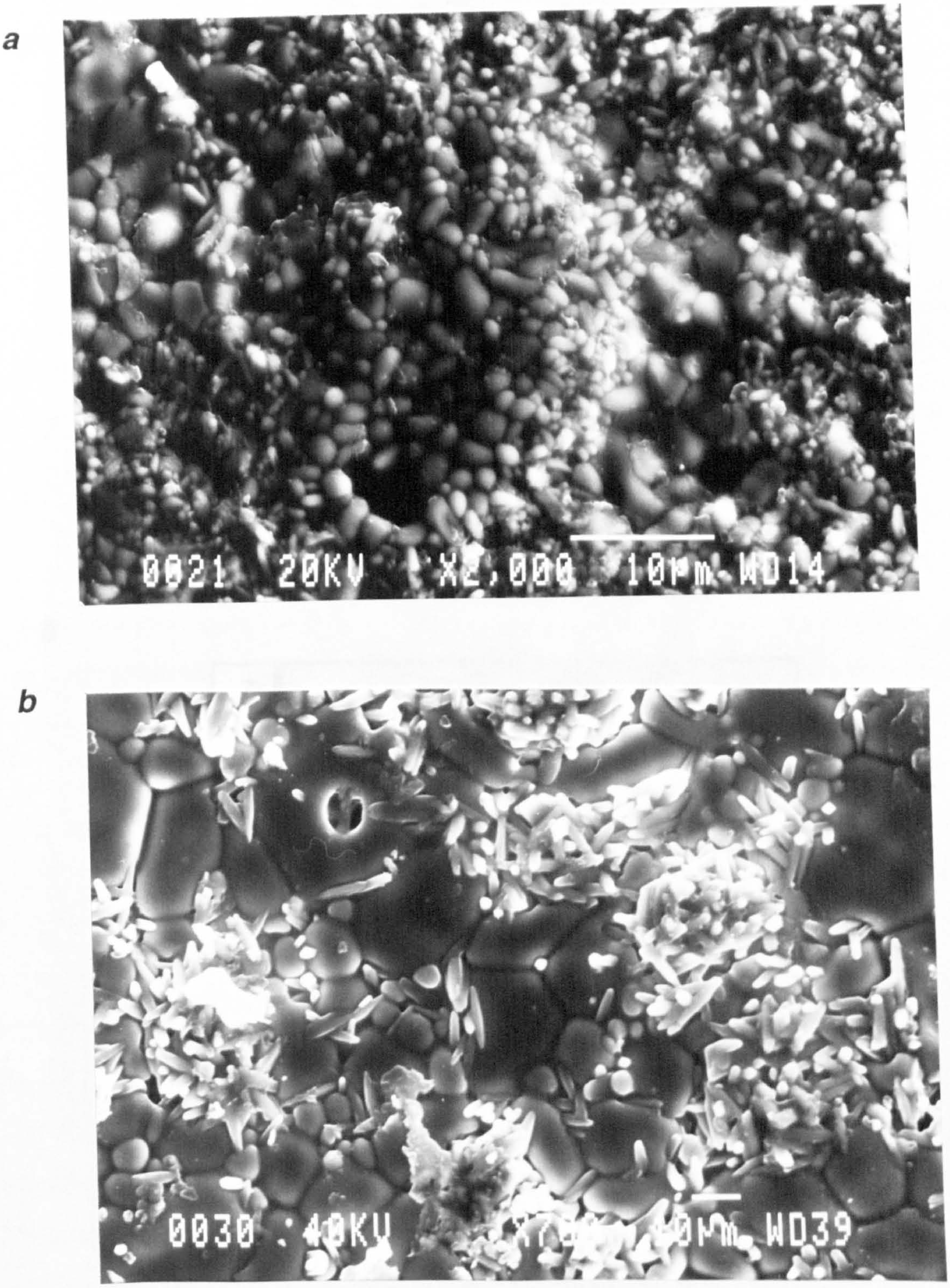

Figure 5.24 Surface of the ZrO_2-Y_2O_3-TiO_2 (B) pressed-powder disk sintered and sintered at (***a***) 1400 and (***b***) 1550 °C, for 1 hour. SE detector was used.

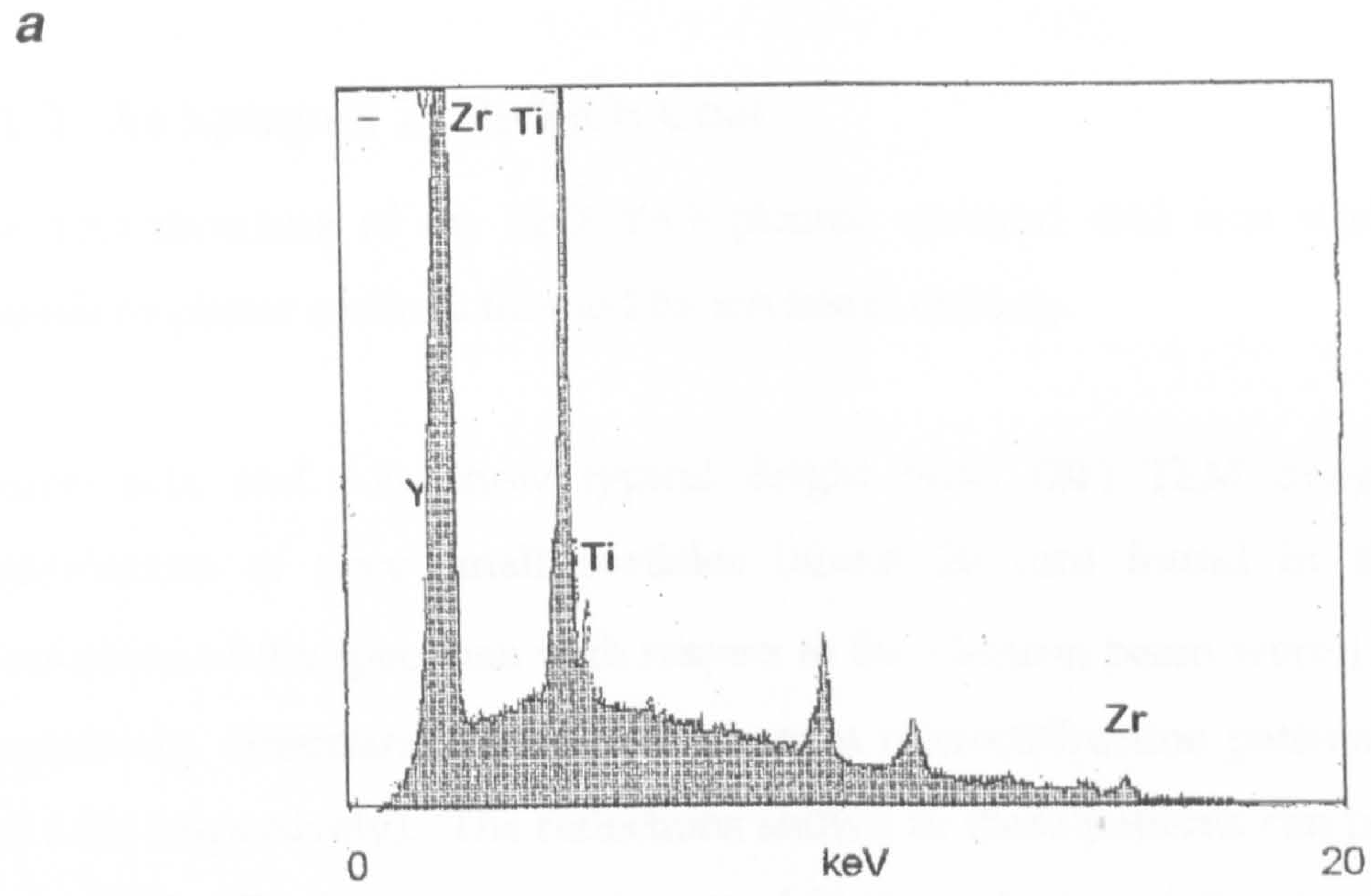

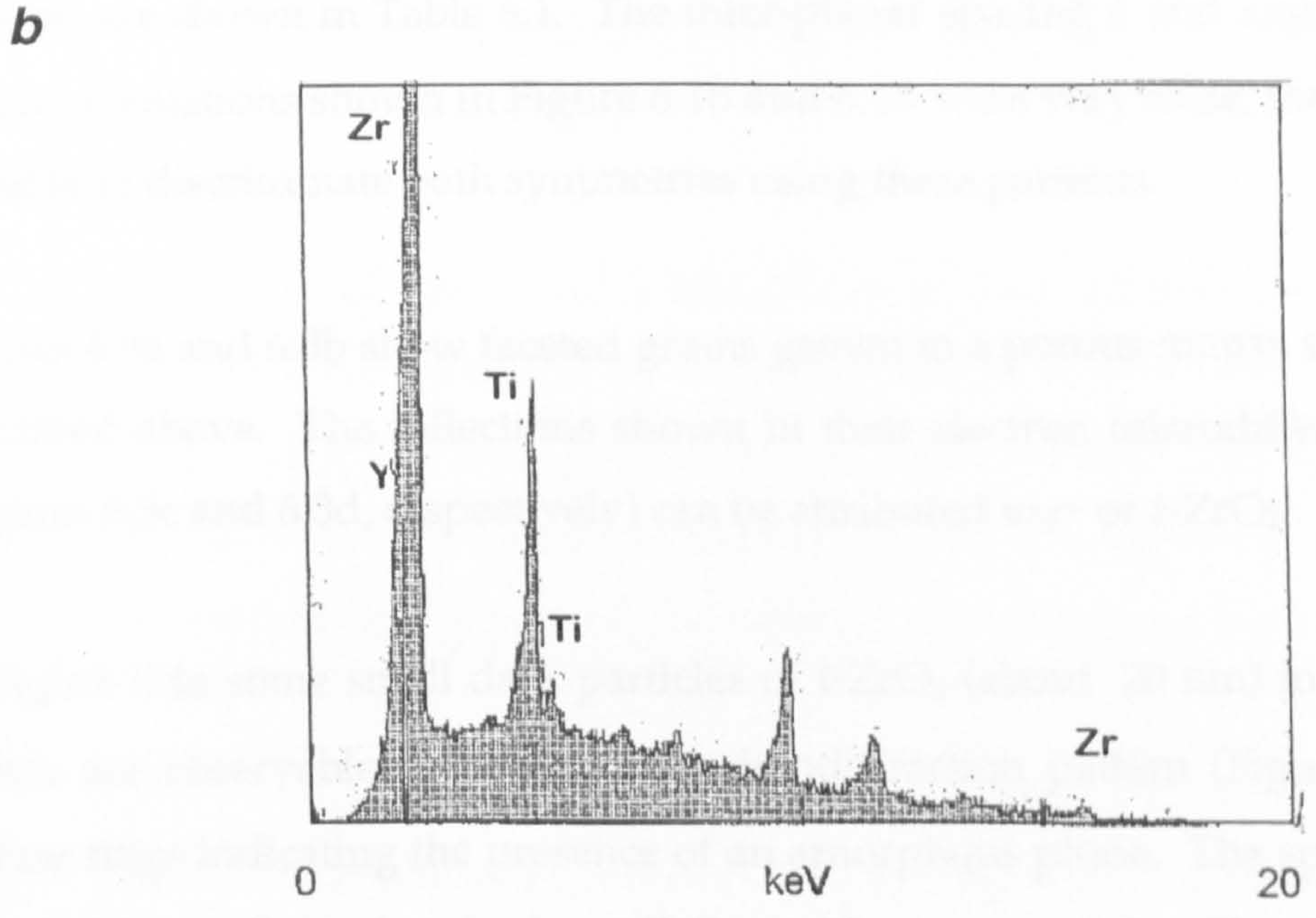

Figure 5.25 EDS analyses of (***a***) elongated and (***b***) equiaxed grains found on the surface of a ZrO_2-Y_2O_3-TiO_2 (B) pressed-powder disk, sintered at 1550 °C, for 1 hour as shown in Figure 5.24b.

6 TRANSMISSION ELECTRON MICROSCOPY

6.1 RESULTS

6.1.1 As Sprayed ZrO_2-Y_2O_3 Coat

The microstructure of the ZrO_2-Y_2O_3 plasma sprayed coat was studied by TEM analysis of planar sections thinned by ion beam etching.

Figures 6.1a and 6.2a show typical Bright Field (BF) TEM images of porous agglomerates of very small particles (about 20 nm) found in this coat. The orientations of the specimen with respect to the electron beam were $[\bar{1}12]$ and [011] respectively, determined from their electron microdiffraction patterns (Figure 6.1b and 6.2b, respectively). The reflections shown in these patterns can be attributed to *c*- or *t*-ZrO_2. The lattice parameters used in the indexing of the electron diffraction patterns are shown in Table 6.1. The inter-planar spacing d and angle ϕ calculated for the orientations shown in Figure 6.1b and 6.2b were very close, therefore it is not possible to discriminate both symmetries using these patterns.

Figures 6.3a and 6.3b show faceted grains grown in a porous matrix similar to those described above. The reflections shown in their electron microdiffraction patterns (Figures 6.3c and 6.3d, respectively) can be attributed to *c*- or *t*-ZrO_2.

In Figure 6.4a some small dark particles of *t*-ZrO_2 (about 20 nm) in a very porous matrix are observable. The electron microdiffraction pattern (Figure 6.4b) shows diffuse rings indicating the presence of an amorphous phase. The spots correspond to reflections allowed only for *t*-ZrO_2 (odd, even, even). The allowed *c*-ZrO_2 reflections are of the type (*odd, odd, odd*) or (*even, even, even*).

Figure 6.5a shows dark grains in a porous matrix. The selected area diffraction pattern (Figure 6.5b) shows intense reflections (brighter spots) attributable to *c*- and *t*-ZrO_2, and less intense reflections (lighter spots) allowed only to *t*-ZrO_2 (type *even, odd, odd*).

Figure 6.6a shows rounded grains, larger than those described above (about 150 nm in diameter). A mottled microstructure can be observed. The selected area diffraction (Figure 6.6b) pattern indicates that they are *m*-ZrO_2 particles in a matrix of *c*- or *t*-ZrO_2. Different variants of *m*-ZrO_2 can be distinguished.

6 .1 .2 As Sprayed ZrO_2-Y_2O_3-TiO_2 Coat

Although it was difficult to find electron transparent zones suitable for TEM observations in the powdered specimen, it was possible to make some observations. Figure 6.7a shows a micrograph obtained from a powdered ZrO_2-Y_2O_3-TiO_2 specimen displaying a particle border with *m*-ZrO_2 twins identified as laths (about 50 nm x 500 nm) and confirmed by its electron microdiffraction pattern (Figure 6.7b). The *m*-ZrO_2 laths exhibit abundant Moirè contrast. The microanalysis of this specimen zone (Figure 6.7c) revealed a very low concentration of titanium. Peaks from copper observed in this EDS correspond to copper from the specimen grid. Figure 6.8a is another micrograph obtained from the powdered ZrO_2-Y_2O_3-TiO_2 specimen. It shows *m*-ZrO_2 particles with laths grown in different directions.

TEM observations of the bond coat/substrate and ceramic coat/bond coat interface regions were restricted by the nature of the sample itself. Figures 6.9a-6.9c show typical SEM micrographs of ion beam etched thin sections of the system ceramic coat/bond coat/substrate. While the substrate and the bond coat have been extensively etched, the ceramic coat has been scarcely thinned.

TEM analysis of the ZrO_2-Y_2O_3-TiO_2 coat microstructure was made on its planar and cross sections. Figure 6.10a shows a BF TEM micrograph of the coat planar section prepared by ion beam etching. Rounded grains (about 50 nm in diameter) with a mottled appearance are observed. The electron diffraction pattern displays reflections allowed for *c*- and *t*-ZrO_2 (Figure 6.10b). DF TEM image shown in Figure 6.10c confirms the mottled microstructure and the presence of some porosity. The microanalysis of this specimen (Figure 6.10d) displays zirconium, yttrium and titanium peaks (Table 6.2).

Similar observations can be made from Figure 6.11a; rounded grains (about 70 nm in diameter) with some intergranular porosity are shown. The diffraction pattern (Figure 6.11b) was not conclusive in discriminating *c*- and *t*-ZrO_2. The mottled microstructure of the grains is revealed by the respective DF image (Figure 6.11c). The EDS indicates the presence of zirconium, yttrium and titanium.

Figures 6.12a and 6.13a show TEM micrographs obtained from thin cross-sections of the ZrO_2-Y_2O_3-TiO_2 coat. Rounded grains with intergranular porosity are observed. An intergranular microcrack can be distinguished in Figure 6.12a. The respective electron diffraction patterns (Figures 6.12b and 6.13b) display reflections permissible for *c*- and *t*-ZrO_2. The intergranular crack observed in Figure 6.12a indicates a weak bond between grains. The EDS of the specimen zone shown in Figure 6.13a reveals the presence of zirconium, yttrium and titanium (Figure 6.13c).

Figures 6.14a and 6.14b correspond to BF TEM micrographs of the coat planar sections. Extensive areas of the observed specimen zones display a mottled contrast. Their electron diffraction patterns (Figures 6.14c and 6.14d, respectively) exhibit intense reflections (brighter spots) corresponding to *c*- or *t*-ZrO_2, and also less intense reflections (lighter spots) attributable only to *t*-ZrO_2. Figure 6.14d presents more high-order *t*-ZrO_2 reflections than Figure 6.14c, this gives an idea of the extension of the *t*-ZrO_2 phase in each case. Figure 6.14e corresponds to the EDS of the specimen zone shown in Figure 6.14b and it indicates the presence of zirconium, yttrium and titanium.

Figure 6.15a shows a BF image of a ZrO_2-Y_2O_3-TiO_2 coat cross-section which displays tetragonal grains with a mottled microstructure. The electron diffraction pattern exhibits reflections corresponding to two variants of *t*-ZrO_2. The corresponding DF image (Figure 6.15c) allows the identification of antiphase boundaries (APBs). The microanalysis of the observed zone indicates the presence of zirconium, yttrium and titanium (Figure 6.15d). Another example of *t*-ZrO_2 particles or precipitates in a *c*-ZrO_2 phase is shown in Figure 6.16a, as determined from its electron diffraction pattern (Figure 6.16b).

Larger grains (about 600 nm in diameter) of *c*- or *t*-ZrO_2 and *m*-ZrO_2 twins were also observed in the ZrO_2-Y_2O_3-TiO_2 coat, as shown in Figures 6.17a-c. Undissolved TiO_2 (rutile) present as rounded grains (100 nm) was identified (Figure 6.18a) as determined by the EDS (Figure 6.18b) and the corresponding electron diffraction pattern (Figure 6.18c).

m-ZrO_2 was observed in the ZrO_2-Y_2O_3-TiO_2 coat as rounded grains (about 100 nm) as shown in Figure 6.19. However, *m*-ZrO_2 was found mainly as twins (Figuges 6.20-6.22). Figures 6.20a and 6.21b show highly twinned *m*-ZrO_2 particles. Although both particles have a similar composition (Figures 6.20c and 6.21b respectively), the titanium concentration in the particles shown in Figure 6.21b is much lower than in the particles shown in Figure 6.20a. An interface between the *m*-ZrO_2 twinned particle and matrix is observed in Figure 6.21a, a microcrack can also be identified. Figures 6.22a-6.23c show mosaics of *m*-ZrO_2 twins; combinations of twins in different directions are observed. The microanalysis of the mosaic shown in Figure 6.23c indicates a low concentration of titanium (Figure 6.23d) when compared with the *c*- and *t*-ZrO_2 previously described.

6 .1 .3 Thermally Treated ZrO_2-Y_2O_3-TiO_2 Coats

A varied and complex microstructure was observed for coats thermally treated at 1400 and 1600 °C. Figures 6.24a and 6.24b are typical BF TEM images of a ZrO_2-Y_2O_3-TiO_2 sample heated at 1400 °C for 24 hours. Particles of *c*- or *t*-ZrO_2, *t*- and *m*-ZrO_2 twins can be observed.

Figure 6.25 shows very porous agglomerates of small particles (about 20 nm) which can correspond to *c*- or *t*-ZrO_2. Large faceted grains (about 200 nm) of *c*- or *t*-ZrO_2 were identified as shown in Figures 6.26-6.27. The grain boundaries are clean and an intergranular microcrack along a few grains is observed (Figure 6.27a).

Twinned *t*-ZrO_2 particles is another microstructural feature observed in the ZrO_2-Y_2O_3-TiO_2 coat thermal treated at 1400 °C. A typical BF TEM of *t*-ZrO_2 twins is shown in Figure 6.28a. The microanalysis reveals a high titanium concentration

(Figure 6.28c). Particles displaying *m*-ZrO_2 laths were also observed in a ZrO_2-Y_2O_3-TiO_2 coat thermal treated at 1400 °C as can be seen in Figure 6.29a.

Microstructural features observed in a ZrO_2-Y_2O_3-TiO_2 coat thermally treated at 1600 °C were also varied and complex. Large grains (> 300 nm) displaying an amorphous grain boundary pocket are observed in Figure 6.30a. A very porous "sponge-like" microstructure is observed in Figure 6.30b. Figure 6.31a shows a large twinned *m*-ZrO_2 particle, its EDS (Figure 6.30c) indicates a negligible concentration of titanium. Figure 6.32a shows *t*-ZrO_2 particles conformed by small grains (about 50 nm). The titanium concentration in these *t*-ZrO_2 particles (Figure 6.32c) is lower than in the case of *t*-ZrO_2 twins described above. Particles of *c*- or *t*-ZrO_2 exhibiting a nanostructure composed by equiaxed grains are observed in Figure 6.33a.

6 .1 .4 ZrO_2-Y_2O_3-TiO_2 Sintered Bodies

Planar sections of the pressed powder sintered at 1350 °C were analysed by TEM, typical images are shown in Figures 6.34 to 6.38. Large faceted grains (about 300 nm) with dislocations and some deformation presenting clean grain boundaries are observed in Figures 6.34a to 6.36a. The corresponding electron diffraction patterns show reflections allowed for *c*- and *t*-ZrO_2. *m*-ZrO_2 was detected as large (> 300 nm diameter) faceted grains (Figure 6.37) and as twinned particles (Figure 6.38).

6 .2 DISCUSSION OF RESULTS

6 .2 .1 As Sprayed ZrO_2-Y_2O_3 Coat

The agglomerates of very small particles observed in the coat (Figure 6.1a, 6.1b) suggest they had insufficient time during the plasma spraying process to be consolidated. In some areas of the specimen, it was possible to notice that consolidation of these agglomerates had started to take place by the appearance of faceted grains (Figures 6.3a, 6.3b). The diffraction patterns obtained from these agglomerates (Figures 6.3c and 6.3d, respectively) showed reflections that could be attributed to *c*- or *t*-ZrO_2, therefore it was not possible to determine the absolute symmetry of these agglomerates. However, it was possible to identify particles or precipitates of t-ZrO_2 in a matrix composed by these porous agglomerates (Figures 6.4a, 6.5a); reflections permissible only for t-ZrO_2 were detected (Figures 6.4b, 6.5b). Since reflections corresponding to the matrix and "extra" reflections associated with t-ZrO_2 were observed (Figure 6.5b), it is very likely that the matrix of agglomerates consisted of c-ZrO_2. The t-ZrO_2 particles in a c-ZrO_2 matrix are a result of the $c \rightarrow t$-ZrO_2 transformation that takes place during the plasma spraying (Section 7.4). Different m-ZrO_2 variants resulting from $t \rightarrow m$ transformation can be identified from diffraction patterns such as Figure 6.6b.

6 .2 .2 As Sprayed ZrO_2-Y_2O_3-TiO_2 Coat

The analysis of the substrate/bond coat and bond coat/ceramic coat interface regions was limited by the nature of the sample itself. Having each component with different etching characteristics gave different thinning rates, thus while the substrate could be totally consumed the ceramic coat had been scarcely thinned (Figure 6.9).

The microstructure of the ZrO_2-Y_2O_3-TiO_2 coat was very heterogeneous and complex as a result of the various phases present (Section 4.1.2) and the different cooling rates that the splats undergo during the plasma spraying. Rounded grains between 50 and 100 nm in diameter corresponding to c- or t-ZrO_2 were found profusely in the observed specimen areas (Figures 6.10-6.13). This morphology suggests the presence of a liquid phase during the plasma spraying process that prevented the grains from consolidating and gave rise to glassy grain boundaries. This glassy phase reduces the coat strength as intergranular microcraks can be observed (Figure 6.12a).

The modulated or "mottled" microstructure of these rounded grains can be attributed to a $c \rightarrow t$-ZrO_2 transformation. This is corroborated by Figures 6.14a and 6.14b whose diffraction patterns disclose the presence of t-ZrO_2 particles or precipitates in a c-ZrO_2 matrix. The "extra" reflection spots of the type *odd, even, odd* found in the electron diffraction pattern of <111> oriented specimens (Figures 6.15c, 6.15d) are forbidden for c-ZrO_2 and attributable only to t-ZrO_2. t-ZrO_2 was also identified by double diffraction spots found in some cases (Figure 6.16a); reflections

110 are not permitted for *t*-ZrO_2, however, due to double diffraction it is possible to observe these reflections.

t-ZrO_2 particles, the product of the *c*→ *t*-ZrO_2 transformation, can be observed in Figure 6.15; at least two *t*-ZrO_2 direction variants are distinguished (Figure 6.15b). The DF image shown in Figure 6.15c evidences the presence of APBs. In a *c*→ *t*-ZrO_2 transformation, the number of different orientation variants dictated by the crystal symmetry is three, with the tetragonal axes along the crystallographic directions [100], [010] and [001] of the parent cubic phase. Thermodynamically, the existence of more than one orientation variant provides a configurational freedom to reduce the total elastic energy arising from a crystal lattice misfit at the *c/t* phase boundaries and the boundaries between different *t*-ZrO_2 orientation variants (**Fan and Chen 1995**). The APBs separate different *t*-ZrO_2 domains nucleated at different points in the parent cubic grain (**Alpérine and Lelait, 1994**).

These microstructural features indicate that the *t*-ZrO_2 corresponds to the "non-transformable" (*t'*-ZrO_2) phase described by **Heuer et al.** (1988) for plasma sprayed ZrO_2-Y_2O_3 coatings which is the product of the non-diffusional *c*→ *t*-ZrO_2 transformation that takes place during the rapid cooling of the plasma sprayed material. Considering the characteristic morphology described for *t*-ZrO_2, it would be possible to determine that grains like that shown in Figure 6.17a, whose electron diffraction is attributable to either *c*- or *t*-ZrO_2 correspond effectively to *t*-ZrO_2.

Although some rounded *m*-ZrO_2 grains were identified in the coat surrounded by a glassy phase(Figure 6.19a), most of the identified *m*-ZrO_2 appeared as twinned particles (Figure 6.20, 6.21). The *m*-ZrO_2 twins are produced during the *t*→ *m*-ZrO_2 transformation. These *m*-ZrO_2 twins are formed in enclosed grains while unconstrained grains could be transformed into a single orientation. Mosaics of *m*-ZrO_2 were also observed displaying internal twins and slip planes (Figure 6.22, 6.23). Microcracks were observed in the interface of the *m*-ZrO_2 twin/matrix (Figure 6.21a), they release the stress concentrated in this zone. The concentration of titanium in *m*-ZrO_2 was lower than in *c*- or *t*-ZrO_2. Heavier twining was found in *m*-ZrO_2 particles with a lower titanium concentration (Figure 6.21a, 6.23c).

Undissolved TiO_2 was identified as rounded grains surrounded by an amorphous phase (Figure 6.18a). Small amounts of zirconium and yttrium identified by EDS (Figure 6.18b) must be located in the amorphous phase. These observations coincide with those obtained by SEM where phases with different titanium concentrations were identified (Section 5.2.2).

6 .2 .3 Thermally Treated ZrO_2-Y_2O_3-TiO_2 Coat

Similar elements observed in the as-sprayed coat were found in the coat thermally treated at 1400 and 1600 °C for 24 hours. Although it was possible to detect some porous agglomerates as described for ZrO_2-Y_2O_3 previously (Section 6.2.1), "ripening" of the microstructure could be identified. Faceted rather than rounded grains were mostly observed (Figures 6.26-6.27a). The strength of coating must have been improved by the clean grain boundaries of these faceted grains. Intragranular microcracks were observed (Figure 6.27a) instead of the intergranular described above (Section 6.2.2). However, increasing the rigidity of the coat would be expected to decrease the ability of the coat to dissipate thermal stresses.

Twinned *t*-ZrO_2 particles were also observed in the coat treated at 1400 °C (Figure 6.28a). Fan and Chen (1995) showed that in the stress-free state, a cubic phase transforms to a single-domain *t'*-phase through intermediate tweed and twin structures, whereas in a clamped condition (i.e. a constrained grain), the twin structure is stable. Hence, the observed *t*-ZrO_2 twins, corresponding to non-transformable *t*-ZrO_2, must be a result of the $c \rightarrow t$ transformation in a clamped condition; the original grain must have been under stress by the polycrystalline structure of the coat. In previous observations of the *t*-ZrO_2 phase, single domain or mottled microstructures were observed. A relatively high concentration of titanium was found associated with *t*-ZrO_2 twins. Laths of *m*-ZrO_2 product of the $t \rightarrow m$-ZrO_2 transformation, as described above (Section 6.2.2), were identified in the coat heated at 1400 °C (Figure 6.29a).

Contrasting features could be observed in the coat heated at 1600 °C. On the one hand, large grains (> 200 nm in diameter) with large amorphous grain boundaries pockets (about 100 nm) product of coalescence of smaller grains were observed (Figure 6.30a). On the other hand, microporous "sponge-like" microstructures, probably originated from gases initially entrapped, were also observed (Figure 6.30b).

Twined *m*-ZrO_2 particles exhibiting slip planes and internal twining were also observed in the coat heated at 1600 °C (Figure 6.31). *t*-ZrO_2 particles with different microstructures such as agglomerates (Figure 6.32a) with a lower titanium concentration compared to that found in the *t*-ZrO_2 twins, and equiaxed nanograins (Figure 6.33a) were observed.

6 .2 .4 ZrO_2-Y_2O_3-TiO_2 Sintered Bodies

The microstructure of the ZrO_2-Y_2O_3-TiO_2 pressed powder sintered at 1350 °C presented clean-boundary faceted grains larger than those found in the ZrO_2-Y_2O_3-TiO_2 coat. A higher strength is associated with the sintered body than the coat, however a smaller ability to accommodate thermal stresses is also associated with the sintered body since rigidity is increased. No evidence of *t*-ZrO_2 mottled microstructure or twins was found. This agrees with the fact that non-transformable *t*-ZrO_2 is not expected as the thermal history of the sintered body is completely different from the plasma sprayed coat. Twinned *m*-ZrO_2 particles were also found in the ZrO_2-Y_2O_3-TiO_2 sintered body which are produced during the $t \rightarrow m$-ZrO_2 transformation as explained for the ZrO_2-Y_2O_3-TiO_2 coat (Section 6.2.2).

6 .3 TABLES AND FIGURES

Table 6.1 Lattice parameters for cubic, tetragonal and monoclinic ZrO_2 used in the electron diffraction pattern indexing

Phase	Lattice Parameter	JCPDS (ref.)
cubic	a = 5.09	27-997
tetragonal	a = 5.12, c = 5.25	17-923
monoclinic	a = 5.14, b = 5.21, c = 5.31, β = 99.2	36-420

Table 6.2 X-ray lines of zirconium, yttrium and titanium used in the microanalysis

Element	Line	Energy (keV)
Zr	Kα	15.73
	Kβ	17.66
	Lβ	2.19
Y	Kα	14.92
	Kβ	16.72
	Lβ	2.06
Ti	Kα	4.51
	Kβ	4.95

Figure 6.1 (***a***) Bright field TEM micrograph of a ZrO_2-Y_2O_3 plasma sprayed coat, showing a very porous microstructure and a small particle size, in the order of 20nm. (***b***) Electron microdiffraction pattern obtained from the area of the specimen shown in (***a***). The diffuse ring indicates the amorphous nature of some particles. The orientation $[\bar{1}12]$ of the specimen to the electron beam, shown in this pattern, does not allow discrimination between *c*- and ***t***-ZrO_2. Bar = 50nm.

Figure 6.2 (***a***) Bright field TEM micrograph of a ZrO_2-Y_2O_3 plasma sprayed coat at a higher magnification. It shows the same porous microstructure shown in Figure 6.1a. Bar = 20nm. (***b***) Electron microdiffraction pattern obtained from the area of the specimen shown in (***a***). The orientation $[011]$ of the specimen does not allow discrimination between the *c*- and ***t***-ZrO_2.

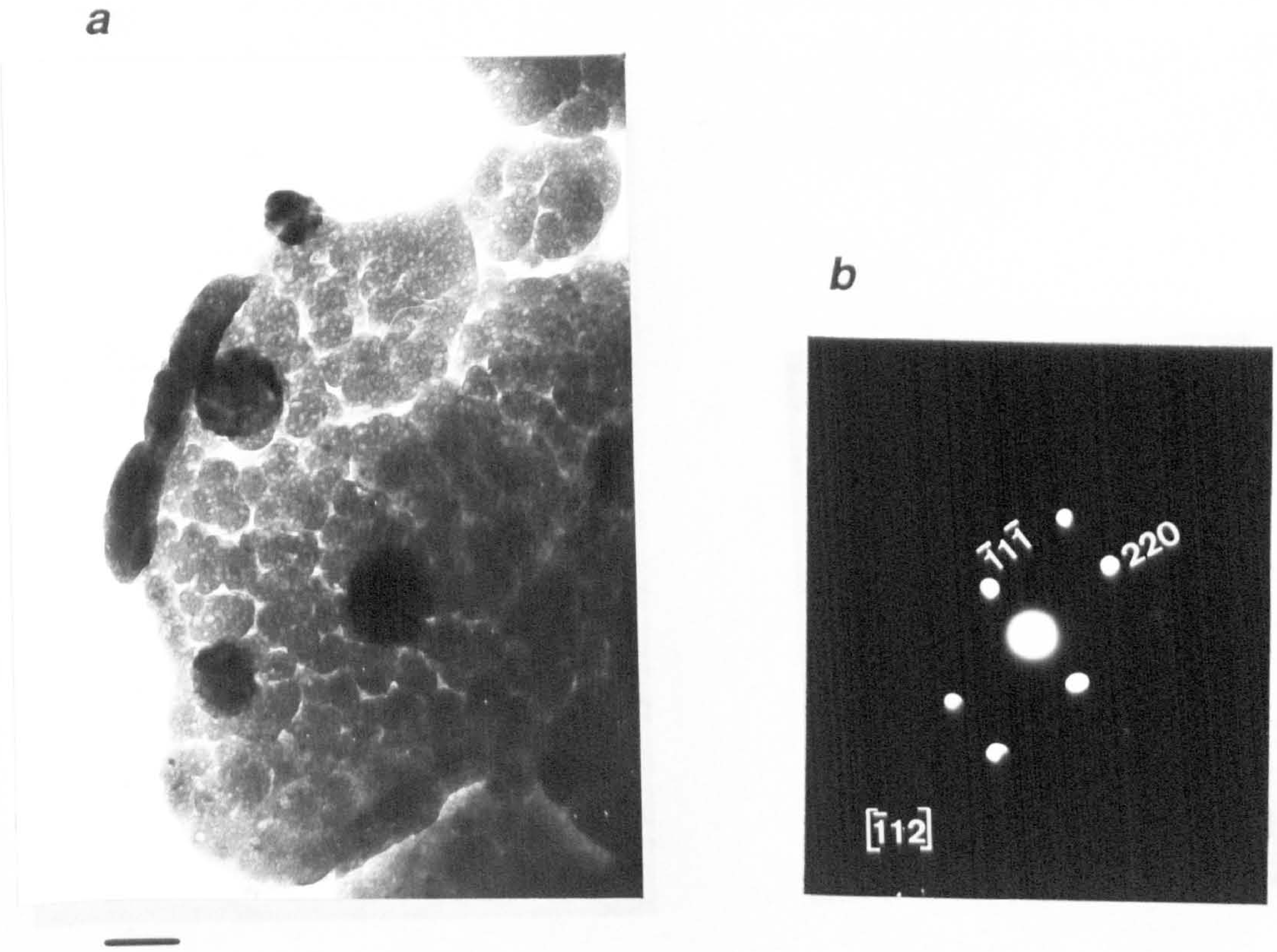
a
b
$\bar{1}1\bar{1}$
220
[$\bar{1}12$]

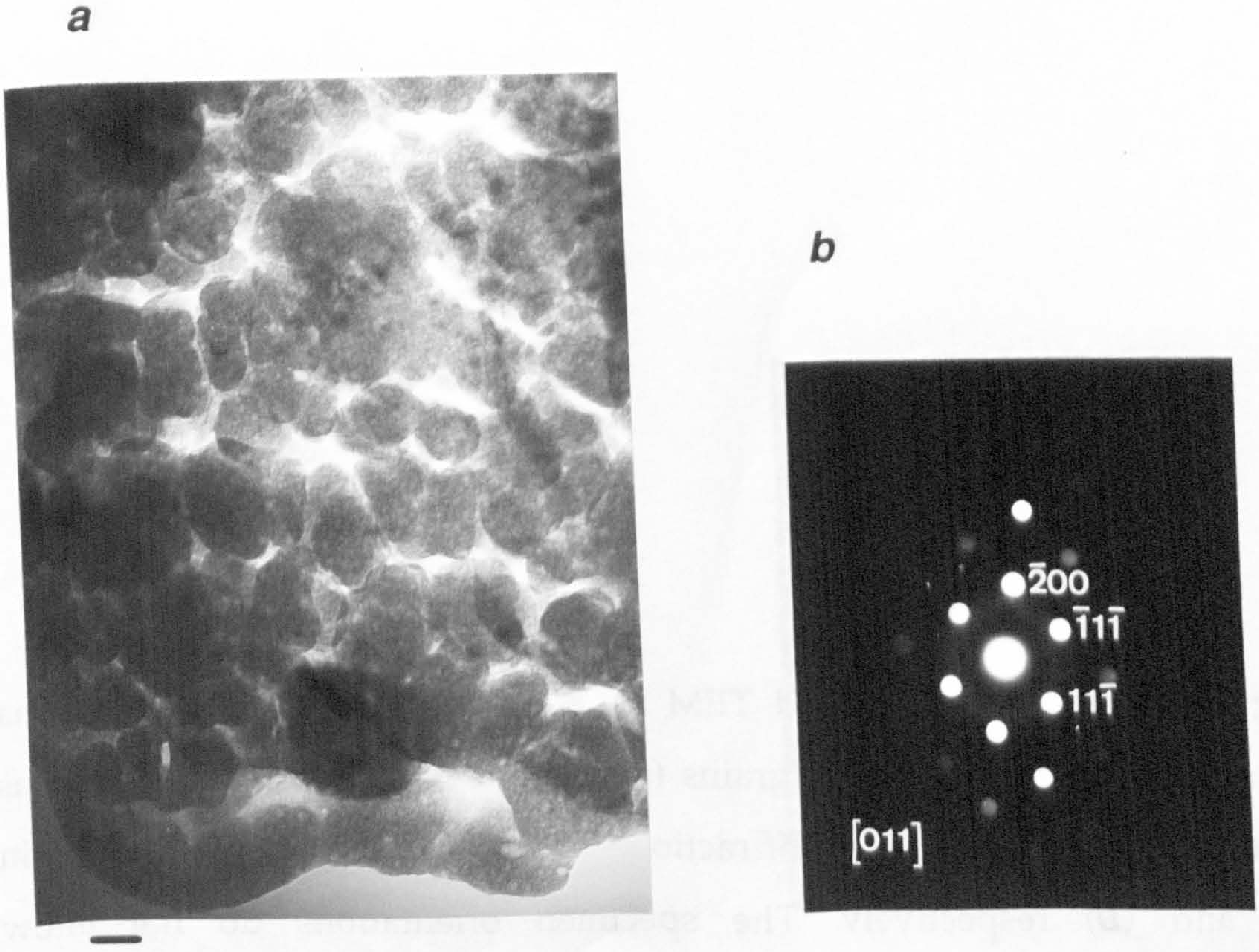
a
b
$\bar{2}00$
$\bar{1}1\bar{1}$
$11\bar{1}$
[011]

Figure 6.3 (***a, b***) Bright field TEM micrographs of a ZrO_2-Y_2O_3 plasma sprayed coat. Some faceted grains (> 100nm) have grown in the porous matrix. (***c, d***) Electron microdiffraction patterns of the new grains shown in (***a***) and (***b***) respectively. The specimen orientations do not allow discrimination between the *c*- and *t*-ZrO_2 symmetries. Bar = 50nm.

a

c

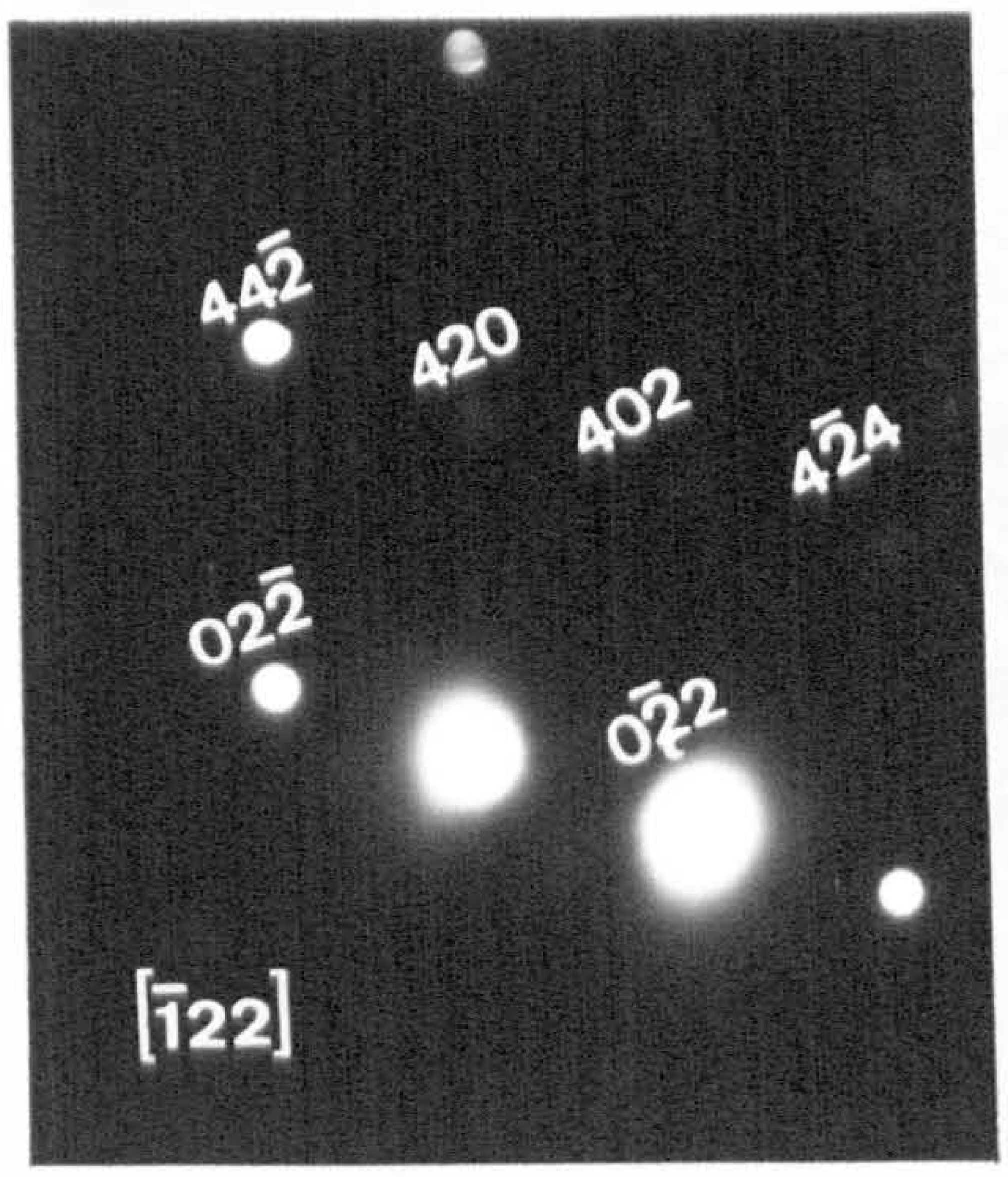
$44\bar{2}$
420
402
$4\bar{2}4$
$02\bar{2}$
$0\bar{2}2$
$[\bar{1}22]$

b

d

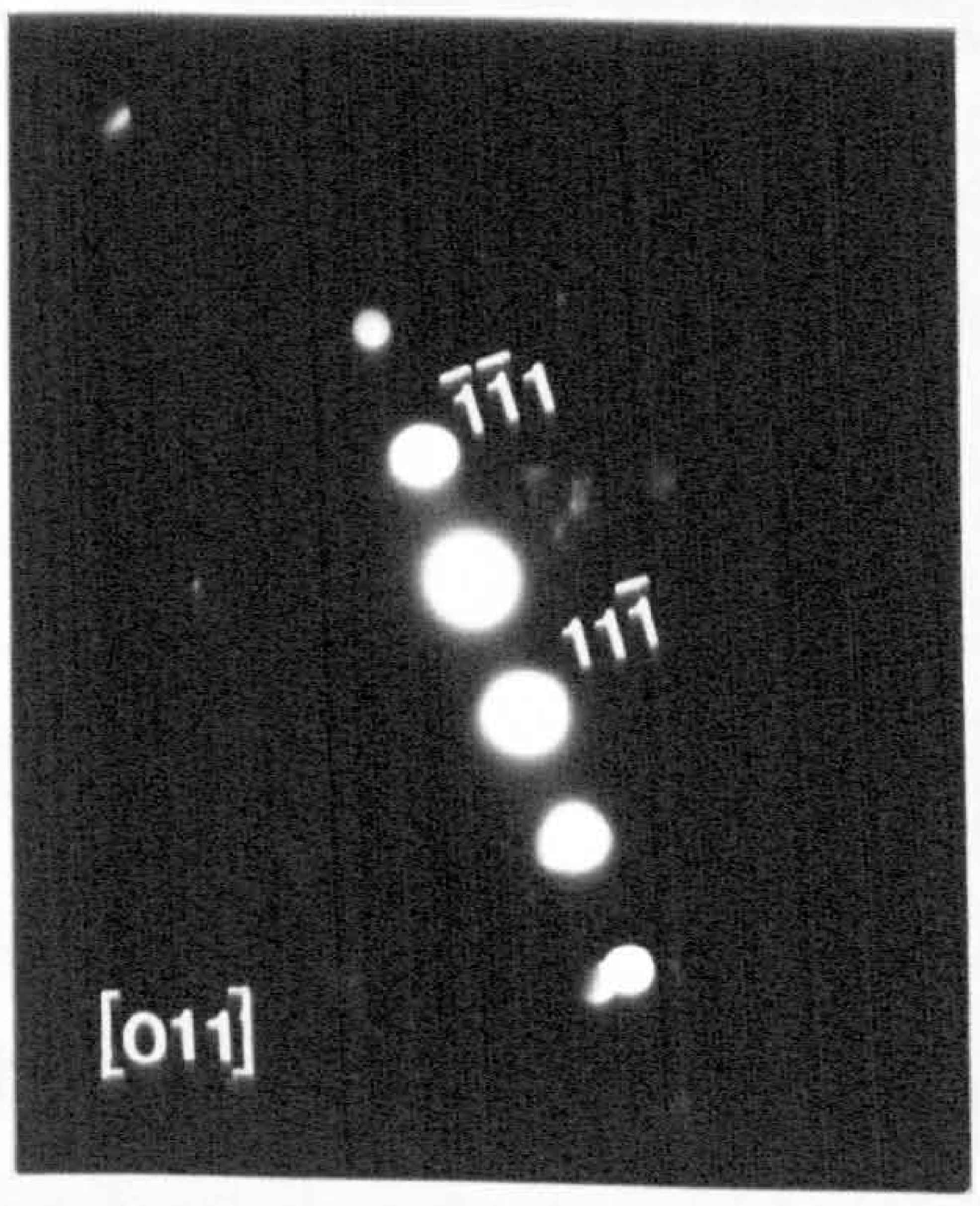
$\bar{1}\bar{1}1$
$11\bar{1}$
[011]

Figure 6.4 (***a***) Bright field TEM micrograph of a ZrO_2-Y_2O_3 plasma sprayed coat. The dark grains (arrowed) have *t*-ZrO_2 symmetry as revealed by the *(odd, even, even)* reflections shown in the electron microdiffraction pattern (***b***) which are not allowed for the *c*-ZrO_2 symmetry. Bar = 20nm.

Figure 6.5 (***a***) Bright field TEM micrograph of a ZrO_2-Y_2O_3 plasma sprayed coat, showing dark *t*-ZrO_2 grains (arrow) in a *c*-ZrO_2 porous matrix, as identified in (***b***) the selected area diffraction pattern. The intense spots correspond to reflections from the *c*- and *t*-ZrO_2 while the lighter spots, *(even, odd, odd)* reflections, are only attributed to *t*-ZrO_2. Bar = 50nm.

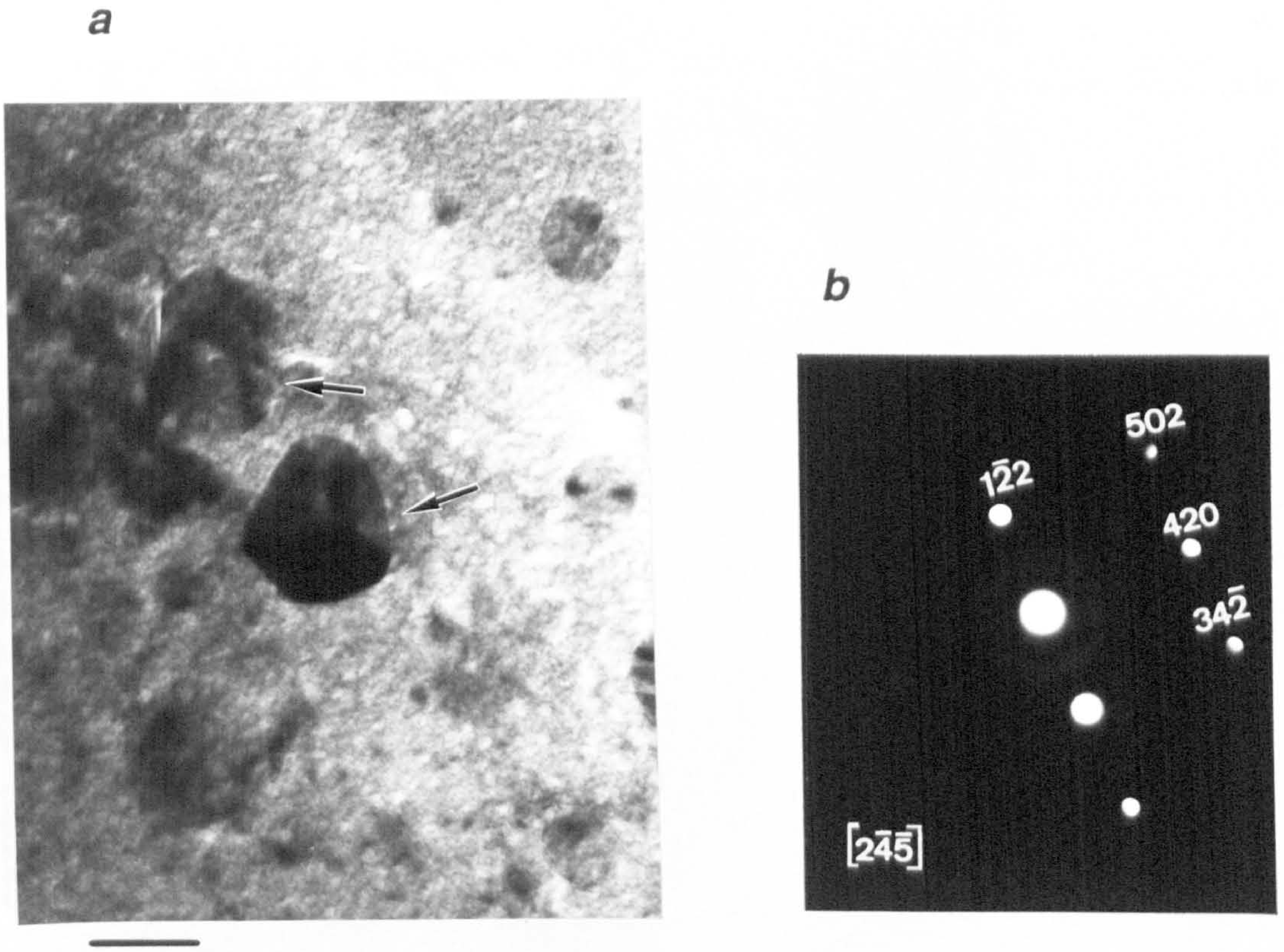
a
b
$1\bar{2}2$
502
420
$34\bar{2}$
[$2\bar{4}\bar{5}$]

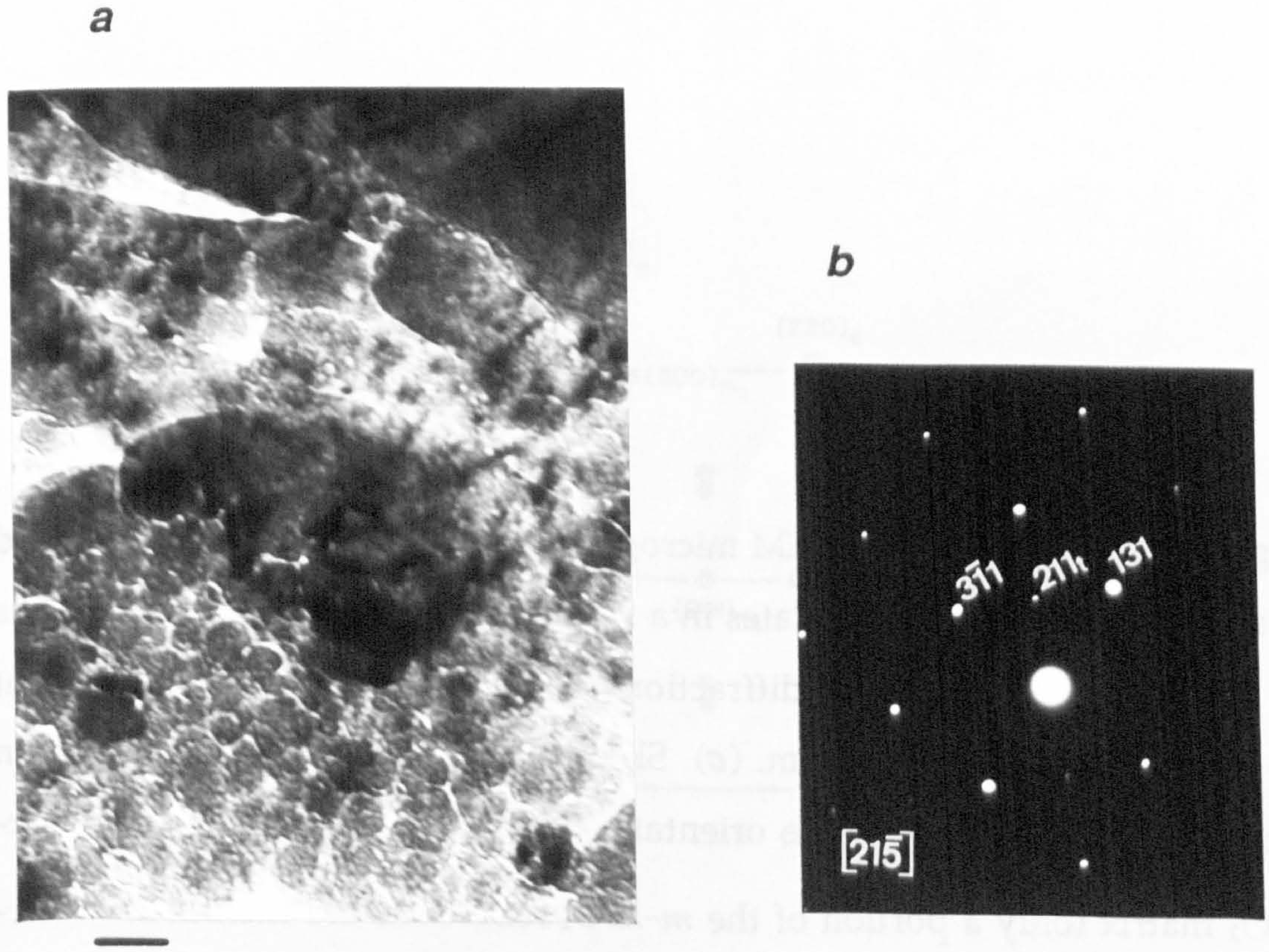
a
b
$3\bar{1}1$
211t
131
[$21\bar{5}$]

Figure 6.6 (***a***) Bright field TEM micrograph of a ZrO_2-Y_2O_3 plasma sprayed coat showing *m*-ZrO_2 precipitates in a matrix of *c*- or *t*-ZrO_2 rounded grains as shown in (***b***) the electron diffraction pattern. A and A* indicate different *m*-ZrO_2 variants. Bar = 100nm. (***c***) Sketch showing the diffraction pattern interpretation involving three orientations of *m*-ZrO_2 grains within the *c*-ZrO_2 matrix (only a portion of the *m*-ZrO_2 reflections are included). ● = *c*-ZrO_2 reflection, • = *m*-ZrO_2 reflection (after Bansal and Heuer, 1975).

a

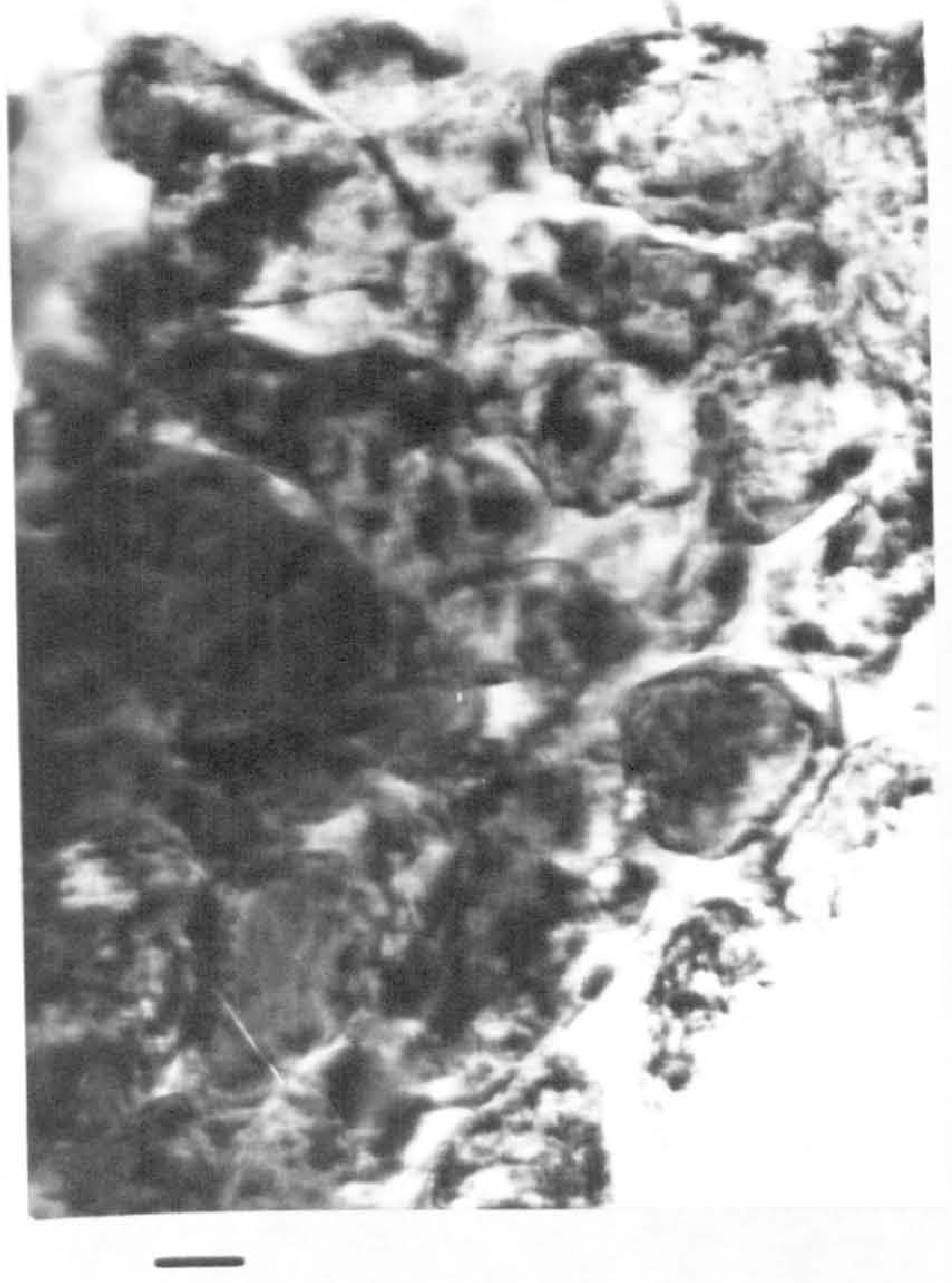

b

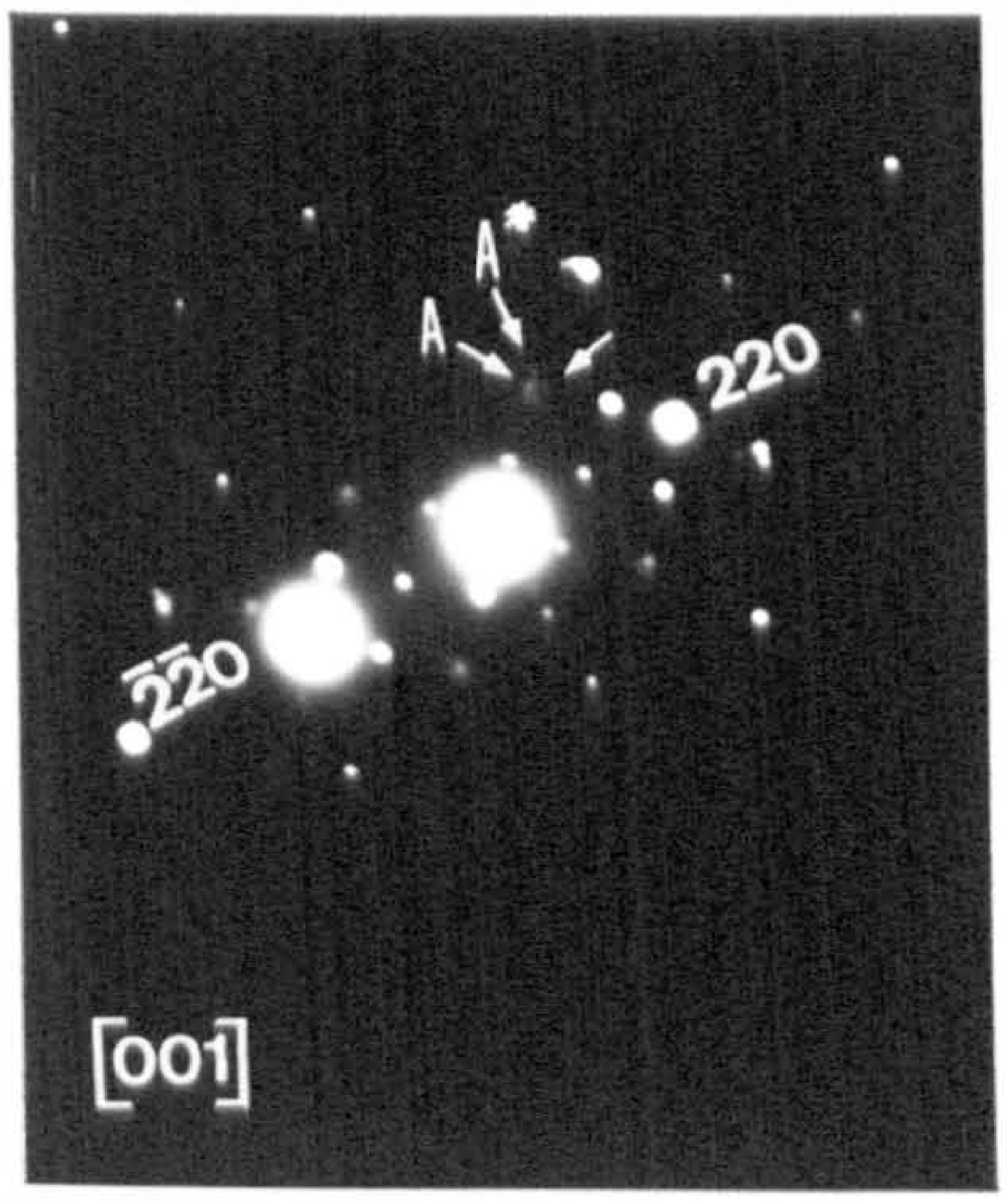
A*
A
220
$\bar{2}\bar{2}0$
$[00\bar{1}]$

c

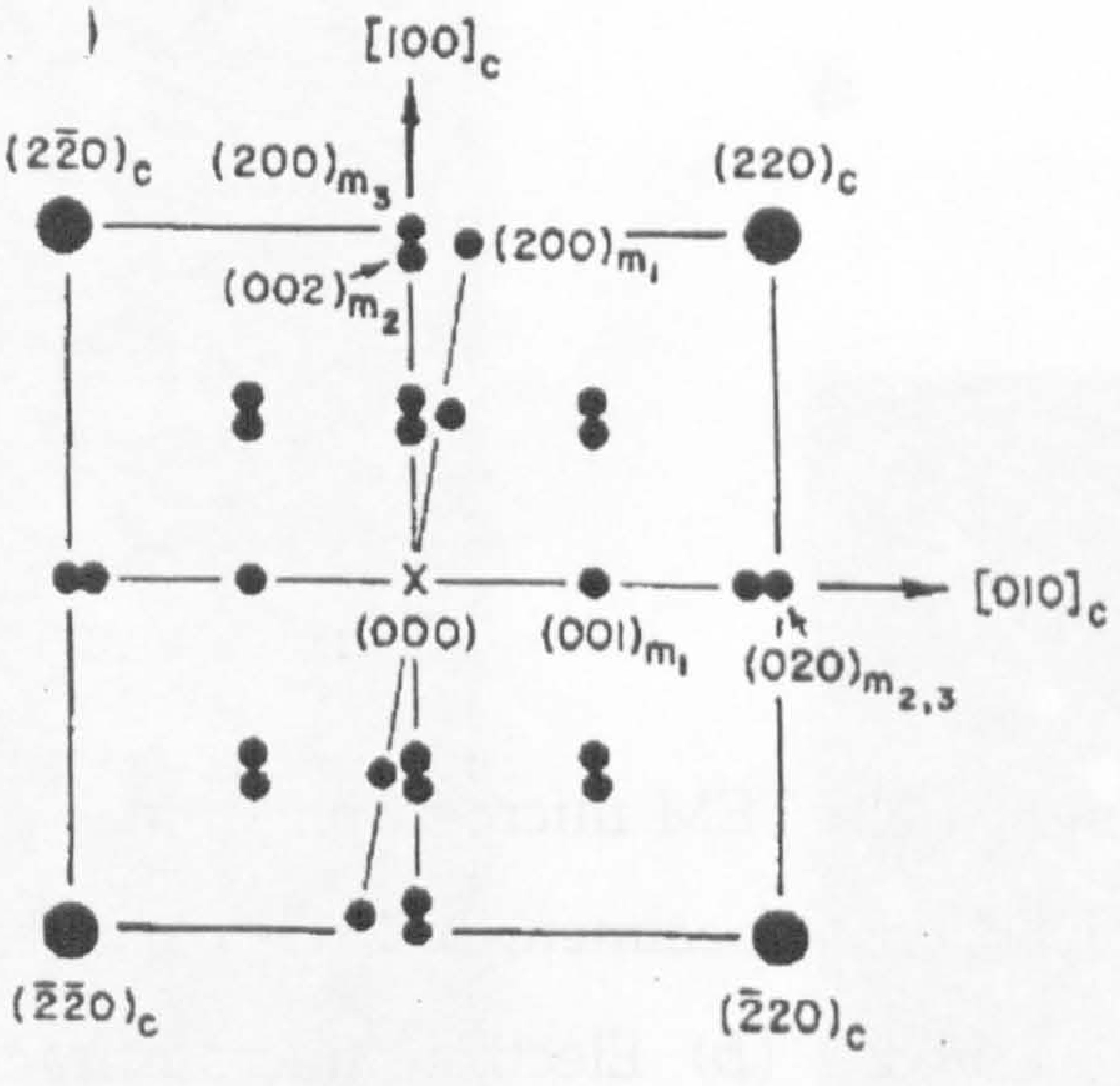
$[100]_c$
$(2\bar{2}0)_c$
$(200)_{m_3}$
$(220)_c$
$(200)_{m_1}$
$(002)_{m_2}$
$[010]_c$
(000)
$(001)_{m_1}$
$(020)_{m_{2,3}}$
$(\bar{2}\bar{2}0)_c$
$(\bar{2}20)_c$

Figure 6.7 (***a***) Bright field TEM micrograph from a powdered ZrO_2-Y_2O_3-TiO_2 plasma sprayed coat specimen; *m*-ZrO_2 laths are observed in a border of a big grain showing Moirè contrast. (***b***) Electron microdiffraction patterns of (***a***). (***c***) EDS of specimen shown in (***a***). A, and A* arrows indicate different *m*-ZrO_2 lath orientations. Bar = 50nm

Figure 6.8 (***a***) Bright field TEM micrograph from a powdered ZrO_2-Y_2O_3-TiO_2 plasma sprayed coat specimen; *m*-ZrO_2 particles grown in different directions are observed. (***b***) Electron microdiffraction pattern of (***a***). Rotation effect has not been corrected. A and A* arrows indicate the different directions of growing. Bar = 50nm.

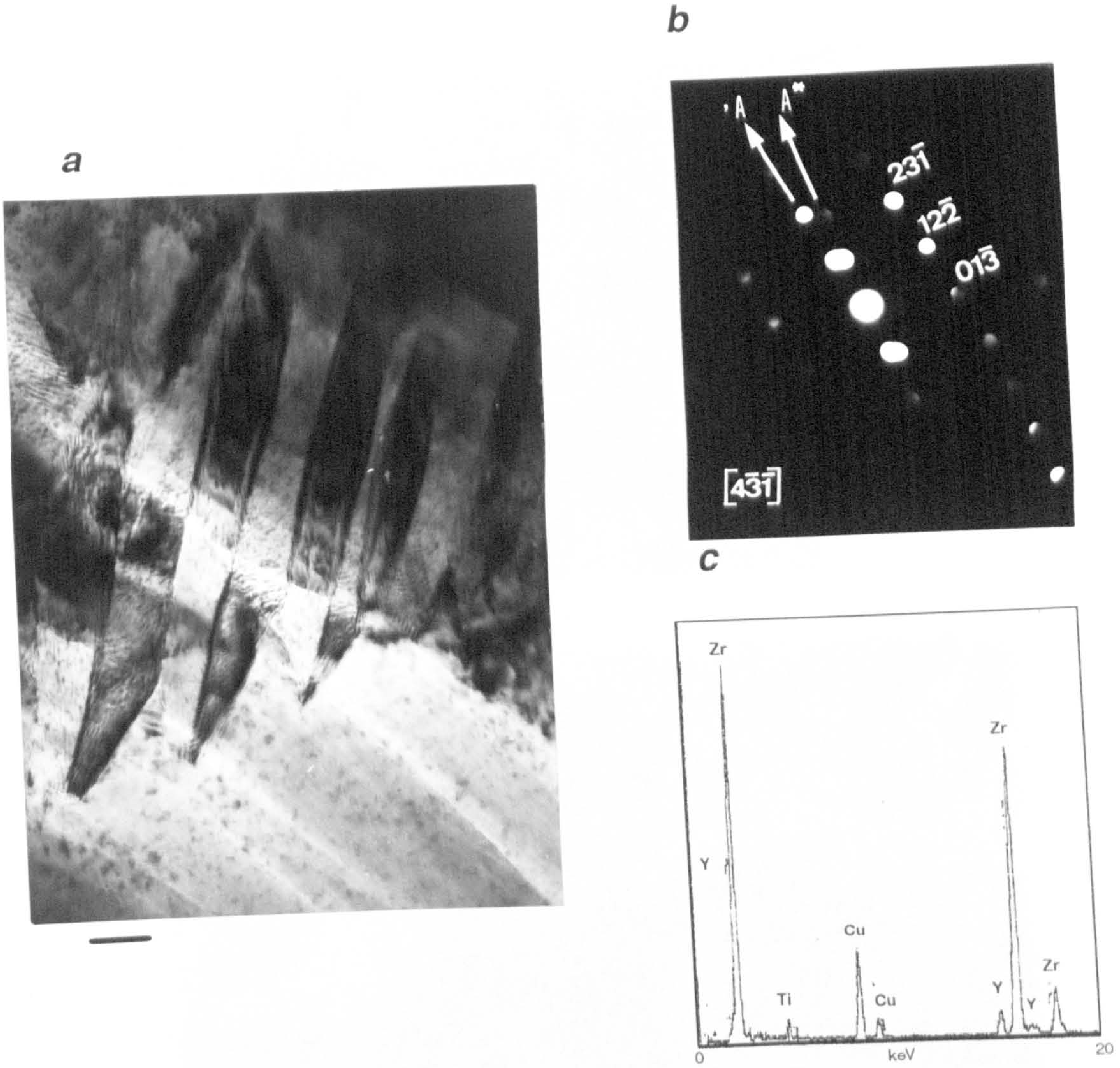
a
b
A
A*
$23\bar{1}$
$12\bar{2}$
$01\bar{3}$
$[4\bar{3}\bar{1}]$
c
Zr
Y
Zr
Cu
Ti
Cu
Y
Y
Zr
0
keV
20

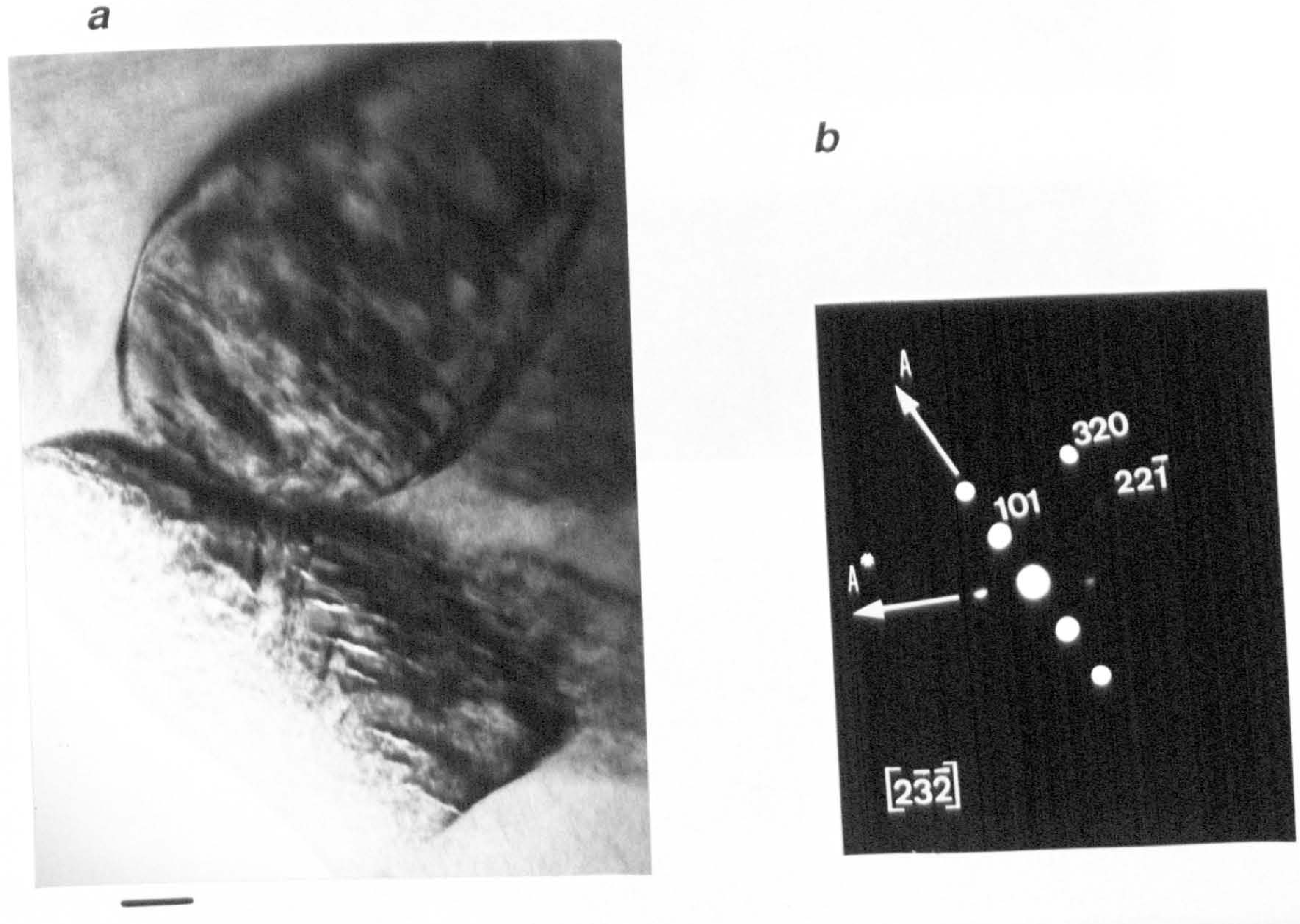
a
b
A
320
101
$22\bar{1}$
A*
$[2\bar{3}\bar{2}]$

Figure 6.9 Transverse SEM micrographs of a ZrO_2-Y_2O_3-TiO_2/NiCrCoAlY plasma sprayed coating specimen thinned by ion beam etching. (***a***) Arrangement of two coating cross-sections after etching; (***b***) closer view showing the ceramic and bond coats and the substrate; (***c***) interface substrate-bond coat. S = substrate, B = bond coat, C = ceramic coat, Cu = copper grid.

a

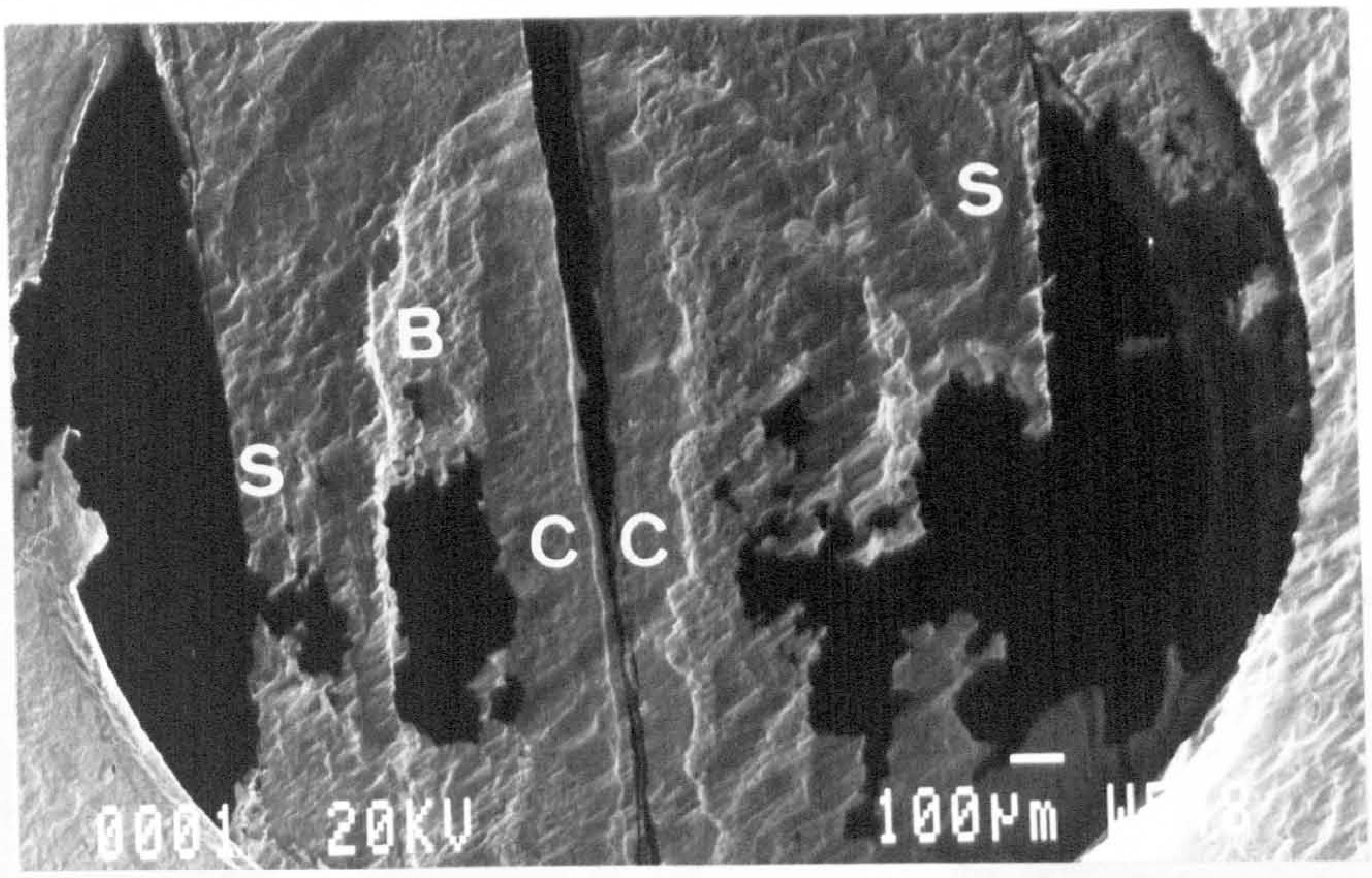
S
B
S
C
C
0001 20KV
100μm WD48

b

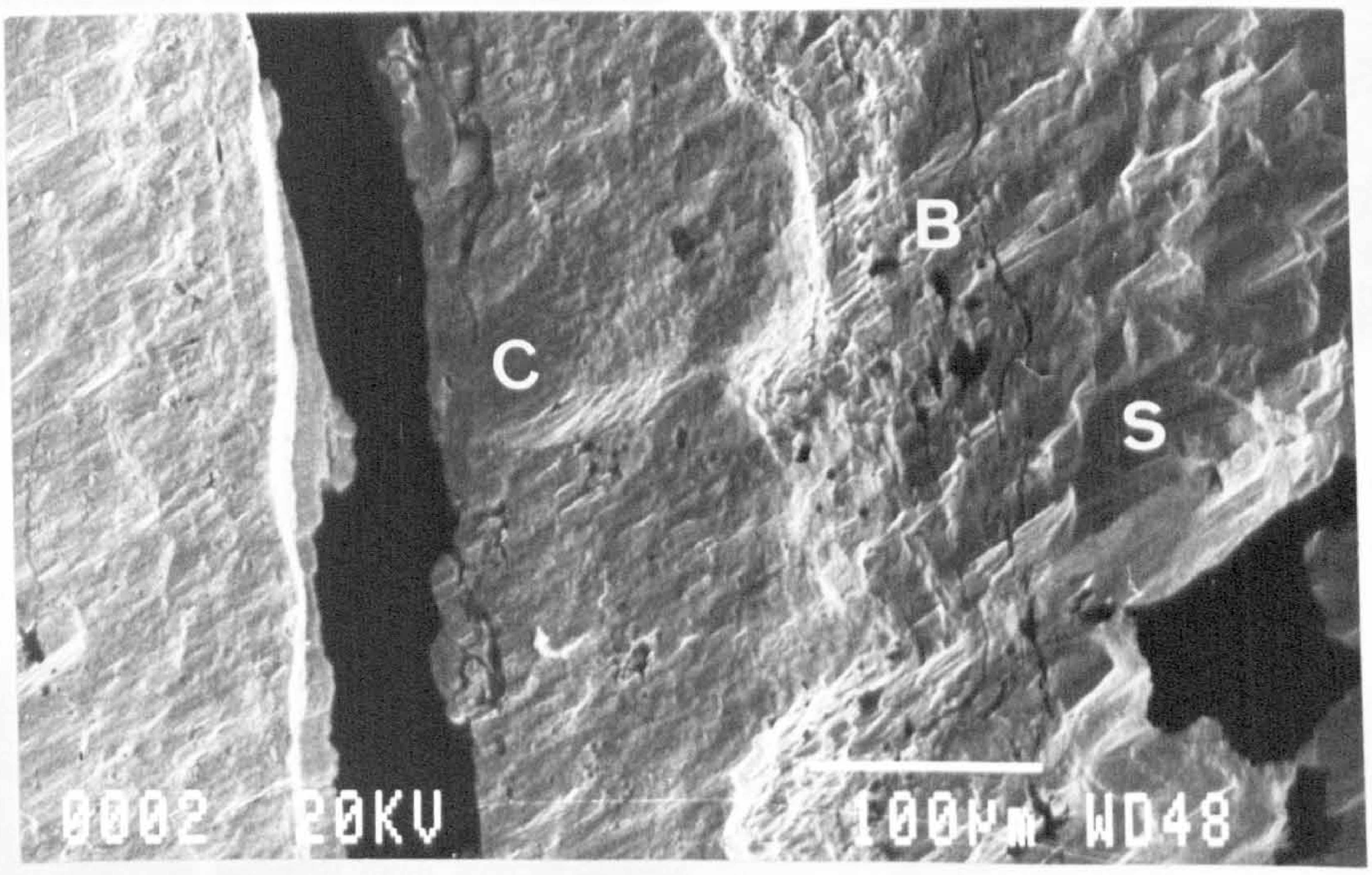
B
C
S
0002 20KV
100μm WD48

c

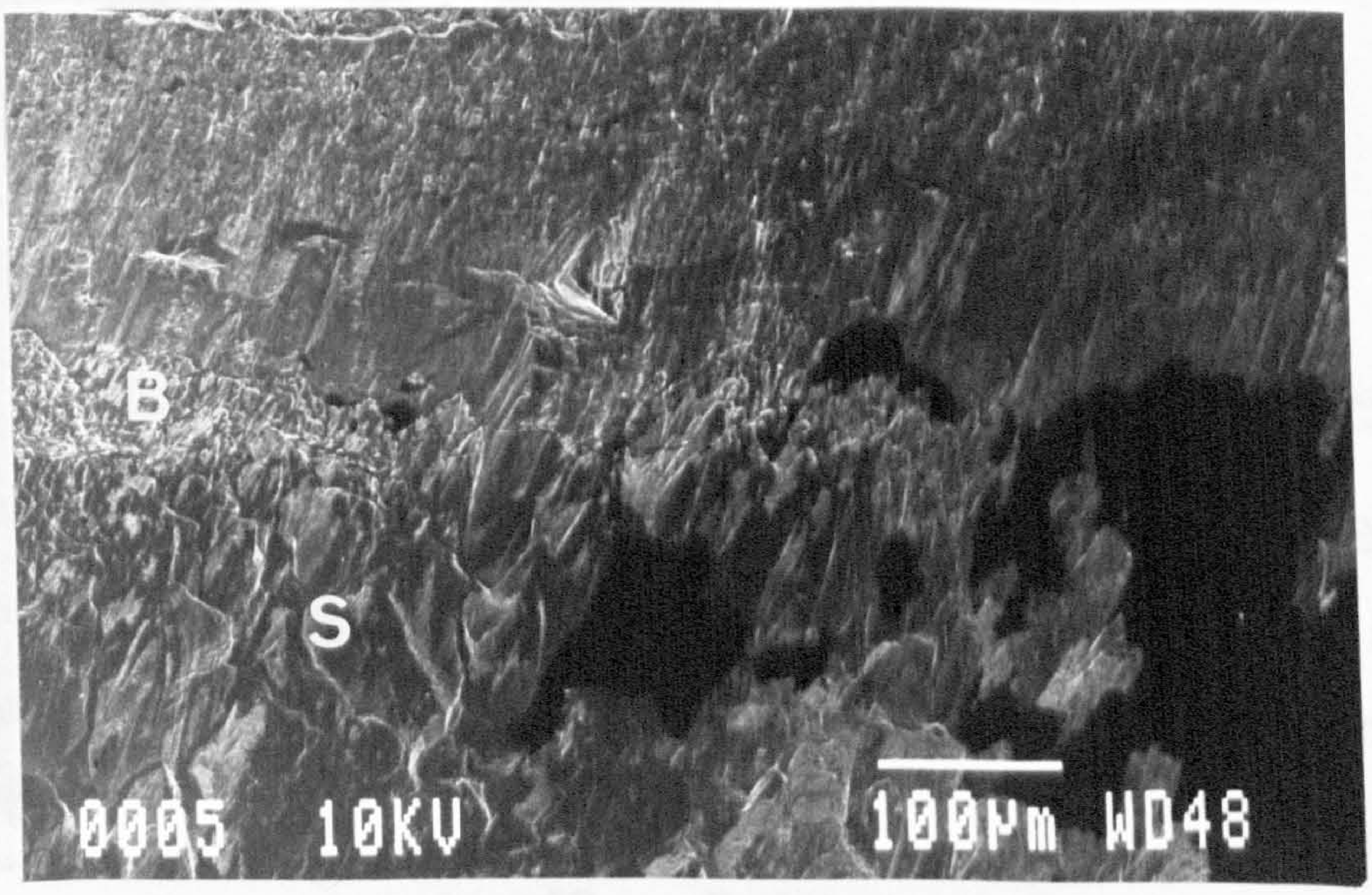
B
S
0005 10KV
100μm WD48

Figure 6.10 (***a***) Bright field TEM micrograph of a ZrO_2-Y_2O_3-TiO_2 plasma sprayed coating specimen prepared by ion beam etching of a planar section; (***b***) electron microdiffraction pattern allowed for *c*- and *t*-ZrO_2 symmetries; (***c***) dark field TEM micrograph of the specimen shown in (***a***) using $\vec{g} = 022$; (***d***) EDS of specimen shown in (***a***). Bar = 50nm.

a

b

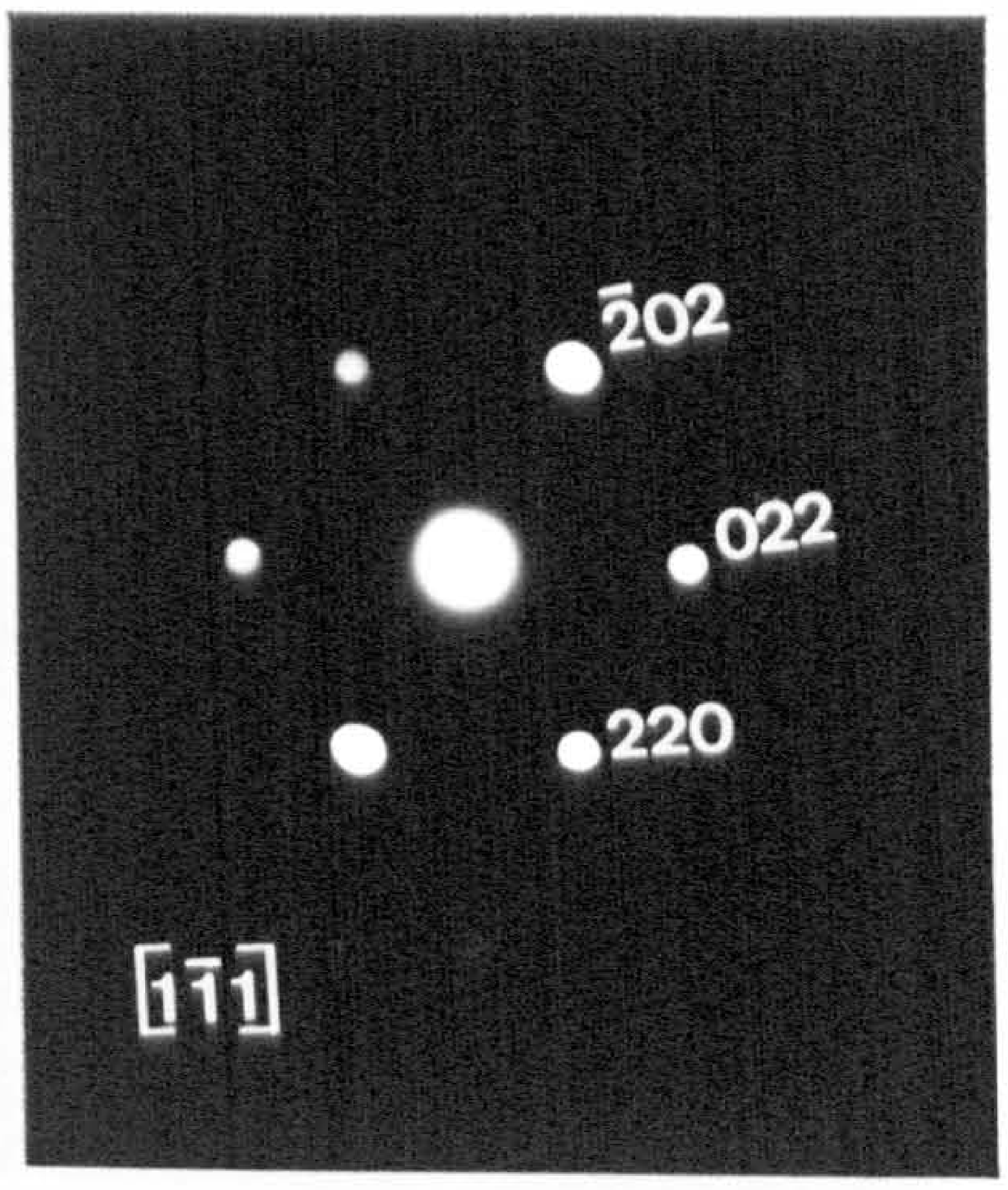
$\bar{2}02$
022
220
$[1\bar{1}1]$

c

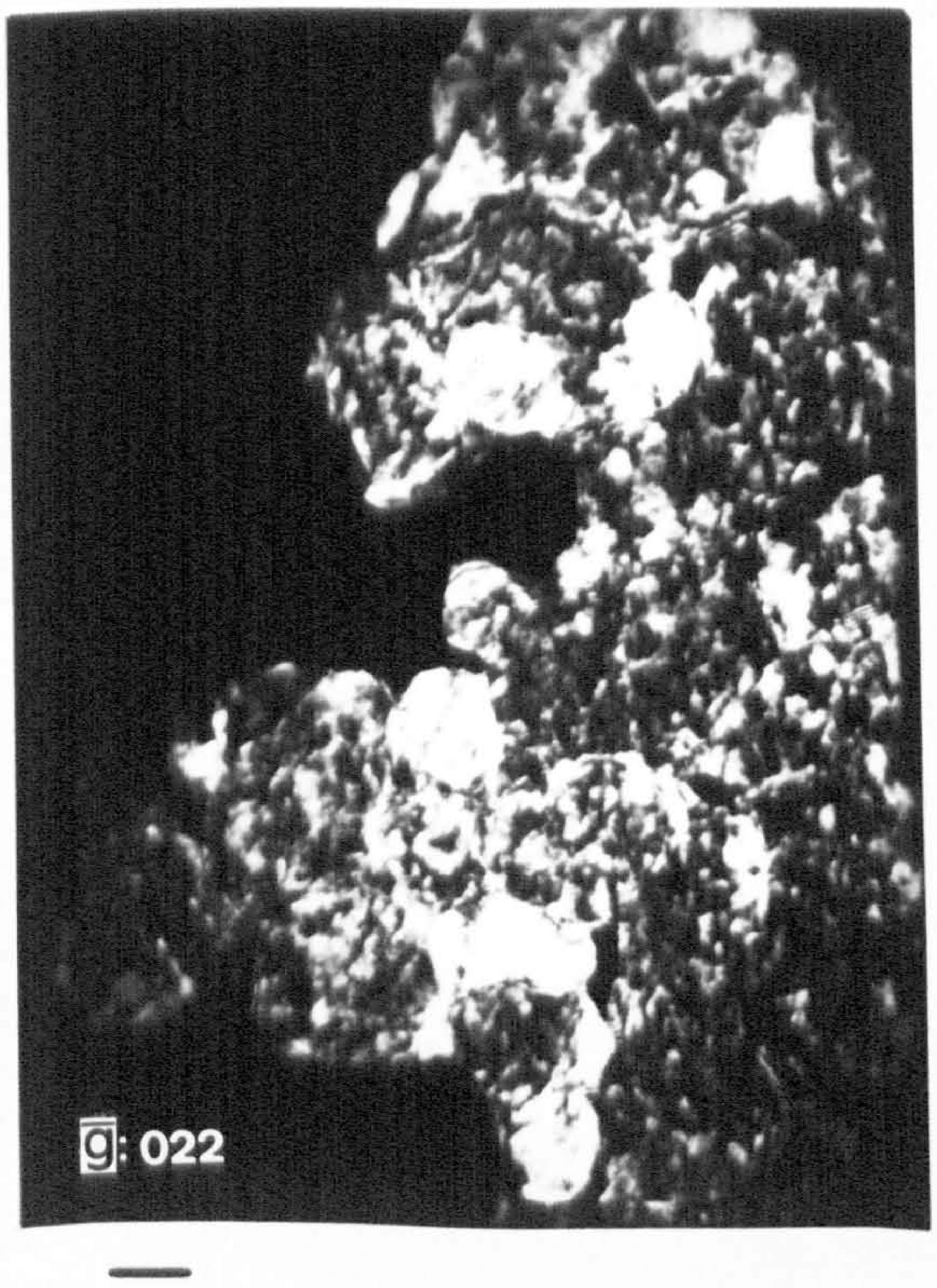
$\boxed{g}$: 022

d

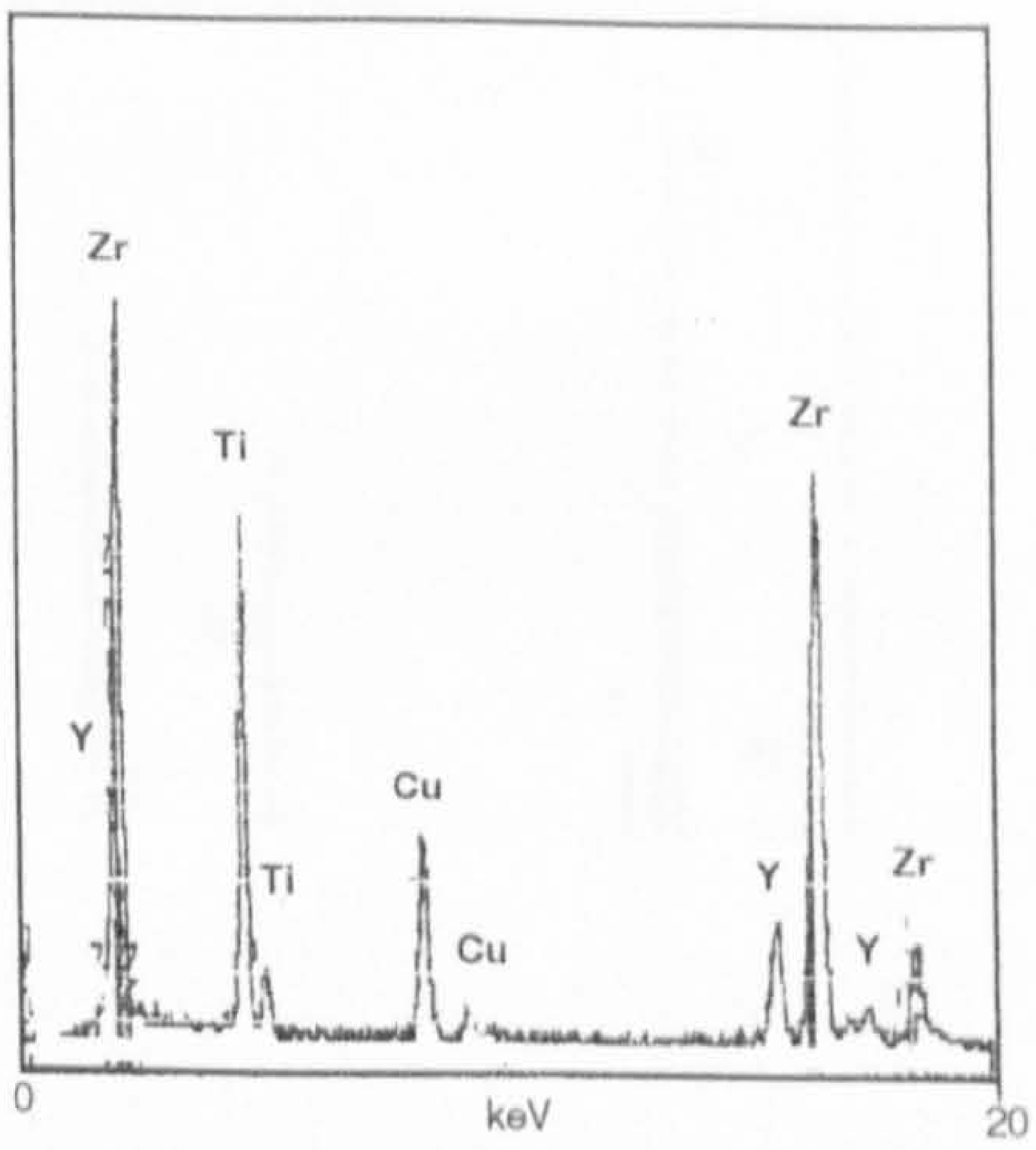
Zr
Ti
Zr
Y
Cu
Ti
Cu
Y
Zr
Y
0
keV
20

Figure 6.11 (***a***) Bright field TEM micrograph of a ZrO_2-Y_2O_3-TiO_2 plasma sprayed coating specimen prepared by ion beam etching (planar section), showing rounded grains > 50nm in diameter; (***b***) electron microdiffraction pattern of specimen shown in (***a***), specimen orientation allows no distinction between *c*- or *t*-ZrO_2; (***c***) dark field TEM micrograph of the same specimen area shown in (***a***) for $\vec{g}$ = 111, displaying a sub-grain "mottled " structure; (***d***) EDS of specimen shown in (***a***). Bar = 50nm.

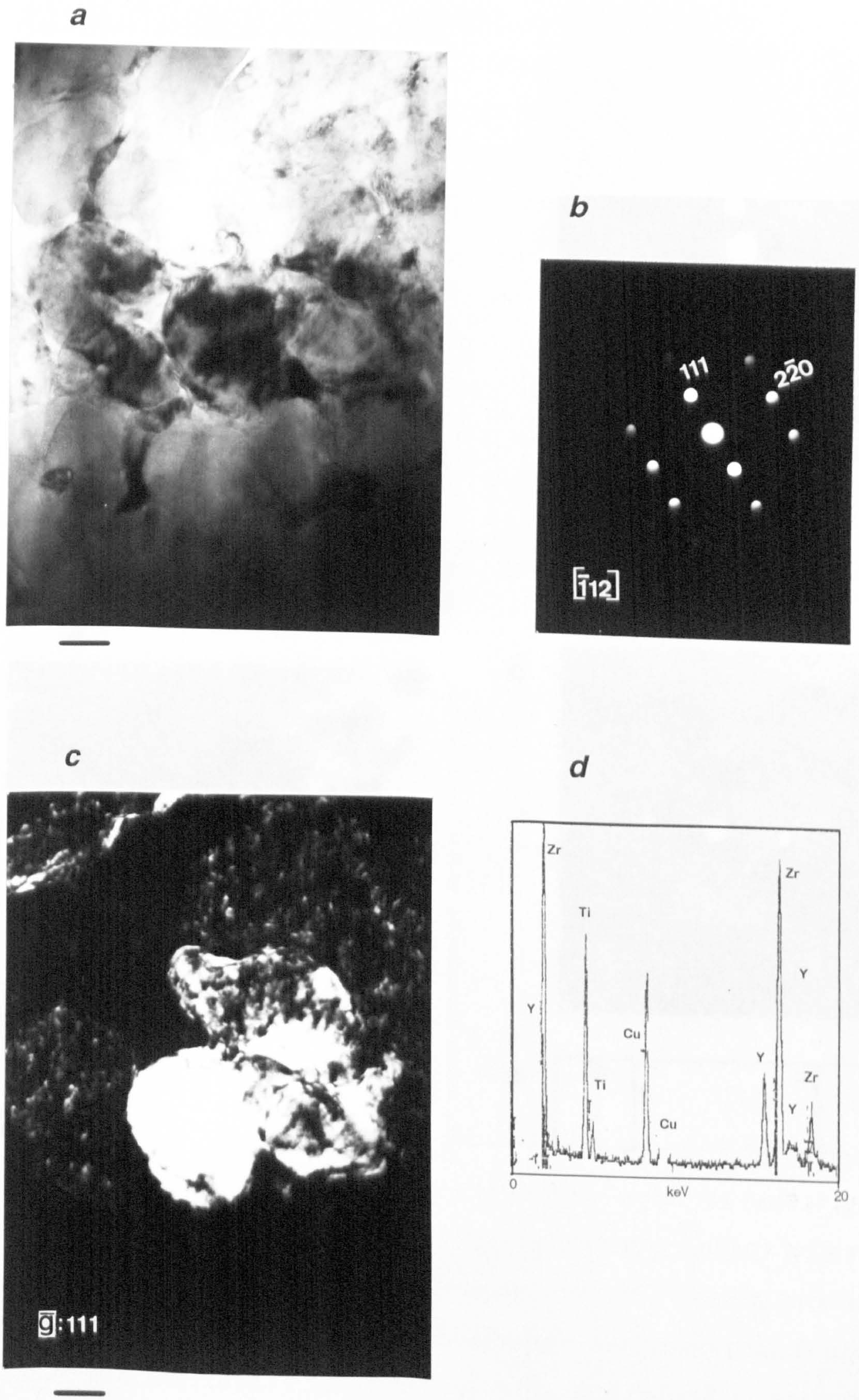
a
b
111
2$\bar{2}$0
[$\bar{1}$12]
c
$\bar{g}$:111
d
Zr
Ti
Y
Cu
Ti
Cu
Y
Zr
Y
Y
Zr
0
keV
20

Figure 6.12 (***a***) Bright field TEM micrograph of a ZrO_2-Y_2O_3-TiO_2 plasma sprayed coating specimen prepared by ion beam etching (cross-section), showing rounded grains > 50nm and an intergranular microcrack (arrows); (***b***) electron microdiffraction pattern of specimen shown in (***a***), shows reflections allowed for *c*- and *t*-ZrO_2. Bar = 50nm.

Figure 6.13 (***a***) Bright field TEM micrograph of a ZrO_2-Y_2O_3-TiO_2 plasma sprayed coating specimen prepared by ion beam etching (cross-section), showing grains > 50nm in diameter and intergranular porosity; (***b***) electron microdiffraction pattern of specimen shown in (***a***), the specimen orientation allows no distinction between *c*- or *t*-ZrO_2; (***c***) EDS of specimen shown in (***a***). Bar = 100nm.

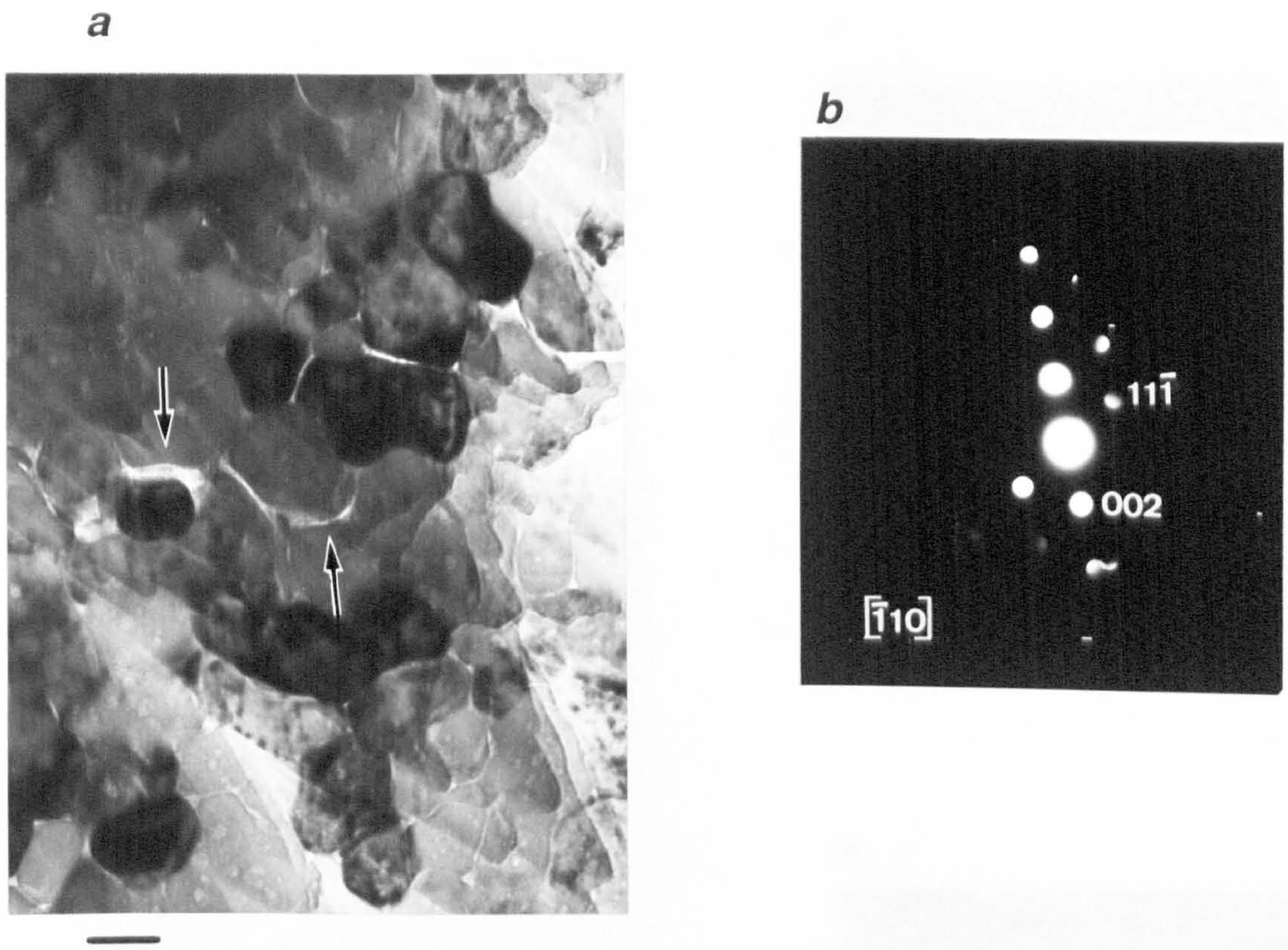
a
b
11$\bar{1}$
002
[$\bar{1}$10]

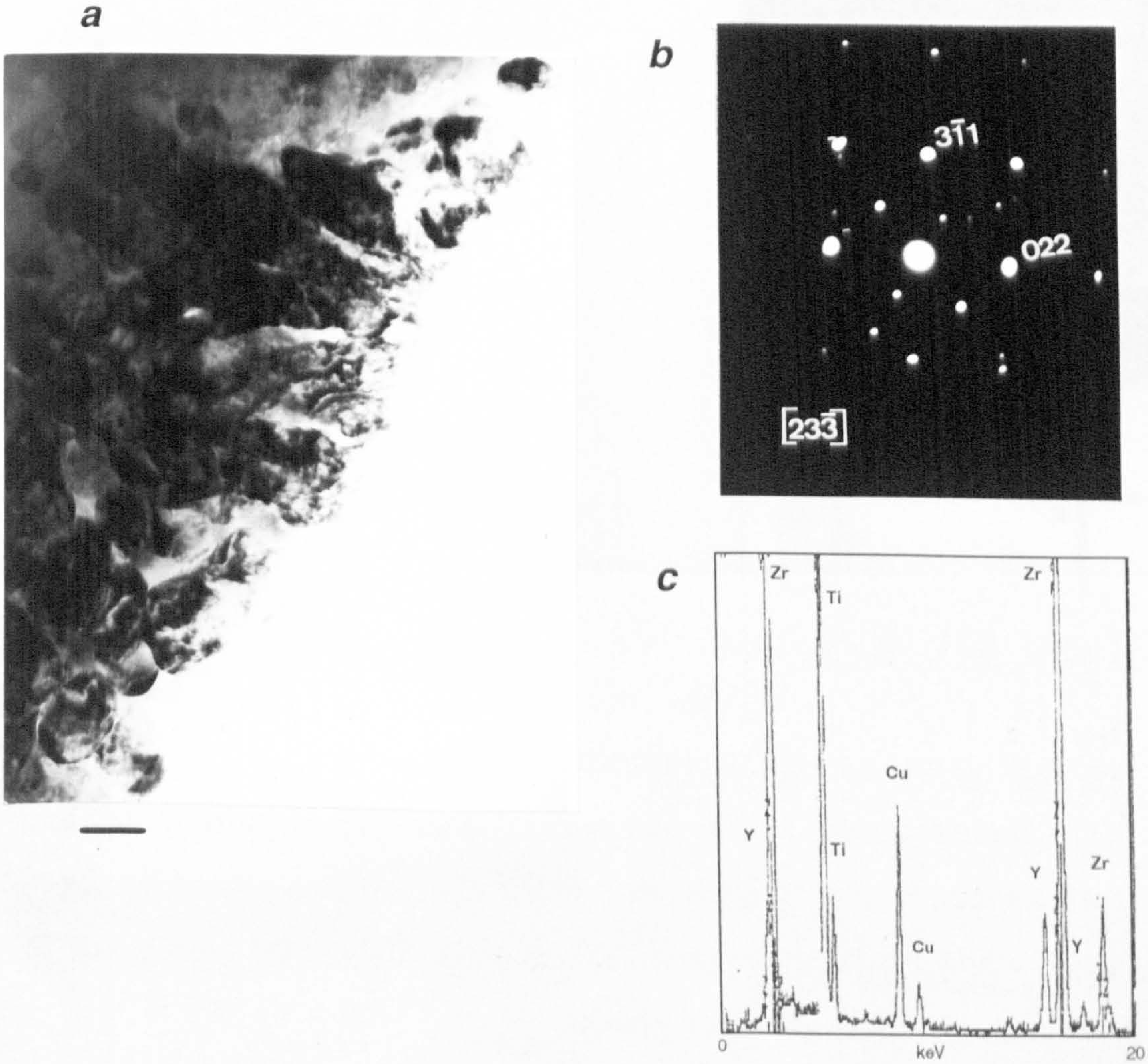
a
b
3$\bar{1}$1
022
[23$\bar{3}$]
c
Zr
Ti
Zr
Cu
Y
Ti
Y
Zr
Cu
Y
0
keV
20

Figure 6.14 (***a***, ***b***) Bright field TEM micrographs of a ZrO_2-Y_2O_3-TiO_2 plasma sprayed coating specimen prepared by ion beam etching (planar section), showing *t*-ZrO_2 precipitates (mottled structure) growing on a *c*-ZrO_2 matrix as seen in the electron microdiffraction patterns (***c***) and (***d***), respectively . Intense spots correspond to reflections caused by the *c*-ZrO_2 phase while lighter spots (arrowed) are only allowed for *t*-ZrO_2. (***e***) EDS of specimen shown in (***b***). Bars = 50nm.

a

b

c

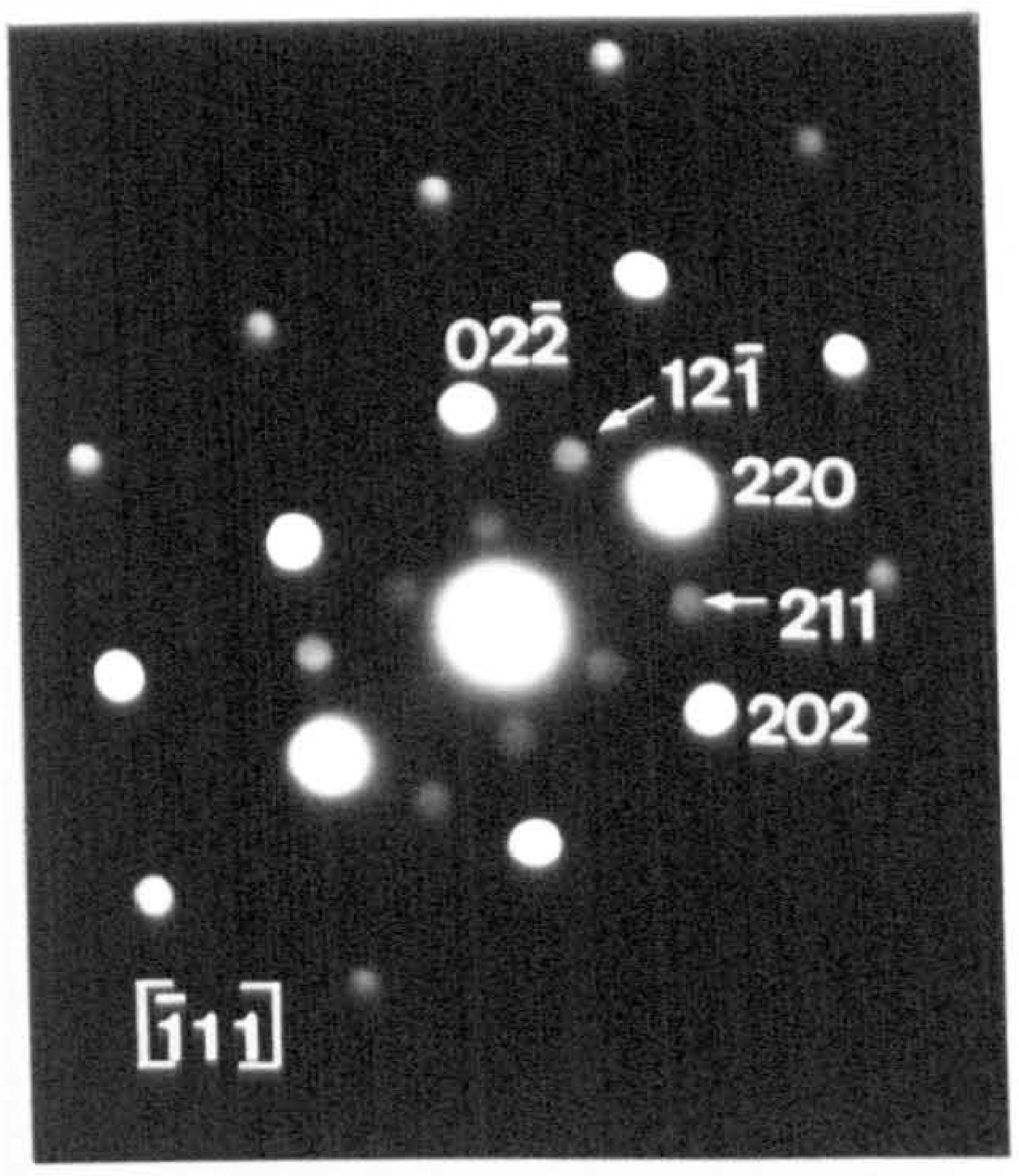
02$\bar{2}$
12$\bar{1}$
220
211
202
[$\bar{1}$11]

d

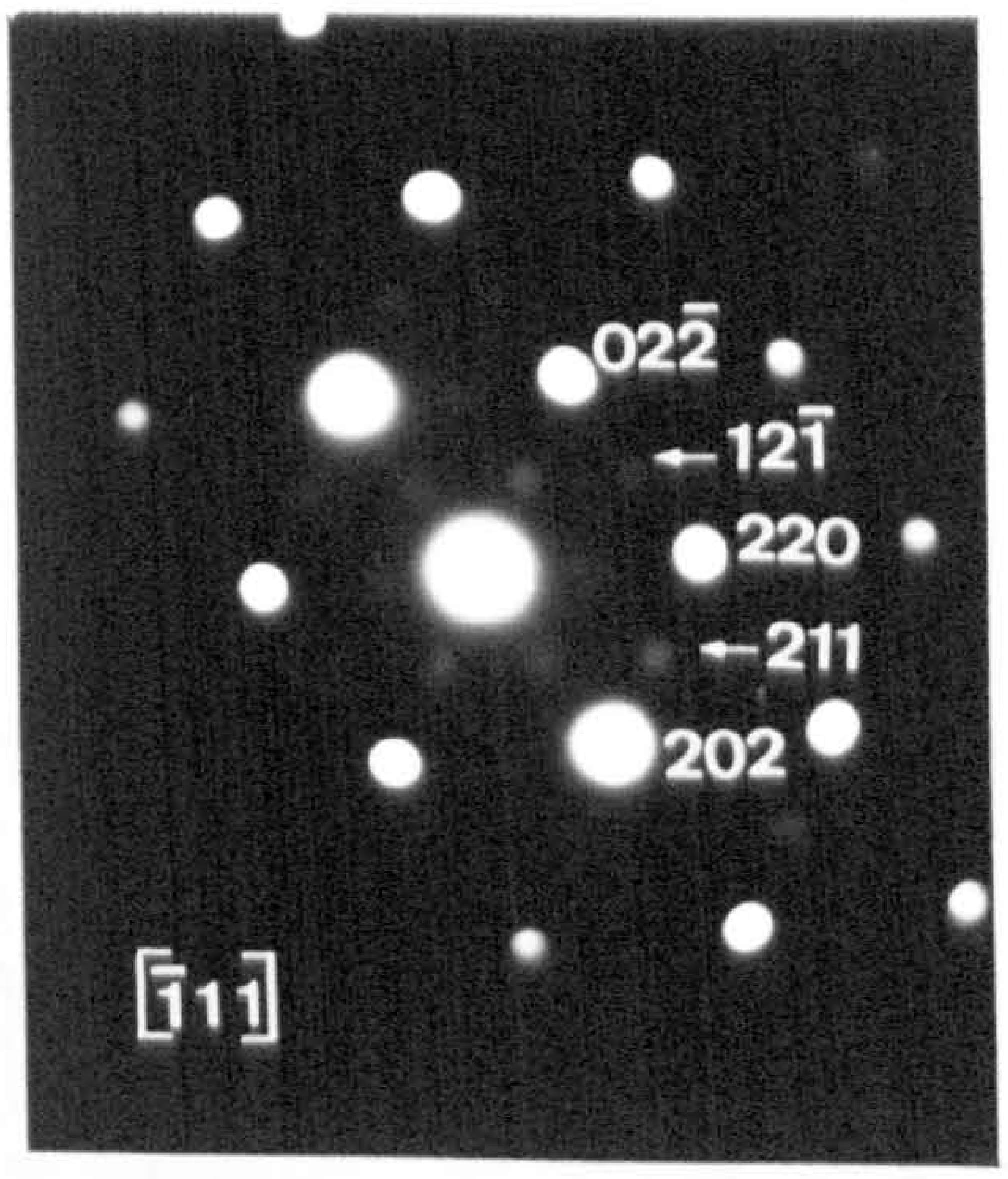
02$\bar{2}$
12$\bar{1}$
220
211
202
[$\bar{1}$11]

e

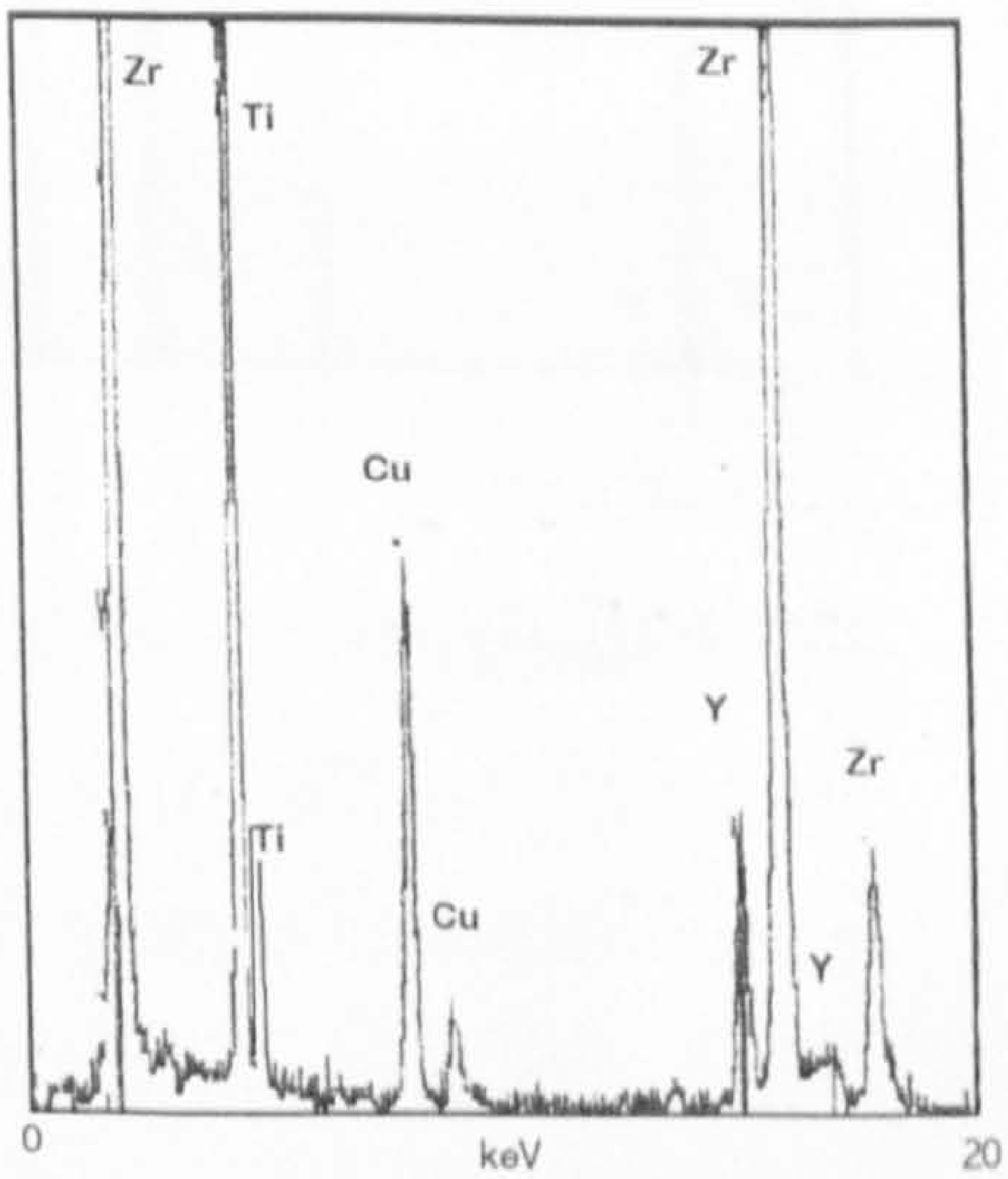
Zr
Ti
Zr
Cu
Y
Zr
Ti
Cu
Y
0
keV
20

Figure 6.15 (***a***) Bright field TEM micrograph of a ZrO_2-Y_2O_3-TiO_2 plasma sprayed coating specimen prepared by ion beam etching (cross-section), showing *t*-ZrO_2 grains as identified by the respective electron microdiffraction pattern (***b***). A and A* arrows indicate different variants of *t*-ZrO_2. (***c***) Dark field TEM micrograph obtained using $\vec{g}$ = 022. Arrows indicate the APBs. (***d***) EDS of specimen shown in (***a***). Bars = 100nm.

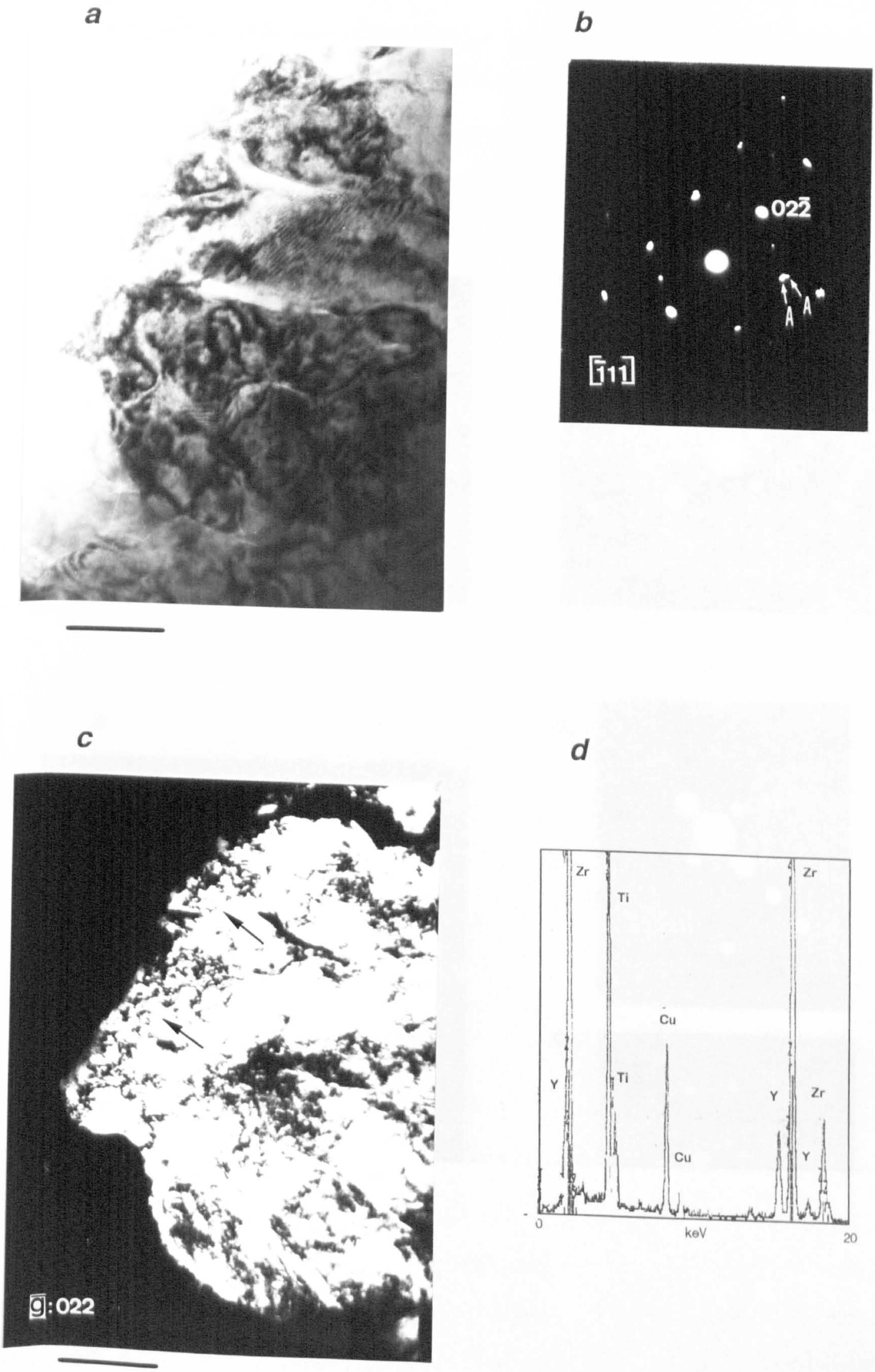
a
b
$02\bar{2}$
A
A
$[\bar{1}11]$
c
g: 022
d
Zr
Ti
Zr
Cu
Y
Ti
Y
Zr
Cu
Y
0
keV
20

Figure 6.16 (***a***) Bright field TEM micrograph of a ZrO_2-Y_2O_3-TiO_2 plasma sprayed coating specimen prepared by ion beam etching (planar section), showing rounded *c*-ZrO_2 grains with *t*-ZrO_2 precipitates (mottled structure) as confirmed by the electron microdiffraction pattern (***b***). Diffraction spots corresponding to the reflections $[\bar{1}10]$ and $[1\bar{1}0]$ (arrows) are not allowed for *t*-ZrO_2, however they are produced by double diffraction. Bar = 50nm.

Figure 6.17 (***a***) Bright field TEM micrograph of a ZrO_2-Y_2O_3-TiO_2 plasma sprayed coating specimen prepared by ion beam etching (cross-section), showing *c*- or *t*-ZrO_2 and twinned *m*-ZrO_2 grains. (***b***) electron microdiffraction pattern from *m*-ZrO_2 grain and (***c***) for the *c*- or *t*-ZrO_2 grain. T = *t*-ZrO_2, C = *c*-ZrO_2, M = *m*-ZrO_2, bar = 200nm.

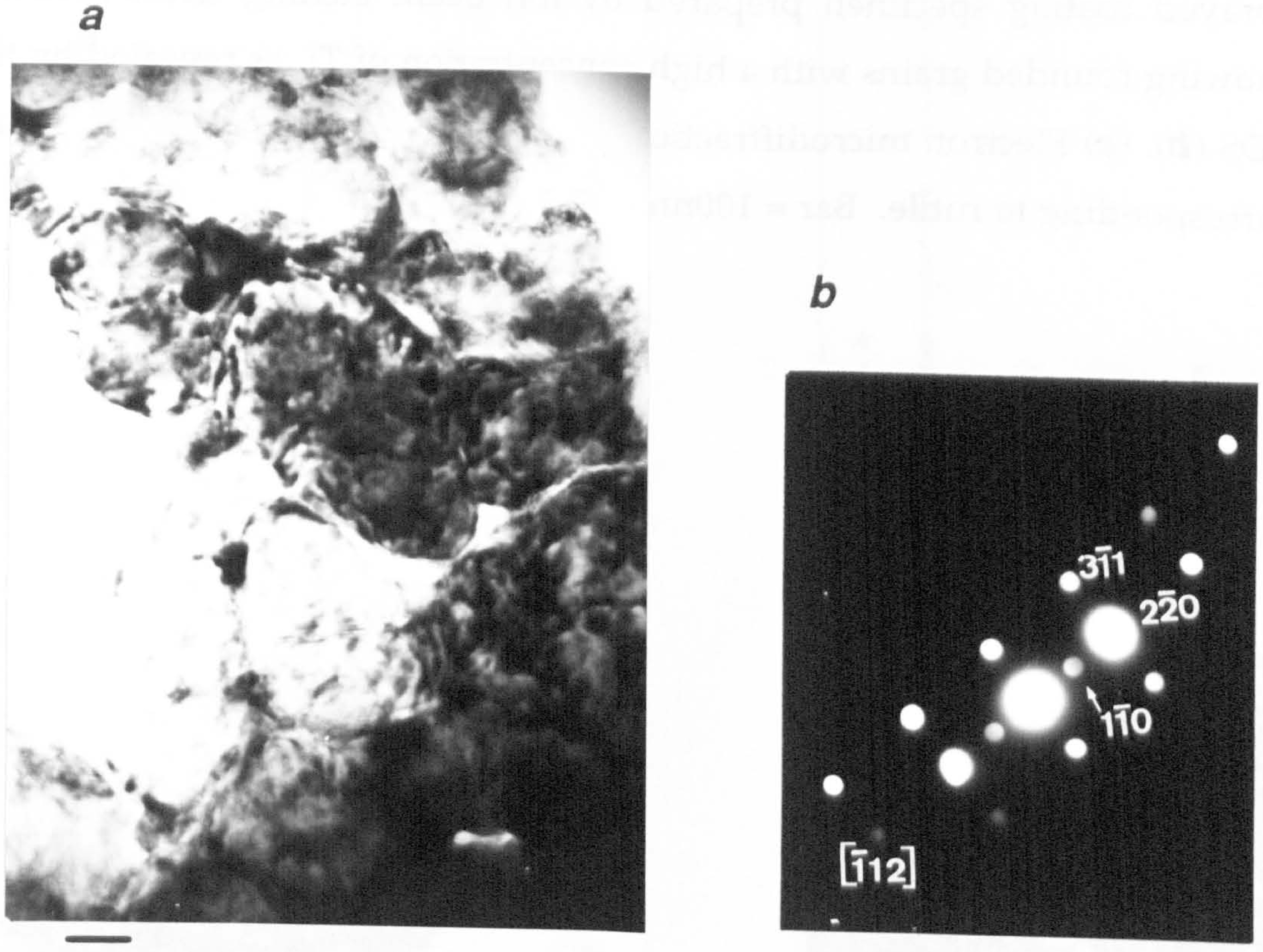
a
b
31̄1
22̄0
11̄0
[1̄12]

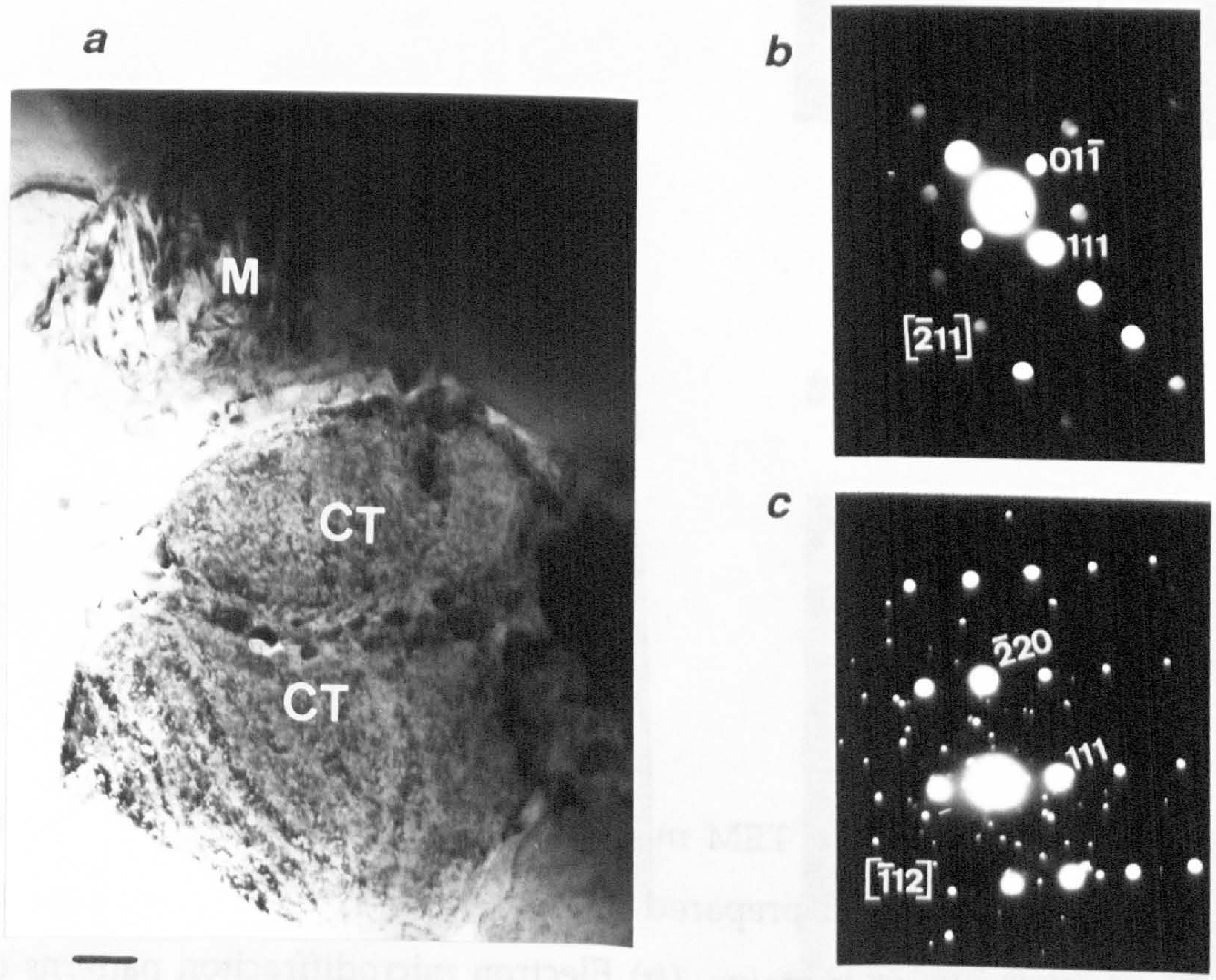
a
M
CT
CT
b
011̄
111
[2̄11]
c
2̄20
111
[1̄12]

Figure 6.18 (***a***) Bright field TEM micrograph of a ZrO_2-Y_2O_3-TiO_2 plasma sprayed coating specimen prepared by ion beam etching (cross-section), showing rounded grains with a high concentration of Ti, as revealed by the EDS (***b***). (***c***) Electron microdiffraction pattern from specimen shown in (***a***), corresponding to rutile. Bar = 100nm.

Figure 6.19 (***a***) Bright field TEM micrograph of a ZrO_2-Y_2O_3-TiO_2 plasma sprayed coating specimen prepared by ion beam etching (cross-section), showing rounded *m*-ZrO_2 grains. (***b***) Electron microdiffraciton patterns of grains observed in (***a***). Bar = 100nm.

b

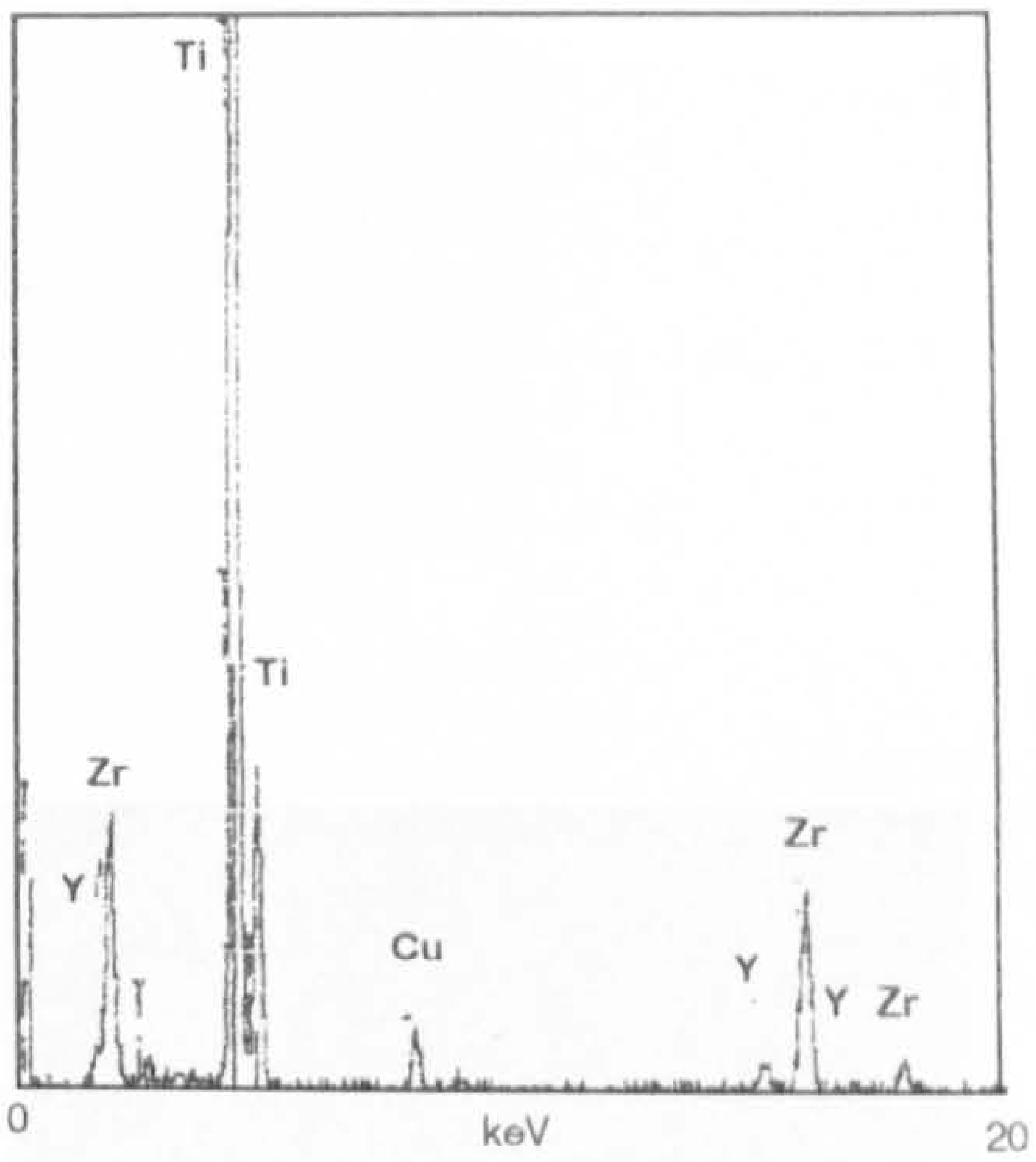
Ti
Ti
Zr
Y
Cu
Zr
Y
Y
Zr
0
keV
20

a

c

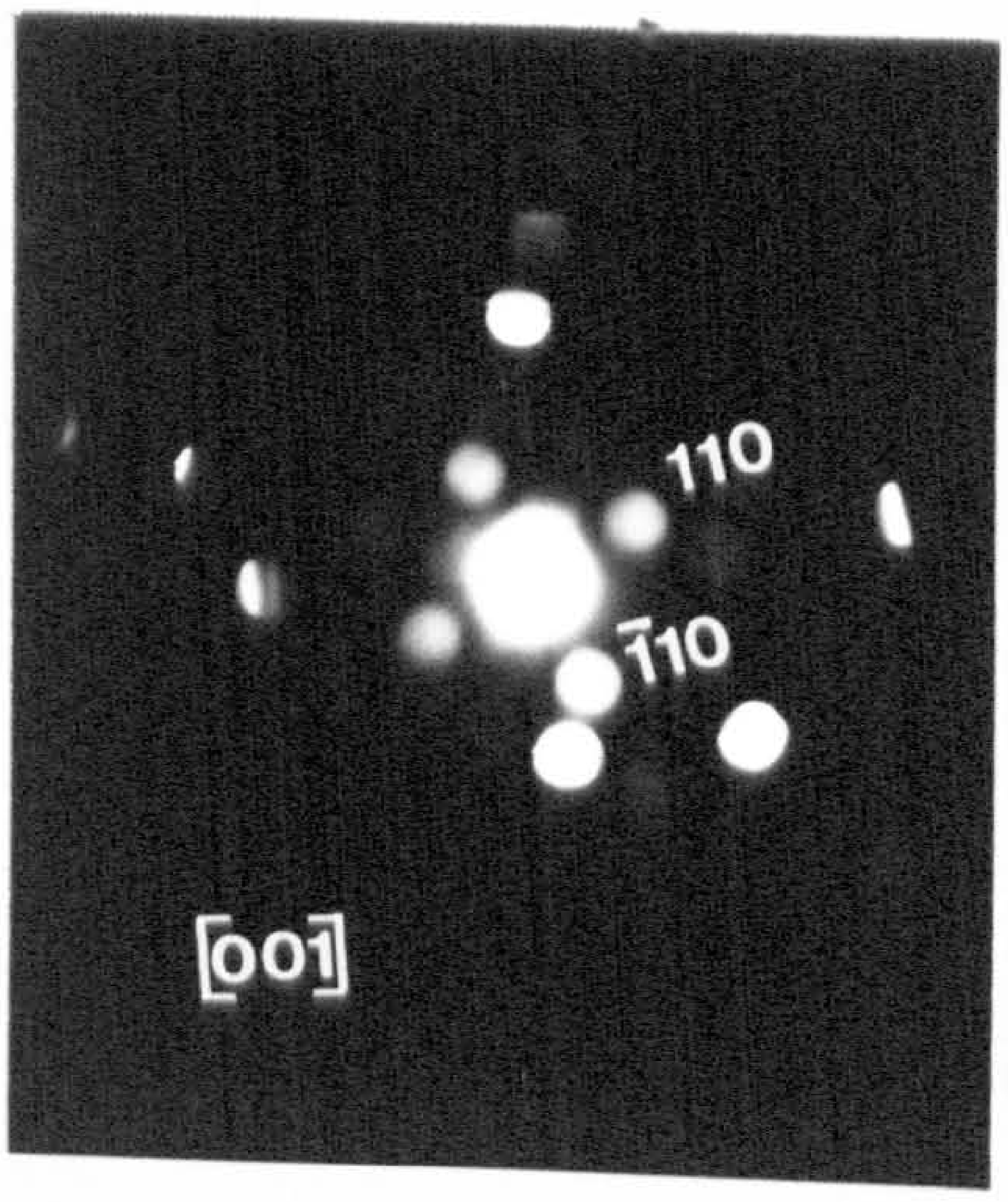
110
$\bar{1}10$
[001]

a

b

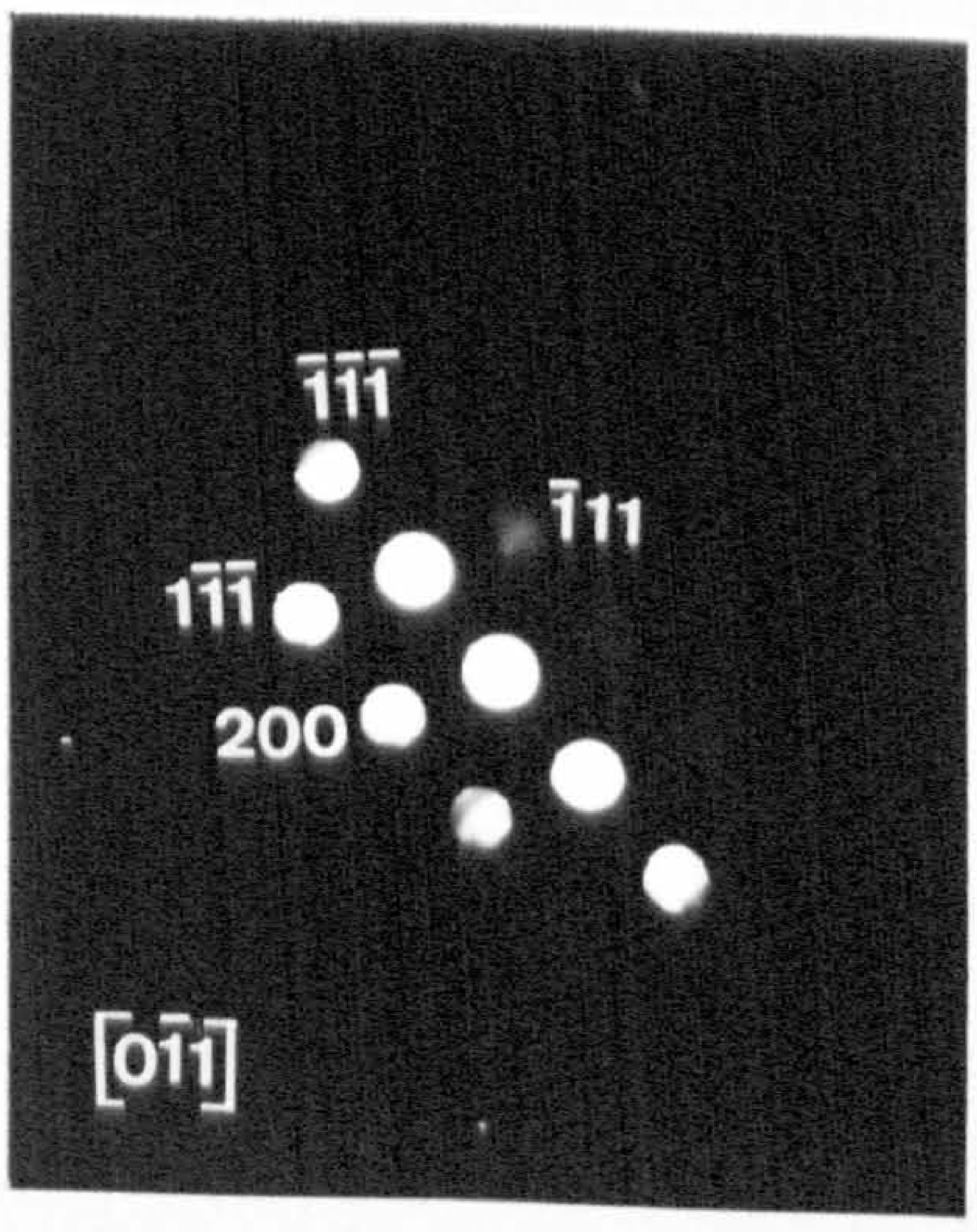
$\bar{1}\bar{1}\bar{1}$
$\bar{1}11$
$1\bar{1}\bar{1}$
200
$[0\bar{1}1]$

Figure 6.20 (***a***) Bright field TEM micrographs of a ZrO_2-Y_2O_3-TiO_2 plasma sprayed coating specimen prepared by ion beam etching (planar section), showing coarsely twinned *m*-ZrO_2 particle. (***b***) Selected area diffraction pattern showing different directions of the *m*-ZrO_2 laths. (***c***) EDS from the specimen shown in (***a***). Bar = 100nm.

Figure 6.21 (***a***) Bright field TEM micrographs of a ZrO_2-Y_2O_3-TiO_2 plasma sprayed coating specimen prepared by ion beam etching (cross-section), showing a highly twinned *m*-ZrO_2 particle. A microcrack is observed in the particle-matrix boundary (arrow). (***b***) EDS from the specimen shown in (***a***). Bar = 200nm.

a

b

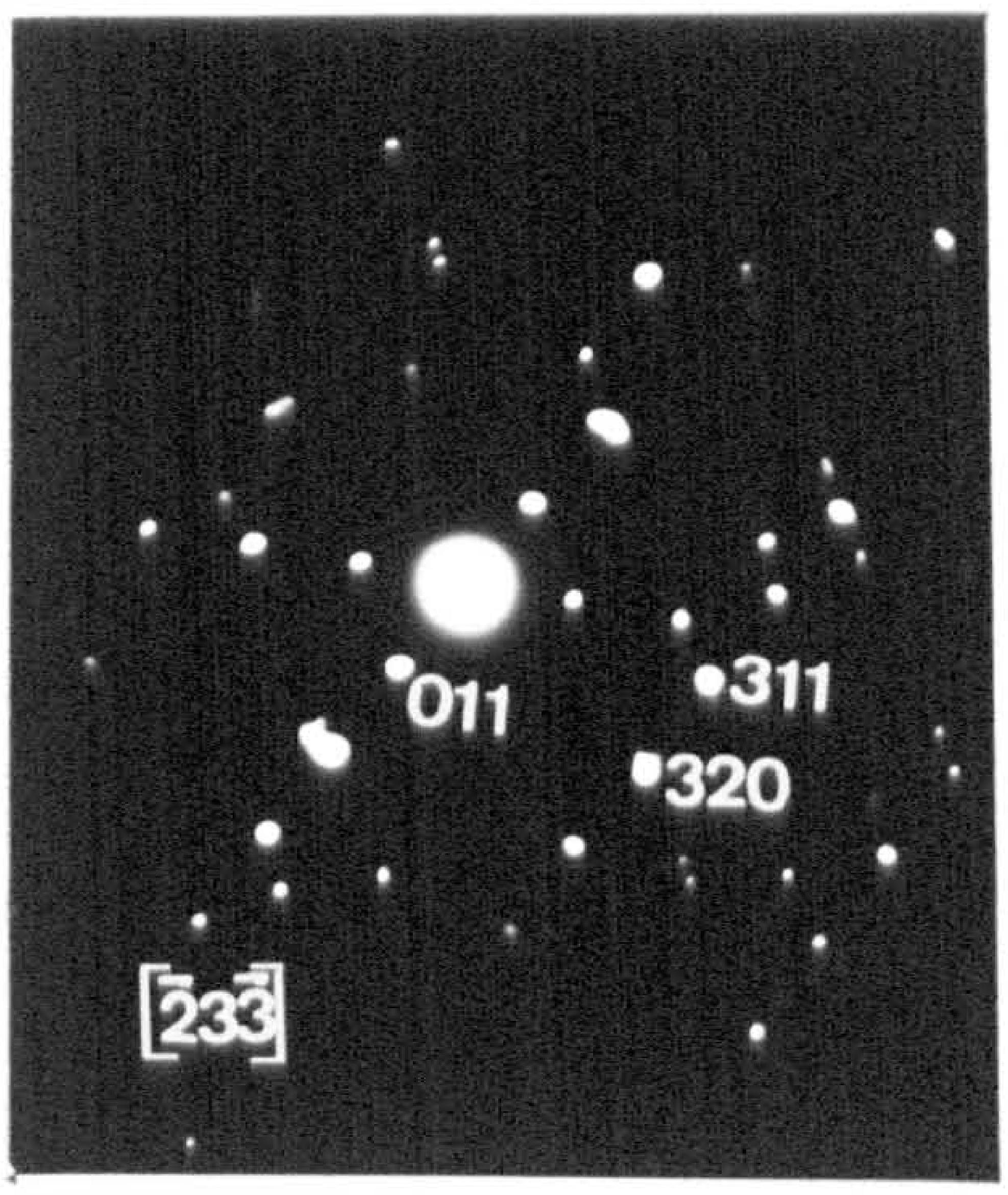
011
311
320
[233]

c

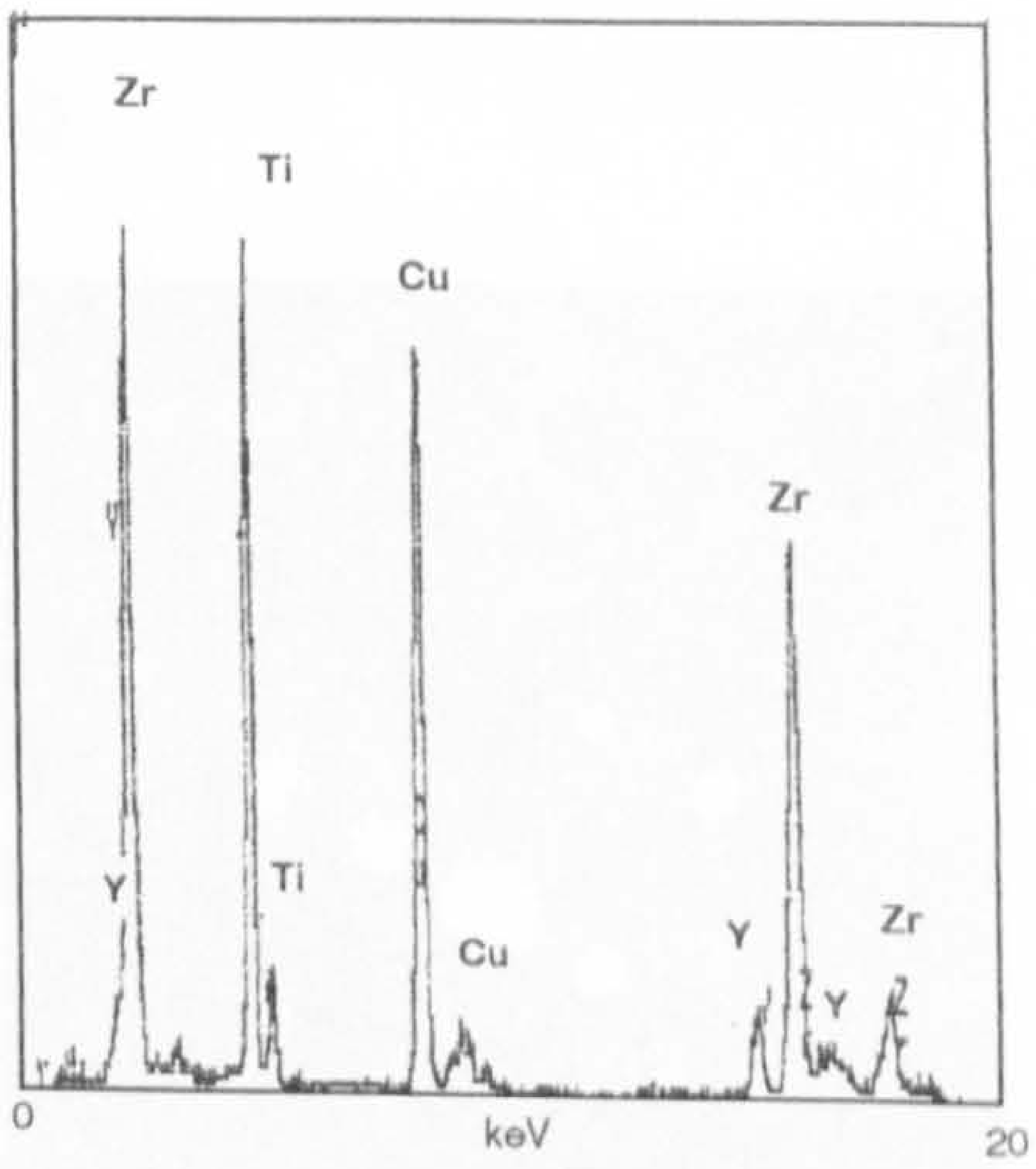
Zr
Ti
Cu
Zr
Y
Y
Ti
Cu
Y
Y
Zr
0
keV
20

a

b

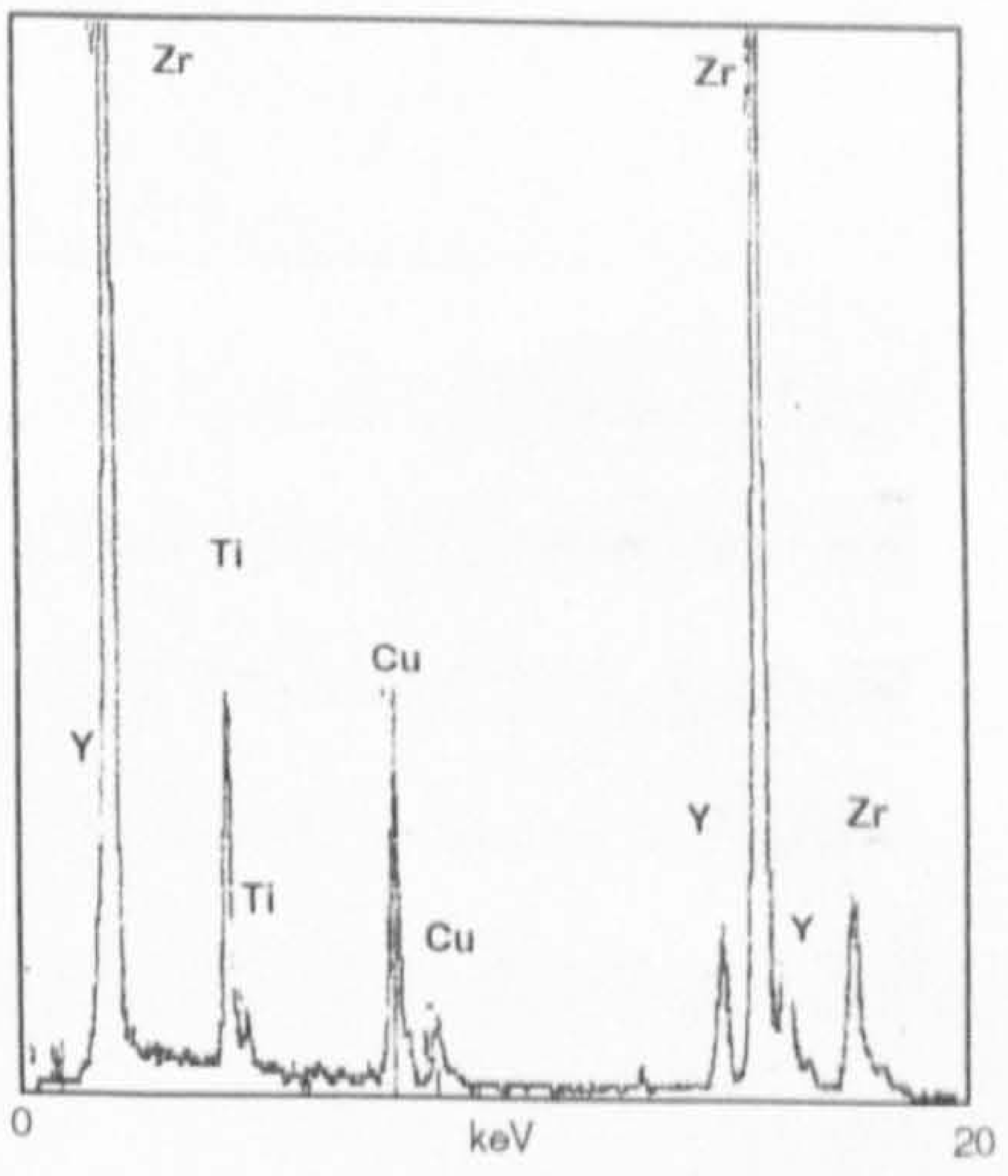
Zr
Zr
Ti
Cu
Y
Y
Zr
Ti
Cu
Y
0
keV
20

Figure 6.22 (***a***) Bright field TEM micrographs of a ZrO_2-Y_2O_3-TiO_2 plasma sprayed coating specimen prepared by ion beam etching (cross-section), showing a mosaic of plate-like *m*-ZrO_2 particles which exhibit extensive Moirè contrast. (***b***) Electron microdiffraction pattern from the specimen area shown in (***a***). (***c***) Dark field TEM micrograph using $\bar{g} = 111$. Bars = 100nm

a

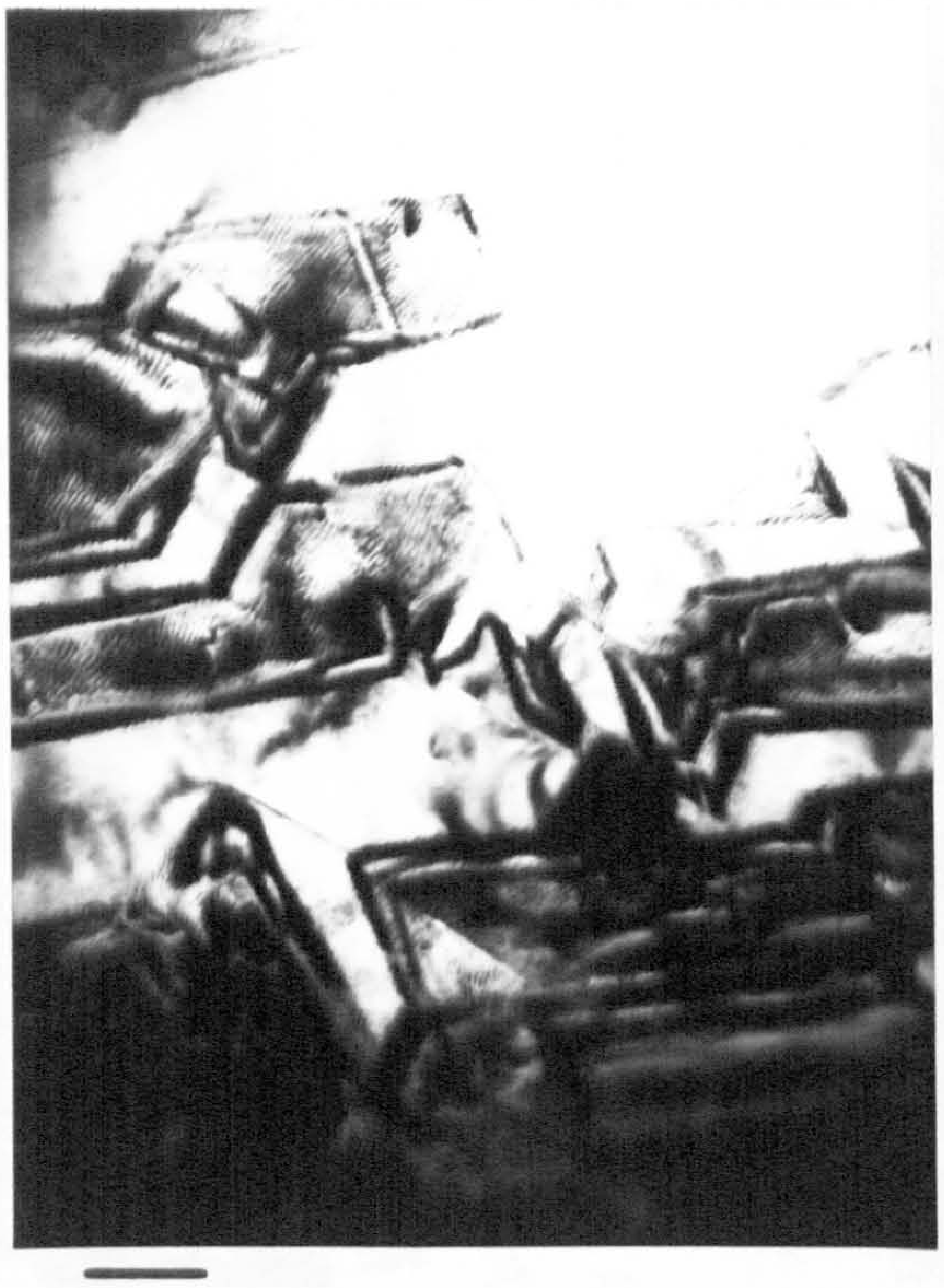

b

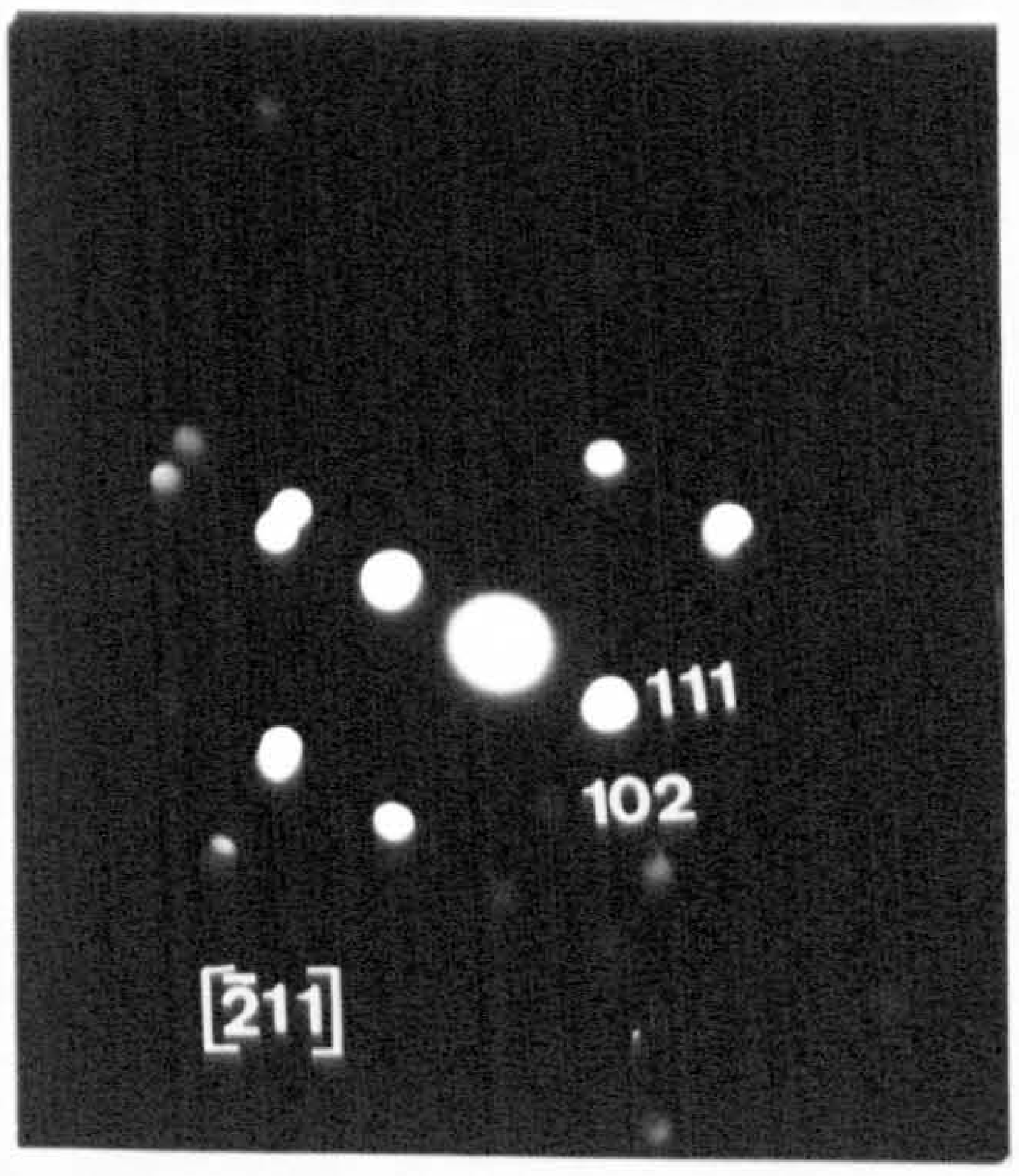

c

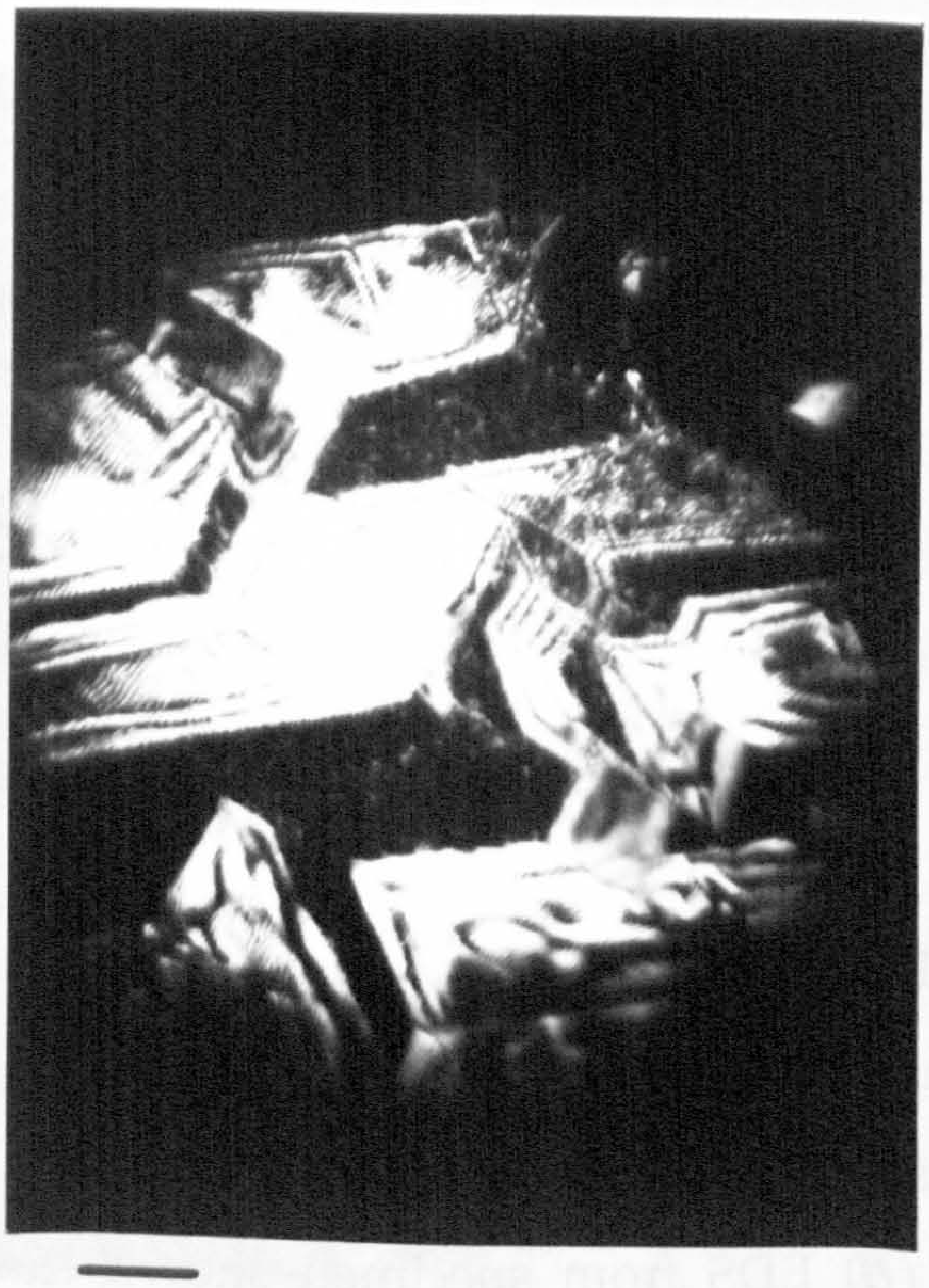

Figure 6.23 (***a-c***) Bright field TEM micrographs of a ZrO_2-Y_2O_3-TiO_2 plasma sprayed coating specimen prepared by ion beam etching (cross-section), showing examples of plate-like *m*-ZrO_2 particle mosaics which exhibit extensive Moirè contrast. (***d***) EDS from specimen shown in (***c***). Bars = 200nm

a

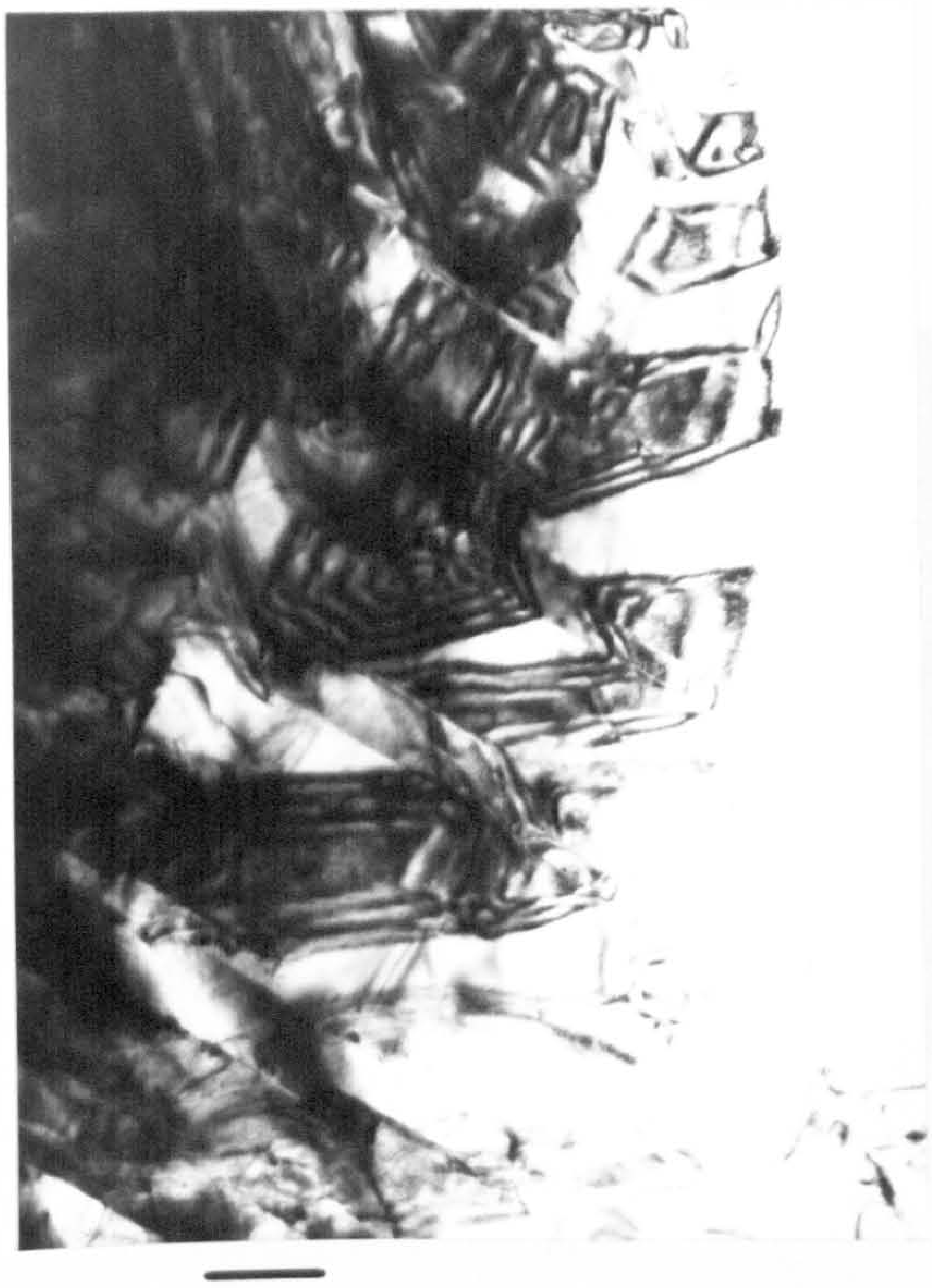

b

c

d

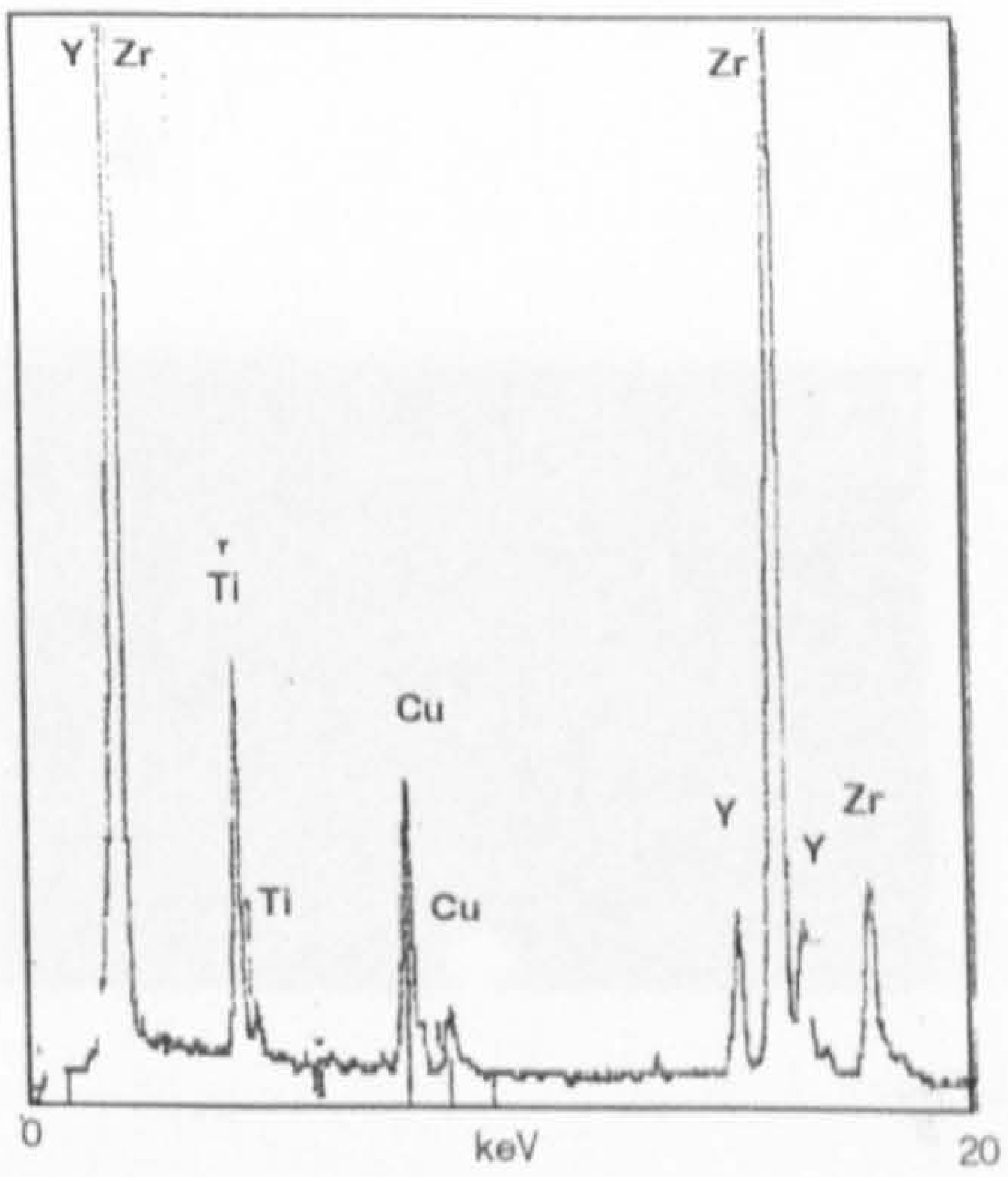

Figure 6.24 (***a***, ***b***) Bright field TEM micrographs from planar sections of a ZrO_2-Y_2O_3-TiO_2 plasma sprayed coating heated at 1400 °C for 24 hours in air. Different microstructural features such as *m*-ZrO_2 laths (M), *t*-ZrO_2 twins (T), faceted *c*- or *t*-ZrO_2 grains (C/T) and partially $t \rightarrow m$ transformed grains (arrows) can be distinguished. Bars = 200nm.

Figure 6.25 (***a***) Bright field TEM micrograph from a planar section of a ZrO_2-Y_2O_3-TiO_2 plasma sprayed coating heated at 1400 °C for 24 hours in air; agglomerates of very small particles can be observed. (***b***) Electron microdiffraction pattern showing reflections allowed to *c*- and *t*-ZrO_2 symmetries. Bar = 50nm.

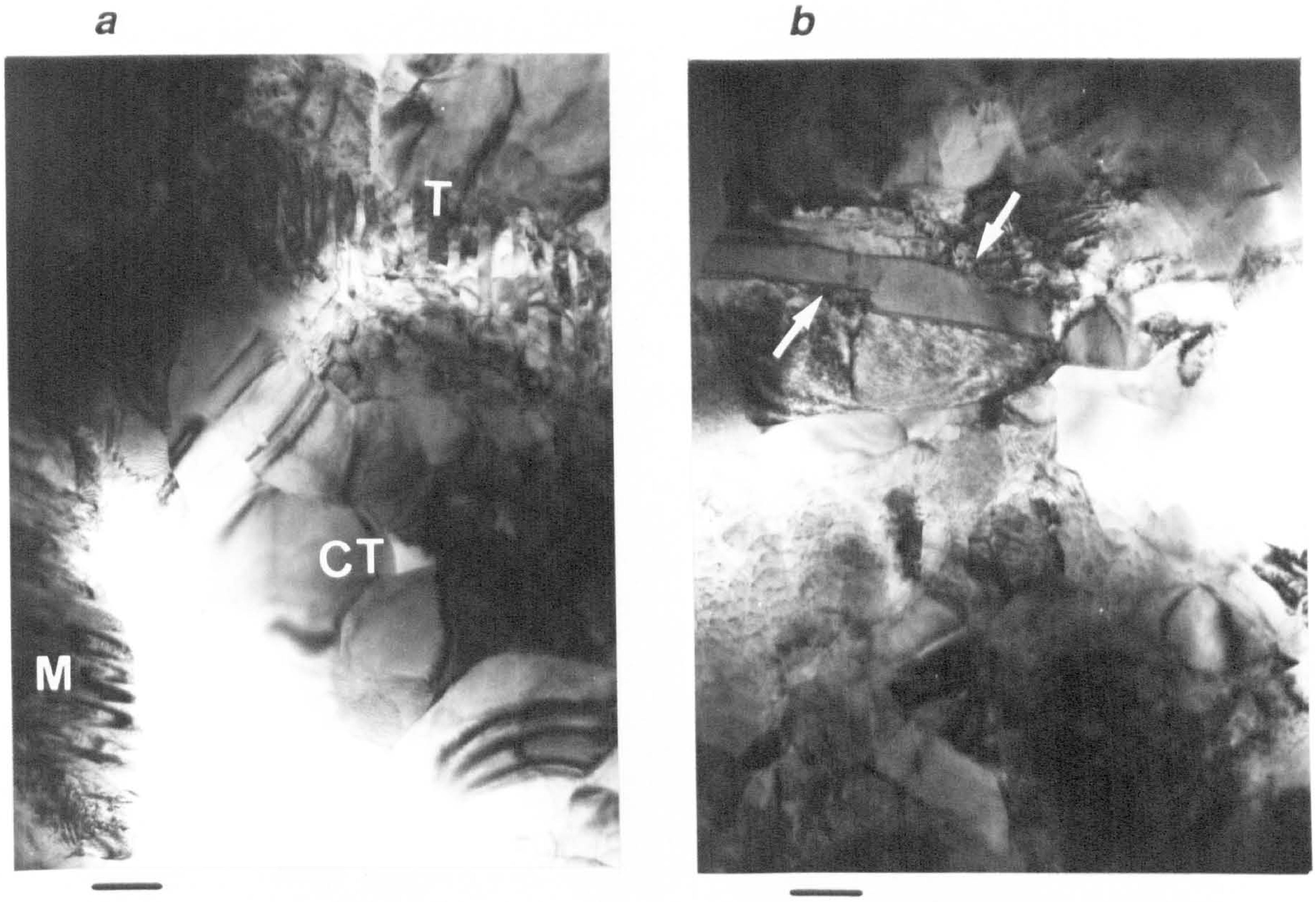
a
b
T
CT
M

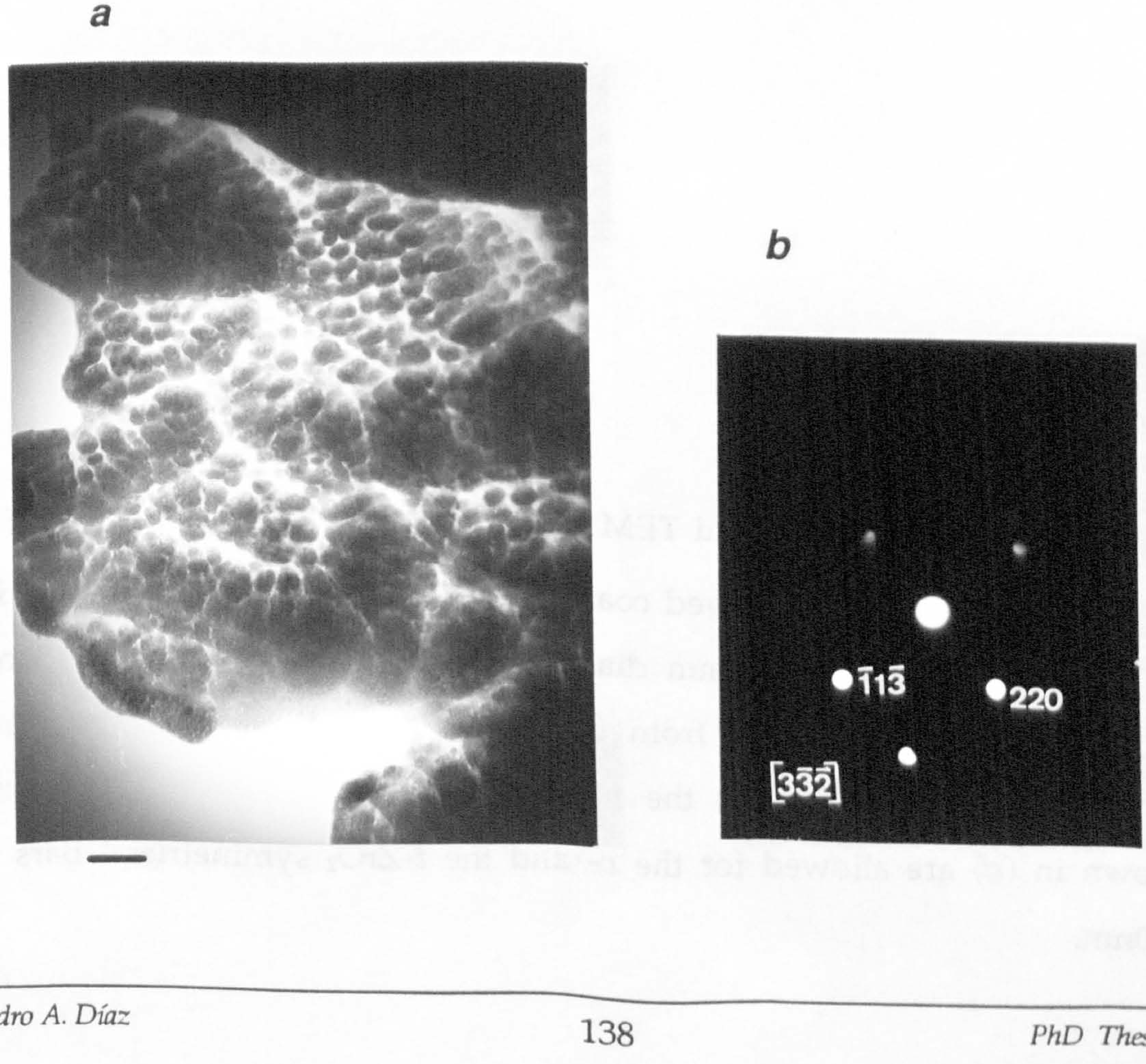
a
b
1̄13̄
220
[33̄2̄]

Figure 6.26 (***a, b***) Bright field TEM micrographs from planar sections of a ZrO_2-Y_2O_3-TiO_2 plasma sprayed coating heated at 1400 °C for 24 hours in air. Faceted grains (> 100nm diameter) are observed. (***c, d***) Electron micro- diffraction patterns from (***a***) and (***b***), respectively. Reflections shown in c) corresponds to the *t*-ZrO_2 symmetry while the reflections shown in (***d***) are allowed for the *c*- and the *t*-ZrO_2 symmetries. Bars = 100nm.

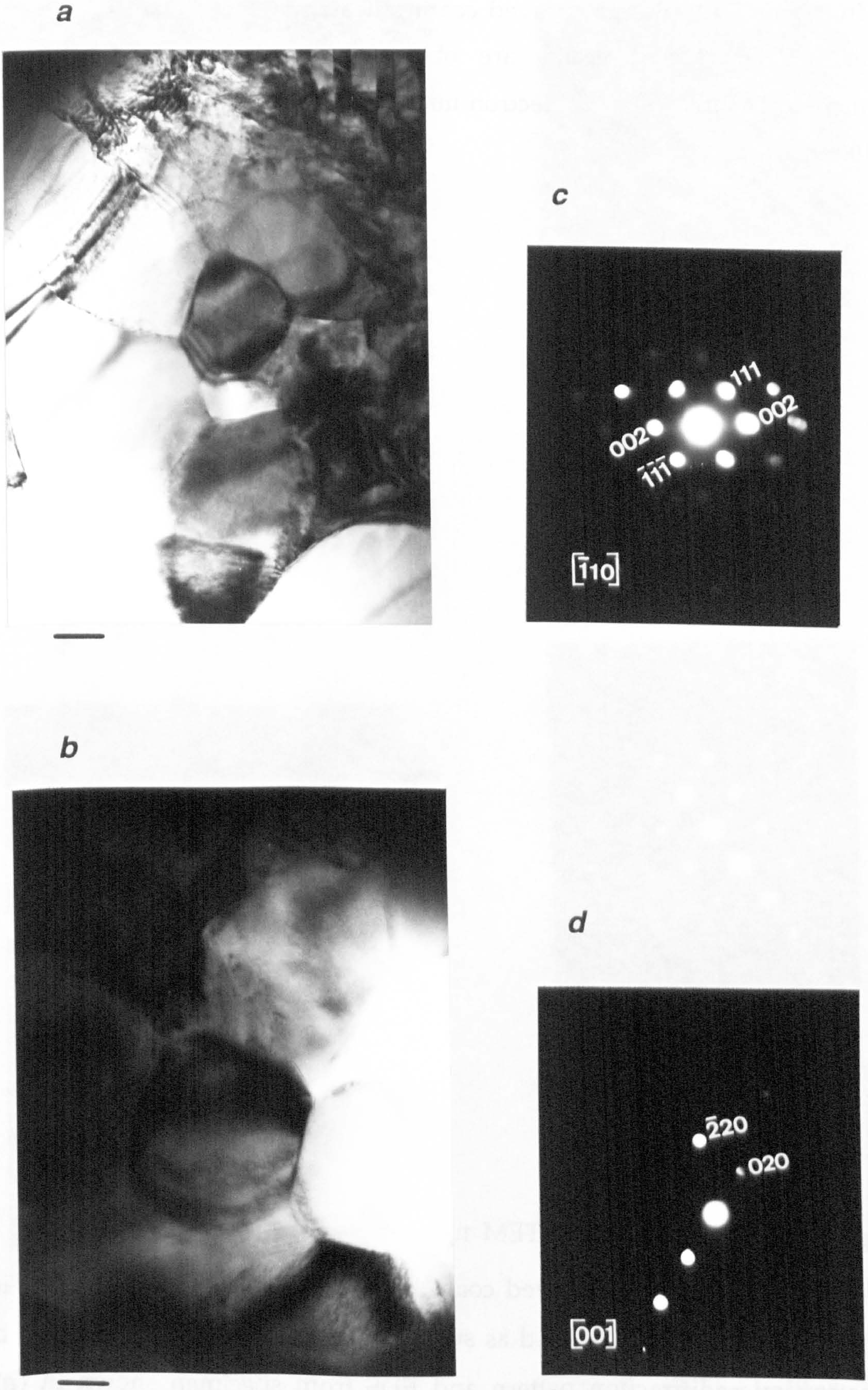
a
c
111
002
002
1̄1̄1̄
[1̄10]
b
d
2̄20
020
[001]

Figure 6.27 (***a***) Bright field TEM micrograph from a planar section of a ZrO_2-Y_2O_3-TiO_2 plasma sprayed coating heated at 1400 °C for 24 hours in air. *t*-ZrO_2 faceted grains are observed displaying an intragranular microcrack (arrows). (***b***) Electron microdiffraction pattern from (***a***). Bar = 100nm.

Figure 6.28 (***a***) Bright field TEM micrograph from a planar section of a ZrO_2-Y_2O_3-TiO_2 plasma sprayed coating heated at 1400 °C for 24 hours in air. *t*-ZrO_2 twins are observed as successive dark and light plates. (b, c) Electron microdiffraction pattern and EDS from specimen shown in (***a***). Bar = 100nm.

a

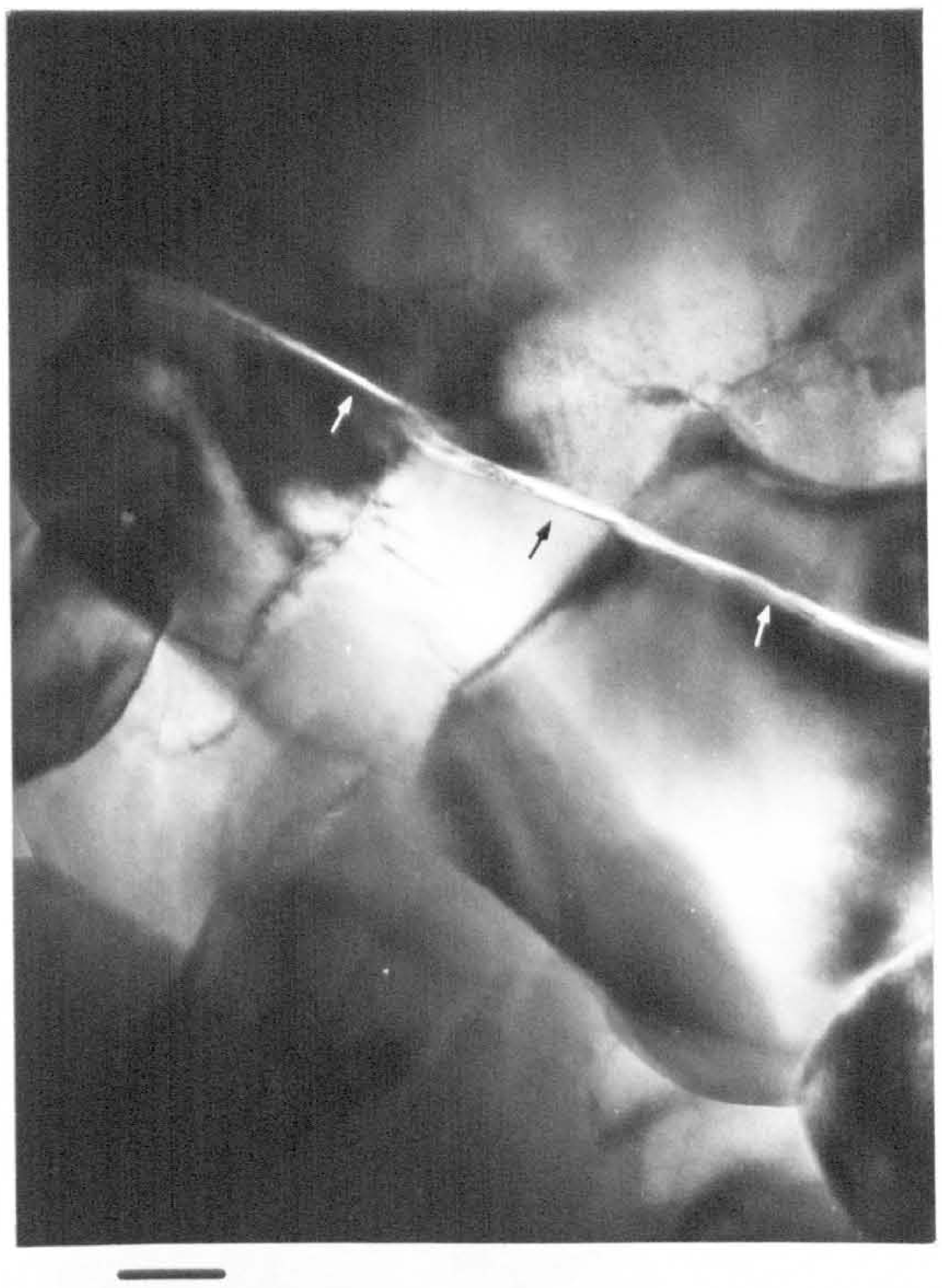

b

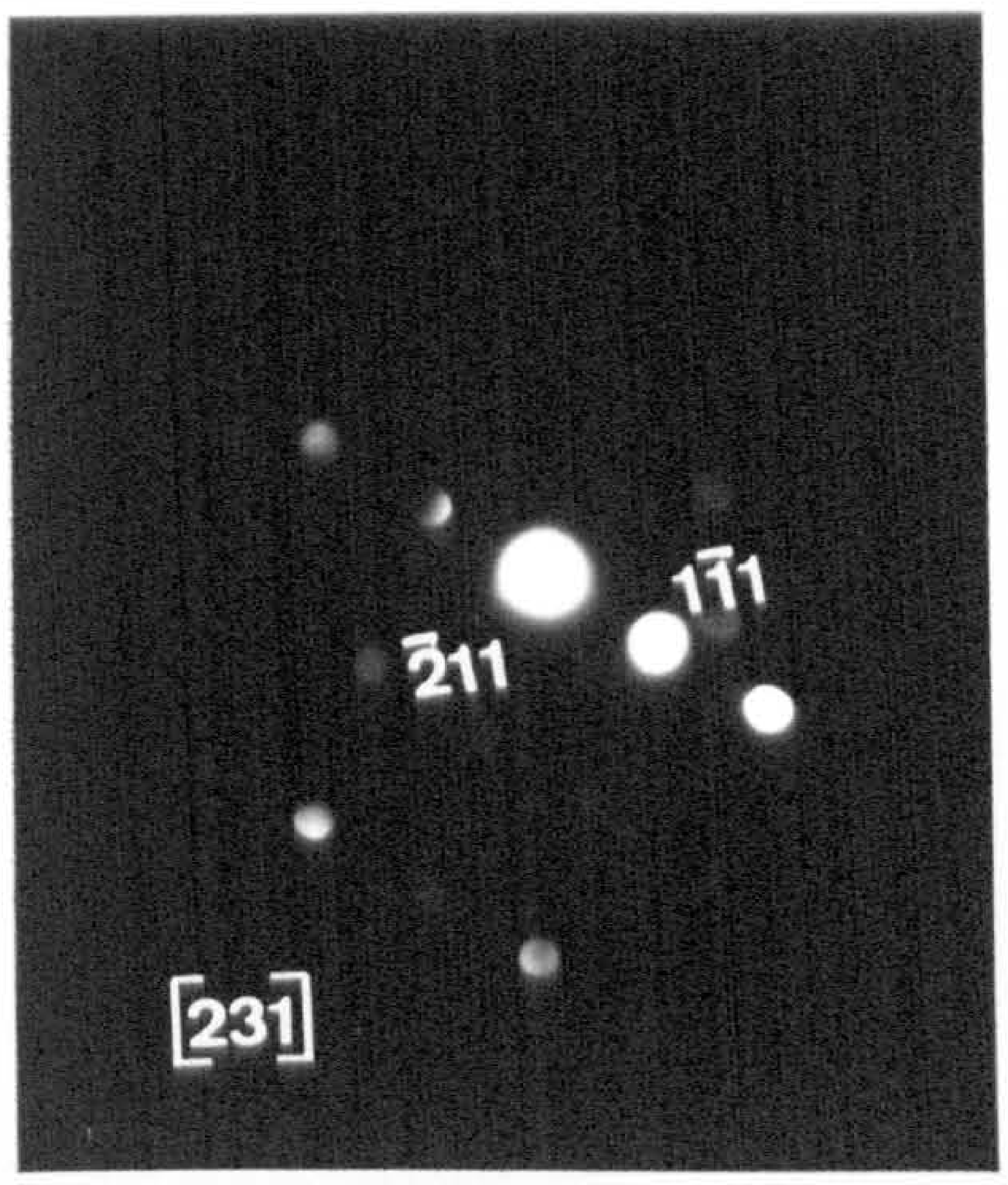
$1\bar{1}1$
$\bar{2}11$
[231]

a

b

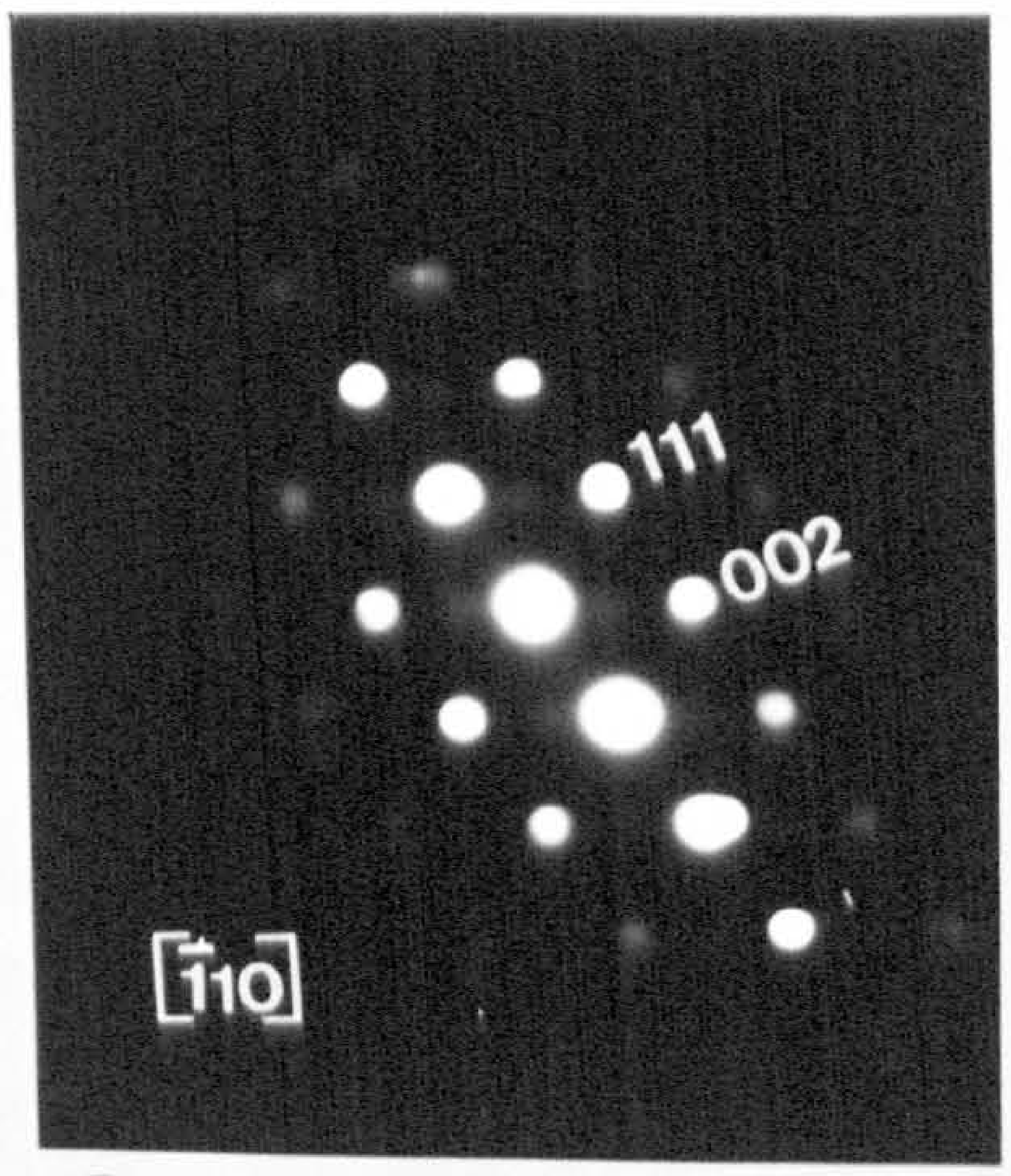
111
002
[$\bar{1}$10]

c

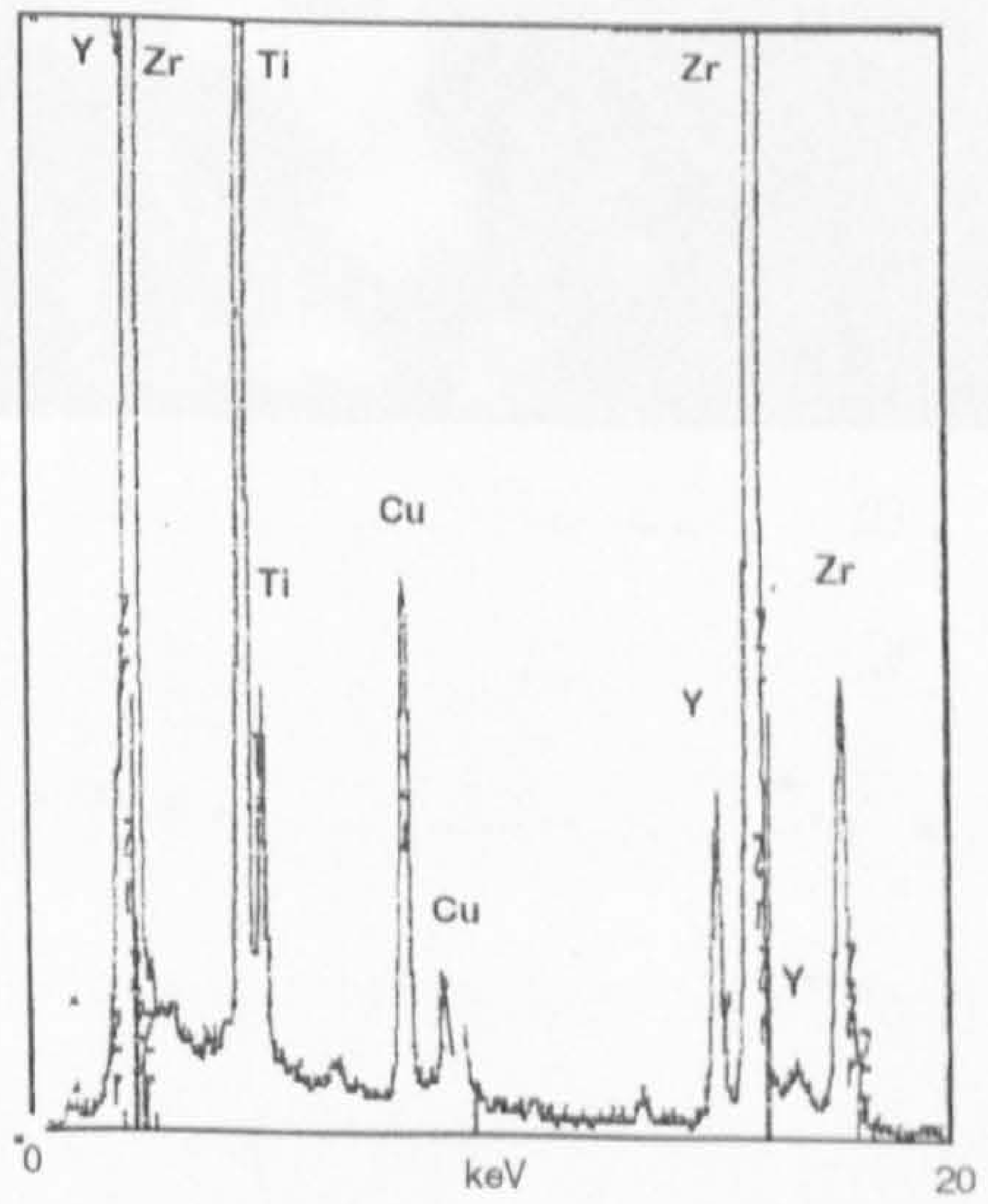
Y
Zr
Ti
Zr
Cu
Ti
Zr
Y
Cu
Y
0
keV
20

Figure 6.29 (***a***) Bright field TEM micrograph from a planar section of a ZrO_2-Y_2O_3-TiO_2 plasma sprayed coating heated at 1400 °C for 24 hours in air, showing *m*-ZrO_2 laths. (***b***) Electron microdiffraction pattern from specimen shown in (***a***). Bar = 100nm.

Figure 6.30 (***a, b***) Bright field TEM micrographs from planar sections of a ZrO_2-Y_2O_3-TiO_2 plasma sprayed coating heated at 1600 °C for 24 hours in air; (***a***) shows large grains with an amorphous grain boundary region (arrowed) located in a pocket, bar = 200nm; (***b***) shows a very porous foam-like microstructure. Bars = 50nm.

a

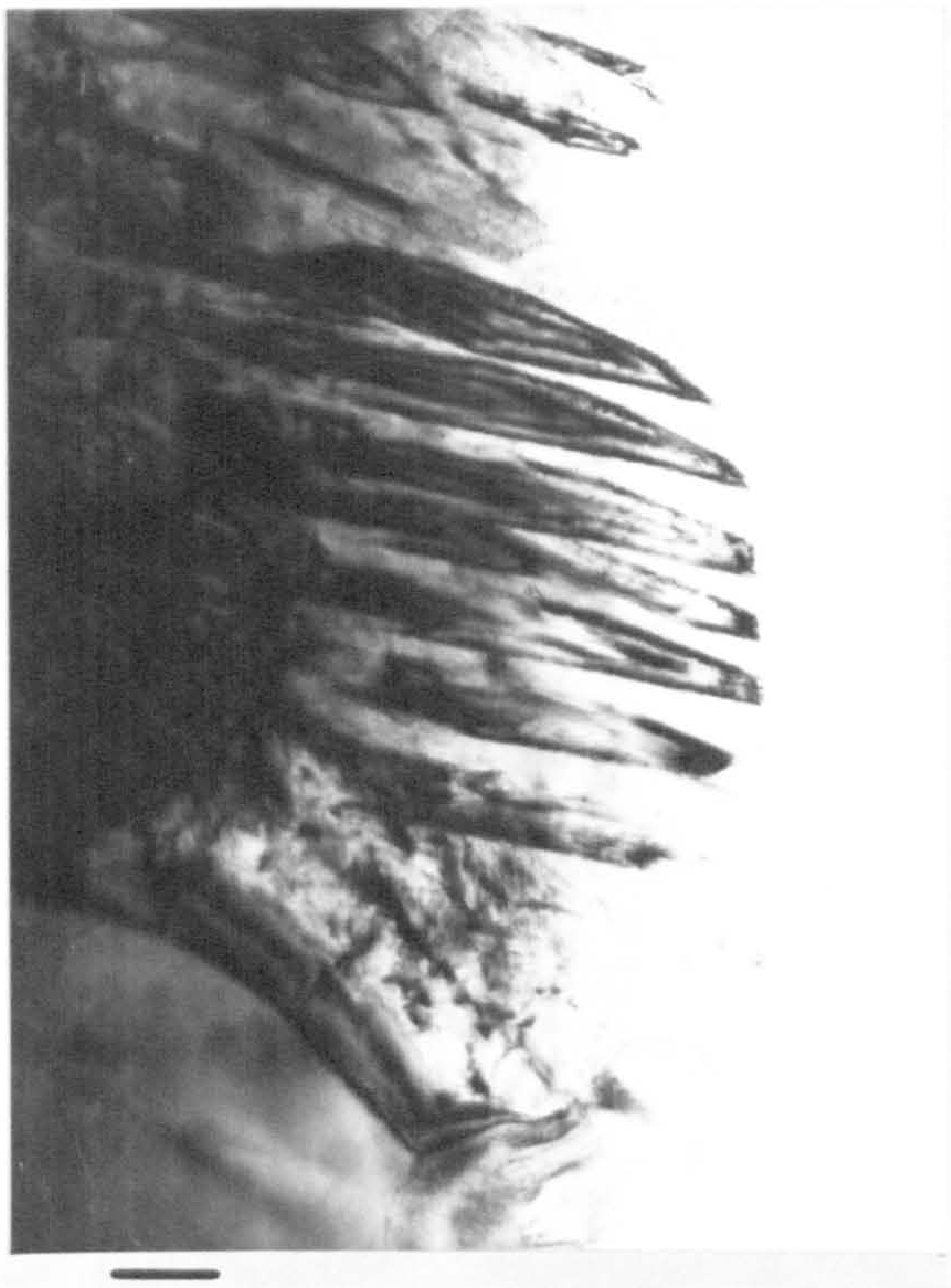

b

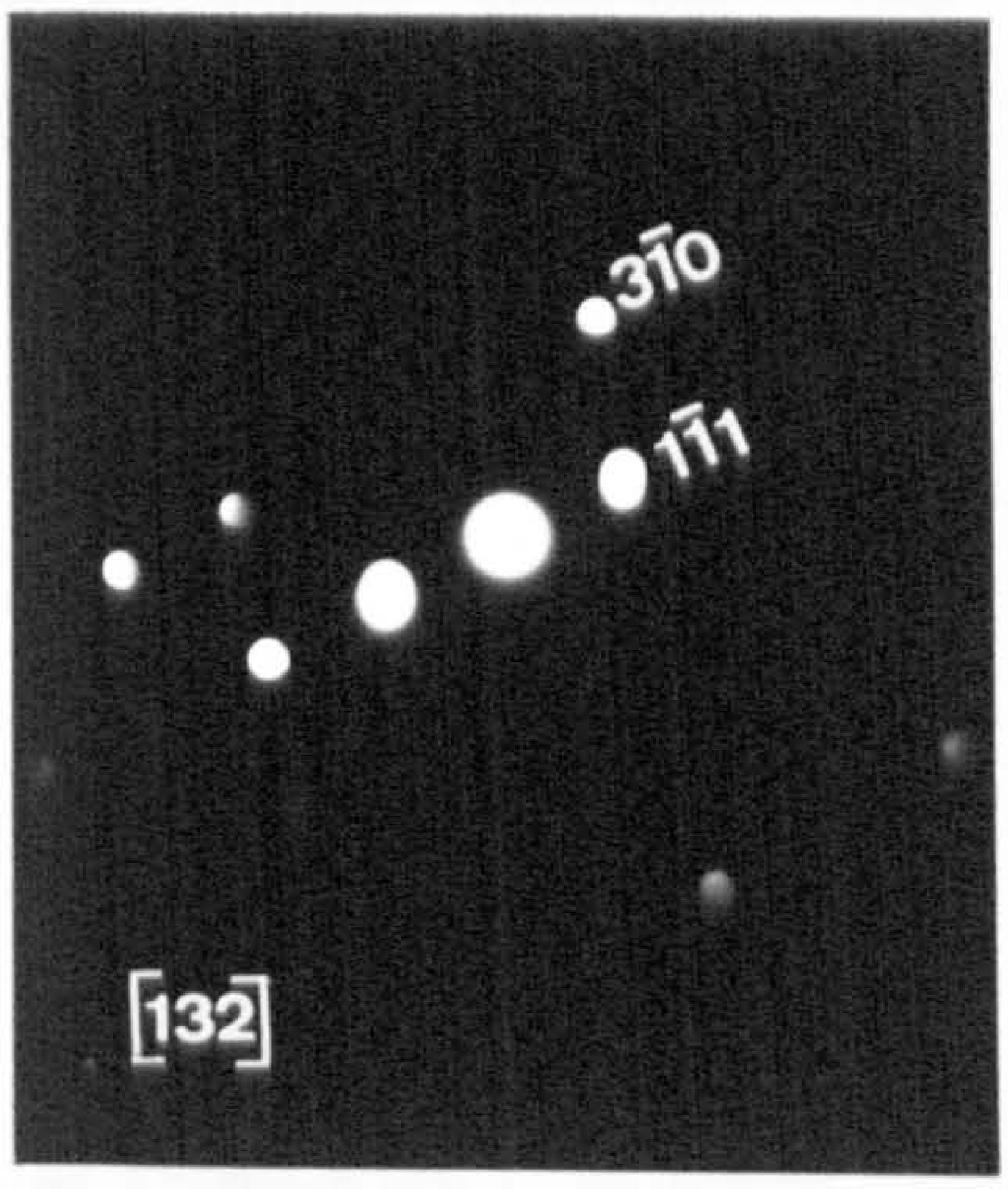

a

b

Figure 6.31 (***a***) Bright field TEM micrograph from a planar section of a ZrO_2-Y_2O_3-TiO_2 plasma sprayed coating heated at 1600 °C for 24 hours in air, showing *m*-ZrO_2 twins. The arrow indicates an intergranular microcrack. (b, c) Electron microdiffraction pattern and EDS from specimen shown in (***a***). Bar = 100nm.

Figure 6.32 (***a***) Bright field TEM micrograph from a planar section of a ZrO_2-Y_2O_3-TiO_2 plasma sprayed coating heated at 1600 °C for 24 hours in air, showing *t*-ZrO_2 grains. (b, c) Electron microdiffraction pattern and EDS from specimen shown in (***a***). Bar = 200nm.

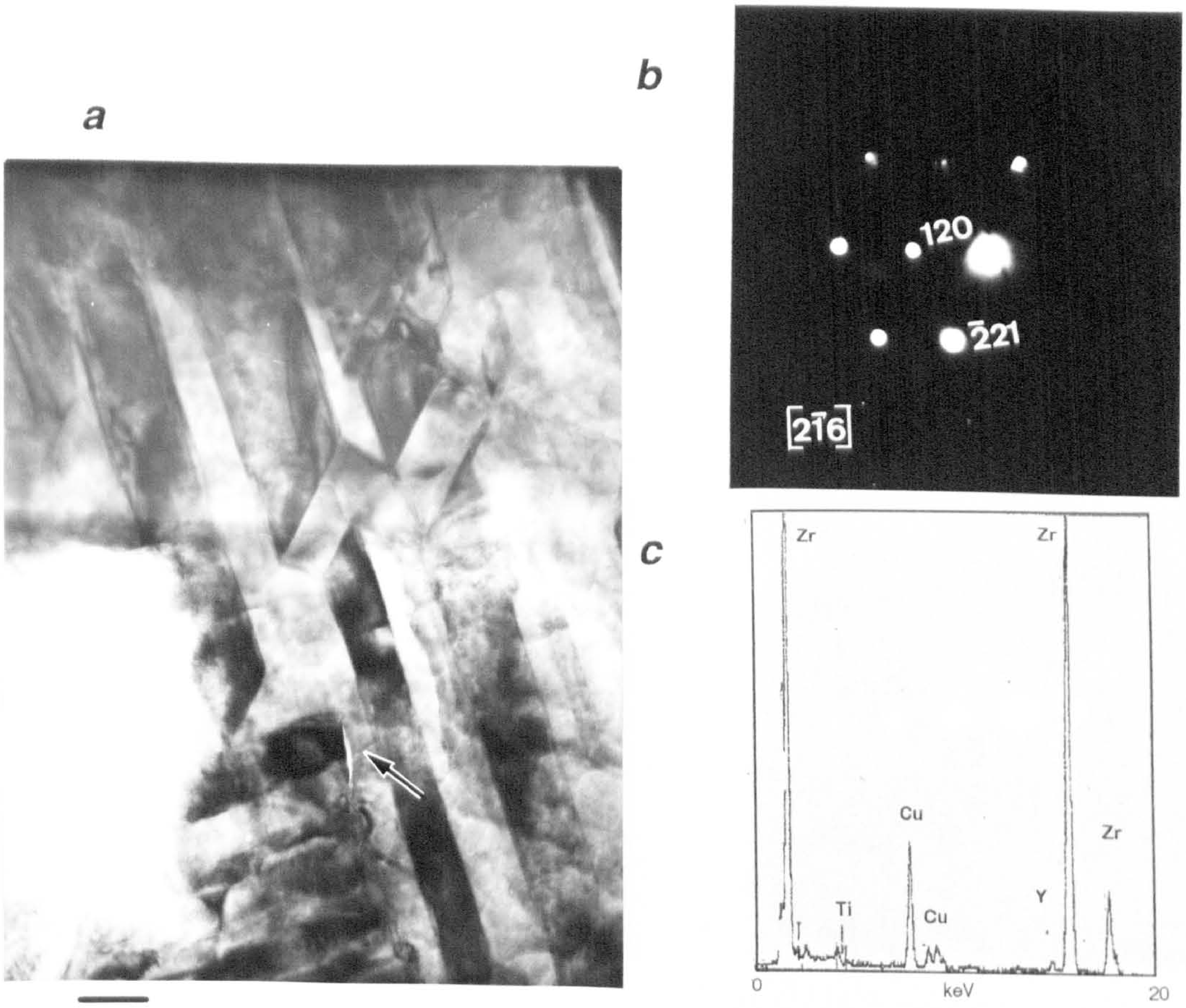
a
b
120
$\bar{2}21$
[$2\bar{1}6$]
c
Zr
Zr
Cu
Zr
Ti
Cu
Y
0
keV
20

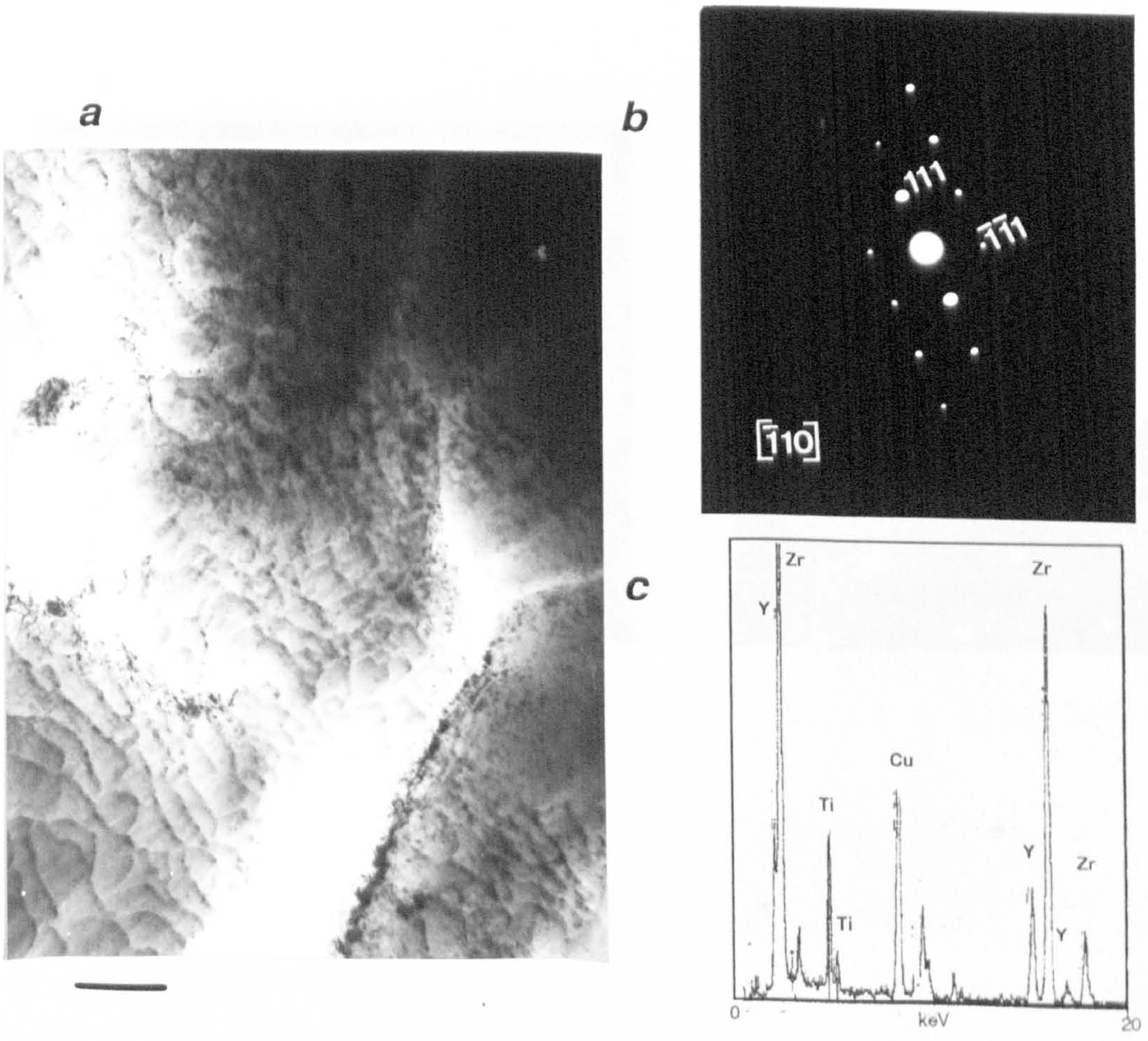
a
b
111
$\bar{1}\bar{1}1$
[$\bar{1}10$]
c
Zr
Y
Zr
Cu
Ti
Ti
Y
Zr
Y
0
keV
20

Figure 6.33 (***a***) Bright field TEM micrograph from a planar section of a ZrO_2-Y_2O_3-TiO_2 plasma sprayed coating heated at 1600 °C for 24 hours in air, showing the nanostructure of some grains. (***b***) Electron microdiffraction pattern from specimen shown in (***a***). The most intense spots correspond to reflections allowed for the *c*- and the ***t***-ZrO_2 symmetries, while the lighter spots (arrows) are allowed for ***t***-ZrO_2 by double diffraction. Bar = 50nm.

Figure 6.34 (***a***) Bright field TEM micrograph from a planar section of ZrO_2-Y_2O_3-TiO_2 pressed powder sintered at 1350 °C for 1 hour. Large faceted grains (> 200nm) are observed which contain dislocations and other deformation substructure. (***b***) Electron microdiffraction pattern from the specimen shown in (***a***); the reflections can be associated with *c*- and ***t***-ZrO_2 symmetries. Bar = 200nm.

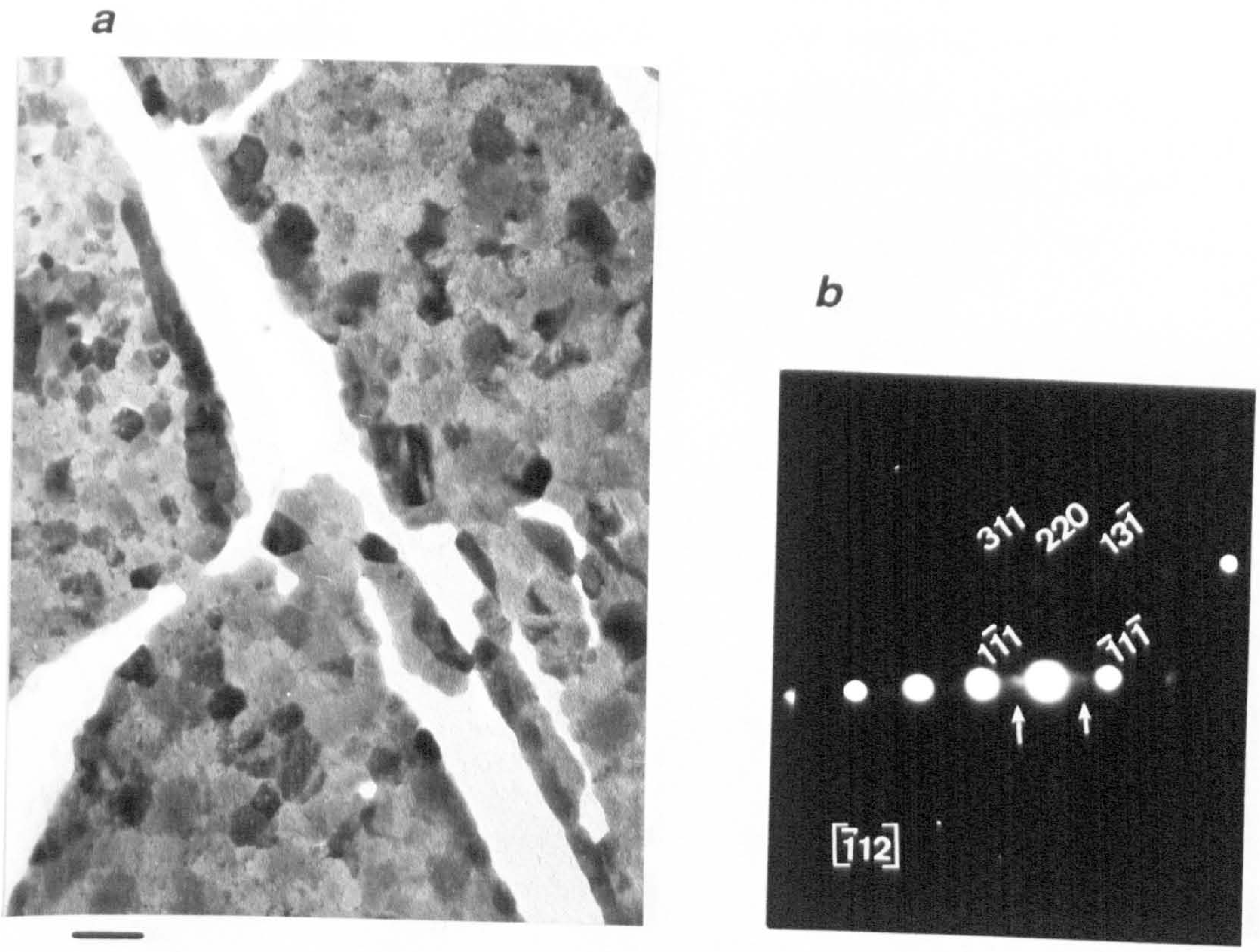
a
b
311
220
13$\bar{1}$
1$\bar{1}$1
$\bar{1}$1$\bar{1}$
[$\bar{1}$12]

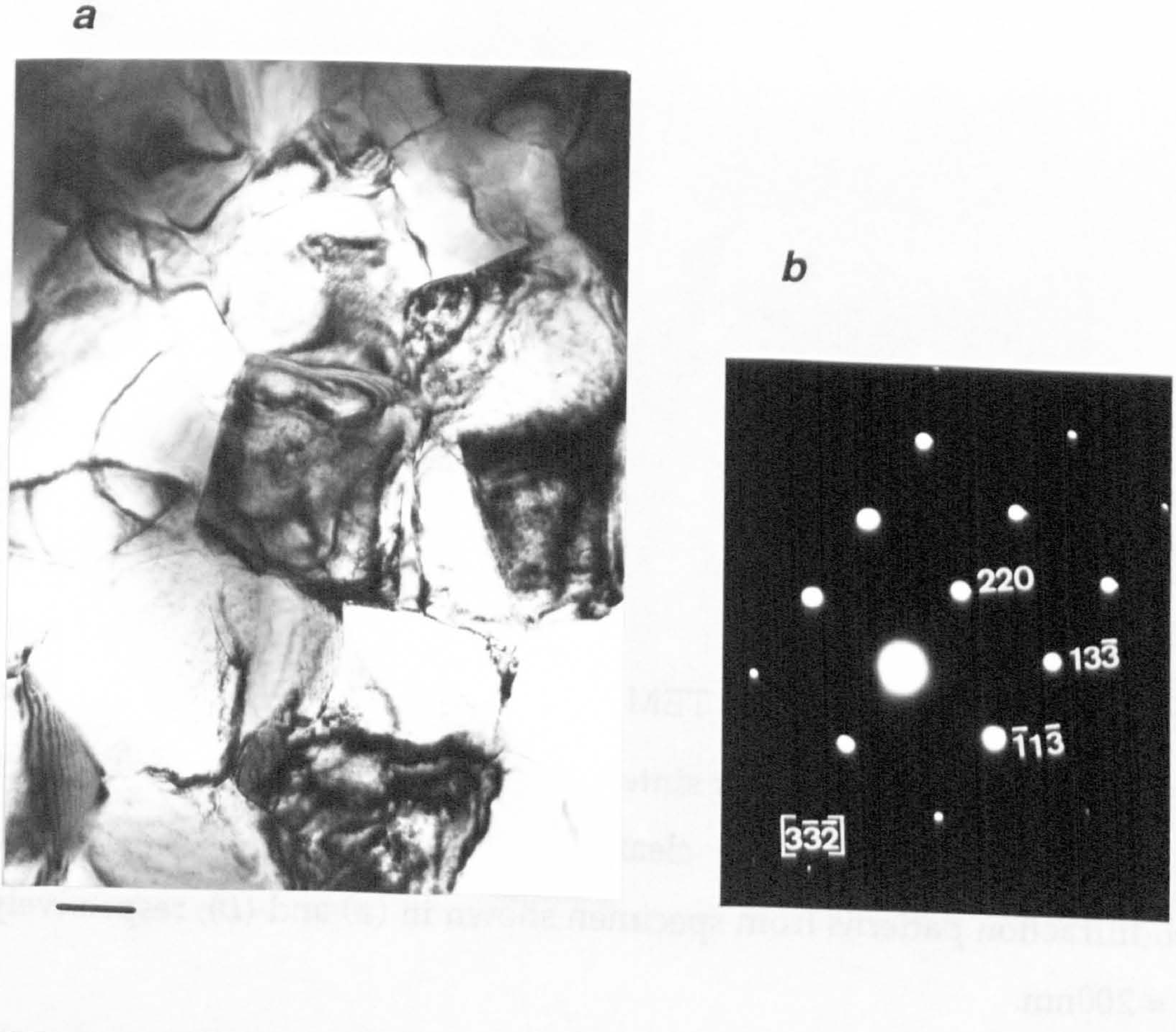
a
b
220
13$\bar{3}$
$\bar{1}$1$\bar{3}$
[3$\bar{3}\bar{2}$]

Figure 6.35 (***a, b***) Bright field TEM micrographs from planar sections of ZrO_2-Y_2O_3-TiO_2 pressed powder sintered at 1350 °C for 1 hour. The faceted grains (*c*- or ***t***-ZrO_2) present clean grain boundaries. (***c, d***) Electron microdiffraction patterns from specimen shown in (***a***) and (***b***), respectively. Bars = 200nm.

a

c

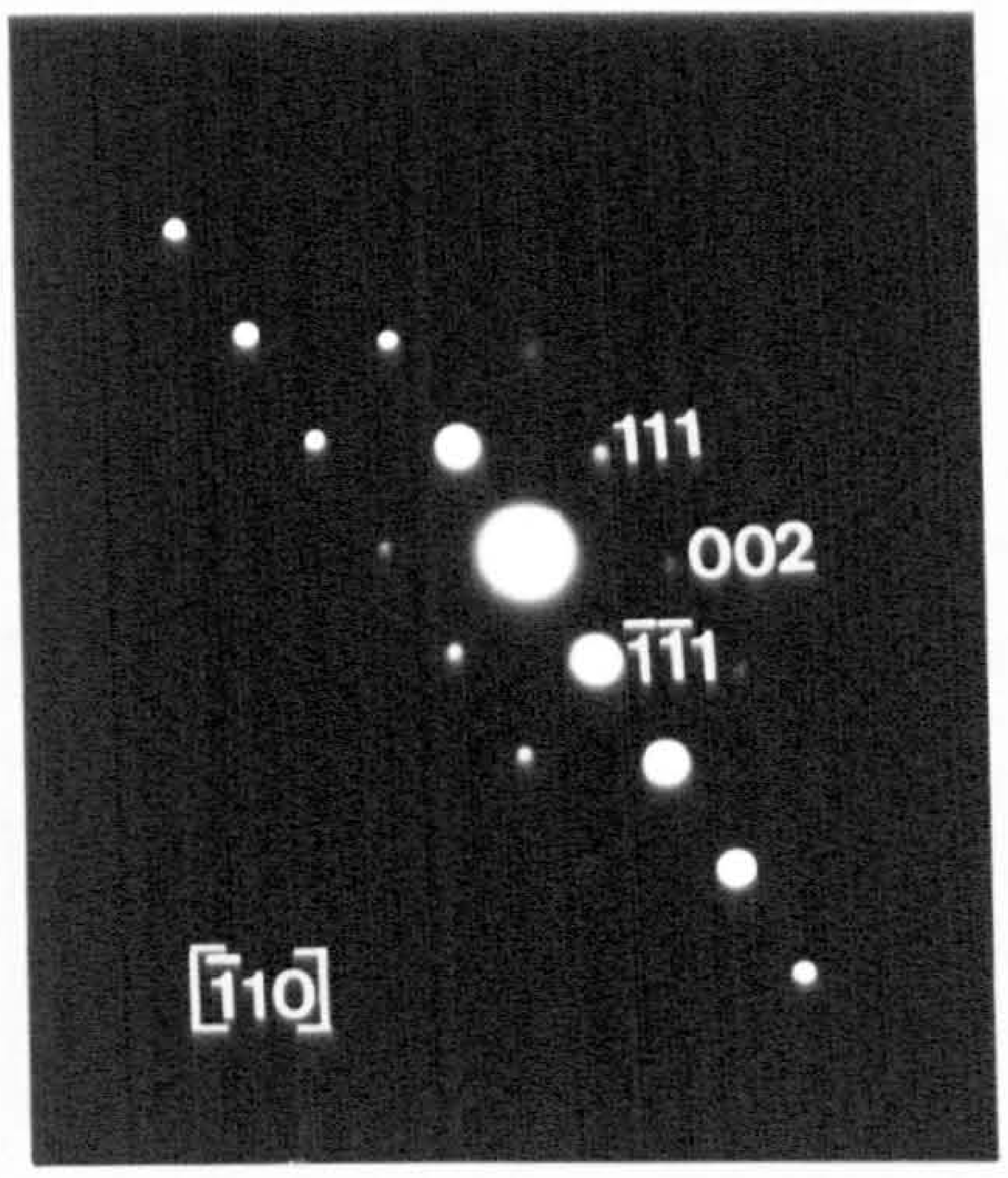

b

d

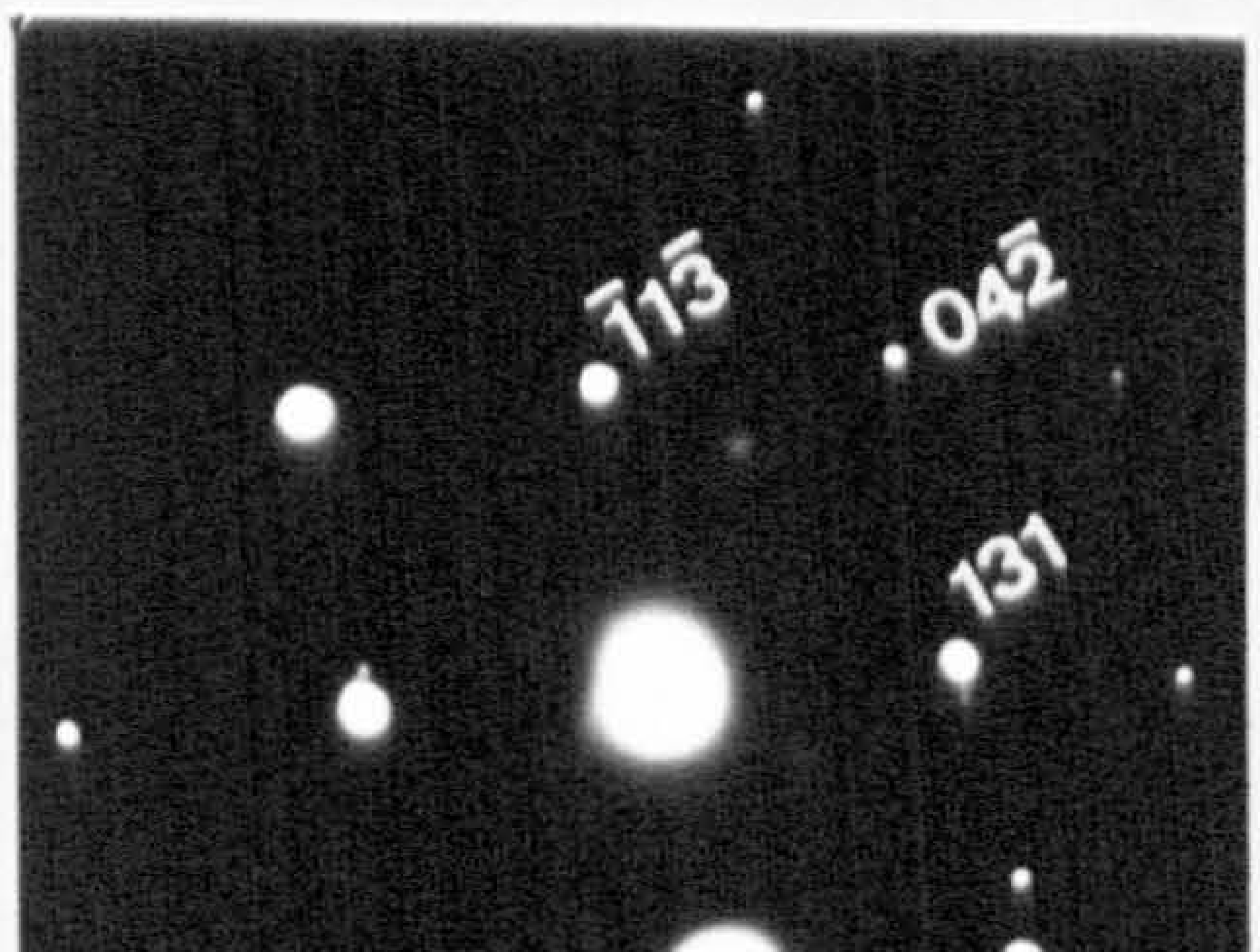

Figure 6.36 (***a***) Bright field TEM micrograph from a planar section of ZrO_2-Y_2O_3-TiO_2 pressed powder sintered at 1350 °C for 1 hour. Large faceted grains (> 200nm in diameter) are observed. (***b***) Electron microdiffraction pattern from specimen shown in (***a***). The spots correspond to reflections allowed for the *c*- and the *t*-ZrO_2. Bar = 200nm.

Figure 6.37 (***a***) Bright field TEM micrograph from a planar section of ZrO_2-Y_2O_3-TiO_2 pressed powder sintered at 1350 °C for 1 hour, showing a large central *m*-ZrO_2 grain as determined by the convergent beam electron diffraction pattern (***b***); excess Kikuchi bands intercept the zone $[0\bar{1}2]$, some first order Laue Zone (FOLZ) diffraction spots have been identified. Bar = 200nm.

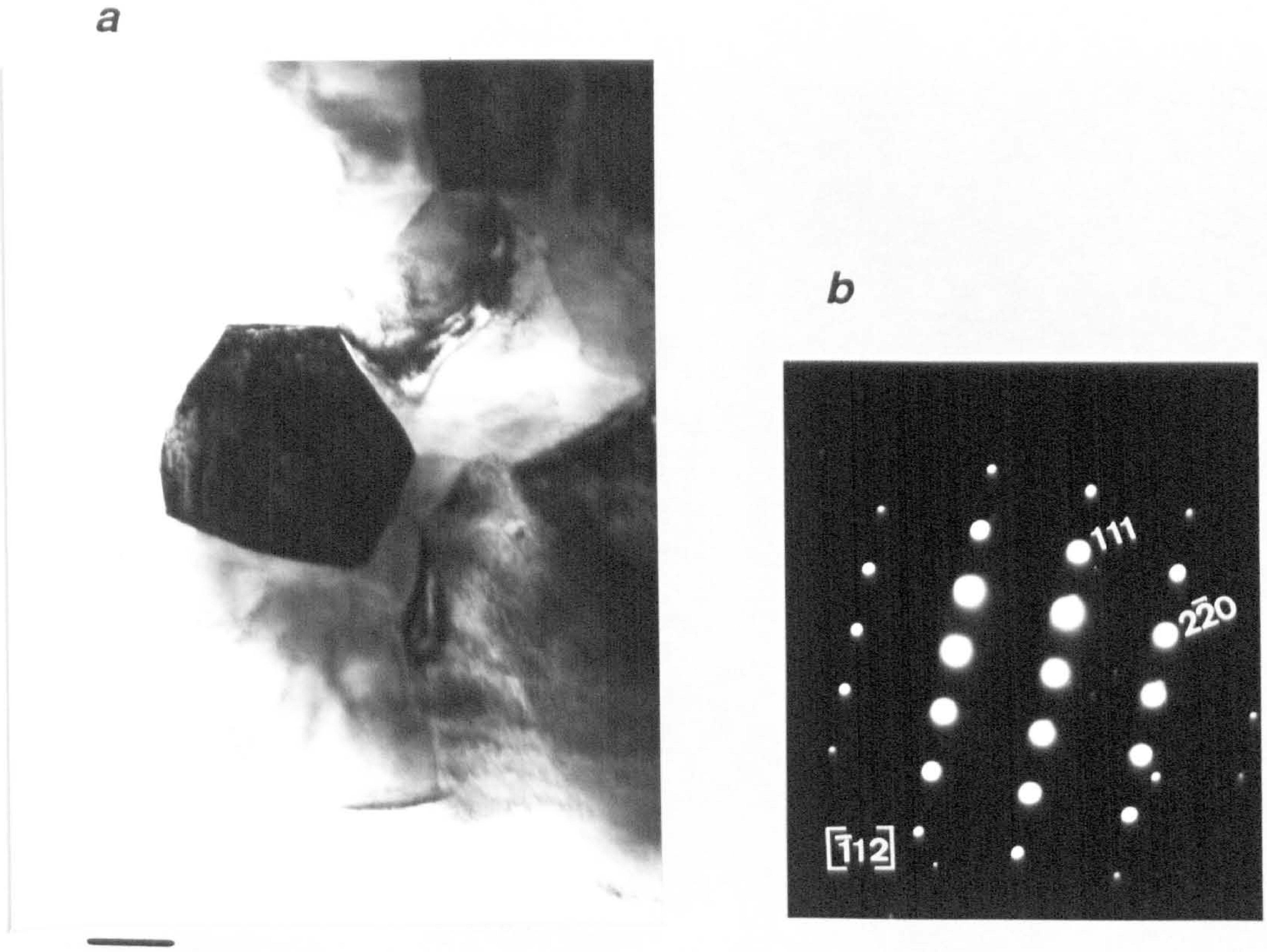
a
b
111
2$\bar{2}$0
[$\bar{1}$12]

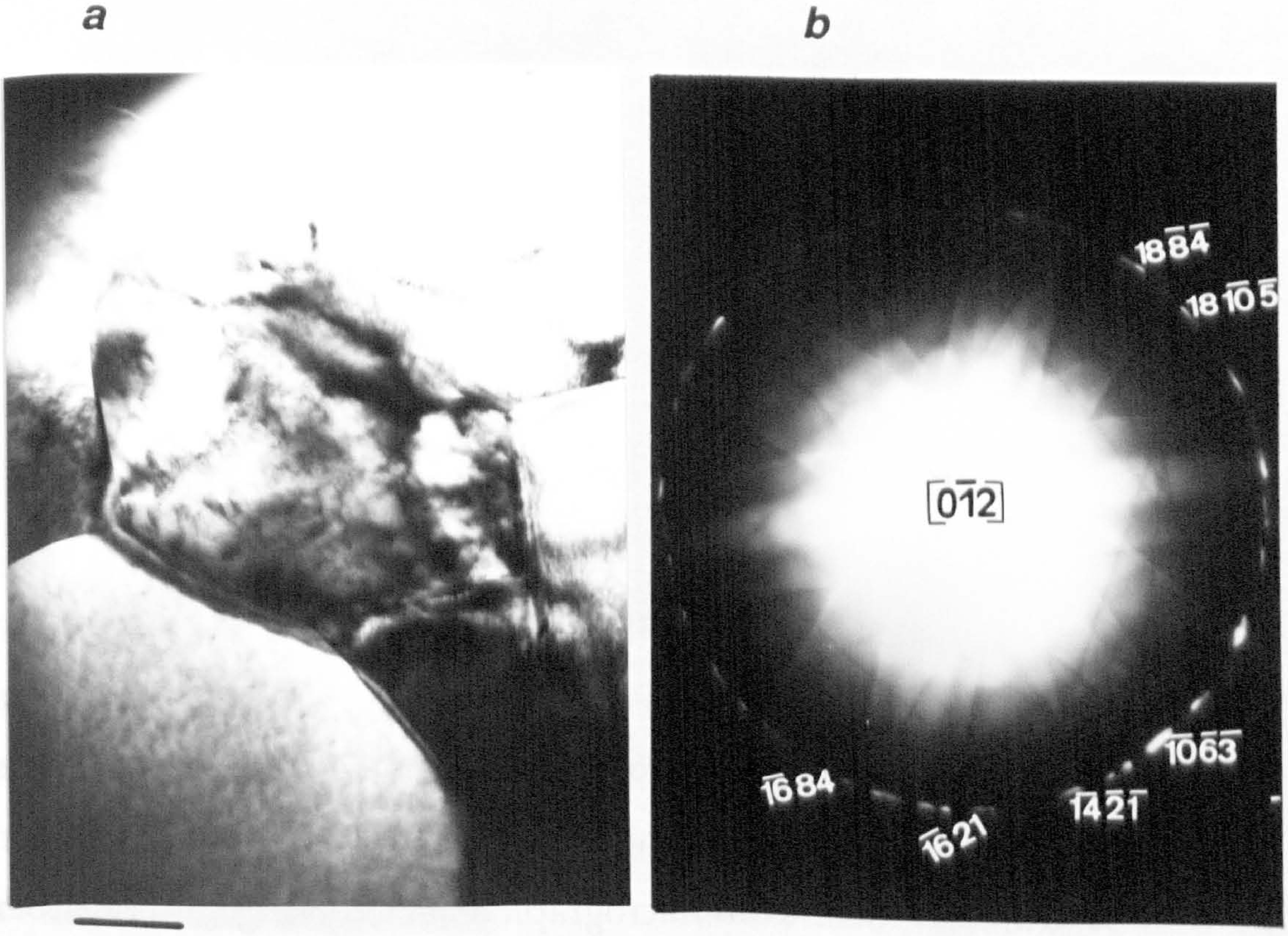
a
b
18$\bar{8}\bar{4}$
18$\bar{10}\bar{5}$
[0$\bar{1}$2]
10$\bar{6}\bar{3}$
$\bar{16}$84
$\bar{16}$21
14$\bar{2}\bar{1}$

Figure 6.38 (***a***) Bright field TEM micrograph from a planar section of ZrO_2-Y_2O_3-TiO_2 pressed powder sintered at 1350 °C for 1 hour, showing a twinned *c*-ZrO_2 grain. Abundant Moirè fringes are observed in the twins as shown in detail (***b***). (***c***) Electron microdiffraction pattern from specimen shown in (***a***). (***d***) Dark field TEM micrograph obtained using $\vec{g}$ = 200. Bar = 100nm.

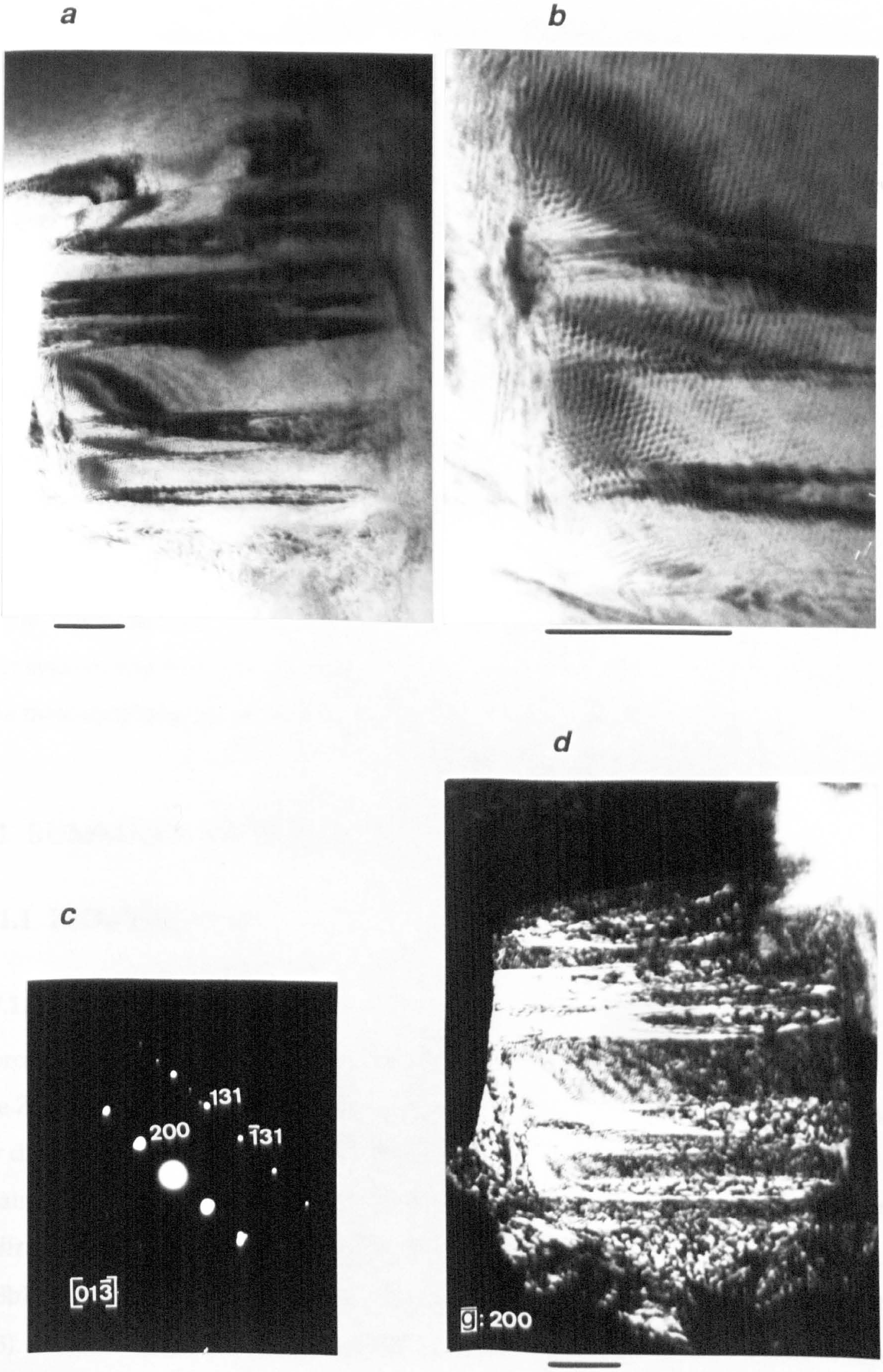
a
b
c
131
200
$\bar{1}$31
[01$\bar{3}$]
d
g: 200

7 GENERAL DISCUSSION

The first Section of this Chapter presents a summary of those aspects examined in the different systems under study: ZrO_2-Y_2O_3 and ZrO_2-Y_2O_3-TiO_2 coats, and ZrO_2-Y_2O_3 and ZrO_2-Y_2O_3-TiO_2 pressed and sintered bodies. The next Section will look more closely at the important trends and results detailed in the summary. Further Sections will examine the mechanisms involved during the plasma-sprayed coating formation and ZrO_2 phase transformations and how they affect the ceramic coat microstructure. The potential of the ZrO_2-Y_2O_3-TiO_2 system as TBCs is analysed in comparison to the well known ZrO_2-Y_2O_3.

In the literature the term *coating* has been used to designate the ceramic layer, or in some other cases the system i.e. ceramic and bond layers. The ceramic layer has also been designated as the *top coat* or *ceramic coat* to distinguish it from the bond coat. In this thesis the term *coating* has been given to the double layer ceramic coat/bond coat system, and the term *coat* to refer to one of those layers: *bond coat* or *ceramic coat*. The main emphasis in this study has been the ZrO_2-Y_2O_3-TiO_2 *coat*.

7.1 SUMMARY OF RESULTS

7.1.1 ZrO_2-Y_2O_3 Coat

7.1.1.1 TEM

Porous agglomerates of very small particles (20 nm in diameter) were observed in the ZrO_2-Y_2O_3 coat by TEM (Figure 6.1a, 6.2a). An amorphous phase was identified by diffuse rings in the electron diffraction pattern (Figure 6.1b). *t*- or *c*-ZrO_2 faceted grains growing in a porous matrix was also observed (Figure 6.3a), from the diffraction of which it was impossible to distinguish between *t*- and *c*-ZrO_2 (Figure 6.3b). Other specimen orientations allowed the identification of *t*-ZrO_2 (Figures 6.4, 6.5). Mottled contrast in larger grains corresponded to *m*- in *t*- or *c*-ZrO_2 (Figure 6.6).

7.1.1.2 SEM

The surface of the coat displayed material deposited as solidified splats or lamellae, some microcracks and evidence of unmelted material as agglomerates and dispersed particles (Figure 5.3b). Cross-sections of the coating ZrO_2-Y_2O_3/ NiCrCoAlY and substrate system were observed by SEM. The ZrO_2-Y_2O_3 coat had a more porous appearance than the NiCrCoAlY bond coat (Figure 5.4b). Fine pores (< 5μm) were distributed through the ceramic coat. Planar and narrow porosity between lamellae and voids of different dimensions (5-30 μm) were also identified. Cracks, some of them branched, were observed in the ceramic coat. Zones of high aluminium concentration were identified in the NiCrCoAlY bond coat (Figure 5.5b).

The surface of a specimen heated at 900 °C showed no evidence of any change (Figure 5.7b). However, some evolution of the microstructure was detected by SEM observation of the cross-section of the coat; the pores looked more rounded and the ends of the voids had been smoothed (Figure 6.8b).

7.1.1.3 XRD

The ZrO_2 phase distribution (molar fraction) calculated from the ceramic coat XRD pattern (Equations 2.2-2.4) corresponded to 0.03 *m*-, 0.25 *t*- and 0.72 *c*-ZrO_2. The XRD pattern of the powdered coat showed no significant differences in comparison with the as-sprayed ceramic. The ZrO_2 phase distribution found in the polished surface of the coat was 0.03 *m*-, 0.28 *t*- and 0.69 *c*-ZrO_2. The ZrO_2 phase distribution in the coat heated at 900 °C for 24 hours showed an increment of the *t*-ZrO_2 content at the expense of the *c*-ZrO_2 content; to 0.04 *m*-, 0.31 *t*- and 0.65 *c*-ZrO_2.

7.1.2 ZrO_2-Y_2O_3-TiO_2 Coat

7.1.2.1 TEM

TEM observations of the in the ZrO_2-Y_2O_3-TiO_2 coat were made on powdered and ion beam thinned specimens. Better TEM observations were achieved with ion beam thinned specimens. Due to the nature of the specimens and difficulties in specimen preparation, the study of the ZrO_2-Y_2O_3-TiO_2/NiCrCoAlY interface was restricted.

m-ZrO_2 twin laths (50 nm x 500 nm) presenting abundant Moirè contrast and a low concentration of titanium, were identified in the border of some grains of the powdered specimens (Figure 6.7). Laths growing in different directions impinging into each other were also observed (Figure 6.8).

Observations on the planar and cross-sections of the coating offered more electron-transparent areas suitable for the TEM analysis. Rounded grains (about 50 nm in diameter) corresponding to *c*- or *t*-ZrO_2 were observed exhibiting a mottled contrast (Figure 6.11). This rounded-grain microstructure presented inter-granular microcracks and porosity (Figure 6.12). *t*-ZrO_2 precipitates were observed to grow in a *c*-ZrO_2 matrix (Figure 6.14). Different *t*-ZrO_2 variants were identified separated by APBs (Figure 6.15). Undissolved TiO_2 (rutile) was present as rounded grains (Figure 6.18) and was identified by EDS and electron diffraction.

m-ZrO_2 was present in the coat as rounded grains (Figure 6.1), but mainly as twins (Figures 6.20-6.21). Some microcracks surrounding twined *m*-ZrO_2 grains were observed (Figure 6.21). Mosaics of *m*-ZrO_2 twins (Figures 6.22-6.23) exhibited abundant Moirè contrast and low titanium concentration.

7.1.2.2 SEM

7.1.2.2.1 Type 1 Specimens

Microstructural discontinuities were observed through the ZrO_2-Y_2O_3-TiO_2 coat; microcracks (Figure 5.3a), coarse and fine porosity similar to those described in the ZrO_2-Y_2O_3 coat were identified. However, a higher proportion of fine porosity was found in the ZrO_2-Y_2O_3-TiO_2 coat (Figure 5.4a). Phases with different titanium concentrations were identified in the ZrO_2-Y_2O_3-TiO_2 coat (Figure 5.6).

7.1.2.2.2 Type 1 Specimen Heated at 900 °C

The surface of the coat heated at 900 °C for 24 hours showed no apparent difference to the as-sprayed coat (Figure 5.7a). However, cross-sectional observations allowed some evolution in the microstructure of the coat, such as the smoothing of voids and pores, to be investigated (Figure 5.8a).

7.1.2.2.3 Type 2 Specimens

A second ZrO_2-Y_2O_3-TiO_2/NiCrCoAlY coating identified as "type 2", a product of another batch of plasma spraying was also analysed by SEM (Figure 5.9a). Comparing the SEM observations of the type 2 cross section with those of type 1 specimens, the concentration and size of the ceramic coat voids were smaller. Phases with different titanium concentration were also identified (Figure 5.9b). Unmelted or incompletely melted ceramic material could also be identified. Round pores, voids and cracks were distributed through the coat thickness (Figure 5.9b). Aluminium-rich zones were more localized in the bond coat of type 2 specimens (Figure 5.9a).

7.1.2.2.4 Fractography

The fracture observed in the as-sprayed ZrO_2-Y_2O_3-TiO_2 had an interlamellar appearance (Figure 5.15a); the cracks propagated mainly through the interlamellar areas without appreciable rupture of the lamellae. The ceramic coat cooled by liquid nitrogen displayed a fracture with an intralamellar appearance (Figure 5.15b). It was possible to identify a columnar microstructure of the deposited lamellae (about 5 µm thick).

7.1.2.3 XRD

The ZrO_2 phase distribution (molar fractions) calculated from the ceramic coat XRD pattern corresponded to 0.15 *m*-, 0.46 *t*- and 0.39 *c*-ZrO_2. The concentration of *t*-ZrO_2 in the ZrO_2-Y_2O_3-TiO_2 coat was almost twice the value found in the ZrO_2-Y_2O_3 coat (0.25 *t*-ZrO_2.). The ZrO_2 phase distribution found in the polished surface of the coat was 0.13 *m*-, 053 *t*- and 0.34 *c*-ZrO_2. The increment of the *t*-ZrO_2 content after heating the coat at 900 °C for 24 hours was more evident than in the ZrO_2-Y_2O_3 coat; 0.16 *m*-, 0.68 *t*- and 0.16 *c*-ZrO_2.

Type 2 specimens showed a slightly different ZrO_2 distribution in comparison with type 1 specimens; 0.07 *m*-, 0.54 *t*- and 0.39 *c*-ZrO_2. $ZrTiO_4$ was identified in this coat (Figure 4.4).

7.1.3 Thermally Treated ZrO_2-Y_2O_3-TiO_2 Coat

7.1.3.1 TEM

7.1.3.1.1 Coats Treated at 1400 °C

Complex microstructures were observed in ZrO_2-Y_2O_3-TiO_2 coats treated at 1400 °C (Figures 6.24a, b). *c*-, *t*- and *m*-ZrO_2 particles were identified by TEM. Porous agglomerates were also observed (Figures 6.25a, b). Large faceted grains of *c*- or *t*-ZrO_2, about 200 nm in diameter indicated grain growth (Figure 6.26). Some large faceted *t*-ZrO_2 exhibited clean grain boundaries and intra-granular microcracks as a result of specimen handling (Figure 6.27). Large twinned *t*-ZrO_2 grains (> 400 nm in diameter) exhibited a high titanium concentration (Figure 6.28). *m*-ZrO_2 laths were observed in the border of some grains (Figure 6.29).

7.1.3.1.2 Coats Treated at 1600 °C

A very porous "sponge-like" microstructure was observed in the specimen treated at 1600 °C (Figure 6.30b). Aggregates of small *t*-ZrO_2 grains, about 50 nm in diameter were observed (Figure 6.32). Bigger grains (>300 nm in diameter) were observed displaying amorphous grain boundary pockets (Figure 6.30a). Slipped *m*-ZrO_2 grains were also observed (Figure 6.31a). Some grains exhibited an equiaxed grain nanostructure (Figure 6.33).

7.1.3.2 SEM

7.1.3.2.1 Failed Coats

Specimen above the thickness specifications (300-500 μm) failed after heating above 700 °C (Figure 5.12). The ceramic coat spalled off, leaving the bond coat exposed (Figure 5.10a). Crystals with high concentration of nickel (Figure 5.10b) were identified in the bond coat after the ceramic coat spalled off. The SEM observation of the failed coat cross-section (Figure 5.13a) revealed a bond coat very irregular in thickness; in some points the ceramic was in direct contact with the substrate. EDS mapping of nickel confirmed the discontinuities in the bond coat (Figure 5.13b).

Distribution of relative porosity and frequency distribution of pores with area ≤ 2 μm^2 (Figures 5.14a, b) were obtained by image analysis of SEM micrographs from the coat cross-sections. At least three population of pores were distinguished. After heating at 900 °C for 24 hours some changes in these distributions were observed although the whole profile was maintained; there was a reduction of the pores having an area < 0.1 μm^2 and an increase in the pores in the range 0.1-0.3 μm^2.

7.1.3.2.2 *Fractography*

ZrO_2-Y_2O_3-TiO_2 coat thermally treated at 900, 1000, and 1100 °C displayed fractures with an intralamellar appearance (Figure 5.16, 5.17). Samples of the coat heated at 1200 and 1400 °C showed transgranular fractures (Figures 5.18, 5.19). The columnar microstructure of the lamellae collapsed in the coat heated at these temperatures, giving rise to small grains (about 1 µm in diameter).

7.1.3.3 XRD

The ZrO_2 phase distribution in the ZrO_2-Y_2O_3-TiO_2 coat (Figure 4.5b) was maintained approximately after thermal treatments (up to 1200 °C) that involved slow cooling rates (in argon). Slight increases of *c*- and *m*-ZrO_2 at the expense of *t*-ZrO_2 were observed at temperatures higher than 900 °C (Figure 4.5b). By contrast, thermal treatments that involved fast cooling rates (air) increased the *t*-ZrO_2 concentration, particularly at temperatures $\geq$ 1200 °C (Figure 4.5a).

7.1.4 Sintered Bodies

Pressed disks of ZrO_2-Y_2O_3 and ZrO_2-Y_2O_3-TiO_2 (A) powders, and ZrO_2-Y_2O_3-TiO_2 (B) powder used for the plasma spraying were sintered at different temperatures.

7.1.4.1 TEM

TEM observations of the planar section of the ZrO_2-Y_2O_3-TiO_2 (B) sintered at 1350 °C showed large *c*- or *t*-ZrO_2 faceted grains (> 200 nm in diameter) displaying clean grain boundaries, dislocations and some deformation (Figures 6.34-6.36). *m*-ZrO_2 faceted grains (Figure 6.37) and twinned particles with Moirè contrast (Figure 6.38) were also observed.

7.1.4.2 Density

The highest density was found in the bodies sintered at 1350°C (Table 5.2). At this temperature the ZrO_2-Y_2O_3 pressed and sintered body had almost reached the theoretical density while the density of ZrO_2-Y_2O_3-TiO_2 (A) and (B) pressed and sintered bodies were 82 and 78 % of the theoretical density, respectively. The density of these decreased when the sintering temperature was increased (Figure 5.20).

7.1.4.3 SEM

7.1.4.3.1 ZrO_2-Y_2O_3 Sintered Bodies

It was difficult to identify the individual grain size in the surface of the ZrO_2-Y_2O_3 disks sintered at 1350 and 1400 °C as it was very small. The grains appeared tightly compacted (Figure 5.21a) while the solid sintered at 1550 °C showed small grains (about 1 µm in diameter) and some larger grains (about 5 µm in diameter, Figure 5.21b).

7.1.4.3.2 ZrO_2-Y_2O_3-TiO_2(A) Sintered Bodies

The surface of the ZrO_2-Y_2O_3-TiO_2 (A) disk sintered at 1400 °C presented grains about 2 µm in diameter (Figure 5.22a) while the product sintered at 1550 °C displayed grown grains (about 6 µm in diameter) and some elongated grains (20-30 µm in diameter) which had a higher titanium concentration (Figure 5.22b).

7.1.4.3.3 ZrO_2-Y_2O_3-TiO_2(B) Sintered Bodies

The ZrO_2-Y_2O_3-TiO_2 (B) disk sintered at 1400 °C presented an irregular distribution of grains with different shapes and sizes, <5 µm in diameter (Figure 5.24a). At 1550 °C some grains had grown at the expense of others. Elongated grains with a high concentration of titanium were also detected (Figure 5.24b).

7.1.4.4 XRD

Most of the ZrO_2 from the ZrO_2-Y_2O_3 and ZrO_2-Y_2O_3-TiO_2(A) sintered bodies was present as *t*-ZrO_2 (Figures 4.7a and b, respectively). The *c*-ZrO_2 mole fraction increased at the expense of the *c*-ZrO_2 concentration as the sintering temperature increased. The ZrO_2-Y_2O_3-TiO_2(B) sintered body consisted of *m*-, *c*-, and *t*-ZrO_2. At a high sintering temperature the *m*-ZrO_2 is reduced and the *t*-ZrO_2 increases slightly (Figure 4.7c).

Comparing the XRD patterns of the ZrO_2-Y_2O_3-TiO_2(A) and ZrO_2-Y_2O_3 pressed and sintered bodies, shifts of the $(004)_t$ reflection towards a higher 2θ angle, and the $(400)_t$ reflection towards a lower 2θ angle were observed. The *t*-ZrO_2 *c* axis is expanded while the *a* axis is contracted, the *c/a* relation increased from 1.007 to 1.012 due to the addition of TiO_2.

7.2 ABOUT THE RESULTS

7.2.1 SEM

The SEM contrast observed in the polished cross-sections of the coatings allowed the identification of the different components of the coating and the evaluation of the porosity of the ceramic coat (i.e. Figure 5.9a). In some cases, the combined use of the secondary and backscattered electron detectors allowed obtaining information on the topography and detection of differences in the composition. Titanium-rich phases exhibited a high backscattered contrast in a zirconium, yttrium matrix due to the difference in atomic number. Zirconium and yttrium produce more backscattered electrons than titanium because they have higher atomic number. Thus, titanium-rich zones appear darker (i.e. Figure 5.9b). By the same principle it was possible to detect aluminium-rich zones in the NiCrCoAlY bond coat (i.e. Figure 5.9a).

The image analysis of the ceramic coat cross-section provided data to study the porosity distribution. This distribution was useful to quantify the changes in the porosity after thermal treatment of the ceramic. The simple inspection of the micrographs was inappropriate for this purpose since the changes registered were very small.

The contrast observed in the polished cross sections of the coatings were unsuitable for a close look at the lamellae microstructure. In this case, the fracture analysis provides a better visualization of the columnar microstructure of the ceramic coat lamellae.

7.2.2 TEM

7.2.2.1 Specimen Preparation

Examination of the ceramic coat by TEM provided a detailed view of the polycrystalline microstructure of the lamella. Although some observations were made on the powdered specimens, better results were obtained by ion beam thinning of the specimens; more electron transparent zones were available for the TEM analysis. Pre-thinning of the specimen was made manually (Section 3.4.3), this pre-thinned specimen thickness was about 100 μm for the coating cross-section. Further polishing caused pulling out of the material with a consequent deterioration in the specimens. The differences in sputtering yield (Section 3.4.2) of each phase: substrate, bond coat and ceramic coat, make it very difficult to obtain a suitable area for TEM analysis of the interfaces (Figure 6.9). Rotation and control of the sputtering angle alleviate this problem. However, the initial specimen thickness is decisive in obtaining desirable results by the ion beam thinning. Good results have been reported in the preparation of cross-sectional specimens of ceramic coats by pre-thinning the specimen with a Dimpler to 20-30μm of thickness prior to ion beam sputtering **(Lelait et al. 1992, Unal et al. 1990)**. Unfortunately this equipment was unavailable in the present study. Therefore, the study of the bond coat-ceramic coat interface was restricted to observations by SEM. TEM was used in the study of the ceramic coat. Planar and cross-sectional specimens were prepared by ion beam sputtering. The thickness of the pre-thinned planar section was about 60μm. Reasonable results were obtained after ion-beam thinning and TEM observations were made.

7.2.2.2 Identification of *t*-ZrO_2

Discrimination of *c*- and *t*-ZrO_2 by electron diffraction proved difficult since their lattice parameters are very close and thus their electron diffraction patterns were often similar. However, reflections obtained from some zone orientations in the specimen, i.e. <$\bar{1}$11>, permitted the identification of *t*-ZrO_2 properly. Appropriate tilting of the specimen to locate these zones was restricted by the small size of the crystals and the thickness of the specimen itself. Therefore, in some cases it was difficult to identify accurately the symmetry of the observed grains. In some cases the characteristic morphology of *t*-ZrO_2 grains helped in determining the grain symmetry.

7.2.3 XRD

Equations 2.2-2.4 used in the calculation of the approximate *c*-, *m*- and *t*-ZrO_2 molar fractions in the ceramic coatings and the pressed and sintered bodies provided a suitable method to evaluate the ZrO_2 phase distribution and to follow its evolution after thermal treatment. XRD results give information on the bulk specimen, while TEM information corresponds to a reduced area of the specimen. For instance, TiO_2 (rutile) grains were identified by TEM in type 2 ZrO_2-Y_2O_3-TiO_2 coats (Figure 6.18), however the corresponding XRD pattern (Figure 4.4) showed no reflections characteristic of TiO_2.

The ceramic coats exhibited X-ray intensities almost one order of magnitude lower than the equivalent pressed and sintered bodies. This made more precise the quantification in the latter specimens. The lower X-ray intensities in the ceramic coats might be linked with the inherent lower thickness and density.

7.2.4 Thermal Treatment

The purpose of performing thermal treatments of the ZrO_2-Y_2O_3-TiO_2/NiCrCoAlY coating in argon and air was to investigate the oxidation of the bond coat and its effect on the stability of the coating. It has been established that oxidation of the NiCrCoAlY bond coat has a deleterious effect on the stability of the ZrO_2-Y_2O_3/ NiCrCoAlY coatings (**Sun et al. 1993a, b**).

The heat treatment of the ZrO_2-Y_2O_3-TiO_2/NiCrCoAlY coatings consisted basically in soaking them at the treatment temperature for 24 hours whether in argon or air (Section 3.5.2). The samples heated in argon were left to cool inside the furnace under a current of argon to eliminate possible oxidation of the bond coat during the cooling process. Another variable to evaluate was the thermal shock resistance of the coating. For this reason the samples treated in air were quenched to room temperature after heating at the treatment temperature.

Only coatings with an irregular layer of NiCrCoAlY bond coat failed after thermal treatments at temperatures higher than 700 °C (Sections 7.5.1). An extensive study of the bond coat oxidation and its effect in the stability of the coating should include evaluations at longer periods of heat treatment and thermal cycling. Unfortunately the lack of the specimens prevented the study from being extended in this direction. However, it was possible to examine other properties of the ceramic coat of thermal treated specimens such as ZrO_2 phase distribution and microstructure which helped to make advances in the understanding of the ZrO_2-Y_2O_3-TiO_2 system for use as TBCs (Section 7.6).

7.3 MECHANISM OF FORMATION OF THE MICROSTRUCTURE OF THE PLASMA-SPRAYED COATING

7.3.1 Lamellae Formation

The microstructure of the ZrO_2-Y_2O_3 and ZrO_2-Y_2O_3-TiO_2 coats exhibited a layered or lamellar structure, mostly parallel to the substrate surface. The lamellae are individual entities that result from the solidification of the plasma-sprayed molten ceramic. During the passage through the plasma arc, the material is heated to in excess of 3000 °C (Harmsworth and Stevens 1992b). However, unmelted material was identified on the surface of the ZrO_2-Y_2O_3 and ZrO_2-Y_2O_3-TiO_2 coats (Figures 5.3a and b, respectively) and occluded into the lamellae (Figure 5.9b). As discussed later, this unmelted material affects the final microstructure of the coating.

The internal microstructure of the lamellae is affected by the velocity and viscosity of the particles reaching the surface (McPherson 1989, Taylor et al. 1992). These are given by the plasma parameters (such as gas flow, current density, torch geometry), spraying variables (deposition temperature of the substrate, surface transverse rates, thickness per pass), and powder density and morphology, which are outside the scope of this thesis.

7.3.2 Lamellae Microstructure

The splats (molten ceramic) experience rapid cooling rates as they reach a cooler surface at high velocities. The rapid cooling rate of the splats determines the microstructure of the lamellae since it stimulates crystal nucleation. The crystal size and morphology within the lamellae are functions of the relative nucleation and growth rates of the crystals from the molten material (**McPherson 1989**). The small grain size (20-50 nm) observed in the ZrO_2-Y_2O_3 (Figure 6.1a) and ZrO_2-Y_2O_3-TiO_2 (Figure 6.12a) is evidence of a high nucleation rate promoted by the rapid cooling. The rounded shape of some grains is an indication of the presence of a liquid phase involved in the process. However, there was some amorphous phase identified by TEM, surrounding the rounded grains and this sometimes exhibited an "sponge-like" microstructure (Figure 6.30b). The amorphous phase is formed by the absence of nucleation in the time interval between the melting point and the glass transition temperature (**McPherson 1989**).

A different crystalline structure was also observed in the coats consisting of very fine equiaxed grains (i.e. Figure 6.3a). **Harmsworth and Stevens (1992b)** found a similar microstructure in a ZrO_2-(8 wt%)Y_2O_3 coat, and suggested that it was caused by changes in the heat transfer during the splat cooling. Rapid crystal growth leads to rapid evolution of the heat of fusion, and an increase in temperature and suppression of further nucleation. However, if the crystal growth is relatively slow further nucleation occurs as the liquid undercools and a very fine equiaxed structure is formed

Fracture of the ZrO_2-Y_2O_3-TiO_2 coat, displayed an internal columnar microstructure of the lamellae (Figure 5.15). This columnar microstructure formed in the lamellae has been explained by **McPherson (1989)** as a consequence of a preferential crystal growth direction. Rapid nucleation occurs at the cooler surface of the flattened droplet with large undercooling and the crystal grows rapidly in the opposite direction to the heat flow forming a columnar grain structure.

7.3.3 Microcracking

Microcracks were observed on the surface of the ZrO_2-Y_2O_3 (Figure 5.3b) and ZrO_2-Y_2O_3-TiO_2 (Figure 5.3a) coats, mostly perpendicular to the lamellae. These microcracks are caused by the internal stresses initiated during the rapid cooling of the splats; stresses produced from the constraint of the thermal contraction of the lamella by the underlying material during cooling. These cracks will not form in metallic coatings because the thermal strain may be accommodated by plastic flow (Pawloski et al. 1985, Heintze and McPherson 1988a).

7.3.4 Porosity

Porosity of different natures was distributed through the ZrO_2-Y_2O_3-TiO_2 and ZrO_2-Y_2O_3 coats (Figures 5.4a, b respectively). Fine porosity included small rounded pores, possibly originating from the gas entrapped during the plasma spraying process, and planar porosity between lamellae. Coarse porosity was mainly localized as voids in the interstices of the lamellae. The unmelted material present in the coat (i.e. Figure 5.9b) reduces the filling of interstices in the splats during the plasma spraying process, promoting the coarse porosity (McPherson 1989). The study of porosity distributions in the ZrO_2-Y_2O_3-TiO_2 coat allowed the identification of at least three porosity populations (Figures 5.14a, b). These results are similar to those reported by McPherson (1989) in Al_2O_3 coatings; he described a bimodal distribution of pores including coarse and fine pores.

Summarising, the mechanisms of formation of the plasma-sprayed ceramic coat determines its heterogeneous and complex microstructure as was evidenced by the TEM and SEM observations. The plasma-sprayed melted material, deposited as splats undergoes high cooling rates which promote rapid nucleation and grain growth in a columnar structure in the opposite direction to the heat flow. Changes in the heat transfer modify the splat-cooling rate with consequent varied effects in the microstructure, such as small grain size, amorphous phase, porous agglomerates and equiaxed grained microstructures. Constraints of the thermal contraction of the splats by the underlying material create internal stresses that the ceramic material is unable to accommodate, causing the formation of microcrack nets. The discontinuous nature of the ceramic deposition by plasma spraying is the origin of a lamellar structure that retains fine and coarse porosity. The unmelted material contributes to the formation of coarse porosity as it prevents the splat interstices from filling. This microstructure plays a very substantial role in determining the performance of the ceramic coat as a TBC.

7.4 ZrO_2 PHASE TRANSFORMATIONS

In this section the different ZrO_2 phase transformations mechanisms that might take place in the ceramic coat during the plasma spraying process or in the as-sprayed condition are discussed.

7.4.1 *c*→ *t*-ZrO_2 Diffusionless Transformation

During the passage through the plasma arc, the ceramic material is heated to temperatures in excess of 3000 °C (**Harmsworth and Stevens 1992b**). Subsequently it is cooled down at a rapid quenching rate of about 10^6 Ks^{-1} (**Anderson 1980**). This prevents any diffusion from occurring.

Taking a look at the free energy versus composition curves for the ZrO_2-Y_2O_3 system (Figure 2.6) which is for a temperature so low that diffusive jumps of atoms cannot occur (**Heuer and Rühle 1983, Heuer et al. 1987, 1988; Butler 1985a**), it is possible to understand the mechanism of the transformation that has taken place in the ZrO_2-Y_2O_3 coat during the plasma spraying. The Y_2O_3 concentration in the ZrO_2-Y_2O_3 coat is 8 wt%, at this concentration the quenched ZrO_2 follows the changes: *melt*→ *c*-ZrO_2 and then a composition invariant *c*→ *t*-ZrO_2 transformation with a consequent reduction of the free energy.

The *t*-ZrO_2 product of this diffusionless *c*→ *t*-ZrO_2 transformation is stable with respect to the monoclinic transformation, and it has been denoted as "non-transformable" to distinguish it from the metastable *t*-ZrO_2. This non-transformable *t*-ZrO_2 has been described as an ubiquitous component in plasma-sprayed ZrO_2-(8 wt%) Y_2O_3 coats (**Miller et al. 1981**).

Similar free energy versus composition diagrams might be used to explain the mechanism of the *c*→ *t*-ZrO_2 transformation in the ZrO_2-Y_2O_3-TiO_2 coat during the plasma spraying process.

7.4.1.1 *t*-ZrO_2 Microstructure

Single domain *t*-ZrO_2 grains (i.e. Figure 6.5) and *t*-ZrO_2 grains exhibiting mottled contrast (Figure 6.14), twinning (Figure 6.28) and APBs (Figure 6.15) were identified in the ZrO_2-Y_2O_3 and ZrO_2-Y_2O_3-TiO_2 coats. **Alpérine and Lelait (1994)** described these microstructural features in a ZrO_2-(8.5 wt%)Y_2O_3 coat. They have been attributed to the non-transformable *t*-ZrO_2 (**Chaim et al. 1985, Miller et al. 1981, Isihizawa et al. 1986, Takeheshi et al. 1986**).

The mottled structure observed for example in Figure 6.14, sometimes called "tweed-like", coarsens and develops into a twin structure. The *t*-ZrO_2 twins (i.e. Figure 6.28) are attributed to the theoretically equal probability that the cubic lattice distortions leading to tetragonal symmetry could be along any of the original <100> axes (**Alpérine and Lelait 1994**); in other words, any of the cubic *a* axes can become the *c* axis of the *t*-ZrO_2. The APBs observed in Figure 6.15c separate different *t*-ZrO_2 domains nucleated at different points of the grain (Figure 6.15b). Thermodynamically, the existence of more than one orientation variant of *t*-ZrO_2 provides a configurational freedom to reduce the total elastic energy arising from the crystal lattice misfit at the *c*/*t*-ZrO_2 boundaries and at the boundaries between different *t*-ZrO_2 orientation variants (**Fan andChen 1995, Heuer et al. 1988**).

However, single domain *t*-ZrO_2 showed none of these microstructural components that indicate the formation of different *t*-ZrO_2 variants during the *c* → *t*-ZrO_2 transformation. Therefore, this transformation might also lead to single domain *t*-ZrO_2. This observation finds correspondence with the findings of **Fan and Chen (1995)**. They stated that transformation twinning will only occur if the *c*-ZrO_2 parent cannot change its volume during the transformation, e.g. a grain constrained in a polycrystalline assembly. Otherwise the final product of the transformation is a single domain *t*-ZrO_2 grain.

7.4.1.2 Effect of *t*-ZrO_2 Microstructure on the Coat Properties

The microstructural components observed in *t*-ZrO_2 provide the coat with a toughening mechanism based in the consumption of energy from a propagating crack by deflection of the crack when the tip reaches one of these components (**Heuer et al. 1987**). *t*-ZrO_2 is associated with a higher toughness in comparison to *c*-ZrO_2, by about three times (**Michel et al. 1993**). **Alpérine and Lelait (1994)** explained the higher toughness due to the lower symmetry of *t*-ZrO_2; there are less cleavage planes in *t*- than in *c*-ZrO_2. Therefore, a crack tip reaching a *t*-ZrO_2 grain is deviated to cleavage planes with the consequent diminution of the crack propagation energy.

7.4.2 Other Transformations

In the light of the free energy diagrams, the final composition of the ZrO_2-Y_2O_3 and ZrO_2-Y_2O_3-TiO_2 coats should be *t*-ZrO_2 only. **Prater and Moss (1983)** found that some ZrO_2-(6-8 wt%)Y_2O_3 coats consisted entirely of *t*-ZrO_2. **McPherson (1989)** reported 95 wt% *t*- and 5 wt% *m*-ZrO_2 in a ZrO_2-(8 wt%)Y_2O_3 plasma-sprayed coat and 85 wt% *t*-, 12 wt% *c*- and 3 wt% *m*-ZrO_2 in a ZrO_2-(6 wt%)Y_2O_3 plasma-sprayed coat. **McPherson and Houghton (1984)** suggested that *c*- and *m*-ZrO_2 contained in some ZrO_2 (6-8 wt%) Y_2O_3 coats were the result of the retention of some unmelted particles within the coat. However, the proportion of *c*-ZrO_2 found in the present study in the as-sprayed ZrO_2-Y_2O_3 and ZrO_2-Y_2O_3-TiO_2 coats (0.72 and 0.39 mole fraction, respectively) are rather high to agree with this premise; the proportion of unmelted material in the as-sprayed ZrO_2-Y_2O_3 and ZrO_2-Y_2O_3-TiO_2 coats are not enough to contribute to the observed high concentration of *c*-ZrO_2. Therefore, some other processes are probably occurring during the plasma spraying of the ZrO_2-Y_2O_3 and ZrO_2-Y_2O_3-TiO_2 coats in this study.

During the plasma spraying, heat diffusion becomes less efficient after the first splats have solidified. Therefore, the cooling rate is reduced in the outer layers. Likewise, a reduction of the cooling rate occurs during the cooling of an individual splat; the columnar grains, developed by a series of nucleation and growth stages, reduce the rate of cooling of the rest of the splat due to insulation from the underlying material (**Harmsworth and Stevens 1992b**). The reduction of the splat cooling rate might allow some diffusional process to occur.

7.4.3 Mechanisms of $c \rightarrow t \rightarrow m$-$ZrO_2$ Transformations

7.4.3.1 ZrO_2-Y_2O_3 Coat

In reference to the ZrO_2-Y_2O_3 phase diagram (Figure 2.11), if diffusion is allowed during the cooling of the splat in the ZrO_2-Y_2O_3 system, the *c*-ZrO_2 would decompose into a high-Y_2O_3 *c*-ZrO_2 and a low-Y_2O_3 *t*-ZrO_2. The latter would undergo further transformation into *m*-ZrO_2. Below 1800 °C diffusion becomes sluggish and the transformations are of diffusionless type. It has been widely accepted that the $t \rightarrow m$-ZrO_2 transformation has a martensitic nature (**Anderson 1988**).

7.4.3.2 ZrO_2-Y_2O_3-TiO_2 Coat

Due to the high content of TiO_2 (26.4 mole %) present in the ZrO_2-Y_2O_3-TiO_2 coats, a direct extrapolation using the ZrO_2-Y_2O_3 phase diagram cannot be made without some other considerations. On the other hand the ZrO_2-TiO_2 phase diagram (Figure 2.15) does not display a *c*-ZrO_2 zone, thus the use of this diagram is unable to predict the presence of *c*-ZrO_2 in the ZrO_2-Y_2O_3-TiO_2 coat.

Titanium is distributed in zones or phases through the ZrO_2-Y_2O_3-TiO_2 coat (i.e. Figure 5.9b). It may be suggested that in the low titanium-concentration zones, the ZrO_2-Y_2O_3 phase diagram might explain the $c \rightarrow t$-ZrO_2 and the consequent $t \rightarrow m$-ZrO_2 transformation in the ZrO_2-Y_2O_3-TiO_2 coat while in higher titanium-concentration zones none of these transformations would take place since no *c*-ZrO_2 is predicted by the ZrO_2-TiO_2 phase diagram.

7.4.3.3 The Martensitic $t \rightarrow m$-ZrO_2 Transformation

The martensitic phase transformation in ZrO_2 can be either athermal (occurring during cooling) or stress-induced (occurring in the region ahead of a crack tip)

(**Heuer et al. 1987**). **Lin et al.** (1990) studied in-situ the $t \rightarrow m$-ZrO_2 transformation in the ZrO_2-Y_2O_3-TiO_2 system by TEM using a cooling stage at -150°C. Some of the samples, with high TiO_2 concentrations were reluctant to undergo the transformation, indicating a lower M_s temperature. Therefore, if there were any transformable t-ZrO_2 in the ZrO_2-Y_2O_3 or ZrO_2-Y_2O_3-TiO_2 coats studied, it would be expected to transform into m-ZrO_2 after cooling below room temperature or by applying external stress. However, neither ZrO_2-Y_2O_3 nor ZrO_2-Y_2O_3-TiO_2 coats showed any increase in the m-ZrO_2 concentration after grinding and polishing their surfaces. Consequently, the stress-induced $t \rightarrow m$-ZrO_2 transformation probably does not occur in the ZrO_2-Y_2O_3 and ZrO_2-Y_2O_3-TiO_2 coats studied.

Nevertheless, the m-ZrO_2 observed in the as-sprayed ZrO_2-Y_2O_3 and ZrO_2-Y_2O_3-TiO_2 coats indicates that the martensitic $t \rightarrow m$-ZrO_2 transformation occurred during the plasma spraying process. The concentrations of TiO_2 and/or Y_2O_3 were lower in m-ZrO_2 (i.e. Figure 6.19) in comparison with that found in c- or t-ZrO_2 (i.e. Figures 6.15, 6.14). Thus the M_s had not been efficiently reduced and consequently the parent t-ZrO_2 (low TiO_2 and/or Y_2O_3) was transformed into m-ZrO_2 during the splat-cooling process. By contrast, in the work reported by **Lin et al.** (1990), the $t \rightarrow m$-ZrO_2 transformation observed in-situ in the sintered ZrO_2-Y_2O_3-TiO_2 systems, corresponded to the transformation of the stabilized or "non-transformable" t-ZrO_2 whose M_s temperature had been lowered; the temperature used in their study was -150 °C.

7.4.3.4 Microstructure of m-ZrO_2

m-ZrO_2 was detected in the ZrO_2-Y_2O_3-TiO_2 coat as heavily twinned grains (i.e. Figures 6.20, 6.21) and mosaics of twins (i.e. Figure 6.22). The m-ZrO_2 twinning may be regarded as deformation twinning resulting from bulk constraints, such as that imposed by the polycrystalline structure (**Bansal, Heuer 1972**). **Evans and Heuer** (1980) suggest that the martensitic $t \rightarrow m$-ZrO_2 transformation is accomplished by the shearing of discrete volumes of material, resulting in a change of shape, and that for a given composition, there is a definite and constant orientation relation between the parent and the product crystals and there exists a definite habit plane. The misfits at the parent/product interface are alleviated periodically by twinned or slipped regions.

Accordingly, the complex *m*-ZrO_2 twins mosaics (i.e. Figures 6.22, 6.23) arise as a result of accommodation by twinning transformations associated with the strains developed during rapid quenching (**Ingel et al. 1988**). The *m*-ZrO_2 formed as laths are nucleated at *t*-ZrO_2 grain boundaries (i.e. Figure 6.7a) and grow and either intersect an opposite grain boundary or impinge on another propagating lath (i.e. Figure 6.8a). Similar microstructural features were reported by **Bestgen et al.** (1988). The intense Moirè contrast observed in some *m*-ZrO_2 twins and laths (i.e. Figures 6.7, 6.23) is caused by the loss of interface coherence (**Porter and Heuer 1979**).

However, single domain *m*-ZrO_2 grains were observed in ZrO_2-Y_2O_3-TiO_2 (i.e. Figure 6.19). They consisted of small rounded grains surrounded by amorphous material and porosity. They were not inserted into a polycrystalline structure, thus there were no constraints from surrounding neighbouring grains. Therefore, it is possible that the *t*→ *m*-ZrO_2 transformation produces a single domain *m*-ZrO_2 in this case.

7.4.3.5 Influence of the *m*-ZrO_2 Microstructure on the Coat Properties

The *t*→ *m*-ZrO_2 transformation induces microcracks around the *m*-ZrO_2 particle matrix interfaces (Figure 6.21a). These microcracks may form a net that dissipates the energy associated with the extension of large cracks (**Miller et al. 1983**). In the light of this toughening mechanism, the presence of *m*-ZrO_2 may be beneficial to the coat. However, it must be at a concentration lower than 0.1 mole %, otherwise it is intolerable; the numerous cracks would endanger the integrity of the coat (**Taylor 1992**).

Summarising, the fast cooling rates that take place during the plasma spraying process prevent any diffusion from occurring. During the ZrO_2-Y_2O_3 splat-cooling, the *c*-ZrO_2 undergoes a composition invariant diffusionless *c*→ *t*-ZrO_2 transformation with a reduction of the system free energy. The resultant *t*-ZrO_2 is reluctant to follow a stress-induced $t \rightarrow m$-ZrO_2 transformation at room temperature. Accordingly, a similar mechanism is thought to operate in the ZrO_2-Y_2O_3-TiO_2 coat. The t-ZrO_2 presents different microstructural components such as twins, APBs separating different t-ZrO_2 orientation variants, and a mottled-contrast morphology which precedes the twins formation. These t-ZrO_2 microstructural components provide a configurational freedom to reduce the total elastic energy arising from the crystal lattice misfit at the c/t-ZrO_2 boundaries and between the different t-ZrO_2 orientation variants. The $c \rightarrow t$-ZrO_2 transformation may lead to a single-domain t-ZrO_2 grain provided the parent grain is not constrained, i.e. by the polycrystalline structure. The microstructural components found in t-ZrO_2 provide the coating with toughening mechanisms based on the deflection of a propagating crack.

However, it is possible that some diffusion processes occur during the plasma spraying; evidence of the t-ZrO_2 decomposition was found in the ZrO_2-Y_2O_3-TiO_2 and ZrO_2-Y_2O_3 coats studied here. Changes in the heat transfer during the splat cooling introduce variations of the cooling rate, allowing some diffusion to take place. t-ZrO_2 decomposes in the ZrO_2-Y_2O_3 coat into high-Y_2O_3 c-ZrO_2 and low-Y_2O_3 t-ZrO_2. The latter follows the martensitic $t \rightarrow m$-ZrO_2 transformation. A similar mechanism may take place in the ZrO_2-Y_2O_3-TiO_2 coat, in the low titanium-concentration zones where the ZrO_2-Y_2O_3 phase diagram dominates while it is ruled out in the high titanium-concentration zones since the ZrO_2-TiO_2 diagram, governing these zones, is unable to explain the transformation. The m-ZrO_2 grains presented twins and mosaics of twins which are to alleviate the misfits between parent and product. However, single domain m-ZrO_2 grains were observed, indicating that $t \rightarrow m$-ZrO_2 transformation may also lead to single domain grains, in unconstrained parent grains. Microcracking surrounding the transformed m-ZrO_2 grain should improve the toughness of the coating. Further $t \rightarrow m$-ZrO_2 transformation in the as-sprayed coating was not observed. Therefore, no appreciable metastable t-ZrO_2 was present in the as-sprayed coating. This is particularly favourable for the coat integrity since the metastable t-ZrO_2 transformation would cause intolerable and deleterious cracking of the coat.

7.5 THE BOND COAT - CERAMIC COAT INTERFACE

7.5.1 SEM

Discontinuities in the bond coat underlying some ZrO_2-Y_2O_3-TiO_2 coats were found to lead to the coating failure by spalling off of the ceramic. The bond coat deforms at high temperatures causing strain isolation in the ceramic coat. On cooling, the bond coat cannot isolate completely the ceramic and biaxial compressive stresses are produced in the ceramic coat (Bennet 1986). A discontinuous bond coat (Figure 5.13) puts the ceramic coat under increasing tension since the resultant strain isolation is not uniform along the ceramic coat; there are some areas where the ceramic coat is in direct contact with the substrate. This gives an extra stress component resulting in the failure of the coat.

EDS analysis of the NiCrCoAlY bond coat showed that aluminium was preferentially concentrated in phases through the coat. This might be an indication of incipient aluminium migration toward the bond coat-ceramic coat interface.

7.5.2 TEM

As discussed before (Section 7.2), examination of the ZrO_2-Y_2O_3-TiO_2/NiCrCoAlY interface was restricted by the nature of the specimen itself and the lack of availability of more sophisticated equipment for the preparation of specimens to be analysed by TEM.

In general, not much work has been done on the study of this interface. Some authors have studied the ZrO_2-Y_2O_3 bond coat interface by TEM. For example Lelait et al. (1992) used classical TEM on transverse thin foil and SIMS to study some ZrO_2-Y_2O_3 coats and reported the formation of an oxide scale at 1100 and 1200 °C in the ZrO_2-Y_2O_3/bond coat interface and segregation of zirconium into this phase. Significant plastic properties were linked to this scale. Harmsworth and Stevens (1992b), after TEM studies on some ZrO_2-Y_2O_3 coats, reported an interfacial amorphous layer rich in nickel, yttrium, zirconium and possible silicon. They linked this layer with the adhesion of the ceramic coat to the bond coat.

7.6 EVOLUTION OF THE CERAMIC COAT MICROSTRUCTURE AFTER THERMAL TREATMENTS

7.6.1 ZrO_2-Y_2O_3 and ZrO_2-Y_2O_3-TiO_2 Coats Heated at 900 °C

The ceramic coats treated at 900 °C for 24 hours experienced slight apparent changes in their morphology; basically "ripening" of the porosity by smoothing and rounding of pores and voids (Figures 5.8a, b). Studying the porosity distribution in ZrO_2-Y_2O_3-TiO_2 in the as-sprayed condition and after heating at 900 °C (Figures 5.9a and 5.9b, respectively), some evolution in the pores size was detected but without affecting the whole porosity profile. This was expected, considering that 900 °C was not a very high temperature and the treatment duration was only 24 hours.

More interesting effects were found in the ZrO_2 phase distribution in both ceramic coats, after cooling. An increased *t*-ZrO_2 concentration at the expense of *c*-ZrO_2 was detected in both coats although to a higher extent in the ZrO_2-Y_2O_3-TiO_2 coat (Tables 4.2, 4.4). A diffusionless *c*→ *t*-ZrO_2 was likely since the specimens were cooled rapidly and diffusion was restricted. This transformation is not linked with deterioration of the ceramic coat integrity; rather, *t*-ZrO_2 is highly desirable in the coat as improved thermal shock resistance and toughness are associated with *t*-ZrO_2 (**Alpèrine and Lelatit 1994, Miller et al. 1983**). The concentration of *m*-ZrO_2 was maintained after the thermal treatment in both coats. The temperature was not high enough to promote the decomposition of *t*-ZrO_2 into high Y_2O_3 *c*-ZrO_2 and low Y_2O_3 *t*-ZrO_2 and the consequent *t*→ *m*-ZrO_2 transformation.

7.6.2 ZrO_2-Y_2O_3-TiO_2 Coat Heated at Higher Temperatures

7.6.2.1 Fracture mechanisms

ZrO_2-Y_2O_3-TiO_2 coats thermally treated at 1000 and 1100 °C for an hour developed fracture surfaces with an interlamellar appearance. The cracks propagated across the lamellae, parallel to their columnar microstructure (Figure 5.17). After thermal treatments at higher temperatures (1200 and 1400 °C), a change in the fracture mechanisms was observed since microstructural evolution of the coating had occurred. Signs of an incipient sintering process were observed in the ZrO_2-Y_2O_3-TiO_2 coat heated at 1200 °C (Figure 5.18) whilst a complete collapse of the lamellar microstructure had taken place in the coat heated at 1400 °C (Figure 5.19). The coat microstructure had developed into a granular form. In this case, cracks were observed to extend along the inter-granular boundaries.

Sintering has been identified as one of the reasons for ceramic coat failure (Taylor 1992); the effective area of the coat is increased and consequently the thermal conductivity, the thermal shock resistance is reduced dramatically and the coat could spall off.

7.6.2.2 ZrO_2 Phase Distribution

ZrO_2-Y_2O_3-TiO_2 coats thermally treated up to 1400 °C for an hour in air experienced *c*→ *t*-ZrO_2 transformations since the concentration of *t*-ZrO_2 increased whilst the *c*-ZrO_2 was reduced. This was more evident at higher temperatures (1200 and 1400 °C) as shown in Figure 4.5a. By contrast, thermal treatments (up to 1200 °C) that involved a slow cooling rate (in argon) apparently caused no important changes in the ZrO_2 phase distribution of the coating (Figure 4.5b).

7.6.2.3 Microstructural Elements after Heating at 1400 and 1600 °C

In general, the same elements described for *c*-, *t*- and *m*-ZrO_2 in the as sprayed ZrO_2-Y_2O_3-TiO_2 coat (Section 7.4.1.1) were found in samples of the coat thermally treated at 1400 and 1600 °C in air. Porous agglomerates were observed (Figure 6.25) and the amorphous phase was still present after these thermal treatments. However, some crystal growth was detected since the grain size was considerably larger (> 200 nm); faceted grains are observed for example in Figures 6.27, 6.30 and 6.35. Twinning in *t*- (Figure 6.28), and *m*-ZrO_2 (Figure 6.31a) grains was identified frequently in the TEM observations.

m-ZrO_2 grains in the as-sprayed coat are transformed to "transformable" *t*-ZrO_2 after thermal treatment at high temperatures. After cooling, this *t*-ZrO_2 will transform to *m*-ZrO_2 again. Similarly, some *c*-ZrO_2 grains will transform into *t*-

ZrO_2 after rapid cooling. The higher proportion of *t*- and *m*-ZrO_2 twinned grains gives an indication of the higher constraints of the respective parent grains caused by crystal growth and the stresses occurring during rapid cooling, since twinning has been linked with these constraints.

In summary, the *c*→ *t*-ZrO_2 transformation took place in the ZrO_2-Y_2O_3-TiO_2 coats when they were rapidly cooled from the treatment temperature. This effect was observed to a greater extent at higher treatment temperatures (1200-1400 °C). Signs of sintering of the ZrO_2-Y_2O_3-TiO_2 coat start appearing after heating at 1200 °C. Some evolution of the ZrO_2-Y_2O_3-TiO_2 coat microstructure is observed such as grain growth. Higher constraints caused by grain growth and quenching are revealed in the coats thermally treated at high temperatures (1200-1400 °C) as a higher incidence of *m*- and *t*-ZrO_2 twinning is observed in these cases.

7.7 PRESSED AND SINTERED BODIES

7.7.1 ZrO_2-Y_2O_3

7.7.1.1 Density and Particle Size

Disks of this powder sintered at different temperatures presented densities very close to the theoretical value (Figure 5.19), registering the highest density at 1350 °C. This corresponded with the results obtained by SEM. Tight aggregates were observed in the pressed body sintered at 1400 °C (Figure 5.21a) while some grain growth was detected at 1550 °C (Figure 5.21b). Small grains corresponded to *t*-ZrO_2 whilst larger grains were *c*-ZrO_2 (Lee and Heuer 1987).

7.7.1.2 ZrO_2 Phase Distribution

The pressed ZrO_2-Y_2O_3 body sintered at 1350 °C consisted basically of *t*-ZrO_2. The *t*-ZrO_2 concentration decreased slightly with a corresponding increase of the *c*-ZrO_2 when the sintering temperature was increased. At 1550 °C larger *c*-ZrO_2 grains were detected on the surface of the sintered product.

7.7.2 ZrO_2-Y_2O_3-TiO_2

7.7.2.1 Density and Particle Size

The ZrO_2-Y_2O_3-TiO_2(A) powder and ZrO_2-Y_2O_3-TiO_2(B) powder used for plasma spraying, in the form of pressed and sintered bodies, presented lower densities compared with the equivalent ZrO_2-Y_2O_3; their highest densities were 82 and 78% of their theoretical densities at 1350 °C, respectively. Their densities were reduced with increased sintering temperatures (Figure 5.20). Further increments in the sintering temperature promote grain growth with a consequent reduction of the density of the sintered bodies due to an increase in size of the grain interstices and intergranular cracks.

Small equiaxed grains were observed in the pressed and sintered ZrO_2-Y_2O_3-TiO_2(A) body (Figure 5.22a). The ZrO_2-Y_2O_3-TiO_2(B) product consisted of equiaxed grains and elongated grains with a high titanium concentration. Pyda et al. (1992, 1993) have reported $ZrTiO_4$ grains growing in the system ZrO_2-Y_2O_3-TiO_2. These grains are believed to hinder the growth of ZrO_2 grains. The presence of $ZrTiO_4$ was not detected by XRD analysis in any of the two ZrO_2-Y_2O_3-TiO_2 systems studied here.

Lower densities and larger grain sizes were associated with the ZrO_2-Y_2O_3-TiO_2(B) sintered body in comparison with (A). In the former case, the TiO_2 concentration was higher (26.4 mole %) than in ZrO_2-Y_2O_3-TiO_2(A) (23.1 mole %). Thus, an increase in the TiO_2 concentration might promote grain growth in the ZrO_2-Y_2O_3-TiO_2 system in the interval of compositions studied. Pyda et al. (1992, 1993) studied the system ZrO_2-Y_2O_3-TiO_2 over a wide range of compositions and found that additions of TiO_2 to the system increased the *t*-ZrO_2 grain size. However, at high concentrations of TiO_2 (23-28 mole %) grain growth was inhibited. They suggested that elongated grains of $ZrTiO_4$ crystallising at the *t*-ZrO_2 grain boundaries were responsible for this phenomenon. Their observations are opposite to the results obtained here from the systems ZrO_2-Y_2O_3-TiO_2(A) and (B). However, it is necessary to notice that the nature of the powder used by these authors was different; they prepared their powder by coprecipitation of the appropriate salts and this ensured a real contact between the constituents involved. By contrast, the powder used here were a powder mixture in the case of ZrO_2-Y_2O_3-TiO_2(A), and a spray dried powder in the case of ZrO_2-Y_2O_3-TiO_2(B). Therefore a simple direct comparison between the results cannot be established.

7.7.2.2 ZrO_2 Phase Distribution

The ZrO_2 phase distribution in the ZrO_2-Y_2O_3-TiO_2(A) sintered body was similar to that described for ZrO_2-Y_2O_3; it consisted mostly of *t*-ZrO_2 whose concentration decreased with higher sintering temperatures (Figure 5.19). By contrast, the ZrO_2 phase distribution in the ZrO_2-Y_2O_3-TiO_2(B) sintered body consisted of *m*-, *c*- and *t*-ZrO_2. The *t*-ZrO_2 concentration increased as the sintering temperature was increased. A higher *t*-ZrO_2 concentration in ZrO_2-Y_2O_3-TiO_2 (B) (26.4 mole fraction TiO_2) than ZrO_2-Y_2O_3-TiO_2(A) (23.1 mole fraction TiO_2) would be expected since a higher TiO_2 concentration promotes the formation of *t*-ZrO_2. Considerations of the particle size should be made to understand this discrepancy. The particle size of powder (B) was about 10 times the particle size of powder (A). Therefore, the particle size of the original powder affects the final ZrO_2 phase distribution in the ZrO_2-Y_2O_3-TiO_2 system.

7.7.2.3 Transformability of *t*-ZrO_2

There is evidence that the transformability of the *t*-ZrO_2 is related to its *c/a* ratio (**Lee and Heuer 1987**). The *c/a* ratio determines the residual strain of a *t*-ZrO_2 particle contained in a *c*-ZrO_2 matrix which will contribute to the transformation process. It is expected that low *c/a* ratio ZrO_2 systems (low tetragonality) present a high transformation resistance (**Lee and Rainforth 1994**). In the light of this reasoning, the *t*-ZrO_2 in the ZrO_2-Y_2O_3-TiO_2 sintered body (c/a = 1.012) has a lower transformation resistance than in the equivalent ZrO_2-Y_2O_3 system (c/a = 1.007) studied here.

To summarise, the ZrO_2-Y_2O_3 and ZrO_2-Y_2O_3-TiO_2 pressed and sintered bodies reached their highest density at 1350 °C; increased sintering temperatures leaded to grain growth and a consequent reduction of the density (Figure 5.20). ZrO_2-Y_2O_3 and ZrO_2-Y_2O_3-TiO_2 (23.1 mole % TiO_2) had similar ZrO_2 phase distributions and they progressed in the same way with the increased temperature, reducing slightly the t-ZrO_2 content. The increased TiO_2 concentration promoted the grain size and decreased the final density in the ZrO_2-Y_2O_3-TiO_2 sintered body. The particle size of the original powder affects the final ZrO_2 phase distribution. A smaller particle size promoted the formation of t-ZrO_2. t-ZrO_2 has a lower *c/a* ratio in the ZrO_2-Y_2O_3-TiO_2 sintered body than in the equivalent ZrO_2-Y_2O_3, thus a lower resistance to the $t \rightarrow m$-ZrO_2 transformation is expected.

7.8 ZrO_2-Y_2O_3-TiO_2 COAT VERSUS ZrO_2-Y_2O_3 COAT

Now that the mechanisms taking place in the formation of the microstructure of the ceramic coat have been discussed, the following sections present a discussion, based on the previous sections, of the more important aspects of the ZrO_2-Y_2O_3-TiO_2 and ZrO_2-Y_2O_3 coats studied here to establish a comparison between them and to consider the potential of ZrO_2-Y_2O_3-TiO_2 system as an alternative TBC.

7.8.1 Two Types of ZrO_2-Y_2O_3-TiO_2 Coat

Although the same ZrO_2-Y_2O_3-TiO_2 powder was used in the preparation of two groups of coatings, differences in the porosity and particularly in the ZrO_2 phase distribution made it necessary to identify them as types 1 and 2 (Table 4.1 and 4.5, respectively). Unfortunately details of the parameters used during the plasma spraying of each group were unavailable. However, some explanations can be proposed based on considerations of the mechanisms discussed. Type 2 coats presented a higher concentration of t-ZrO_2 (0.54 mole fraction) at the expense of m-ZrO_2 (0.07 mole fraction) than type 1 coats (0.46 and 0.15 mole fraction, respectively). The $t \rightarrow m$-ZrO_2 transformation occurred to a lesser extent than in type 2 coats. Therefore, it can be said that more efficient cooling took place in the type 2 coat and thus diffusion processes like the decomposition of t-ZrO_2 were restricted. An improved cooling rate of the ZrO_2-Y_2O_3-TiO_2 splats might have been achieved by adjustment of different preparation parameters, for instance, increasing the substrate cooling and reducing the number of plasma passes on the surface per unit time.

7.8.2 Morphology

Similar discontinuous microstructures were observed in ZrO_2-Y_2O_3-TiO_2 and ZrO_2-Y_2O_3 coats. The same type of porosity and network of microcracks were seen. The ZrO_2-Y_2O_3-TiO_2 coats, however, exhibited phases defined by a preferential concentration of TiO_2. The presence of these high titanium-concentration zones might provide the ZrO_2-Y_2O_3-TiO_2 coat with a toughening mechanism: a propagating crack may be deviated when it reaches an interface between two zones with different titanium concentrations. Properties associated with the effective transverse area of the coat, such as thermal conductivity and elasticity coefficients would be affected at a similar level in both coats.

7.8.3 ZrO_2 Phase Distribution

A higher concentration of *t*-ZrO_2 is found in the ZrO_2-Y_2O_3-TiO_2 coat than in the equivalent ZrO_2-Y_2O_3 coat (0.46 and 0.25 mole fraction, respectively). The TiO_2 promotes the formation of *t*-ZrO_2 during the plasma spraying of ZrO_2-Y_2O_3-TiO_2 in comparison with ZrO_2-Y_2O_3; TiO_2 was found to be preferentially associated with *t*-ZrO_2. The presence of *t*-ZrO_2 in the ceramic coat is highly desirable because of its favourable properties such as higher toughness and thermal expansion coefficient in comparison to *c*-ZrO_2 (**Alpèrine. and Lelait 1992, Miller et al. 1983**). Hence, the TiO_2 improves the performance of the ZrO_2-Y_2O_3-TiO_2 as a TBC by increasing the *t*-ZrO_2 concentration.

7.8.4 Transformability

A higher *c*/*a* ratio for *t*-ZrO_2 was found in the ZrO_2-Y_2O_3-TiO_2 sintered body (1.012) in comparison with the equivalent ZrO_2-Y_2O_3 product (1.007). This was linked to a lower resistance to transformation of the *t*-ZrO_2 in the ZrO_2-Y_2O_3-TiO_2 sintered body (Section 7.7.2.3). Consequently, it might be thought that *t*-ZrO_2 in the ZrO_2-Y_2O_3-TiO_2 coat has a relative lower resistance to transformation than in the ZrO_2-Y_2O_3 coat. However, no transformation of the stabilized species was observed in any of the coats studied. It is likely that this effect would be observed when the M_s temperature is reached by cooling the coats below room temperature. Therefore, this is not a significant factor to consider in the evaluation of the ZrO_2-Y_2O_3-TiO_2 coat.

7.8.5 The Cooling Rate

The *c*→ *t*-ZrO_2 transformation was produced in the ZrO_2-Y_2O_3-TiO_2 and ZrO_2-Y_2O_3 coats by rapid cooling of the coat heated at high temperatures, with a consequent increase of the *t*-ZrO_2 concentration. This effect was observed to a greater extent in the ZrO_2-Y_2O_3-TiO_2 coat. Since *t*-ZrO_2 starts decomposing after long periods of service at a high temperature, it may be thought that rapid cooling rates would compensate for this effect by increasing the final *t*-ZrO_2 concentration. The ability of a rapid cooling rate to balance the *t*-ZrO_2 in the in-service coat should be studied in detail since this would extend the life of the or ZrO_2-Y_2O_3-TiO_2 coat.

7.8.6 Sinterability

ZrO_2-Y_2O_3-TiO_2 coats treated at 1200 °C showed evidence of an incipient sintering process. Sintering is undesirable in the ceramic coat, it has detrimental effects on the integrity of the coating since the thermal shock resistance of the ceramic coat is reduced considerably. The possible effect of TiO_2 on the sinterability of the ZrO_2-Y_2O_3-TiO_2 coat should be studied in detail to determine the extent of its effect on the in-service coating stability.

7.9 FINAL REMARKS

Finally, the study presented here leads to an understanding of the mechanisms of the formation of the microstructure of the plasma-sprayed ZrO_2-Y_2O_3-TiO_2 coat. Likewise, it helps to elucidate the mechanisms of transformation in the coat that determine the distribution of the ZrO_2 phases that evolve during the plasma spraying process and those that occur during thermal treatments. Further this study helps the understanding and prediction of the possible behaviour of the ZrO_2-Y_2O_3-TiO_2 system as a TBC. Nevertheless, further studies are required for the complete understanding of the ZrO_2-Y_2O_3-TiO_2 as discussed in Section 8.2.

8 CONCLUSIONS AND SUGGESTIONS FOR FURTHER WORK

8.1 CONCLUSIONS

A comparative study of ZrO_2-Y_2O_3-TiO_2 and ZrO_2-Y_2O_3 plasma sprayed coats has been made. TEM, SEM and XRD were used in the characterization of the as-sprayed and as-thermal treated coats. The information gained was used to study the mechanisms of the formation of the microstructure of the ZrO_2-Y_2O_3-TiO_2 and ZrO_2-Y_2O_3 coats. The mechanisms involved in the different ZrO_2 transformations that take place during the plasma spraying process and those occurring during thermal treatment of the coats, that determine the final ZrO_2 phase distribution were also identified.

The techniques of analysis used in the study provided relevant information on the system. For instance the image analysis of SEM micrographs of the ZrO_2-Y_2O_3-TiO_2 coat cross-sections supplied data to evaluate the porosity of the coat and to detect small changes after thermal treatment of the coat, which is rather difficult to do by simple inspection of the micrographs. The study of the ZrO_2-Y_2O_3-TiO_2 fracture surfaces provided a suitable view of the coat lamellae to investigate their microstructure. On the other hand, TEM provided a detailed view of the polycrystalline microstructure of the lamellae. XRD analysis permitted the quantification of the ZrO_2 phase distribution and the evaluation of the changes it undergoes after different thermal treatments.

The polycrystalline lamellae microstructure observed in the ZrO_2-Y_2O_3-TiO_2 and ZrO_2-Y_2O_3 coats is determined by the mechanisms that take place during the cooling of the molten ceramic material (splats). The heterogeneous and complex microstructure observed in the lamellae presented varied components such as agglomerates of small grain size (20-50nm), equiaxed grains and amorphous phases. The rapid cooling rate stimulates a series of nucleation events and grain growth, producing crystals growing in a columnar structure in the opposite direction to the heat flow, normal to the underlying surface. Changes in the heat transfer modify the splat-cooling rate which affects the resultant microstructure. The splats are unable to accommodate internal stresses that had their origins in the constraints of the underlying material, restricting the splat contraction, and thus microcrack networks perpendicular to the splat were produced to alleviate these stresses. The discontinuous nature of the lamellae deposition provides the coat with a planar porosity and coarse porosity localized in the splats interstices. Unmelted material contributes to the coarse porosity since it prevents the interstices from filling. The resultant microstructure plays a predominant role in defining the properties of the ceramic as TBCs.

The cooling rate of the material during the plasma spraying process determines the ZrO_2 phase distribution in the coat. Rapid quenching prevents diffusion processes from occurring in the ceramic coat. Diffusionless $c \rightarrow t$-ZrO_2 transformation occurs as the ZrO_2-Y_2O_3 splats are rapidly cooled, for a Y_2O_3 concentration and at a temperature that t-ZrO_2 is thermodynamically more stable than c-ZrO_2, with a consequent reduction in the free energy of the system. A similar mechanism is expected to take place in the ZrO_2-Y_2O_3-TiO_2 coat. The resultant t-ZrO_2 is reluctant to undergo a $t \rightarrow m$-ZrO_2 transformation. For this reason it has been designated as "non-transformable" t-ZrO_2. The t-ZrO_2 present has characteristic microstructural features such as twins, antiphase boundaries separating different t-ZrO_2 orientation variants, and mottled-contrast grains. The latter is a previous stage to the twin formation. The existence of more than one variant of the t-ZrO_2 provides a configurational freedom to reduce the total elastic energy arising from the crystal lattice misfit at the c/t-ZrO_2 boundaries and at the boundaries between t-ZrO_2 orientation variants. The $c \rightarrow t$-ZrO_2 transformation may lead to single domain t-ZrO_2 grains if the c-ZrO_2 parent grain is free of constraints. The microstructural components observed in t-ZrO_2 provide the coat with toughening mechanisms based on the deflection of the propagating crack.

Some diffusion may occur during the splat-cooling step of the plasma spraying. Reduction of the splat-cooling rate by different mechanisms may allow some diffusion to occur. Accordingly, decomposition of *t*-ZrO_2 into a high-Y_2O_3 *c*-ZrO_2 and a low-Y_2O_3 *t*-ZrO_2 takes place during the cooling of the ZrO_2-Y_2O_3 splats. The latter ZrO_2 follows a martensitic *t*→ *m*-ZrO_2 transformation. Since titanium is distributed in phases in the ZrO_2-Y_2O_3-TiO_2 coat, the *c*→ *t*→ *m*-ZrO_2 transformations described take place in the low titanium-concentration zones and the ZrO_2-Y_2O_3 phase diagram may be used to explain them. Conversely, the high titanium-concentration zones are better approximated by the ZrO_2-TiO_2 phase diagram which is unable to explain the transformations mentioned. Diffusional decomposition of *t*-ZrO_2 occurs to a lesser extent in the coats than the diffusionless *c*→ *t*-ZrO_2 transformation since the final concentration of *m*-ZrO_2 is very low. *m*-ZrO_2 grains showed microstructural features characteristic of the martensitic transformation: twins, mosaics of twins and slipped regions. These microstructural components alleviate the misfits between the *t*-ZrO_2 parent and the *m*-ZrO_2. However, it has been found that the martensitic *t*→ *m*-ZrO_2 transformation may lead to a single domain *m*-ZrO_2 grain, provided the parent *t*-ZrO_2 grains are free of constraints. Microcracks associated with the *t*→ *m*-ZrO_2 transformation appear between the transformed grain and the matrix. These microcracks improve the coat toughness by a microcrack-toughening mechanism. Metastable or "transformable" *t*-ZrO_2 was not detected in the coats as further stress-induced *t*→*m*-ZrO_2 transformation was not observed.

Small changes in the porosity occurred in the ZrO_2-Y_2O_3 and ZrO_2-Y_2O_3-TiO_2 coats thermally treated at 900 °C for 24 hours. A rapid cooling from this temperature caused an increase in the *t*-ZrO_2 concentration at the expense of *c*-ZrO_2, thus *c*→ *t*-ZrO_2 transformation occurred. The same transformation occurred in a greater extent in the ZrO_2-Y_2O_3-TiO_2 coat thermally treated at higher temperatures. By contrast, ZrO_2-Y_2O_3-TiO_2 coats cooled slowly from thermal treatment temperatures up to 1200 °C, basically maintained their phase distribution. Rapid cooling rates might provide a compensation mechanism to the slow decomposition that *t*-ZrO_2 experiences after long periods of service of the coat at high temperature. Sintering starts taking place in the ZrO_2-Y_2O_3-TiO_2 coat thermally treated at 1200 °C. Thus a collapse of the lamellar microstructure is observed and a granular microstructure evolves instead of it. This has deleterious consequences on the coat integrity when high service temperature are used.

Microstructural components similar to those in the as-sprayed ZrO_2-Y_2O_3-TiO_2 coat, such as an amorphous phase and porous agglomerates of small particles were observed in the coat after thermal treatments at 1400 and 1600 °C. In addition, some evolution of the microstructure was also observed in the thermally treated ZrO_2-Y_2O_3-TiO_2 coats, such as crystal growth and more accentuated *t*- and *m*-ZrO_2 twinning. The latter microstructural components are evidence of the higher constraints of the parent grains which had their origins in the crystal growth and the rapid cooling.

The monolithic ZrO_2-Y_2O_3, ZrO_2-Y_2O_3-TiO_2 (23.1 mole% TiO_2) and ZrO_2-Y_2O_3-TiO_2 (26.4 mole% TiO_2) products reached their highest density after sintering at 1350 °C. Higher sintering temperatures promoted grain growth and reduction of the final density. ZrO_2-Y_2O_3 and ZrO_2-Y_2O_3-TiO_2 (23.1 mole% TiO_2) monolithic product consisted basically of *t*-ZrO_2 whose concentration was reduced as the sintering temperature was increased. The increased content of TiO_2 promotes the grain size and decreases the final density in the ZrO_2-Y_2O_3-TiO_2 system. The particle size of the powder to be sintered affects the ZrO_2 phase distribution in the final product; a smaller particle size increases the concentration of *t*-ZrO_2. The lower *c/a* ratio of *t*-ZrO_2 in ZrO_2-Y_2O_3-TiO_2 in comparison with that in ZrO_2-Y_2O_3 is linked with a lower resistance to the *t*→*m*-ZrO_2 transformation. However no evidence was found to support this link in the conditions used in this study.

Finally, comparing the ZrO_2-Y_2O_3 and ZrO_2-Y_2O_3-TiO_2 coats it can be said that TiO_2 increases considerably the *t*-ZrO_2 content in the coat which should improve the toughness and thermal shock resistance of the coat. However, ZrO_2-Y_2O_3-TiO_2 coats showed signs of sintering after thermal treatment at 1200 °C which is detrimental to the coat integrity and performance as a TBC. It was found that in the case of pressed and sintered bodies there was possibly a lower resistance of *t*-ZrO_2 to transform to *m*-ZrO_2 in the ZrO_2-Y_2O_3-TiO_2 than in the ZrO_2-Y_2O_3.

8.2 SUGGESTIONS FOR FURTHER WORK

Further work should be done to increase the understanding of the ZrO_2-Y_2O_3-TiO_2 system as a TBC and to determine the real possibilities of this material as an alternative choice to the better known ZrO_2-Y_2O_3 coat. It should be noticed that advances in this area require the study of the ZrO_2-Y_2O_3 system as well since relatively little information is available on some topics related to it as shown below.

It would be interesting to study and to compare the ageing effect on the ZrO_2-Y_2O_3-TiO_2 and ZrO_2-Y_2O_3 coat microstructures over longer periods of heating (> 100 hours) at high temperature. Some microstructural features have been reported in ZrO_2-Y_2O_3 plasma sprayed coats aged at 1100 °C for 100 hours possibly related to a slow decomposition of the "non-transformable" *t*-ZrO_2 (Lelait and Alpérine 1994). Decomposition of *t*-ZrO_2 in the ZrO_2-Y_2O_3-TiO_2 thermally treated at different temperatures for 24 hours was not established fully. Longer periods of treatment would be required to evaluate further the decomposition of the *t*-ZrO_2 phase. TEM and EDS analyses of appropriate thin sections of the aged ZrO_2-Y_2O_3-TiO_2 and ZrO_2-Y_2O_3 coats would allow the identification of new microstructural features and their link with a possible migration of Ti and/or Y. From the information obtained from such experiment, mechanisms that explain the formation of the microstructural elements in the ZrO_2-Y_2O_3-TiO_2 and ZrO_2-Y_2O_3 during ageing could be proposed. It would also be interesting to investigate using XRD the relative transformability of *t*-ZrO_2 in both coats after ageing processes.

Little attention has been given to the study of the interface between the bond coat and the ceramic coat which has a predominant role in the ceramic coat adhesion and consequently in the stability of the overall coating. Therefore, further work should be addressed in this direction. A comparative study of this interface in the ZrO_2-Y_2O_3-TiO_2/NiCrCoAlY and ZrO_2-Y_2O_3/NiCrCoAlY coatings should be done, with strong emphasis on TEM observations and EDS analyses. For this purpose, a suitable specimen preparation technique must be used because it is essential to the success of the analysis. Pre-thinned transverse sections (20-30μm) of the coating can be obtained using a dimpler. Fine control of the sputtering angle and continuous rotation of the specimen during the ion-beam thinning would provide suitable areas of the specimen for the TEM observations. It would be interesting to evaluate the nature of the interface, thickness, composition and evolution after thermal treatments and thermal cycling. The information gained might be used to understand the mechanisms involved in the formation and evolution of this interface after thermal treatment. The possible influence of the ceramic coat and the bond coat compositions on the interface formation should also be determined.

The addition of TiO_2 to the system ZrO_2-Y_2O_3 increases the final concentration of *t*-ZrO_2 in the coat which improves its toughness and thermal shock resistance. This constitutes an advantage of ZrO_2-Y_2O_3-TiO_2 over ZrO_2-Y_2O_3 when they are used as TBCs. Another effect attributed to the addition of TiO_2 to the system ZrO_2-Y_2O_3 is the improvement in the stability of the ceramic in humid environments at lower temperature (300-500 °C). In this environment the ZrO_2 is destabilized since the Y_2O_3 is "extracted" from the system by the formation of the corresponding hydroxide. A similar mechanism is believed to take place when the system is exposed to an environment with corrosive elements like vanadium and sulphur. It would be interesting to investigate and compare the stability of ZrO_2-Y_2O_3-TiO_2 and ZrO_2-Y_2O_3 coats in these environments after different periods of exposure. XRD would allow the study of the system stability which is given by changes in the ZrO_2 phase distribution. Changes in the morphology could be evaluated by SEM analysis of the surface and cross-section of the coatings. A detailed view of the microstructure of the coat and its evolution could be obtained by TEM. XPS and SIMS analyses would provide information regarding the chemical compounds formed during the exposure of the coat in a given environment and their distribution profiles in the surface layers of the coat. Mechanisms that take place in both systems might be proposed using the information gained. This would aid the understanding of the ZrO_2-Y_2O_3-TiO_2 and ZrO_2-Y_2O_3 coat systems and their behaviour in different environments, which in turn would help to predict their suitability and service life in a given environment.

Sintering is undesirable in a ceramic coat used as a TBC since it increases the thermal conductivity, and reduces the thermal shock resistance. The ZrO_2-Y_2O_3-TiO_2 coat studied here indicated sintering after thermal treatment at temperatures higher than 1200 °C, thus TiO_2 may be promoting the sintering of the ceramic coat. It is therefore important to evaluate effectively the possible influence of TiO_2 and the variation of its concentration in the process of sintering of the ZrO_2-Y_2O_3-TiO_2 coats. ZrO_2-Y_2O_3-TiO_2 coats with different TiO_2 concentrations (lower and higher than the used in this study, 26.4 mole%) should be prepared to investigate this effect. The degree of sintering could be followed by observation of the fracture surface of the coat after thermal treatment at temperatures of about 1200 °C. A more detailed evaluation of the particle size resulting in each case might be done by TEM analysis of replicas from cross-sections surfaces of the coat. An optimisation of the TiO_2 concentration interval could then be produced, whereby the sintering effect is reduced.

9. REFERENCES

ALPÉRINE, S. and LELAIT, L. (1994) Microstructural Investigation of Plasma-Sprayed Yttria Partially Stabilized Zirconia TBC. *J. Eng. Gas Turbine & Power. Trans. of ASM*, 116, 258.

ANDERSON, C. (1988) Phase Stability and Transformation Toughening in Zirconia in *Advances in Ceramics*: Science and Technology of Zirconia III, S. Somiya et al. (Editors), Am. Ceram. Soc., Ohio, USA, Vol. 24, p 184.

ARFELLI, M., INGO, G. M. and MATTOGNO, G. (1990) XPS Investigation of Impurity Phase Segregation in 25.5wt%CeO_2-25Y_2O_3-72ZrO_2 Plasma Sprayed Thermal Barrier Coatings. *Surface and Interface Analysis*, 16, 1/12, 452.

ASHWORTH, D. R. (1969) A Method of Determining the Bulk Density of Ceramics. *J. Brit. Ceram. Soc.*, 6, 3, 70.

BANSAL, G. and HEUER, A. H. (1972) On a Martensitic Phase Transformation in Zirconia (ZrO_2) I. Metallographic Evidence. *Acta Metall.*, 20, 1281. (1975) Precipitation in Partially Stabilized Zirconia. *J. Am. Ceram. Soc.*, 58 5/6 235.

BATEMAN, C., NOTIS, M. and LYMAN, C. (1988) Phase Equilibria and Phase Transformations in ZrO_2-TiO_2 and ZrO_2-MgO-TiO_2 Systems in *Advances in Ceramics.*: Science and Technology of Zirconia III, S. Somiya et al. (Editors), Am. Ceram. Soc., Ohio, USA, Vol. 24, p 31.

BENNER, R. E. and NAGELBERG, A. S. (1981) Characterization of ZrO_2-Y_2O_3 Thermal Barrier Coatings by Raman Spectroscopy. *Thin Solid Films*, 84, 89.

BENNETT, A. (1986) Properties of Thermal Barrier Coatings. *Mater. Sci. Tech.*, 2, 257.

BESTGEN, H., CHAIM, R. and HEUER A. H. (1988) Thin Foil Phase Transformations of Tetragonal ZrO_2 in a ZrO_2-8wt%Y_2O_3 Alloy. *J. Am. Ceram.* Soc., 71, 10, 826.

BIELICKI, R., DAHMEN, U., THOMAS, G. and WESTMACOTT, K. H. (1988) Transmission Electron Microscopy Investigation of Orthorhombic-Type Phase in Stabilized Zirconias. *Advances in Ceramics:* Science and Technology of Zirconia III, S. Somiya et al. (Editors), Am. Ceram. Soc., Ohio, USA, Vol. 24, p 485.

BRANDON, J. R. AND TAYLOR, R. (1989) Thermal Properties of Ceria and Yttria Partially Stabilized Zirconia Thermal Barrier Coatings. *Surf. Coat. Tech.*, 39, 143.

BRINDLEY, W. and LEONHARDT T. (1993) Metallographic Techniques for Evaluating of Thermal Barrier Coatings. *Materials Characterization*, 24, 2, 93.

BROWN, F. and DUWEZ, P. (1954) The Zirconia-Titania System. *J. Am. Ceram. Soc.*, 37, 3, 129.

BUTLER, E. P. (1985a), Transmission Electron Microscopy of Zirconia Ceramics. *J. Microscopy* ,140, 2 , 171. (1985b) Transformation-Toughened Zirconia Ceramics. *Mat. Sci. and Tech.*, 1, 417.

CHAIM, R., RÜHLE, M. and HEUER, A. H. (1985) Microstructural Evolution in ZrO_2 12wt%Y_2O_3 Ceramic. *J. Am. Ceram. Soc.*, 68, 8, 427.

CHANG, S. F., CHAO, C. H., WU, B. C., LEU, R. Q. and CHANG, E. (1991) Zirconia/Pack-Aluminised Co-29Cr-6Al-1Y Thermal Barrier Coatings. *J. Vacuum. Tech.*, A9, 4, 2099.

CHEN, H., LIU, Z. Y. and CHUANG, Y. C. (1992) Degradation of Plasma-Sprayed Alumina and Zirconia Coatings on Stainless Steel during Thermal Cycling and Hot Corrosion. *Thin Solid Film*, 223, 56.

DeMASI-MARCIN, J., and GUPTA, D. K. (1994) Protective Coatings in the Gas Turbine Engine. *Surf. Coat. Tech.*, 68/69, 1.

EVANS, A. G. and HEUER, A. H. (1980) Review: Transformation Toughening in Ceramics: Martensitic Transformation in Crack Tip Stress Field. *J. Am. Ceram. Soc.*, 63, 5/6, 241.

EVANS, P. (1984) Quantitative X-ray Diffraction Analysis of Polymorphic Mixes of Pure Zirconia. *Brit. Ceram. Trans. Journal*, 83, 39.

FAN, D. and CHEN, L. (1995) Computer Simulation of Twin Formation during the Displacive c→t′ Phase Transformation in the Zirconia-Yttria System. *J. Am. Ceram. Soc.*, 78, 3, 767.

FANCEY, K., YOUNG, S. J., JAMES, A. S. and MATTHEWS, A. (1993) The Microstructural and Thickness Uniformity of Zirconia Coating Produced by r-f-plating. *Mater. Sci. Eng.*, A163, 171.

GARVIE, R. C. (1965) The Occurrence of Metastable Tetragonal Zirconia as a Crystallite Size Effect. *J. Phys. Chem.*, 69, 4 , 1238. (1975) Ceramic Steel? *Nature*, 258, 703.

GARVIE, R. C. and NICHOLSON, P. (1972) Structure and Thermomechanical Properties of Partially Stabilized Zirconia in the CaO-ZrO_2 System. *J. Am. Ceram. Soc.*, 55, 3, 152.

GOODHEW, P. J. (1973) Specimen Preparation in Materials Science in Practical Methods in Electron Microscopy, A. Gauer (Editor), North Holland Pub., London, p. 83. (1984) Specimen Preparation for Transmission Electron Microscopy of Materials, in Microscopy Handbook, Royal Microscopical Society, Vol. 3, Oxford Science Pub., p 20.

GREEN, R. (1973) Fracture Toughness of a Partially Stabilized ZrO_2 in the System CaO-ZrO_2. *J. Am. Ceram. Soc.*, 56, 12, 619.

HABERKO, K., PYDA, W. and BUCKO, M. M. (1991) Zirconia Polycrystal in the System TiO_2-Y_2O_3-ZrO_2. Ceramics Today-Tomorrow's Ceramics, Edited by P. Vicenzini, Elsevier Science Publishers, p 1563.

HARMSWORTH, P. D. and STEVENS, R. (1989) The Microstructure of Zirconia Thermal Barrier Coatings. *Complex Microstructures*, 42, 123, Proceedings of British Ceramic Society, Ed R. Stevens. (1992a) Phase Composition and Properties of Plasma Sprayed Zirconia Thermal Barrier Coatings. *J. Mater. Sci.*, 27, 611. (1992b) Microstructure of Zirconia-Yttria Plasma Sprayed Thermal Barrier Coatings. Ibid., 616.

HEINTZE, G. and McPHERSON, R. (1988a) Structures of Plasma-Sprayed Zirconia Coatings in *Advances in Ceramics:* Science and Technology of Zirconia III, Somiya et al. (Editors), Am. Ceram. Soc., Ohio, USA, Vol. 24, p 431. (1988b) Fracture Toughness of Plasma Sprayed Zirconia Coatings. *Surf. Coat. Tech.*, 34, 15.

HEUER, A. H. and RÜHLE, M. (1983) Phase transformation in ZrO_2-containing Ceramics, in *Advances in Ceramics:* Science and Technology of Zirconia II, N. Claussen et al. (Editors), Am. Ceram. Soc., Ohio, USA, Vol. 12 p 1.

HEUER, A. H., CHAIM, R. and LANTERI, V. (1987) The Displacive Cubic-Tetragonal Transformation in ZrO_2 Alloys. *Acta Metall.*, 35, 3 , 661. (1988) Review: Phase Transformations and Microstructural Characterization of Alloys in the

System Y_2O_3-ZrO_2, in *Advances in Ceramics:* Science and Technology of Zirconia III, S. Somiya et al. (Editors), Am. Ceram. Soc., Ohio, USA, Vol. 24, p 3.

HIROTA, Y. (1986) HRTEM Observation of Zirconia Ceramics. *J. Electron Microscopy,* 35, 1, 102.

HOFMANN, H., MICHEL, B., GAUCKLER, L. J. (1989) Zirconia 88: Advances in Zirconia Science and Technology, Edited by S. Meriani and C. Palmonari. Elsevier Applied Science, London, p 119.

INGEL, R. P, LEWIS, D., BENDER, B. A. and SEMKEN, S. C. (1988) Properties and Microstructures of Rapidly Solidified Zirconia-based Ceramics Alloys, in *Advances in Ceramics:* Science and Technology of Zirconia III, S. Somiya et al. (Editors), Am. Ceram. Soc., Ohio, USA, Vol. 24, p 385.

ISHIGURO, T. (1985) High Resolution Electron Microscopy of Zirconia Ceramics. *J. Electron Microscopy,* 34, 3, 215.

ISIHIZAWA, N., SAIKI, A. and TAKEHESHI, Y. (1986) Twin Related Tetragonal Variants in Yttria Partially Stabilized Zirconia. *J. Am. Ceram. Soc.,* 69, 2, C18.

IWAMOTO, N. (1985) Characterization of Plasma-Sprayed Zirconia Coatings by X-ray Diffraction and Raman Spectroscopy. *Thin Solid Films,* 127, 129.

JAMARINI, F., KOROTTEN, R., LANG, R. V., OUELLETTE, M. F., YANG, K. L., BERTRAM, R. W. and PARAMESWARAN, V. R. (1992) Compositionally Graded Thermal Barrier Coatings for High Temperature Aero Gas Turbine Components. *Surf. Coat. Tech.,* 54/55, 58.

JASIM, K. (1992) Characterization of Plasma Sprayed Layers of Fully Yttria Stabilized Zirconia modified by Laser Sealing. *Surf. Coat. Tech.,* 53, 75.

JONES, R. (1989) High Temperature Vanadate Corrosion of Yttria Stabilized Zirconia coating on Mild Steel. *Surface and Coating Technology,* 37, 271. (1991) Development of Hot Corrosion-Resistant Zirconia Thermal Barrier Coatings. *Materials at High Temperatures,* 9, 4, 228.

KOUNTOUROS, P. and PETZOW, G. (1993) Defect Chemistry Phase Stability and Properties of Zirconia Polycrystal. Science and Technology of Zirconia V, Edited by S. Bawald, M. Bannister and R. Hannink, Technomic Publishing Company, Pennsylvania, USA, p 30.

LEE, R. R. and HEUER, A. H. (1987) Morphology of Tetragonal ZrO_2 in a Ternary (Mg, Y)-PSZ. *J. Am. Ceram. Soc.*, 72, 208.

LEE, W. E. and RAINFORTH, M. (1994) Ceramic Microstructure: property and control by processing, Chapman and Hall, London, p 317.

LELAIT, L., ALPÉRINE, S., DIOT, C. and MÈVREL, M. (1989) Thermal Barrier Coatings: Microstructural Investigation after Annealing. *Mater.Sci. Eng.*, A121, 475.

LELAIT, L., ALPÉRINE, S. and MÈVREL, M. (1992) Alumina Scale Growth at Zirconia-MCrAlY Interface: A Microstructural Study. *J. Mater. Sci.*, 27, 5.

LIH, H., CHANG, E., CHAO, C. H. and TSAI, M. L. (1992) Effect of Pre-Aluminization on the Properties of ZrO_2-8wt%Y_2O_3/Co-29Cr-6Al-1Y Thermal Barrier Coatings. *Oxidation of Metals*, 38, 1/2, 99.

LIH, W. (1991) Effects of Bond Coat Pre-oxidation on the Properties of ZrO_2-8wt% Y_2O_3/Ni-22Cr-10Al-1Y Thermal Barrier Coatings. *Oxidation of Metals*, 36, 3/4, 221.

LIN, C. L., GAN, D. and SHEN, P. (1990) The Effects of TiO_2 addition on the Microstructure and Transformation of ZrO_2 with 3 and 6 mol.% Y_2O_3. *Mater. Sci. Eng.*, A129, 147.

LIU, H. S, CHEN, S. and SHEN, P. (1993) Effect of NiO Dissolution on the Microstructural Development of t'ZrO_2 with 5 mol Y_2O_3. *J. Mater. Sci.*, 28, 3991.

MAJUMDAR, R. (1991) X-ray Photoelectron Spectroscopic Studies on Yttria Stabilized Zirconia and its Surface Transformations. *Thin Solid Films*, 206, 349.

McPHERSON, R. (1989) A Review of Microstructure and Properties of Plasma Sprayed Ceramic Coatings. *Surf. Coat. Tech.*, 39, 1/3, 173.

McPHERSON, R. and HOUGHTON, M. E. (1984) Yttria-Partially Stabilized Zirconia Plasma Sprayed Coatings. *J. Aust. Ceram. Soc.*, 26, 2, 23.

MEIER, S. M. and GUPTA, D. K. (1994) The Evolution of Thermal Barrier Coatings in Gas Turbine Engine Applications. *J. Eng. Gas Turbines and Power*, 116, 250.

METCO Inc. (1984) Metco 143 Zirconia, Titania, Yttria Composite Powder. *Technical Bulletin*. Metco Inc, N. J (USA).

MICHEL, D., MAZEROLLES, L. and PÉREZ, M. (1993) Fracture of Metastable Tetragonal Zirconia Crystals. *J. Mater. Sci.*, 18, 2618.

MILLER, R. A., GARLICK, R. G. and SMIALEK, J. L. (1983) Phase Distribution in Plasma Sprayed Zirconia Yttria, *J. Am. Ceram. Bull.,* 62, 12, 1355. (1987) Current Status of Thermal Barrier Coatings-An Overview. *Surf. Coat. Tech.,* 30, 1.

MILLER, R. A., and LOWELL, C. E. (1982) Failure Mechanisms of Thermal Barrier Coatings exposed to elevated temperatures. *Thin Solid Films,* 95, 265.

MILLER, R. A., SMIALEK, J. L. and GARLICK, R. G. (1981) Phase Stability in Plasma-Sprayed Partially Stabilized Zirconia Yttria, in *Advances in Ceramics:* Science and Technology of Zirconia, A. H. Heuer and L. W. Hobbs (Editors), Am. Ceram. Soc., Ohio, USA, Vol. 3, p 241.

NETTLESHIP, I. and STEVENS, R. (1987) Tetragonal Zirconia Polycrystal (TZP)- A Review. *Int. J. High Tech. Ceram.,* 3, 1.

PANDOLFELLI, V. C., NETTLESHIP, I. and STEVENS, R. (1989a) The Influence of Titania on Stabilization and Sintering of Tetragonal Zirconia in *Complex Microstructures.* Edited by R. Stevens, Brit. Ceram. Soc., Vol. 42, 139.

PANDOLFELLI, V. C., RAINFORTH, W. M. and STEVENS, R. (1989b) Tetragonal Zirconia Polycrystals in the ZrO_2-TiO_2-CeO_2 System, in *Euroceramics,* Properties of Ceramics. Ed. G. de With, Elsevier Applied Science, London Vol. 2, p 161.

PAWLOWSKI, L., LOMBARD, D. and FAUCHAIS, P. (1985) Structure-Thermal Properties-Relationship in Plasma Sprayed Zirconia Coatings. *J. Vacuum Sci. Tech.,* A3, 6, 2494.

PETTIT, F. S. and GOWARD, G. W. (1983) Gas Turbine Applications in *Coatings for High Temperature Applications,* Ed. E. Lang, Applied Science Publishers, London, p 341.

PORTER, D. and HEUER, A. H. (1979) Microstructural Development in MgO-Partially Stabilized Zirconia (Mg-PSZ). *J. Am. Ceram. Soc.,* 62, 5/6, 298.

PRATER, J. AND MOSS, R. W. (1983) Effect of the Coating Structure on the Adherence of Sputter-Deposited Oxide Coatings. *Thin Solid Films,* 107, 455.

PYDA, W., HABERKO, K., BUCKO, M. M., AND FARYNA, M. (1992) A Study on Preparation of Tetragonal Zirconia Polycrystals (TZP) in the TiO_2-Y_2O_3-ZrO_2 System, *Ceram. International,* 18, 321. (1993) TZP in the TiO_2-Y_2O_3-ZrO_2 System, in Science an Technology of Zirconia V, S. Badwal et al. (Editors), Technomic Publishing Co., Pennsylvania, USA, p 137.

RECKZIEGEL, A. (1993) Properties and Applications of Advanced Zirconia Ceramics. *CFI Ceramic Forum International*, 63, 7/8, 378.

RÜHLE, M. (1988) TEM Studies on Phases and Phase Stabilities of Zirconia Ceramics. *Physica*, **B150**, 86.

RÜHLE, M. and HEUER, A. H. (1983) Phase Transformation in ZrO_2-containing Ceramics II: The Martensitic Reaction in t'-ZrO_2, in *Advances in Ceramics:* Science and Technology of Zirconia II, N. Claussen et a. (Editors), Am. Ceram. Soc., Ohio, USA, Vol. 12, p 14.

SAKUMA, T., YOSHIZAWA, Y. and SATO, H. (1986) The Metastable Two-Phase Region in the Zirconia-Rich part of the ZrO_2-Y_2O_3 System. *J. Mater. Sci.*, **21**, 1436.

SCHWIER, G. (1986) Plasma Spray Powders for Thermal Barrier Coating in *Advances in Thermal Spraying* Proceedings of the Eleventh International Thermal Spraying Conference, Montreal Canada, p 277.

SCOTT, H. G. (1975) Phase Relationships in Zirconia-Yttria System. *J. Mater. Sci.*, **10**, 1527.

SHIOJIRI, M., HIROTA, Y., ISSHIKI, T., MAEDA, T. and SEKIMOTO, S. (1988) A High Resolution Transmission Electron Microscopy Study of ZrO_2-CaO Films. *Thin Solid Films*, **162**, 235.

SUBBARAO, E. (1981) Zirconia-an overview, in *Advances in Ceramics:* Science and Technology of Zirconia , A. H. Heuer and L. W. Hobbs (Editors), Am. Ceram. Soc., Ohio, USA, Vol. 3, p 1.

SUN, J., CHANG, E. and WU, B. C. (1993a) Performance of CVD Al_2O_3 Intermediate Layer between Zirconia Top Coat and NICrAlY Bond Coat. *Mater. Trans., JIM*, **34**, 7, 614.

SUN, J., CHANG., WU, B. C. and TSAI, C. H. (1993b) The Properties and Performance of (ZrO_2-8wt%Y_2O_3)/(Chemically Vapour-Deposited Al_2O_3)/(Ni-22wt%Cr-10wt%Al-1wt%Y) Thermal Barrier Coatings. *Surf. Coat. Tech.*, **58**, 93.

TAKEHESHI, Y., SAIKI, A. and ISIHIZAWA, N. (1986) Analytical Electron Microscopy of Yttria Partially Stabilized Zirconia Crystal. *J. Am. Ceram. Soc.*, C3.

TAYLOR, R. (1992) Thermal Properties and Microstructure of two Thermal Barrier Coatings. *Surf. Coat. Tech.*, **54/55**, 53.

TAYLOR, R., BRANDON, J. R., MORREL, P. (1992) Microstructure, Composition and Property Relationships of Plasma-Sprayed Thermal Barrier Coatings. *Surf. Coat. Tech.*, 50, 141.

TORAYA, H. (1984a) Calibration Curve for Quantitative Analysis of the Monoclinic-Tetragonal ZrO_2 System by X-ray Diffraction, *J. Am. Ceram. Soc.*, C119. (1984b) Quantitative Analysis of Monoclinic-Stabilized Cubic ZrO_2 Systems by X-ray Diffraction. Ibid., C183.

UNAL, O., HEUER, A. H., MITCHELL, T. E. (1990) Preparation of Cross Sectional Specimens of Ceramics Thermal Barrier Coatings for Transmission Electron Microscopy. *J. Electron Microscopy Techniques*, **14**, 307.

WU, B. C, CHAO, C. H., CHANG, E., and CHANG, T. C. (1990) Effects of Bond Coat Pre-aluminising Treatment on the Properties of ZrO_2-8wt%Y_2O_3/(Co-29Cr-6Al-1Y) Thermal Barrier Coatings. *Mater. Sci. Eng.*, A124 , 215.

WU, B. C., CHANG, E., CHANG, T. C. and TU, D. (1989a) Degradation Mechanisms of ZrO_2-8wt%Y_2O_3/Ni-22Cr-1A0Al-1Y Thermal Barrier Coatings. *J. Am. Ceram. Soc.*, 72, 2, 212.

WU, B. C., CHANG, W., TU, D. AND WANG, S. L. (1989b) Microstructures, Properties and Failure Analysis of (ZrO2-8wt%Y_2O_3/(Co,Ni)-Cr-Al-Y) Thermal Barrier Coatings. *Mater. Sci. Eng.*, A111, 201.